Directional detection of WIMPs and searches for axions in extra dimensions with the MIMAC detector

Cyprien Beaufort

THÈSE

Pour obtenir le grade de

DOCTEUR DE L'UNIVERSITÉ GRENOBLE ALPES

École doctorale : PHYS - Physique
Spécialité : Physique Subatomique et Astroparticules
Unité de recherche : Laboratoire de Physique Subatomique et Cosmologie (LPSC)

Directional detection of WIMPs and searches for axions in extra dimensions with the MIMAC detector

Détection directionnelle de WIMP et recherche d'axions en dimensions supplémentaires avec le détecteur MIMAC

Présentée par :

Cyprien BEAUFORT

Direction de thèse :

Daniel SANTOS Directeur de recherche CNRS, LPSC – Grenoble	Directeur de thèse

Rapporteur·rices :

Jocelyn MONROE
Professeure, Royal Holloway – London

Igor IRASTORZA
Professeur, Unizar – Zaragoza

Thèse soutenue publiquement le **29 septembre 2022**, devant le jury composé de :

Jocelyn MONROE Professeure, Royal Holloway – London	Rapportrice
Igor IRASTORZA Professeur, Unizar – Zaragoza	Rapporteur
Elisabetta BARACCHINI Professeure, GSSI – l'Aquila	Examinatrice
Gabriel CHARDIN Directeur de recherche CNRS, Laboratoire APC – Paris	Examinateur
Frédéric MAYET Professeur, UGA-LPSC – Grenoble	Président

Contents

Acknowledgments

Although written by a single person, this thesis is the result of a multitude of collective discussions and knowledge sharing; it is a continuation of previous works and should thus be seen as the emerging part of a collective underground bubbling. I was lucky enough to start my thesis in a healthy and encouraging team, working on a well-functioning detector and with the tools at the lab needed to carry out experiments, while being surrounded by the people who built the detector. Beyond this beneficial working environment, the support of my family and friends and all the good times spent together have played a considerable role in this thesis.

Daniel, I'm very grateful for your involvement in my thesis, for your optimism and positivity, and for believing in me, often more than myself. Thank you for all that I have learned from you, and for guiding me through the twists and turns of the PhD while leaving me room for my experiments. I also thank you for having been available every time I came to see you, answering my questions and doubts, but also for taking the time to discuss non-scientific subjects and for having understood their importance to me.

I also want to thank Nadine, Olivier, and Mar for their considerable help during those years. Nadine, I don't know how many times I knocked on your door asking "do you have a few minutes?" and then having discussions way longer than a few minutes. I'm impressed by the extent of your skills from simulations to experiments. Thank you Olivier for never ruling out a hypothesis before considering it seriously. Your very precise understanding of gaseous detectors has definitely been a precious guide for me when developing SimuMimac or analyzing the many IQF campaigns. Finally, thank you Mar for your patience and pedagogy when answering my numerous questions about the axions. It is very appreciable to work on a topic knowing that whatever the difficulties we encounter, you will find a solution to them.

I here want to thank the thesis committee for reading my manuscript, for the feedback, and for the nice discussions. Thank you also Fabrice for introducing me to the MIMAC adventure; Marine for helping me in getting started and for your support at AMANDE, even when my clumsiness changed our experimental plans; Ali for always having kind words to say; Jeff, the Comimac whisperer, who can handle many difficult experiments; Charling for all the helping discussions and wise advise; Yi for the numerous skype exchanges. I also want to thank all the colleagues from the lab, in particular the ones on the third floor for the nice atmosphere. Special thanks to Lohan, besides being an excellent friend, for the countless coffee breaks at which you proposed clever solutions to my issues. I also want to thank Felix and Tiffany for your patience when I'm disorganized and for showing me unexplored corners of the lab.

On another level, although important for me, I want to thank the PhD students collective of CGT. Besides spending time with very nice people, what we have done together brought more sense to this thesis, helped me in sharing the difficulties of the PhD and energized me.

Le remerciement le plus dur à écrire, celui pour lequel les mots perdent leur sens, s'adresse à mes parents et à mes sœurs. Il n'est pas de façon de le formuler correctement tellement votre amour, notre amour, imprègne toutes les dimensions de ma vie.

Enfin, un immense merci à Léo, Nada, Lucie, Lohan, Mathou, Flo, Juliette et Zoé. Il y aurait trop de choses à dire, plein d'images me viennent en tête. J'ai une chance incroyable de vous avoir dans ma vie. Je vous aime.

Introduction

Multi-scale astrophysical and cosmological observations converge to a scenario in which the majority of the matter of the universe would be made of a non-relativistic massive particle. While the existence of dark matter (DM) is almost commonly accepted, its nature remains unknown since it still escapes detection. The experimental identification of a DM particle is then a burning challenge. In this thesis, we study the WIMP and the axion, which are often viewed as the two most compelling DM candidates. We approach the WIMP through the prism of directional detection, so far the only admitted strategy to unambiguously identify a WIMP, although this strategy of detection has faced technological challenges that have limited its spread. We will demonstrate that directional detection is now mature enough for probing WIMPs with masses down to GeV. For the axion, we propose a journey into extra spatial dimensions. Extra dimensions are theoretically motivated and, when curled up, they are experimentally allowed up to a size of 1 μm, which is quite large for particle physics. If extra dimensions exist, the axion would be free to propagate into them, leading to drastic consequences for its detection. We will revise the phenomenology of the higher-dimensional axion when it is produced in the Sun.

The MIMAC detector could simultaneously search for WIMPs and higher-dimensional axions. This gaseous detector operates at low-pressure and it measures the energy of a charged particle while it reconstructs, at the same time, its track in three dimensions. MIMAC is then a directional detector. The main limitations for directional detection appear at low energy, so this thesis focuses on extending the MIMAC scope of possibilities towards low-energy regions: our studies mainly concern particle detection with energies in the keV-range, requiring to operate the detector at high gain. In a gaseous detector, the measured signal is a combination of an electronic component and an ionic one. At high gain, the ionic signal plays a complex role that, as we will see, distorts the track reconstruction while improving the detector sensitivity. In this thesis, we dig into such a contradiction: we exploit the additional information offered by the improved sensitivity in order to compensate for the deteriorated track. By controlling the effect of the ionic signal, we develop new directional tools resulting in, to the best of our knowledge, the world-leading directional performance in the keV-range.

The extension of the MIMAC detection region towards low energy, by operating at high gain, is also a requirement for efficient detection of a higher-dimensional axion decay in the detector. While we will discuss axion detection, our work will mainly focus on the revision of the solar axion model in the frame of extra dimensions. We will see that the axions could orbit the Sun and accumulate over cosmic times, resulting in promising explanations for some puzzling solar observations while also significantly constraining a possible detection on Earth. Searching for DM is exciting and frightening at the same time because it means confronting the unknown and moving forward into the darkness. In this adventure, we have been guided by many discussions and this thesis can thus be seen as the reflect of a collective work. Besides the MIMAC team, we here emphasize the central role played by Mar Bastero-Gil in the presented revision of the solar axion model in large extra dimensions.

The thesis is articulated around three parts. The first one motivates the DM hypothesis and introduces the main elements for WIMP and higher-dimensional axion searches. In Chapter 1, we review the history of missing mass and the main observations that have built the DM hypothesis. Chapter 2 is dedicated to WIMP detection, from galactic halo models to the event rate in an Earth-based detector, with a particular focus on the differences between non-directional and directional detection. We derive in Chapter 3 some phenomenologically interesting expressions for the higher-dimensional axion, from the solar production rate to the number density as a function of the distance to the Sun.

The second part of the thesis concerns the MIMAC strategy of detection. We start by introducing in Chapter 4 the physical processes involved in particle detection with a MIMAC-like detector. Chapter 5 enters the details of MIMAC from an operating approach: how to measure the energy, reconstruct a 3D track, identify a particle, and discriminate the background. Chapter 6 presents the specificities of high-gain measurements and we introduce `SimuMimac`, a homemade simulation tool that played a crucial role in the understanding of the interplay between the electronic and the ionic signals at high gain.

After the phenomenology and the simulation works presented in the two first parts of the thesis, the

third one is dedicated to the main experimental results. Chapter 7 concerns the Ionization Quenching Factor, a crucial quantity required for determining the energy of a nuclear recoil, which we measure in an SPC based on a NEWS-G sensor, another gaseous detector sharing similarities with MIMAC. The directional performance of MIMAC in the keV-range is determined experimentally in Chapter 8, in which we develop new directional tools at high gain for reconstructing mono-energetic neutron spectra at 27 keV and 8 keV. Chapter 9 revises the constraints applying to the higher-dimensional axion and evaluates the MIMAC possibilities for detecting it. Finally, we summarise the main conclusions of the thesis and we draw the contours of possible extensions of this work and its prospects.

Part I

A journey into the dark side

Chapter 1

The dark matter puzzle

Unseen bodies may, for aught we can tell, predominate in mass over the sum-total of those that shine; they possibly supply the chief part of the motive power of the universe.

Agnes Mary Clerke – 1903 [1]

The statement that 84% of the matter in the universe would be composed of unknown particles can appear astonishing at first glance. The rise of the DM hypothesis follows a tumultuous path and it emerges from a specific context. In other words, the motivations for the existence of a hidden particle do not only depend on a set of puzzling observations, but they are also embedded into a particular historical and scientific situation. In this introductory chapter, we aim to briefly describe such a context and lay the foundation of the DM hypothesis. We start by reviewing the history of missing mass in Section 1.1 and the questions it raised. Section 1.2 is dedicated to the observational evidence for DM at multiple scales which have led to the almost unanimously accepted hypothesis of DM. In Section 1.3 we introduce the main candidates solving the DM problem, as well as alternate theories.

1.1 A brief history of missing mass

1.1.1 Early history

Dark matter is often viewed as a recent concept since it represents one of the hottest topics of modern particle physics. For instance in 2021, the website NASA/ADS refers on average more than three publications per day with "dark matter" written in the abstract. However, the idea of hidden massive objects influencing the motion of visible objects appears during the whole history of cosmology. The

first occurrences of this idea can be found in the ancient Greek cosmology [2], for instance when the Pythagorean astronomer Philolaus postulated the existence of an invisible counter-Earth, or when Ptolemy introduced an extra transparent sphere into his model in order to account for the precession of the equinoxes. While such hidden objects were not motivated by gravitational considerations, they can anyway be discussed in the framework of dark matter since they are transparent. They highlight the human "taste" for invisible objects, even in the context of science.

The prediction of the existence of an unseen companion to the Sirius star by the German astronomer Bessel in 1844 [3] is probably the first modern example of the introduction of a missing mass to explain the unexpected motion of a star [4]. The observation of the predicted Sirius B, a few decades later, can thus be interpreted not only as the first discovery of a white dwarf [5], but also as a remarkable illustration of the predictive power of the Newtonian theory. Similarly, perturbations in the motion of Uranus led the French astronomer Le Verrier to predict the existence of Neptune in 1846. His calculations were so accurate that it took less than a day of observations to discover the planet [6]. It is worth pointing out that during the 60 years preceding the discovery of Neptune, Newton's laws of gravity were seriously questioned due to the anomalous trajectories of Uranus [7]. This situation share similarities with the current one since it raises the following question: is there a missing mass explaining the motion of astrophysical bodies, or is there an issue with the gravitation theory?

The twist in the history happened when Le Verrier, strengthened by his success with Neptune, postulated the existence of Vulcan, a planet in between Mercury and the Sun in order to explain the anomalous precession of the perihelion of Mercury. As it is well known, General Relativity fixed the issue of the motion of Mercury, and Vulcan was never observed. This anecdote cautions us about possible fails in the predictive power of the Newtonian theory when applied out of its validity domain.

Some astronomers of the XVIII$^{\text{th}}$ and XIX$^{\text{th}}$ centuries were convinced of the existence of "dark stars" that could not directly be detected and they studied mechanisms that could explain the invisibility of such bodies. A famous example can be found in the works of Michell and Laplace [8] who independently postulated the existence of invisible bodies. In their view, light is affected by the laws of gravity so it should exist massive enough bodies from which light cannot escape. This is the concept of black hole, even if it relies on the wrong assumption that light motion can be described by the Newtonian gravitation law. Another example of dark bodies was faint stars, as detailed in the work of Agnes Mary Clerke [1], who were defined as stars in a senile stage that were no longer able to shine, or only feebly, a concept close to the modern definition of a white dwarf. One more example concerns dark nebulae which are dense clouds able to obscure part of the light emitted from objects behind them. This concept was first introduced at the end of the XVIII$^{\text{th}}$ century by William and Caroline Herschel [9], Caroline Herschel being considered the first occidental woman to get a salary as a scientist [10].

While more details about the history of DM can be found in references [4] and [11], we now have several elements describing the scientific context that led to the rise of the DM hypothesis. During the early history of cosmology and astrophysics, invisible objects have often been predicted from theoretical considerations or as explanations for anomalous observations. Some of such objects have later been discovered experimentally, increasing the confidence in the predictive power of the Newtonian laws.

1.1.2 The birth of the dark matter hypothesis

At the beginning of the XX$^{\text{th}}$ century, astronomers studied stellar dynamics in more detail by measuring mass distributions and velocity dispersions. It led to the modern conception of dark matter popularized during the 1930s.

Stars in a galaxy are mainly rotating in the galactic plane, but they also have a vertical motion, *i.e.* they oscillate up and down the galactic plane. Since the vertical motion is related to the gravitational force in the disk, its measurement enables determining the amount of matter in the galactic disk from gravitational effects. Kapteyn and Jeans compared such a measurement to the mass distribution expected from visible stars in order to determine the amount of dark matter (as it was already called) in the galactic disk of the Milky Way. In 1932, the Dutch astronomer Jan Oort used the same approach to more sophisticated available data. He obtained that dark matter would represent about 60% of the mass density of the galactic disk [12]. Being conservative, he claimed that this value corresponds to

Figure 1.1: The Starry Night – Vincent van Gogh – 1889

an upper limit due to his non-exhaustive counting of visible stars and could possibly be reduced to a negligible fraction. His result was quite in agreement with Jeans's study who wrote in 1922 the famous sentence "there must be about three dark stars in the universe to every bright star" [13]. The studies of the galactic disk from Kapteyn, Jeans, and Oort played an important role in the spread of the idea of dark matter in the community of astronomers.

Let us now share more details while discussing the work of the Swiss astronomer Fritz Zwicky who definitely cannot be ignored in a history of dark matter. In 1933, Zwicky measured the radial velocity (velocity component along the line-of-sight) of 8 galaxies located in the Coma cluster and he found a velocity dispersion around 1000 km/s. Zwicky decided to apply the Virial theorem of thermodynamics to determine the mass of a galaxy cluster. The Virial theorem states that the average potential energy of a stationary bounded system is twice as large as its average kinetic energy. It then gives a relation between the mass distribution of the system and its velocity dispersion. After estimating the size of the system (*i.e.* the Virial radius) and plugging his measurements of the velocity dispersion, he obtained a total mass of around 3×10^{14} $M_\odot$ for the Coma cluster [14]. However, when counting the visible galaxies in the cluster and considering a mean galaxy mass suggested by Hubble, he arrived at a cluster mass of about 10^{12} $M_\odot$. This mass discrepancy in the Coma cluster was puzzling. Zwicky interpreted it as evidence of the presence of dark matter. He also noted that without dark matter, the radial velocity of the galaxies would exceed the escape velocity, so the cluster would be unstable and one would observe galaxies "flying apart" [7]. In 1936, Smith [15] applied the procedure of Zwicky to the Virgo cluster. Based on measurements of 32 galaxies, he arrived at a mass discrepancy of a factor of ~ 200, similar to Zwicky's result for the Coma cluster. In 1937, Zwicky refined his analysis of the Coma cluster [16] using three methods: Virial theorem, gravitational lensing, and statistical mechanics; showing once again a large mass discrepancy.

The papers of Zwicky and Smith had a few impacts in the 30s, while they have likely been read by well-known astronomers of the time [7]. One reason could come from the uncertainties of the measurements, and in particular since it was not known if the Virial theorem was applicable on extragalactic distances, nor if clusters were in equilibrium (requirement to apply the theorem). But the main reason probably lies in non-scientific considerations. Zwicky was a successful astronomer [17] who brought important contributions to studies of supernovae, neutron stars, cosmic rays, gravitational lensing, *etc.*, but Zwicky was also famous for being irascible and arrogant. He was involved in several conflicts with Hubble who, at that time, had a major influence on the astronomer community. Finally, "[astronomers] were more comfortable with ignoring [Zwicky's results] than with accepting the conclusions they require" [17]. For an extensive analysis of the work of Zwicky and its acceptance into the astronomer community, we refer to Tricia Close-Koenig's thesis [7].

The 1930s are often considered as the decade of birth of the dark matter hypothesis due to observations of discrepancies between the mass retrieved from dynamical effects compared to the lumi-

nous mass of visible bodies; observations performed both at the galactic and the extragalactic scales. However, the subject lay dormant until the end of the 1970s when the dark matter hypothesis was eventually adopted [18] due to technological improvement leading to overwhelming evidence and once the astronomer community was prepared to accept the paradigm shift.

1.1.3 Epistemological views on dark matter

In the works described in the previous section and until the late '80s, dark matter refers to bodies too faint to be detected (gas clouds, dust, dwarfs, *etc.*). On the contrary, today's view on dark matter refers to non-baryonic matter. To say it briefly, we are searching for particles that are not yet known. This conception is even more radical and one must then carefully search for new particles.

Postulating the existence of an "invisible" matter seems to be contradictory to Popper's view of science that must be falsifiable, *i.e.* that an experiment should be able to validate or refute a theory. How to demonstrate the existence of something invisible? The resolution is found by applying a condition: we assume DM is not "fully invisible". This assumption is mandatory to separate science from belief: in this framework, the DM hypothesis is falsifiable and one can search for DM. But what happens if DM is "fully invisible", for instance if it is composed of a stable particle interacting only through the gravitational force? In the frame of current knowledge, that is without a robust theory of quantum gravity, it is vain to search for a purely gravitational stable particle due to the weakness of gravity (about 10^{40} times weaker than the electromagnetic force). However, one can use the logic of Ockham's razor: let us first consider the theories with the fewest assumptions that are the easiest to be falsified.

Dark matter represents a model for explaining astrophysical and cosmological observations, but it turns out to be a descriptive rather than a predictive model since the characteristics of a DM particle are unknown. Dark matter being defined negatively, that is by what it cannot be and by what it cannot do, speculations on the nature of DM are numerous and the absence of detection of a DM particle cannot prove it does not exist. However, one can consider the situation from another perspective: dark matter acts as a guide in particle physics. Physics beyond the Standard Model often postulates the existence of particles to cope with deficiencies of the Standard Model. Some of such putative particles, such as the axion or some supersymmetric particles, prove to be excellent DM candidates, even if they have not been introduced for this purpose. In increasing the theoretical motivations associated with a new particle, the DM hypothesis can set priorities in particle physics searches.

Ten years ago, the Higgs boson was detected for the first time at the LHC, completing the picture of the Standard Model. It would however be pretentious to consider that all particles have been discovered. Several clues suggest the opposite, for instance the strong CP problem or neutrino oscillations. While technological improvement is performed, detectors and telescopes are probing unexplored regions with feeble signals. If one accepts the reasonable idea that mankind has not yet discovered all existing particles, the next particle to be discovered could possibly be a DM particle.

1.2 Observational evidence for DM

In this section, we review the main observational evidence, from galactic to cosmological scales, that build the dark matter hypothesis. For more detail we refer to [19].

1.2.1 At the galactic scale

Rotation curve

One striking evidence for dark matter, and probably the most important from a historical perspective, comes from the rotation curve of spiral galaxies. A rotation curve corresponds to the profile of the circular velocity of the stars and gas in a galaxy, v_θ, as a function of their distance to the center of the galaxy, r. Newtonian dynamics teach us that v_θ evolves as a function of r and the mass profile $M(r)$. For spiral galaxies, most of the mass is contained in the bulge of the galaxy, *i.e.* close to the

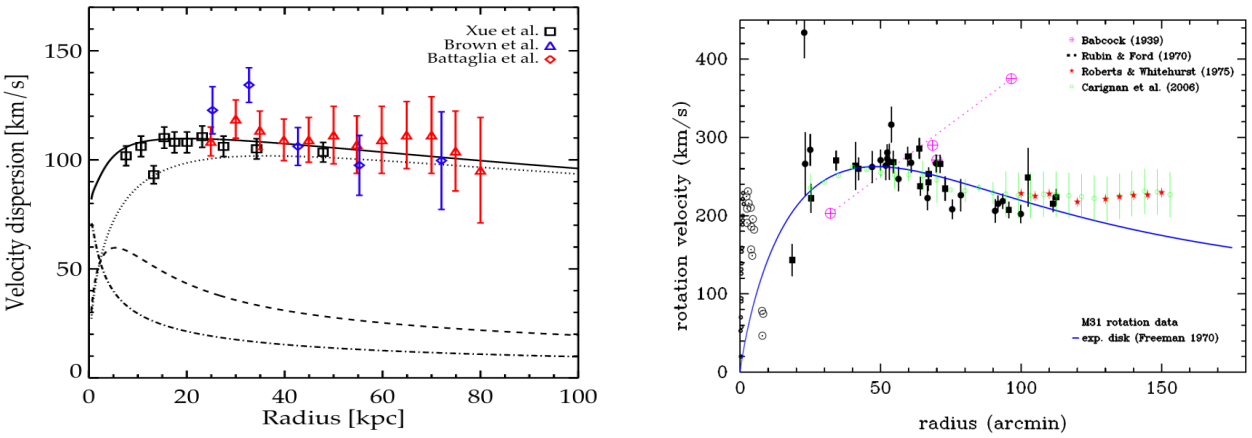

Figure 1.2: Examples of rotation curves in spiral galaxies.
Left: rotation curve of the Milky Way, figure extracted from [22]. The dot-dashed curve and the dashed curve are predictions from visible components, respectively in the bulge and the disk, whereas the dotted curve corresponds to the supposed dark matter halo. The solid curve is the sum of all three components.
Right: rotation curve of the Andromeda galaxy, figure from [4]. The solid blue line corresponds to predictions from visible components. The black dots and squares correspond to the work of Vera Rubin and Kent Ford [23] who contributed significantly in popularizing the dark matter hypothesis. One can see in the figure that Rubin's data was not sufficiently conclusive about the flatness of rotation curves, but it paved the way for additional studies and has later been extended to further radii, as also presented in the figure.

center and, for large enough r, the mass profile $M(r)$ becomes constant. In this situation, the circular velocity decreases as $v_\theta \propto r^{-1/2}$.

Measurements of $v_\theta(r)$ in spiral galaxies can be performed from Doppler shift of characteristics emission lines, for instance the HI line (21 cm line) corresponding to a transition in the energy state of a neutral hydrogen atom. Surprisingly, the measured rotation curves do not follow the expected behaviour but they instead are "flat" at a large radius. Two examples are presented in Figure 1.2. In both cases, one can see that rotation curves predicted from visible components follow tendencies that disagree with measurements. Such a discrepancy is not an isolated phenomenon since it is observed in many spiral galaxies [20, 21].

The flatness of the rotation curves at a large radius suggests the presence of a non-visible matter contributing significantly to the total gravitational potential of the galaxy. This non-visible matter would extend way beyond the visible disk, with a radius about 10 times larger, and would be distributed in a spherical halo surrounding the galaxy. More details about the halo structure will be given in Section 2.1. Without any assumption on the nature of the non-visible matter but only relying on Newtonian dynamics, the introduction of a supposed dark matter halo enables to solve the measurements discrepancies on rotation curves, as one can see for instance in the left panel of Figure 1.2. The total amount of dark matter surrounding the galaxies remains difficult to estimate [19], in particular since we do not know how far the haloes extend. However, one can show that the proportion of dark matter often dominates significantly over visible matter, exhibiting a strong inverse correlation to the galaxy luminosity [21]: in low brightness galaxies, the dominant contribution to the rotation curve is attributed to dark matter.

Gravitational microlensing

Another evidence for dark matter at the galactic scale is given by gravitational microlensing. Gravitational lensing is described by General Relativity: a massive object (lens) moving across the line of sight of a luminous source will deflect its light and one will observe a distorted image. In the case of microlensing, the mass of the lens is too small to induce well-resolved light displacement but it influences the brightness of the source. Another specificity of the microlensing regime is the assumption of a point-like lens that consequently passes by the source in a time ranging between a few hours up to a few years [24]. Observation via gravitational microlensing consists in measuring variations in the

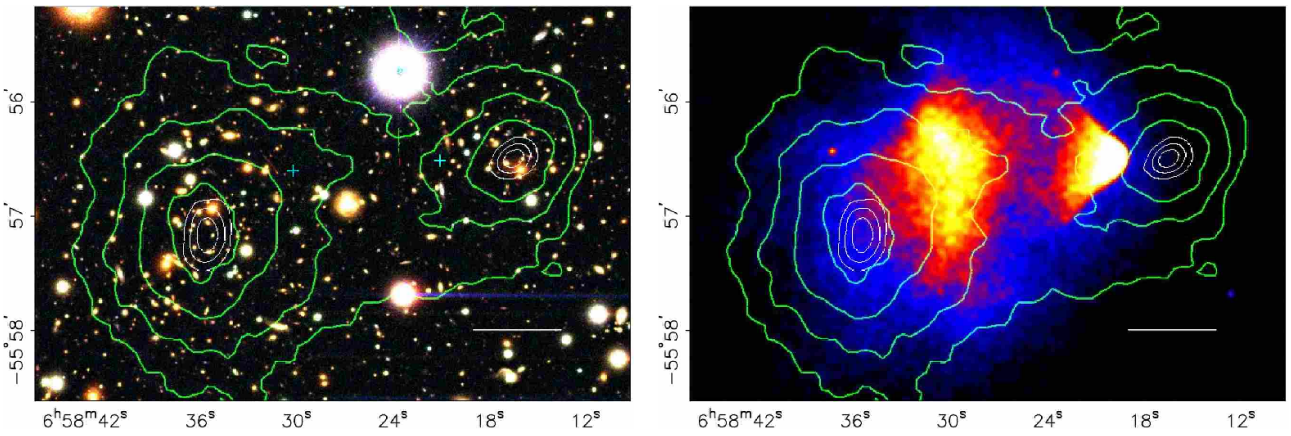

Figure 1.3: Observations of the bullet cluster, figures extracted from [30]. In both figures, the green contours show the gravitational potential reconstructed from gravitational lensing.
Left: optical measurements from the Magellan telescope.
Right: X-ray measurements from the Chandra telescope.

brightness of a luminous object.

Gravitational microlensing is of particular interest for direct detection since it maps locally the dark matter. In contrast to the rotation curve method that estimates the total mass of the galaxy, gravitational microlensing breaks the visible to dark matter degeneracy. From this method, dark matter is estimated to represent 90% of the mass of the Milky Way at the maximum of the rotation curve [25]. It is worth pointing out that the local amount of dark matter estimated from gravitational lensing and rotation curves agree [26].

Some astrophysical objects, such as brown dwarfs, neutron stars, or black holes, emit very few radiations and consequently are non-luminous. For this reason, they have been proposed as components of the dark matter halo surrounding galaxies under the generic name of MACHO (massive astrophysical compact halo object). Gravitational microlensing can be used to search for MACHOs and some of them have been discovered in our galaxy [27,28]. The searches have also established the masses of such objects and they show that MACHOs cannot contribute to more than 8% of the Milky Way halo. In other words, while it is well known that MACHOs exist, they can reasonably be ignored.

1.2.2 At the scale of galaxy clusters

The mass of a galaxy cluster can be inferred from several methods as the Virial theorem approach already discussed. Another method relies on the intergalactic gas emitting X-rays via bremsstrahlung, showing a dependency on the velocities of the gas molecules which is related to gravity in the cluster. Finally, improvements in gravitational lensing now place this method as the main one to determine the mass of a cluster. Compared with microlensing, this method considers a stable phenomenon instead of a transient one. All methods conclude that dark matter is present in substantial quantity in galaxy clusters.

The comparison between gravitational lensing and X-ray emissions can lead to very interesting results. A famous example is the study of the merging of two galaxy clusters. A galaxy cluster is composed of galaxies, plasma, and dark matter. During the collision of two clusters, galaxies and plasma behave differently. Galaxies behave as collisionless particles since they are separated by large distances so they statistically never collide. On the opposite, the intergalactic plasma has a large electroweak cross-section [29] so it decelerates and is stripped away by ram pressure. In other words, galaxies and plasma spatially decouple during cluster collisions. What about dark matter?

The so-called *Bullet cluster* is one cluster merging that brings an answer to the previous question. It is of particular interest since the collision trajectory is almost perpendicular to the line of sight and since it is one of the most X-ray luminous clusters known [31]. In Figure 1.3 one can see the expected decoupling between galaxies and plasma: the galaxies observed in the left panel (optical) are located further away from the plasma in the right panel (X-rays). The interesting feature is the position of the

gravitational potential peak observed via gravitational lensing: the majority of the mass is spatially coincident with the galaxies. Since dark matter represents the main component of the mass of the cluster, these observations are evidence of non-collisional dark matter. Similar observations concluding in the presence of non-collisional DM have also been obtained for other merging clusters [32–36]. Observations combined with numerical modelling set stringent upper limits on the self-interacting cross-section of a DM particle [35, 37].

1.2.3 At the cosmological scale

The most stringent constraints on DM and the most elegant evidence for its existence come from combinations of observations at the cosmological scale. They also allow to estimate the total amount of DM in the universe. We need to briefly introduce some elements of the standard model of cosmology (called Lambda cold dark matter, ΛCDM) in order to describe how to constrain its components.

While we have previously discussed the case of galaxies, which correspond to local inhomogeneities of matter, the distribution of matter at large scales in the universe can be considered homogeneous and isotropic. This is the cosmological principle that, coupled with general relativity, sets the basis of ΛCDM. It is convenient to introduce the cosmological density parameter, $\Omega = \rho/\rho_c$, a normalized quantity that links the energy density ρ with the critical energy density ρ_c required to have a flat universe. The total mass-energy density of the universe can be separated into three contributions [38]:

$$\Omega_{\text{tot}} \;=\; \Omega_m + \Omega_r + \Omega_\Lambda \tag{1.1}$$

- **Matter density** $\Omega_m = \Omega_b + \Omega_{nb}$ separated into baryonic matter Ω_b and a non-baryonic component, Ω_{nb}, mainly composed of dark matter.
- **Radiation density** Ω_r composed of photons and neutrinos.
- **Vacuum energy density** Ω_Λ that accounts for the accelerated expansion of the universe. This quantity is related to dark energy, an unknown form of energy with negative pressure that would counterbalance gravitational effects. It is also related to the cosmological constant Λ.

The ΛCDM model remarkably describes the evolution of the universe and it has survived an impressive quantity of precision observational tests. It is a robust, explanatory, and predictive model that parametrizes the universe with only a few variables: 6 in the most studied case (for instance in Planck's analysis [39]) while additional parameters have been proposed [38, 40]. The ΛCDM model nevertheless suffers from tensions and difficulties, for a recent review of the successes and challenges of the model we refer to [41]. We will now describe some of the cosmological probes leading to the determination of the density parameters in Eq (1.1).

Cosmic Microwave Background (CMB)

The CMB is the relic radiation that has been emitted at the epoch of photon decoupling when the universe became transparent. As long as the universe was filled with a hydrogen plasma, radiations were continuously absorbed. This absorption stopped with the formation of neutral hydrogen atoms, and photons started to propagate. At first order the CMB is isotropic but it also has small temperature anisotropies $\Delta T/T \sim 10^{-5}$ related to fluctuations in the gravitational potential, and consequently to fluctuations in density [42]. After decoupling, about 380 000 years after the Big Bang, the photons stop scattering and today's measurements of the CMB reveal the pattern of the density perturbations at the epoch of the decoupling.

The CMB is analyzed in terms of power spectra. The temperature anisotropies are usually expanded into [19]:

$$\frac{\Delta T}{T}(\theta,\phi) \;=\; \sum_{l=2}^{+\infty} \sum_{m=-l}^{+l} a_{lm}\, Y_{lm}(\theta,\phi) \tag{1.2}$$

where $Y_{lm}(\theta,\phi)$ are spherical harmonics. The variance of the temperature field as a function of the multipole l fully characterizes the anisotropies. The baryon and matter densities affect the oscillations

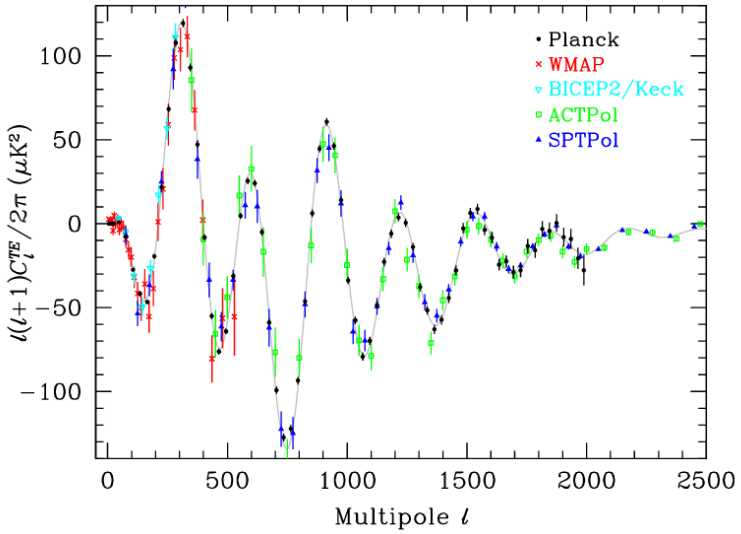

Figure 1.4: CMB power spectrum of the TE signal (Temperature and E-mode polarization) that correlates density and velocity perturbations. Several measurements are represented in the figure. The solid line corresponds to the best fit of the Planck data with the 6-parameters ΛCDM model. Figure extracted from [38].

of the photons and consequently the amplitudes and the positions of the peaks on the CMB power spectrum. A compilation of measurements of a CMB spectrum is presented in Figure 1.4. The position of the first peak determines Ω_m whereas the ratio of the first-to-second Doppler peaks determines Ω_b [43]. The amplitudes of the odd peaks increase with the baryon density [44]. Note that the cosmological parameters of the ΛCDM model are extracted from an overall fit of the data.

Baryon acoustic oscillation (BAO)

In a similar fashion to the CMB, BAOs correspond to acoustic waves formed in the primordial plasma and they teach us about the baryonic matter density. Baryonic and non-baryonic matter behave differently in the primordial plasma. Baryons experience gravity but also the opposite effect of radiation pressure. The non-perfect balance between those two effects generates baryon acoustic oscillations in the plasma. Non-baryonic matter does not directly interact with photons and is thus mostly affected by gravity. After decoupling, density perturbations due to non-baryonic matter grow in place whereas baryonic perturbations are carried away in regions where radiation forces dominate [45]. Measurements of the BAO exhibit a typical feature with a peak created by baryons that have experienced gravitational effects due to non-baryonic matter. The analysis of the power spectrum of the BAO determines Ω_m and the Hubble constant [46], so it also constrains the ratio Ω_m/Ω_b.

Big-Bang nucleosynthesis (BBN)

BBN is the synthesis of nuclei of the light elements (up to ^{7}Li) in the first few minutes of the universe. Predictions of today's abundance of such elements are in good agreement with observations and they span nine orders of magnitude [38]. The only discrepancy between predictions and observations is for the abundance of ^{6}Li and ^{7}Li.

The description of BBN relies on the Standard Model and the nuclear cross-sections that have been precisely measured in laboratory experiments. The only cosmological quantity involved in the standard BBN model is the baryonic density Ω_b [47]. Measurements of today's abundances thus constrain Ω_b.

Combined constraints on ΛCDM

The cosmological probes can be combined to constrain the cosmological parameters that will be estimated from a MCMC[1] method. An example of combinations in several parameter spaces is shown in

[1]Markov Chain Monte Carlo

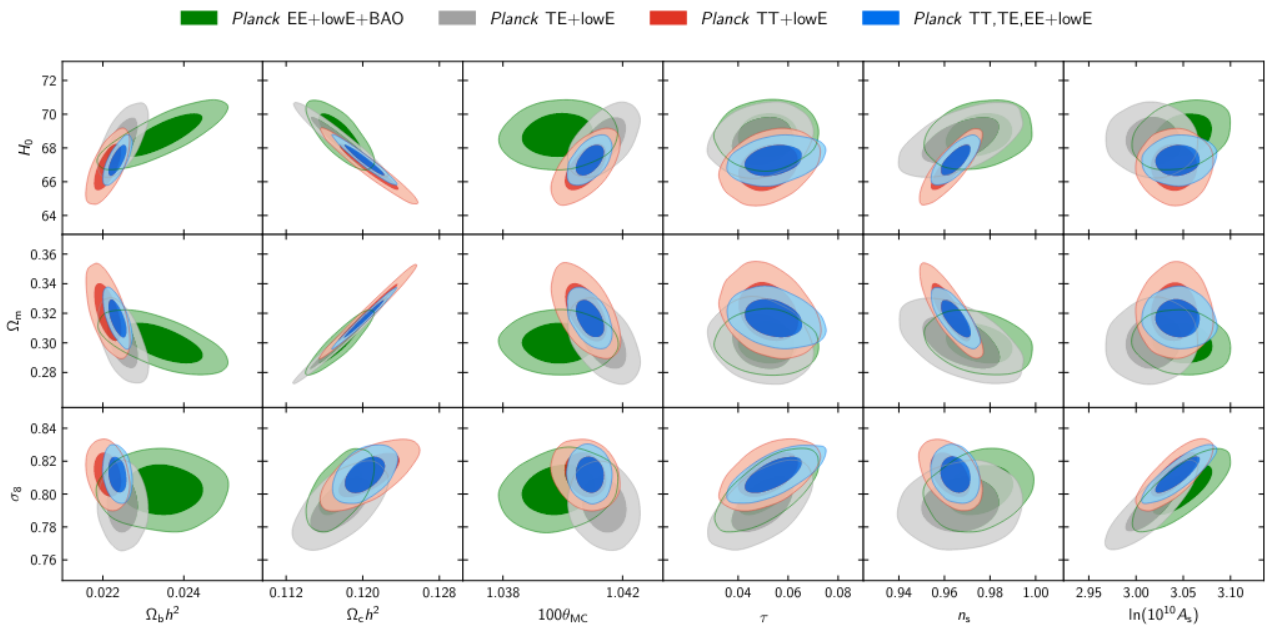

Figure 1.5: Constraints on the parameters of the ΛCDM model from combined cosmological probes. The parameters on the bottom are the free parameters of the MCMC analysis while parameters on the left axis are derived quantities. Contours at 68% and 95% confidence level are also shown. Figure extracted from the *Planck* 2018 results [39].

Figure 1.5. Recent estimations of the density parameters are presented in Table 1.1. The results are weakly dependent on the cosmological model considered. The total matter-energy density is compatible with a flat universe that is achieved for $\Omega_{\text{tot}} = 1$.

Component	Density parameter	Planck results 68% limits
Non-baryonic matter	Ω_{nb}	0.2607 ± 0.0019
Baryonic matter	Ω_b	0.0489 ± 0.0003
Radiation	Ω_r	$\sim 9 \times 10^{-5}$
Vacuum energy density	Ω_Λ	0.6889 ± 0.0056
Total matter-energy density	Ω_{tot}	0.9993 ± 0.0019

Table 1.1: Cosmological density parameters from the *Planck* 2018 results [39]. The results are the best-fit values obtained from a combination of CMB spectra, CMB lensing, and BAO. The helium mass fraction is predicted from BBN.

The analyses of several sources of data at cosmological scales indicate that only $\sim 5\%$ of the matter-energy content of the universe is formed of baryonic matter and relativistic particles. In other words, 95% of the energy content of the universe is still unknown. Dark matter represents 26% of the total energy budget and 84% of the matter content of the universe.

Structure formation

Let us address the question of how large-scale structures, such as galaxies or galaxy clusters, are formed in the universe. Several models are under study and dark matter plays the central role in all of them. The approaches usually rely on N-body simulations starting from the initial conditions of a primordial universe and studying its evolution.

Before decoupling, the universe is homogeneous while there exist some density perturbations. Let us see how the nature of DM influences the evolution of the density perturbations. At the decoupling, if

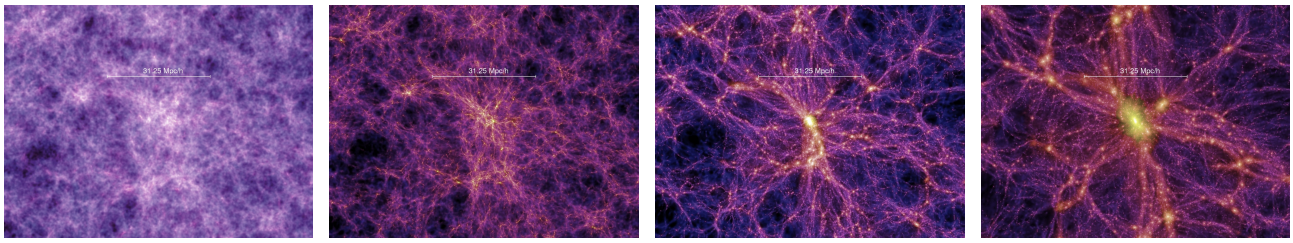

$z = 18.3$ ($t = 0.21\,\mathrm{Gyr}$) $z = 5.7$ ($t = 1.0\,\mathrm{Gyr}$) $z = 1.4$ ($t = 4.7\,\mathrm{Gyr}$) $z = 0$ ($t = 13.6\,\mathrm{Gyr}$)

Figure 1.6: Millennium simulations of the time evolution of a region in the universe. From Max-Planck Institute webpage, credit Springel et al.

the DM particles are relativistic (we talk about *hot* dark matter, HDM), the radiation pressure is large enough to erase density perturbations on small scales (smaller than scales forming galaxy clusters) and large-scale gas structures are first formed. Such structures gravitationally collapse as the universe cools down and give rise to smaller structures like galaxies. However, this "top-down" scenario has been ruled out since simulations show that an HDM-dominated universe would form structures that significantly differ from observations [48].

The currently favoured scenario is made of *cold* dark matter, CDM, meaning that the DM particles are non-relativistic at the time of structure formations. The successful ΛCDM model relies on this assumption. In this case, structures grow hierarchically from small clumps that merge to form galaxies and later galaxy clusters due to gravitational instabilities. This "bottom-up" scenario is supported by several simulations such as Millennium [49], ν^2GC [50], and Illustris [51]. They start from a set of initial conditions based on cosmological observations (as the *Planck* results) filled with billions of particles and they trace the evolution of the universe in regions of a few billion light-years wide. An example of the results of the Millennium simulation is presented in Figure 1.6.

Simulations based on a CDM-dominated universe very successfully reproduce the observed large-scale structures in the universe even if they obtain some discrepancies at galactic and sub-galactic scales [49, 52, 53]. This is a strong indication that cold and collisionless dark matter would be the key driver of structure formation in the universe.

1.3 What's the matter?

We have previously described the overwhelming observational evidence for the existence of DM. However, the nature of DM remains unknown. DM particle still escapes detection for two main reasons: first, dark matter is *dark*, meaning that it rarely produces signals in a detector; second, the requirements for a decent DM candidate can be fulfilled by multiple models so a large number of candidates continue to be proposed.

The main requirements for a DM candidate are the following:

- *Massive.* DM must necessarily be massive since we observe its gravitational influence.
- *Feebly interacting.* DM should only interact very feebly with Standard Model particles, or not interact at all. It implies that DM is probably electrically neutral and not color-charged.
- *Stable.* The lifetime of a DM particle must at least exceed the age of the universe since we still observe its gravitational influence.
- *Non-baryonic.* Cosmological observations previously detailed show that dark matter is non-baryonic.
- *Not hot.* The velocity of a DM particle at the epoch of decoupling should be compatible with structure formation.
- *Abundant.* The present quantity of DM particles should match the observations.

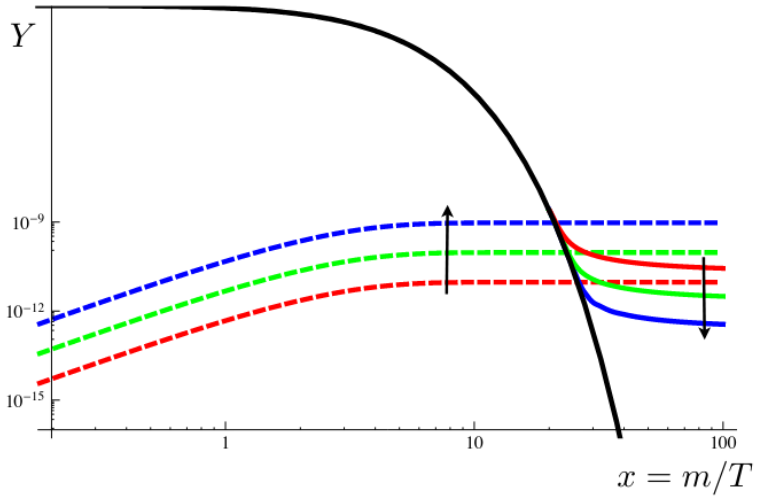

Figure 1.7: Evolution of the DM yield Y as a function of $x = m/T$ describing the time. The *freeze-out* scenario is represented in solid coloured and the *freeze-in* one in dashed coloured. The black solid line illustrates the case of a DM density at equilibrium. The arrows indicate the effect of increasing the interaction rate between DM and SM particles. The three colors correspond to three different coupling values between DM and SM particles. Figure extracted from [58].

The conditions that a DM candidate must fulfill are mainly defined negatively: from observations, we progressively establish what DM cannot be. Very interestingly, it is now certified that dark matter cannot be any known particle. For instance, neutrinos were initially proposed as non-baryonic DM since they have the "undisputed virtue of being known to exist" [54]. However, progress in cosmological observations ruled them out for being hot and not abundant enough. Searching for DM represents then a window toward the intense topic of physics Beyond the Standard Model (BSM).

1.3.1 The zoo of candidates

A considerable number of DM candidates have been proposed over the years, see for instance [19], [55] and [56]. Most of them are connected to problems in particle physics. We will here briefly introduce some candidates.

Let us first give a few words about DM genesis, *i.e.* about how the observed DM abundance can arise from the content of the early universe. We describe the two main proposed mechanisms: the *freeze-out* and the *freeze-in* scenarii. If the coupling to SM particles is large enough, DM can reach thermal equilibrium with SM particles in the early universe. DM particles interact and annihilate into lighter species as long as the interaction cross-section is competitive compared to the universe expansion rate. At some point, DM decouples to SM particles and the DM comoving number density reaches a constant value. This is the *freeze-out* scenario. On the contrary, in the *freeze-in* scenario, the DM coupling to SM particles is too small to reach the thermal equilibrium in the early universe. DM abundance is then initially small but it continuously increases due to DM production from the decay or annihilation of SM particles. The DM abundance eventually freezes to a constant value when SM density becomes small due to Boltzmann suppression. This asymptotic value is called *thermal relic density* and it corresponds to the number density of DM particles that survive to the present day. Figure 1.7 shows simplified schematics of the two mechanisms. More details on DM genesis and additional production mechanisms can be found in [57].

Feebly Interacting Massive Particle (FIMP)

FIMPs are particles with tiny interaction with SM fields and are consequently produced by the freeze-in mechanism. The most famous FIMP is the sterile neutrino. We know from the detection of neutrino oscillations that neutrinos are massive whereas they are treated as massless in the SM. One way to fix the contradiction is to introduce right-handed neutrinos having no interaction with SM gauge fields,

hence the name *sterile* neutrino. Sterile neutrinos with masses in the keV-range could play the role of DM [59]. If sterile neutrinos exist and are responsible for both dark matter and baryon asymmetry, then one could use the anthropic principle to explain why there are, at least, three generations of fermions [60].

FIMPs encounter increasing popularity, in particular because the tiny FIMP-SM interactions would be mediated by heavy fields ($10^{10}-10^{16}$ GeV) that appear in some theories BSM as in Grand Unification Theories (GUTs) or in the seesaw mechanism. The right DM abundance could be obtained from a FIMP freeze-in scenario, which has recently been called the "FIMP wonder" [61].

Weakly Interacting Massive Particle (WIMP)

The WIMP is probably the most studied DM candidate. WIMPs are typically produced thermally via the freeze-out mechanism. The WIMP is a class of massive particles with interactions with SM particles of the order of the weak interaction. In other words, the annihilation cross-section of the WIMP is approximately set by the weak scale, $\langle \sigma_A v \rangle \sim \alpha^2/M^2_{\text{weak}}$, where α is the fine-structure constant, and the WIMP mass typically ranges from MeV to TeV. Very interestingly, when considering DM as WIMP in the freeze-out mechanism, the predicted relic density corresponds to the magnitude of the observed one [62,63]. This coincidence is called the "WIMP miracle" and has strongly contributed to turning the WIMP into the leading DM candidate.

We must point out that the "WIMP miracle", although striking, is somehow a simplified picture. We refer to [64] for constructive criticism on this point. For instance, the relevant quantity to achieve the correct relic density is the ratio between the coupling and the WIMP mass. One can still obtain the observed thermal relic density for a wide range of masses and coupling. Note also that freeze-out is not the only way to produce WIMPs and it sometimes occults other processes. Nevertheless, the WIMP miracle is a powerful idea as long as it is stated as: a WIMP particle, having mass and coupling comparable to the SM ones, can yield the observed DM abundance.

WIMPs are predicted in multiple BSM theories, for instance, the Two Higgs Doublet models [65], the Little Higgs models [66], the Twin Higgs models [67], or also in theories with extra dimensions [68]. The most famous theoretical framework predicting WIMPs is supersymmetry (SUSY). SUSY is a spacetime symmetry that relates bosons to fermions, so it turns a bosonic state into a fermionic one, and vice-versa. Each particle from the SM is associated with a SUSY particle called a *superpartner*. The main motivations for SUSY are the gauge coupling unification at high energy and a framework to solve the hierarchy problem [69, 70]. So far, no SUSY signal has been observed at LHC. However, the recent development of the SUSY models, related to string theory or the CP problem, are still well-motivated and relevant [71, 72].

We here briefly introduce the neutralino, a SUSY particle considered as the leading WIMP candidate. We restrict ourselves to the framework of the Minimal Supersymmetric Standard Model (MSSM), a low-energy SUSY model that leads to the minimal SUSY particle content consistent with phenomenology. Fermions are associated with bosons, for instance the squarks or the sneutrinos. The gauge fields are associated with fermionic partners: the bino $\tilde{B}$ and the winos $\tilde{W}^3$, $\tilde{W}^+$, $\tilde{W}^-$. Two Higgs doublets are required in the MSSM to set the mass of all fermions. It leads to 5 free Higgs states that are associated with their fermionic partners, the higgsinos, in particular the two superpartners of the neutral Higgs $\tilde{H}^0_1$ and $\tilde{H}^0_2$. As in the SM, after the electroweak symmetry breaking, gauge eigenstates with identical quantum numbers mix and one can obtain the physical mass eigenstates by diagonalization of the mass matrix. In this process, bino, wino, and neutral higgsinos combine to give 4 neutralinos. The lightest neutralino, $\tilde{\chi}^0_1$, can be expressed as [19]:

$$\tilde{\chi}^0_1 = N_{11}\tilde{B} + N_{12}\tilde{W}^3 + N_{13}\tilde{H}^0_1 + N_{14}\tilde{H}^0_2 \tag{1.3}$$

The neutralinos are electrically neutral, do not have a color charge, and interact with SM particles with the strength of the weak interaction. The $\tilde{\chi}^0_1$ neutralino, being the lightest one, is a stable particle. This is a direct consequence of the introduction of the invariance of a new symmetry, called *R-parity*, that conserves the baryonic number and the leptonic number in SUSY, as in the SM. The expected mass of $\tilde{\chi}^0_1$ is model-dependent, but it is mainly constrained between 50 GeV and 600 GeV [38]. The lightest neutralino exhibits thus all required properties for an ideal cold dark matter candidate.

Self-Interacting Dark Matter (SIDM)

The CDM model, while remarkably explanatory at large scales, fails to describe some observations at the sub-galactic scale [73]. As an example, simulations based on collisionless CDM predict the existence of massive dark matter subhaloes around the Milky Way, so massive that they should form stars. Surprisingly, the most massive subhaloes observed in the Milky Way are not associated with bright satellites [74], *i.e.* they failed forming stars, whereas some lighter subhaloes are. This is known as the *too big to fail* problem. One way to solve the discrepancies between observations and simulations is to introduce self-interacting DM particles. In this case, heat is transferred from the hotter outer part of the halo to the colder center. A SIDM scenario would make no difference with ΛCDM at a large scale but it can fix some issues at a sub-galactic scale [75].

SIDM is characterized by the ratio σ/m of the self-scattering cross-section per unit particle mass. The DM self-interaction can in principle be independent of the DM-SM interaction, so direct detection experiments do not constraint σ/m. Constraints mainly come from astrophysical considerations, for instance by studying the Bullet cluster previously described [76]. The proposed and experimentally allowed ratio to solve small-scale issues lies around $\sigma/m \simeq 0.1$ cm^2/g (~ 0.2 barn/GeV) [77]. This value is very large compared to a usual particle physics value. For instance, the expected σ/m of a WIMP is around 10^{-14} barn/GeV. The SIDM cross-section would then be comparable in magnitude to nuclear cross-sections for visible matter [78], depending on the mass of the particle. It has been shown that a SIDM particle with mass at the GeV scale or below, so a strongly-interacting massive particle (SIMP), could be produced thermally in the early universe and could match the observed value for the DM relic density [79]. Ironically this is called the "SIMPlest miracle".

Axion-Like Particle (ALP)

The ALPs are hypothetical massive bosons, scalar or pseudoscalar, which are predicted in several extensions of the SM [80, 81]. The ALP is a generic class of particles that arise from the spontaneous breaking of a global $U(1)$ symmetry at an intermediate scale. The ALP is defined as having a non-trivial relation between its mass and its coupling to photons. For this reason, it appears as a generalization of the axion proposed to solve the strong CP problem. We will study the axion in Chapter 3 so we here only state some important remarks while more detail will be presented later. Even if ALPs were at first not postulated to address the dark matter problem, they are among the most compelling CDM candidates. They would be non-thermally produced in the early Universe and they would interact feebly with SM particles since such interactions are suppressed by the scale of the ALP symmetry breaking [82, 83].

The expected ALP mass ranges over more than twenty orders of magnitude depending on the considered models. The standard axion is usually considered as having a mass around 10 μeV [84] and strong bounds on ALP properties arise from astrophysical and cosmological considerations [85–87], in particular in the intermediate mass range (keV-MeV). This mass range receives increasing experimental interest [88–90] since such massive ALPs could play a role in the abundance of light elements produced during the BBN [91], or could explain a resonance observed in particular nuclear transitions in atoms [92, 93]. The recent excess discovered by the direct detector Xenon1T stimulated the discussion about ALPs of intermediate mass [94–96].

We restrain our visit to the zoo of DM candidates to this brief presentation although the above classification is far to be exhaustive. In this work we will address in detail WIMP and ALP, since they are the two most studied DM candidates and since the MIMAC detector could search simultaneously for both of them.

1.3.2 Alternate theories

The astrophysical and cosmological observations described in Section 1.2, taken as DM shreds of evidence, rely on gravitational theories: Newtonian Dynamics (ND) or General Relativity (GR). On this basis, one arrives at the conclusion that there is a large amount of missing mass in the universe.

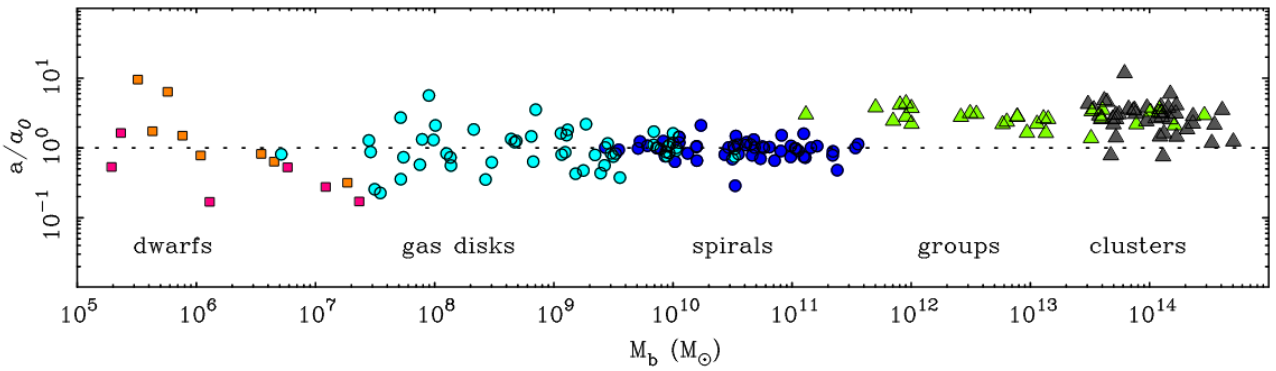

Figure 1.8: The acceleration parameter a/a_0 versus the baryonic mass for several extragalactic systems. Figure extracted from [99].

Alternatively, one can modify gravitational theories to account for the mass discrepancies without introducing any dark particle. Such an alternate paradigm has been proposed in the 80s, with a strong interest in the leading theory called Modified Newtonian Dynamics (MOND). In the MOND view, DM does not exist and the observed mass anomalies are due to incorrect extrapolation of standard theories of gravity at scales where they have not been independently tested [97]. For a brief introduction to MOND theories we refer to [98], and to [99] for extensive details.

The backbone of MOND is to consider that ND and GR do not correctly describe weak-field dynamics, *i.e.* systems with low accelerations (from galactic scale and above). The boundary between MOND and GR/ND is described by a_0, an acceleration constant that plays a similar role that $\hbar$ for separating classical and quantum contexts, or that c for separating relativity and classical mechanics. At high acceleration, for $a \gg a_0$, MOND recovers standard dynamics. In the other case, when $a \ll a_0$, the force of gravity scales as $F \simeq ma^2/a_0$. MOND is then considered as an effective theory of a still unknown larger framework. The value of $a_0 \simeq 10^{-10}$ m s^{-2} [98] is determined from a large set of observations and enables an interpretation of some measurements over ten decades of baryonic mass, as presented in Figure 1.8. Interestingly this order of magnitude for a_0 was proposed in the pioneer MOND paper [100] and remains forty years later. The acceleration constant is related to cosmological quantities via the relation $2\pi\, a_0 \simeq cH_0 \simeq c^2 \left(\Lambda/3\right)^{1/2}$ where H_0 is the Hubble constant and Λ the cosmological constant.

At the galactic scale, MOND is explanatory and predictive since a dozen of tests of the MOND theory at this scale has been successfully performed [97,99]. The initial motivation for MOND was the explanation of the flat rotation curve in spiral galaxies. A direct consequence of the MOND theory concerns the Baryonic Tully-Fisher relation (BTF) that relates the baryonic mass of a galaxy, M_b, to its flat rotation velocity, V_f, via the relation $M_b \propto V_f^x$. MOND predicts a slope of $x = 4$ exactly, no matter the size or the surface brightness of the galaxy, since only the total mass of the baryons plays a role and not their distribution in the galaxy. While some measurements indicate a slope of ~ 4 for intermediate mass galaxies [101, 102], recent measurements on a diversified sample led to a slope closer to ~ 3 [103] . Recently, the observation of the radial acceleration relation (RAR) [104] in more than 150 galaxies has been interpreted as one more observed prediction of MOND. The RAR states the existence of a tight correlation between the dynamical mass of a galaxy and its baryonic mass. In other words, it indicates that baryons are responsible for the dynamics of the galaxy. This observation seems in opposition with the DM hypothesis while being predicted by MOND. However, in the MOND view the RAR should be universal whereas it is not observed at the scale of galaxy clusters [105].

Several MOND theories have been proposed over the years, most of them trying to build a relativistic framework for MOND [4]. One challenge was to describe gravitational lensing, which has been achieved fifteen years ago. However, most relativistic MOND theories introduce new fields, arbitrary functions, and free parameters [99], which limits their predictive power and indicates that they are at best effective theories. For these reasons, the MOND paradigm is still limited in making predictions and explanations at the cosmological scale and for structure formation. One of the strongest

limitations of MOND theories is the lack of explanation of the CMB power spectrum. While the ratio between the first and second CMB peaks can be derived from a no-CDM model, the third peak should be small in a baryon-dominated universe [106]. It is only since 2021 that a MOND theory has been able to fit the CMB data through a new relativistic extension [107]. Some previous solutions required the introduction of a sterile neutrino [108], *i.e.* a DM particle.

MOND theories play a considerable role in challenging the DM hypothesis. They push further the contours of our understanding of the mass discrepancies in the universe. However, even if remarkably predictive at galactic scales, MOND theories suffer from a lack of predictions at the cosmological scale. As an important drawback, MOND theories require the introduction of cold DM, although about ten times less than in the DM picture [109]. A no-CDM MOND model inevitably fails to achieve a scenario for structure formation allowed by observational constraints [110]. Once again we must mention the *Bullet cluster* described in Section 1.2. The fact that the gravitational mass of the merging clusters coincides with the galaxies' positions supports the CDM hypothesis whereas such observation is hardly explainable in the case of modified gravity and it requires extensions of MOND accounting for non-trivial geometries [111, 112].

The MOND picture suffers from several inconsistencies and failures to explain observations. Its relativistic extensions require *ad hoc* parameters and many models exist, which makes difficult to determine MOND predictions. One must also mention that modifying Newtonian laws leads to drastic consequences such as, for instance, violation of the cosmological principle. For a detailed review of the MOND cosmological difficulties we refer to the quite old but complete article of [113]. Finally, we point out that the need for dark matter (or modified gravity) occurring for galaxies with acceleration around $2\pi\, a_0 \simeq cH_0$ also appears in CDM models. Such an acceleration value would correspond to the transition between DM-dominated systems to luminous matter-dominated systems [114].

Alternate theories to DM, in particular MOND as the leading one, must be seriously considered and investigated. Firstly because, even if less explanatory than CDM, they are not ruled out. Secondly, they push further our understanding of gravity and the description of the missing mass problem. Thirdly, some models try to incorporate both CDM and MOND, for instance *MONDian dark matter* that behaves as MOND at the galactic scale, and as CDM at larger scales [115].

Summary

The missing mass problem pointed out almost a century ago remains one of the most active topics in particle physics. Postulating the existence of unseen bodies for explaining the motion of visible matter in the universe has been commonly used over the history of astronomy. This approach led to significant progress, for instance the discovery of Neptune, but it also sometimes failed when the Newtonian theory was applied out of its validity domain. The modern conception of dark matter was popularized during the 1930s when several astronomers observed discrepancies between the visible and the total mass of some galaxies and galaxy clusters. While commonly accepted today, it took decades for the DM hypothesis to be spread among the astronomers' community. Let us quote Vera Rubin on this point from an interview in 1989 [116]: *I think many people initially wished that you didn't need dark matter. [...] But I think that observations were undeniable enough so that most people just unenthusiastically adopted it.* The paradigm shift described in this citation can presently be considered with enthusiasm since the search for DM particles often acts as a guide for theories Beyond the Standard Model.

Decades of observations have drawn the contours of the DM hypothesis, setting more and more constraints on the models. Observations performed at multiple scales, from the galactic scale up to the cosmological one, and from multiple probes such as CMB, gravitational lensing, baryon acoustic oscillations, or Big-Bang nucleosynthesis, converge to the same conclusion: 84% of the mass content of the universe seems to be composed of non-baryonic matter. This DM would have played a central role in the formation of the structures that we observe today in the universe. The requirements for a dark matter candidate are loose: a massive stable particle, feebly interacting with SM particles, non-baryonic, non-relativistic, and being produced abundantly. Many theoretical models predict the existence of such particles, having specificities so they can be searched by experiments.

While strongly debated for a long time, the DM hypothesis is now commonly admitted although

some physicists dig into gravity to find alternatives. Detectors are improving their abilities and are probing new phase space regions day after day. The following years, perhaps the next decade, will be decisive for the DM problem. The detection of a DM particle would cause incredibly fruitful progress in multiple fields of physics. However, if DM continues to escape detection, the community would at some point need to readjust the course of its searches. By making a parallel with the already mentioned *too big to fail* problem for stars formation in galaxies, we can say that we have entered into an epistemological era where the DM hypothesis received so much support that its failure, if it happens, would have drastic consequences.

Chapter 2

Direct and directional detection of WIMP

"Danglard, can you see it?" said Adamsberg in a level tone of voice. "The Shade?"
[...]
"It's there, Danglard. It's hiding the light. Feel it? It's surrounding us, looking at us."
"A dark presence?" he suggested.
"Something like that. All around us."

Fred Vargas [117]

Astrophysical and cosmological observations indicate that DM would form haloes surrounding galaxies, the Milky Way (MW) among them. The Earth's motion around the galactic center produces a flux of DM particles in an Earth-based detector. It thus implies that experiments can detect DM by *direct means*: by measuring *in situ* DM properties like mass, interaction cross-section, lifetime, *etc.* This *direct detection* strategy offers a large set of methods to search for many different DM candidates, from DM-nucleus scattering to DM decay inside a detector. The main advantage of this approach is the control of the background in specially designed experiments to access detection of rare events.

Direct detection is one of the three strategies for WIMP searches, along with indirect detection and WIMP production in colliders. Indirect detection searches for Standard Model particles produced either by WIMP annihilation or by WIMP decay, and that could be detected on Earth or by spatial telescopes [118]. It uses astrophysical probes, such as γ-rays, neutrinos, or cosmic rays, to observe

a signal that could not be explained by other means than DM. The collider strategy of detection consists in producing WIMPs by colliding Standard Model particles in high-energy collisions [119]. Since DM particles would escape detection, one standard approach to probe the dark sector consists in searching for a missing transverse momentum. Although indirect detection and collider searches are two promising strategies, and complementary to direct detection, their description is out of the scope of this work and we only mention them for completeness.

Direct detection usually refers to the measurement of the energy released by a nuclear recoil induced by a DM-nucleus scattering, *i.e.* by an elastic collision between a DM particle and a nucleus of the detector. We will show how this method, while very powerful for setting constraints on DM properties, is limited by an irreducible background and does not provide tools for an unambiguous DM detection. However, any DM-nucleus scattering will induce a nuclear recoil with an anisotropic angular distribution correlated with the Earth's motion [120, 121]. The simultaneous measurements of the energy and the direction of a DM-induced nuclear recoil would lead to the identification of a DM particle without ambiguity. This is the principle of *directional detection* initially proposed by David Spergel [122] in the case of WIMP. In this chapter, we will limit our discussions to WIMPs although similar analyses can be performed for any DM particle producing elastic scattering on a nucleus. We start by describing the phenomenology of the WIMP in Section 2.1, from the galactic halo to the WIMP-nucleus scattering event rate. In Section 2.2 we dedicate particular attention to the principles of non-directional direct detection as well as their limitations. The paradigm of directional detection is presented in Section 2.3 where we show how it allows to detect without ambiguity a WIMP and we propose a state of art of directional detection in Section 2.4.

2.1 Phenomenology of the WIMP

2.1.1 The galactic WIMP halo

Direct detection of WIMP depends on the spatial and velocity distributions of DM particles in the galaxy. The model of the DM halo surrounding the Milky Way thus plays an important role in WIMP detection. In the standard approach, the halo can be considered as a gas of collisionless and self-gravitational particles whose distribution in the phase-space evolves according to the Boltzmann equation [123]:

$$\frac{\partial f}{\partial t} \; + \; \mathbf{v} \cdot \nabla f \; - \; \nabla \phi \cdot \frac{\partial f}{\partial \mathbf{v}} \; = \; 0 \tag{2.1}$$

where ϕ is the gravitational potential and $f(\mathbf{r}, \mathbf{v}, t)$ is the distribution function. Since the volume of a detector, V, is negligible compared to the DM halo volume, the detector will be sensitive to the velocity distribution of the WIMPs:

$$f(\mathbf{v}) = \frac{1}{V} \int d^3\mathbf{r}\, f(\mathbf{r}, \mathbf{v}, t_0) \tag{2.2}$$

with t_0 the current time. Modelling the DM halo consists in determining the distribution function, $f(\mathbf{r}, \mathbf{v}, t)$, by solving the Boltzmann equation Eq. (2.1) coupled with the Poisson equation used to relate the gravitational potential to the distribution function:

$$\nabla^2 \phi \; = \; 4\pi G \rho(\mathbf{r}) \; = \; 4\pi G \int d^3\mathbf{v}\, f(\mathbf{r}, \mathbf{v}, t) \tag{2.3}$$

where G is the gravitational constant and $\rho(\mathbf{r})$ is the WIMP density. The main difficulty is to develop halo models that agree with astrophysical constraints and N-body simulations, keeping in mind that several models can lead to significant differences in the predicted event rate in a detector [124]. Let us discuss the *Standard Halo Model* (SHM) that assumes that the halo is an isotropic and isothermal sphere with a density profile evolving as $\rho(r) \propto 1/r^2$. Such assumptions lead to a galaxy rotation velocity that remains constant as a function of the distance r to the galactic center, as discussed in the previous chapter. One can show that the velocity distribution in the rest frame of the galaxy is given

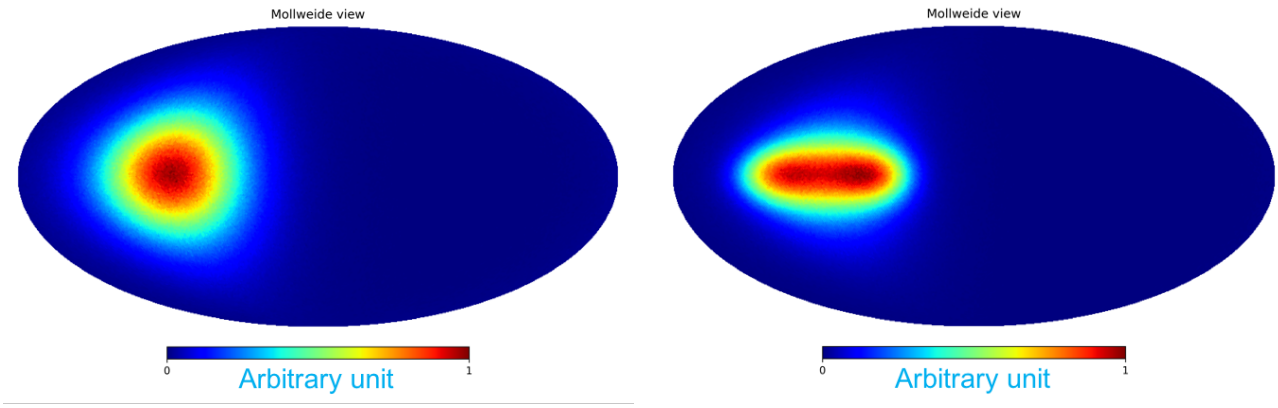

Figure 2.1: Mollweide projections of the galactic distribution of the WIMP signal for the two-component halo described by Eq. (2.5). The left plot corresponds to pure halo component model with $r = 0$; whereas the right plot is obtained with $r = 0.5$.

by a Maxwellian distribution [125]:

$$f(\mathbf{v}) \;=\; \frac{N}{(2\pi\sigma_v)^{3/2}}\,\exp\big(-\frac{\mathbf{v}^2}{2\sigma_v^2}\big) \tag{2.4}$$

where N is a normalization constant and where the expression is only valid for velocities lower than the escape velocity, otherwise the halo extends to infinity. The velocity dispersion σ_v can be related to the circular speed $\sigma_v = v_c/\sqrt{2}$, with a value usually of $v_c = 220 \pm 20$ km/s determined from measurements of the Milky Way rotation curve. In the SHM, the historically used value for the local WIMP density is of order $\rho_0 \simeq 0.3$ GeV/cm^3.

While the SHM is commonly used in data analyses, it is an approximated model, and N-body simulations of galaxy formation deviate systematically from it [38, 125]. They instead favour halos that are anisotropic, triaxial (for which $\sigma_{v_x} \neq \sigma_{v_y} \neq \sigma_{v_z}$) and that contain substructures; we refer to [126] for a detailed review. The goal is to determine the velocity distribution from observation, as done recently for instance in [127] where they used the latest data released by the Gaia satellite to infer the DM distribution in the vicinity of 8 kpc from the center of the Galaxy, which is around the Solar system. They traced the galactic DM by stars and found that the Milky Way halo has two major components:

$$f(\mathbf{v}) = \xi_{\rm h} f_{\rm h}(\mathbf{v}) + \xi_{\rm s} f_{\rm s}(\mathbf{v}) \tag{2.5}$$

where $\xi_{\rm h,s}$ is the ratio factor that quantifies each component satisfying $\xi_{\rm h} + \xi_{\rm s} = 1$. While $f_{\rm h}(\mathbf{v})$ is the triaxial Gaussian distribution halo component, $f_{\rm s}(\mathbf{v})$ is a substructure component that could be formed by a younger merger event. The latter component can be characterized by a double Gaussian, which only takes opposite parameters in the radial direction, and other parameters are the same.

$$f_{\rm h}(\mathbf{v}) \propto \mathcal{N}\left(\boldsymbol{\mu}_{\rm h}, \boldsymbol{\Sigma}_{\rm h}\right), \quad f_{\rm s}(\mathbf{v}) \propto \tfrac{1}{2}\left[\mathcal{N}\left(-\boldsymbol{\mu}_{\rm s}, \boldsymbol{\Sigma}_{\rm s}\right) + \mathcal{N}\left(\boldsymbol{\mu}_{\rm s}, \boldsymbol{\Sigma}_{\rm s}\right)\right] \tag{2.6}$$

Here $\mathcal{N}(\boldsymbol{\mu}, \boldsymbol{\Sigma})$ is the three-dimensional Gaussian distribution with $\boldsymbol{\mu} = (\mu_r, \mu_\theta, \mu_\phi)$ and $\boldsymbol{\Sigma} = (\sigma_r, \sigma_\theta, \sigma_\phi)$ taken from [127]. With a large uncertainty of its fraction contribution, we can parametrize it with

$$r = \frac{\xi_{\rm s}}{\xi_{\rm h} + \xi_{\rm s}} \in [0, 1] \tag{2.7}$$

The WIMP direction distribution and the distribution of the nuclear recoil angle in direct detection with different r value can be found in [128]. Here without loss of generality, in Figure 2.1, we show the Mollweide projections of the angular distribution of the two-component Galactic WIMP signal with $r = 0$ and $r = 0.5$. One can see the anisotropy of the WIMP angular distribution in the galaxy.

The Gaia data indicates that the Solar System is travelling through a DM halo with a speed of $v_\odot = (233 \pm 3)$ km/s towards the direction of the Cygnus constellation and that the local DM density would be updated to $\rho_0 = (0.55 \pm 0.17)$ GeV/cm^3 [38]. The velocity distribution can be translated into

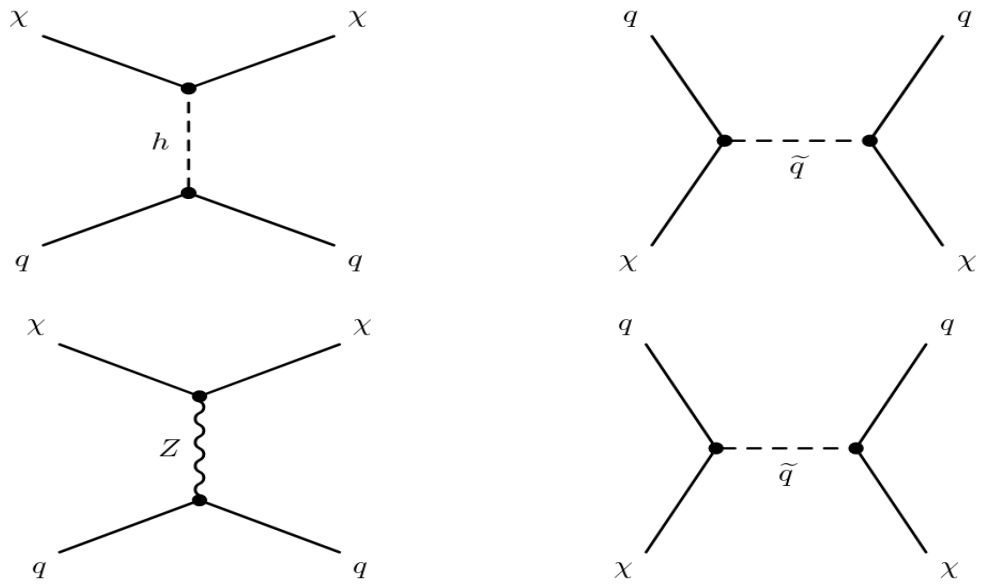

Figure 2.2: Feynman diagrams of the elastic scattering of a WIMP χ from quarks [129]. Top: spin-independent (scalar) interaction. Bottom: spin-dependent (axial) interaction.

lab frame through a Galilean transformation $f(\mathbf{v}, t) = f_{\text{gal.}}(\mathbf{v} + \mathbf{v}_{\text{lab}}(t), t)$ where $\mathbf{v}_{\text{lab}}$ is the lab velocity that takes into account the motion of the galaxy, the Sun's motion, and the Earth's motion [125]. The dominant contribution is the velocity of the galaxy described by $v_\odot$ and the total WIMP velocity, in the lab frame of a detector on Earth, is of order $\sim$ 300 km/s. A still open question concerns a possible rotation of the DM halo, in particular if the halo would be formed by the merging of multiple substructures that could induce a non-zero angular momentum. A rotation of the DM halo could either enhance or reduce the relative velocity of the Solar System in it, and consequently influence the event rate in a detector. However, the DM halo is usually considered static. Under this assumption, we can conclude the relative motion of the Solar System in the DM halo would induce a WIMP *wind* in the opposed direction of its motion, leading to an anisotropy of the angular distribution. In other words, one expects WIMPs to enter a detector on Earth, the large majority of them coming from the direction of the Cygnus constellation.

2.1.2 Interaction WIMP-matter

As already discussed, WIMP is expected to interact with ordinary matter, even feebly, otherwise they would be too abundant today since they would not have annihilated in the Early Universe [129]. The WIMP must have a coupling to quarks, and consequently to nuclei, that enables direct detection by the elastic scattering of a WIMP from a nucleus. Let us briefly describe the WIMP-matter interaction and the corresponding cross-sections. The details of the calculations are out of the scope of this work and we refer to [129] for additional information. The procedure consists in first determining the interactions between WIMP and quarks and gluons. The interactions are later generalized to nucleons before being added coherently according to the nuclear state of an atom, by including nuclear form-factors. For non-relativistic WIMP, two dominant interactions contribute to the WIMP-nucleus cross-sections: the spin-dependent (noted SD and also called *axial*) and the spin-independent (noted SI and also called *scalar*). The corresponding Feynman diagrams for the interactions with quarks are shown in Figure 2.2.

Spin-independent

The SI contribution can be decomposed into two components for a general WIMP: a scalar-scalar coupling and a vector-vector coupling, expressed by the Lagrangian [129]:

$$\mathcal{L}^{SI} = f_q^S \bar{\chi}\chi\bar{q}q + f_q^V \bar{\chi}\gamma_\mu\chi\bar{q}\gamma^\mu q \tag{2.8}$$

where f_q^S and f_q^V are respectively the scalar and vector coupling constants. Note that this is the general SI Lagrangian for a WIMP, but that the vector term turns to zero when the WIMP is a Majorana particle, as a neutralino for instance.

The SI WIMP-nucleus differential cross-section, with respect to the nuclear recoil energy E_R, can be written as a simple expression [130] under the approximation that the WIMP couplings to a neutron and to a proton are identical:

$$\left(\frac{d\sigma}{dE_R}\right)_{SI} = \frac{4\mu A^2 (f^p)^2}{\pi v^2} F_{SI}^2(E_R) \tag{2.9}$$

where $\mu = m_\chi m_N/(m_\chi + m_N)$ is the reduced mass of the WIMP-nucleus system, A is the atomic number, f^p is the coupling to protons that can be determined from the coupling to the quarks and to the gluons. $F_{SI}^2(E_R)$ is the nuclear form-factor for coherent interactions and it is defined as the Fourier transform of the density distribution of the nucleus; it depends on the model of the density distribution. Several models exist but one can show that most of them are not distinguishable for recoil energies below 10^3 keV [131]. Usually, the SI form-factor is given by the Helm model that expresses it as a function of the momentum transfer q [132]:

$$F_{SI}^2(q) = \left(\frac{3j_1(qR_0)}{qR_0}\right)^2 e^{-q^2 s^2} \tag{2.10}$$

where j_1 is the first order spherical Bessel function, $R_0 = \sqrt{R^2 - 5s^2}$ where $R \simeq 1.2\, A^{1/3}$ fm is the nuclear radius and $s \simeq 1$ fm is the nuclear skin thickness.

Spin-dependent

The SD contribution arises from an axial-vector coupling between a WIMP and a quark. Let us consider the case of a fermionic WIMP, as the neutralino for instance, that differs from the case of a bosonic WIMP. The Lagrangian is given by [130]:

$$\mathcal{L}^{SD} = a_q^A \left(\bar{\chi}\gamma^\mu\gamma_5\chi\right)\left(\bar{q}\gamma_\mu\gamma_5 q\right) \tag{2.11}$$

where a_q^A is the axial coupling between the WIMP and the quark q. The differential cross-section can be given by:

$$\left(\frac{d\sigma}{dE_R}\right)_{SD} = \frac{32\mu}{\pi v^2} G_F^2 \frac{J+1}{J}\left(a_p\langle S_p\rangle + a_n\langle S_n\rangle\right)^2 F_{SD}^2(E_R) \tag{2.12}$$

where G_F is the Fermi constant, where J is the total angular momentum of the nucleus, $\langle S_{p,n}\rangle$ are the expectation values of the spin content of the proton or neutron group in the nucleus that can be determined from nuclear models. a_p and a_n are the elastic scattering amplitudes on proton and neutron, respectively, that can be computed from the coupling to the quarks.

While usually determined experimentally, the SD form-factor can also be parametrized empirically as [133]:

$$F_{SD}^2(q) \simeq \exp\left(-\frac{q^2 R_A^2}{2}\right) \tag{2.13}$$

with $R_A = 1.7A^{1/3} - 0.28 - 0.78\left(A^{1/3} - 3.8 + \sqrt{(A^{1/3} - 3.8)^2 + 0.2}\right)$ fm which, for fluorine recoils with energies above 10^2 keV, cannot be distinguished from experimental form-factors [131].

It is convenient to express the total differential cross-section as:

$$\frac{d\sigma}{dE_R} = \frac{m_N}{2\mu_N^2 v^2}\left(\sigma_0^{SI} F_{SI}^2(E_R) + \sigma_0^{SD} F_{SD}^2(E_R)\right) \tag{2.14}$$

in which the energy dependency of the form-factors has been separated from σ_0, the cross-sections computed at zero-momentum transfer. Several comments can be done at this stage:

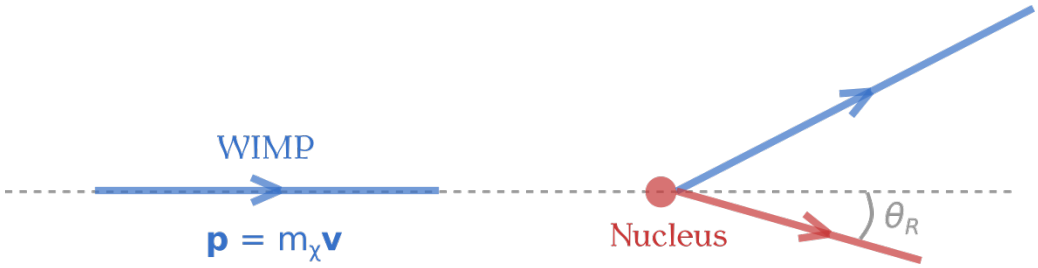

Figure 2.3: Kinematics of a WIMP-nucleus elastic scattering in the lab frame.

- The WIMP is a generic class of particles that can have very different properties, so the cross-section calculations are then model-dependent. On the one hand, this appears as an issue to determine model-independent cross-sections. On the other hand, direct detection of WIMP by scattering on several target nucleus would enable to discriminate between multiple WIMP candidates.
- The SD interaction channel only opens for nucleus with non-zero spin content. Direct detectors interested in this channel will then choose a target nucleus with an unpaired neutron or proton such as ^{1}H, ^{7}Li, ^{19}F, ^{73}Ge, ^{129}Xe, ^{131}Xe, *etc.*
- The detection strategies from the SD channel or the SI one can significantly differ. Direct detectors usually favours heavy nuclei as targets to enhance the SI contribution that scales with the atomic number. However, accessing the directional information requires using a light nuclei as a target. The comparison between the SI and SD contribution is model-dependent but in the MSSM one can show that the SD contribution dominates over the SI one for atomic numbers up to $A \simeq 20$ [129], with about 3 orders of magnitude difference in the case of ^{1}H.

2.1.3 Event rate

The WIMP can be treated as non-relativistic since its velocity in the lab frame is of order ~ 300 km/s. The kinematics of the WIMP-nucleus scattering is shown in Figure 2.3 and the recoil energy is given by:

$$E_R = 2v^2 \frac{\mu^2}{m_N} \cos^2\theta_R \tag{2.15}$$

where $\mu = m_\chi m_N/(m_\chi + m_N)$ is the WIMP-nucleus reduced mass and where θ_R is the scattering angle, *i.e.* the angle between the initial WIMP direction and the direction of the nuclear recoil after the collision, that we will later note $\hat{\mathbf{r}}$. Taking a standard velocity of 300 km/s, a WIMP with a mass of 30 GeV will transfer maximal energy of about 2 keV on a proton and of 14 keV on fluorine. When considering the largest WIMP velocities allowed from the halo models, the maximal energy transfer remains lower than ~ 10 keV/nucleon.

Directional detection is interested in measuring the energy of the nuclear recoil as well as its direction. For this reason, we will consider the double-differential event rate, that is the recoil rate per unit energy and unit direction, which is given by:

$$\frac{d^2R}{dE_R\, d\Omega_R} = \frac{\rho_0}{m_\chi m_R} \int d^3v \, \frac{d^2\sigma}{dE_R\, d\Omega_R} \, v f(\mathbf{v}) \tag{2.16}$$

where ρ_0 is the local WIMP density, $f(\mathbf{v})$ is the WIMP velocity distribution in the lab frame and $\frac{d^2\sigma}{dE_R\, d\Omega_R}$ is the double-differential WIMP-nucleus cross-section.

We will now rewrite $\frac{d^2\sigma}{dE_R\, d\Omega_R}$ in a more convenient way. Let us remark that momentum conservation implies that $\cos\theta_R = q_R/(2v\mu)$ where q_R is the momentum of the recoil. This condition can be mathematically imposed in Eq. (2.16) thanks to a Dirac delta $\delta\big(\cos\theta_R - q_R/(2v\mu)\big) = v\,\delta\big(\mathbf{v}\cdot\hat{\mathbf{r}} - v_{\min}\big)$ where

$$v_{\min} = \sqrt{E_R m_N/(2\mu^2)} \tag{2.17}$$

is the minimal WIMP velocity required for producing a nuclear recoil of energy E_R. We can then rewrite the double-differential cross-section as:

$$\frac{d^2\sigma}{dE_R\, d\Omega_R} = \frac{1}{2\pi}\frac{d\sigma}{dE_R}\, v\, \delta\big(\mathbf{v}\cdot\hat{\mathbf{r}} - v_{\min}\big) \tag{2.18}$$

We can now make use of Eq. (2.14) to write the double-differential event rate as:

$$\frac{d^2R}{dE_R\, d\Omega_R} = \frac{\rho_0}{4\pi m_\chi \mu^2}\left\{\sigma_0^{SI}\, F_{SI}^2(E_R) + \sigma_0^{SD}\, F_{SD}^2(E_R)\right\}\hat{f}(v_{\min}, \hat{\mathbf{r}}) \tag{2.19}$$

where we have followed the approach of Gondolo [134] by introducing the three-dimensional Radon transform of the WIMP velocity distribution:

$$\hat{f}(v_{\min}, \hat{\mathbf{r}}) = \int d^3v\, \delta\big(\mathbf{v}\cdot\hat{\mathbf{r}} - v_{\min}\big)\, f(\mathbf{v}) \tag{2.20}$$

that is expressed in unit of inverse speed. The Radon transform presents some interesting properties for analytical integration over some halo models or for applying a change of referential. We also point out that:

$$\int d\Omega_w \hat{f}(w, \hat{\mathbf{w}}) = 2\pi \int_{v>|w|} d^3v \frac{f(\mathbf{v})}{v} \tag{2.21}$$

that can be used to integrate the double-differential event rate over the solid angle to recover the event rate per unit energy, a valuable quantity for direct detection when the directional information is not required.

Directional detection is based on the event rate per unit energy and per unit solid angle, Eq. (2.19), which depends on model-dependent parameters from nuclear physics (the form factors and the spin content), particle physics (the zero-momentum cross-sections), and models of the WIMP halo (the local WIMP density and the velocity distribution).

2.2 Non-directional direct detection

We have seen that a WIMP can scatter off a nucleus and consequently produce a nuclear recoil in the active volume of an Earth-based detector. Let us now introduce the main concepts of non-directional direct detection of WIMPs and we refer to [135] for a clear and recent review. We consider a detector as non-directional if it only measures the energy of the WIMP-induced nuclear recoil but it does not provide any information about its direction.

The WIMP signal is searched in the keV-range, or even below, since the recoil energy spectra can be approximated, at first order, by an exponential function. For this reason, direct detectors must operate with an energy threshold as small as possible. The second requirement for a WIMP direct detector is the ability to search for rare events. For instance, if we consider a WIMP mass of 100 GeV, a SI cross-section of $\sigma_0^{SI} = 10^{-8}$ pb, and a fluorine target, we expect a scattering event rate of order $\mathcal{O}(1)$ event/year/kg in the SHM. This place a strong constraint on the acceptable background level. The main direct projects build large detectors to increase the number of target nuclei and hence the number of WIMP-nucleus scattering events.

2.2.1 Direct strategies of detection

The main WIMP detection strategy consists in searching for WIMP-induced nuclear recoils that have been discriminated from the background. The detection of a WIMP-like signal is determined by a statistically significant excess over the expected background. It relies then on sophisticated background mitigation strategies and simulations of the expected background level, we will come back on these limitations later. A nuclear recoil releases its energy through three processes: heat, ionization, and scintillation. We will discuss in Section 4.2 and in Chapter 7 the fact that the energy released by a nuclear recoil can appear as quenched compared to the energy released by an electron. While this

quenching effect almost does not concern heat, it must be considered in detectors measuring ionization or scintillation. It is convenient to write keV_{nr} when talking about the kinetic energy of the nuclear recoil, and keV_{ee} for the electron equivalent recoil energy that can be quenched compared to the energy released by an electron of the same kinetic energy.

A complementary approach for searching for WIMPs is the annual modulation. As we have seen, the event rate depends on the relative velocity of the WIMPs with respect to the detector. Due to the Earth's motion around the Sun, one expects a periodic change in the differential event rate between winter and summer. The annually modulating recoil rate can be approximately expressed as [136]:

$$\frac{dR}{dE_R}(E_R, t) \simeq B(t) + S_0(E_R) + S_m(E_R)\cos\left\{\omega(t - t_0)\right\} \tag{2.22}$$

where $B(t)$ is a (possibly time-dependent) background, S_0 is the unmodulated signal, S_m is the modulated part corresponding to about 5% of S_0, $\omega = 2\pi/\text{year}$ is the period and t_0 is the phase of the modulation. The annually modulating WIMP signal is usually considered statistically significant for detection of $> 10^4$ events [137].

For more than a decade, the DAMA/LIBRA experiment has claimed to have detected an annually modulated signal, meeting the requirements for a WIMP signal, in the energy region $(1 - 6)$ keV at 9.2σ confidence level for a total exposure of 1.13 ton $\times$ years [138]. Similar anomalies have also been reported by CoGeNT [139] and CRESST-II [140]. However, an important doubt accompanied these results, since possible systematics effects could bias the analyses [141, 142], and since the phase-space region of the results was excluded by other direct experiments. Finally, the COSINE-100 experiment has been designed to cross-check DAMA's claim by using the same crystal detectors. After almost two years of data taking, the experiment has not observed any signal consistent with WIMP and the results seem to rule out the DAMA's claim for WIMP detection [143]. This controversy teaches us the complexity of searching for WIMP and highlights the importance of cross-checking the results by independent and complementary detection methods.

Increasing interest concerns the searches for light WIMP with mass in the MeV-range for which very few experimental constraints have been placed because such light WIMPs would not transfer enough momentum to the nuclear recoils for being detected. In other words, detection of nuclear recoil cannot be used to search for MeV WIMP. To probe this mass region, two alternate strategies have been proposed. The first one relies on the WIMP-electron scattering [144, 145]. In this inelastic process, the WIMP transfers a large fraction of its kinetic energy to the electrons, leading to a small ionization signal of a few electrons, that could be observed in detectors with single-electron sensitivity. This method could, in principle, probe WIMPs of masses down to a few hundred keV however the background in this energy region is mainly unknown.

Finally, we mention another promising strategy to search for sub-GeV WIMPs: detection using the Migdal effect. The Migdal effect states that, after an interaction, a moving nucleus is not immediately followed by its electron cloud, so their relative motion can lead to the ionization or the excitation of the nuclear recoil. The excited atom relaxes by emission of X-rays or Auger electrons, leading to additional energy deposition in the active volume [146]. The Migdal effect would be able to excite the inner orbitals, leading to extra energy deposition up to a few keV [147]. The effect is described in Figure 2.4. While the Migdal effect has been observed in radioactive decays of light and heavy elements [148–151], it has so far not been observed in nuclear scattering, so its use in direct DM experiments is still hypothetical and is conditioned to an experimental detection.

In the presence of a transition due to the Migdal effect, injecting an extra ionization energy E_e in the volume, the differential event rate for a nuclear recoil of energy E_R is given by [152]:

$$\frac{d^3R}{dE_R\, dE_e\, dv} = \frac{d^2R_{\text{nr}}}{dE_R\, dv}\left|Z_{\text{ion.}}(E_R, E_e)\right|^2 \tag{2.23}$$

where the transition rate is:

$$\left|Z_{\text{ion.}}(E_R, E_e)\right|^2 = \sum_{nl}\frac{1}{2\pi}\frac{d}{dE_e}\, p^c_{q_e}\left(nl \to E_e\right) \tag{2.24}$$

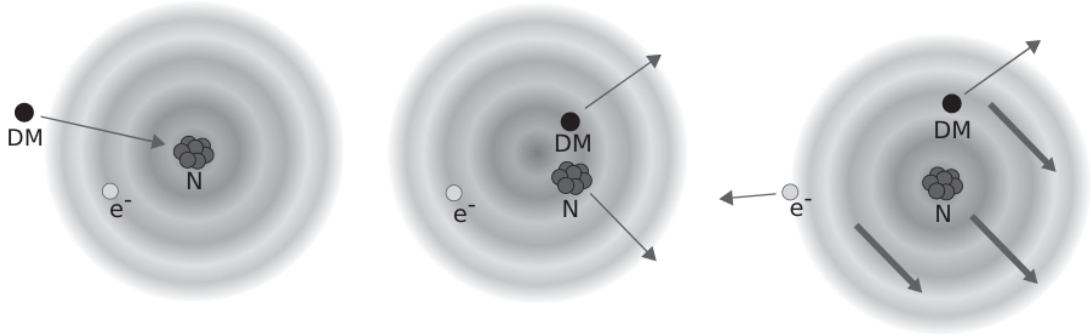

Figure 2.4: Illustration of the hypothetical Migdal effect. After an elastic scattering of a DM particle on a target nucleus (left), the nucleus moves but the electrons do not follow immediately (middle). Electrons eventually catch up with the nuclear recoil (right) resulting in possible ionization and excitation of the atom. The excited atom relaxes by emission of X-rays or Auger electrons whose energy can be larger than the ionization energy of the nuclear recoil. Figure extracted from [152].

where $p^c_{q_e}(nl \to E_e)$ is the probability of emitting an electron with final energy E_e and quantum number (n, l), the probability depending on the target material, and where $q_e = m_e\sqrt{2E_R/mN}$ is the electron momentum in the nucleus rest frame. The energy spectrum of the additional ionization energy is obtained by integrating Eq. (2.23) over the recoil energy and the WIMP velocity. The total energy deposited in the volume is given by $\Delta E = E_e + E_{nl}$ where E_{nl} is the binding energy of the electron before emission. The maximal energy of a WIMP-induced nuclear recoil, and the maximal additional energy deposited by the Migdal effect, are linked by [147]:

$$E_R^{max} = \frac{\mu}{m_N}\Delta E^{max} \tag{2.25}$$

where μ is the reduced mass previously introduced. One can see that, when the Migdal effect is kinematically allowed, the extra electronic energy deposited can be larger than the nuclear recoil energy. For instance, a WIMP of mass 500 MeV scattering off a xenon target can produce $\Delta E^{max} \simeq 1.8$ keV whereas $E_R^{max} \simeq 0.03$ keV [152]. Here we can see the main advantages of the Migdal effect for light-WIMP searches. First, a sub-GeV WIMP can produce electronic energy above the nuclear recoil energy, up to a few keV, enabling to probe lower mass regions. Second, the extra energy is deposited as X-rays or Auger electrons, so it is not affected by quenching effects.

2.2.2 State of art

Direct detectors must be able to measure the energy of a WIMP-induced nuclear recoil by at least one of the signal channels (heat, ionization, scintillation). So far, no detector has successfully measured the three channels simultaneously. We introduce some detector technologies, as presented in Figure 2.5, and we refer to [135, 137] for more details. The list below is not exhaustive.

- **Scintillating crystal detectors**, such as NaI(Tl) or CsI(Tl), efficiently produce optical photons that are read by low-background photomultipliers (PMT). The main advantages are the rather simple design, the stability enabling to operate over large periods, and the high target mass enhancing the SI interaction. However, they have some large intrinsic background that can hardly be discriminated and they operate with a relatively high threshold ($\simeq 8$ keV$_{\rm nr}$ for Na). Due to the important background, they usually exploit the annual modulation of the DM signal. The main current detectors are DAMA/LIBRA, ANAIS-112, COSINE-100, and SABRE.

- **Cryogenic detectors (bolometers)** are interested in the heat signal, propagated as phonons in crystals, measured as a temperature increase after an interaction. These detectors must operate at cryogenic temperatures (typically < 50 mK) and they usually are made of doped crystals, such as Ge or Si. All modern experiments also measure a second channel, either scintillation or ionization,

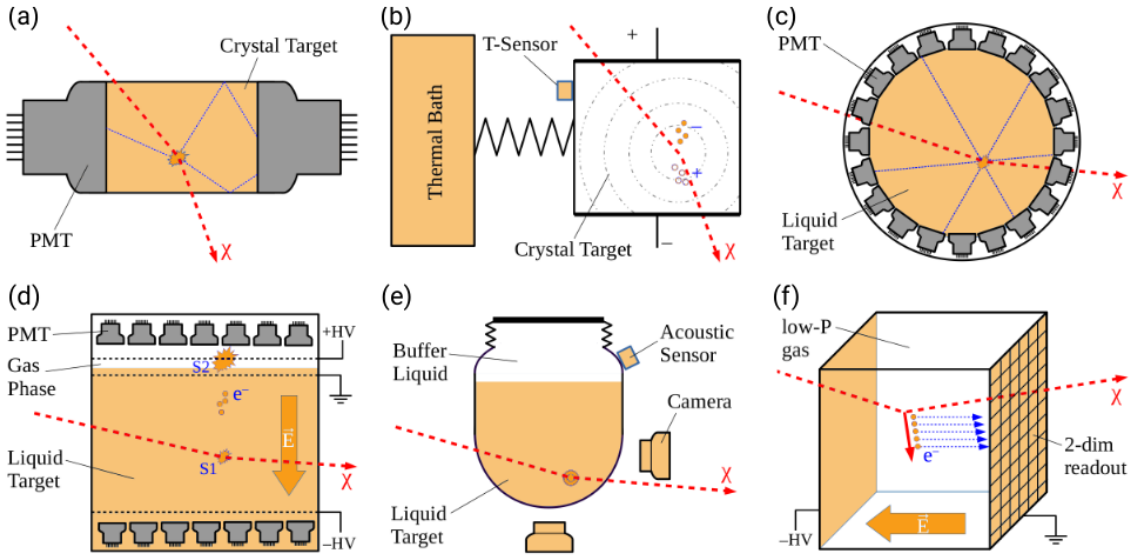

Figure 2.5: Schematics of the working principles of the most common detectors for direct searches: (a) scintillating crystal; (b) bolometer; (c) single-phase and (d) dual-phase liquid noble gas detectors; (e) bubble chamber; (f) directional detector based on TPC with micro-pattern 2D readout. Figure extracted from [135].

significantly improving the background discrimination down to ~ 5 keV$_{\mathrm{nr}}$ since the amount of energy released by each channel depends on the recoil type. The main advantages of bolometers are the energy measurement via heat (that is almost not affected by quenching effects), their excellent energy resolution, and their good background rejection power thanks to the two-channel measurements. The detection threshold can be lowered down to a few tens of eV by applying a bias voltage although it decreases the efficiency of the electron-recoil discrimination. The drawbacks of such detectors are the challenging and expensive operation at cryogenic temperatures, and the limitation to kg-scale to reach a low-energy threshold. The main current detectors are EDELWEISS-III, CRESST-III and SuperCDMS.

- **Single-phase noble liquid detectors** exploit noble gases, such as Xenon or Argon, that are excellent scintillators and can be ionized. An atom that has been excited by a particle interaction combines with a neutral atom to form an excimer that decays into two stable atoms by emission of a UV photon of known wavelength. The primary scintillation light is measured by PMTs surrounding the active volume. In the liquid state, such detectors reach a large mass, exceeding the ton-scale. They benefit from efficient electron-recoil discrimination since the scintillation pulse shape depends on the relative orientation of the two atomic spins in the excimer state, which itself depends on the ionization density, and then on the interaction type. The main project currently using this technology is DEAP-3600 and we also mention XMASS which operated up to 2019.

- **Dual-phase noble liquid detectors** measure the primary scintillation as well as the ionization. They are based on a TPC principle so the primary electrons drift towards the surface of the liquid that is separated, thanks to a grid, to a gas phase where they induce avalanches, producing secondary scintillation. The primary scintillation signal is called S1 whereas the secondary scintillation signal, which depends on the ionization, is called S2. The ratio S2/S1 is correlated with the ionization density and then leads to background rejection. The measurement of S1 and S2 enables to locate the interaction in the volume with millimetre precision. The main projects based on dual-phase detectors are XENON1T, LUX-Zeplin (LZ), PANDAX-4T, and DarkSide-20k (not started yet).

- **Bubble chambers** rely on liquids whose temperature is kept close to the boiling point. When sufficient energy is deposited in a small volume, it generates a bubble. The number of bubbles, as

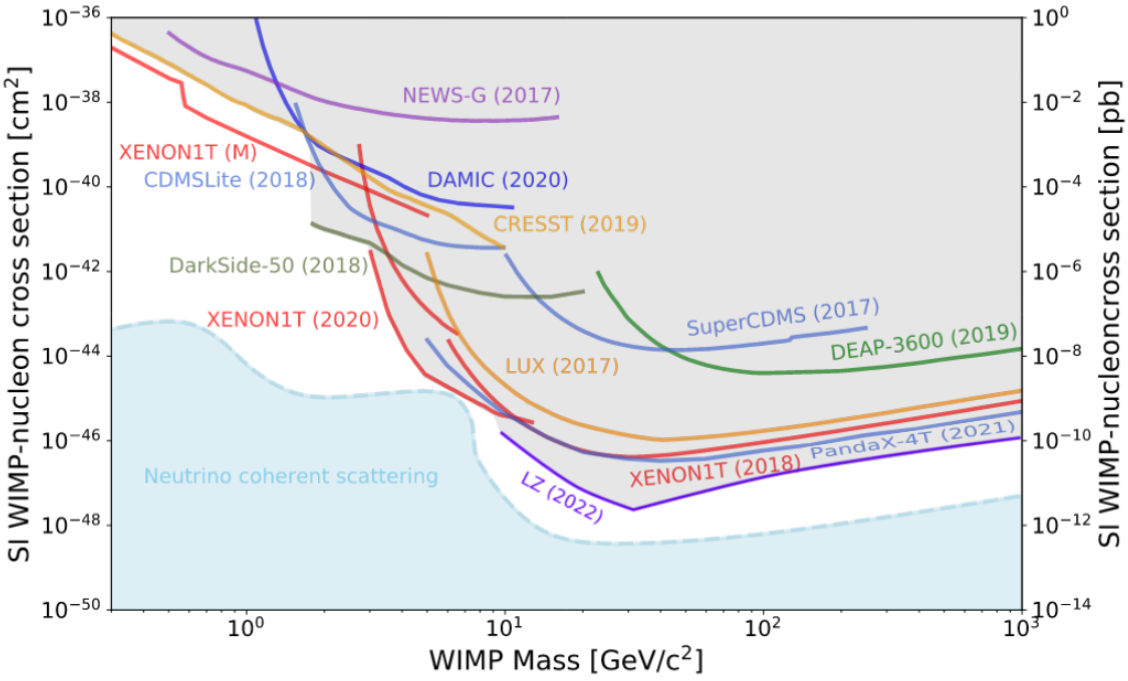

Figure 2.6: Status of the exclusion limits on the SI cross-section in the SHM. The gray shaded area is the currently excluded region. Label "M" refers to experiments exploiting the hypothetical Migdal effect. Figure adapted from [38] with recent data.

well as their positions, is measured by cameras. Bubble chambers cannot measure the deposited energy, however they are almost free from electronic events since the ionization density must be large enough to overpass the threshold and then generate a bubble. To the author' knowledge, the only active bubble chamber for WIMP searches is the PICO-40 detector.

- **Gaseous TPCs** detect the primary ionization of the particle interaction in the active volume and, when coupled to a 2D micro-pattern readout, can be used for directional detection. Since this is the technology described in this thesis, we do not enter here into details. Let us mention the TREX-DM detector and the NEWS-G detector, both of them searching for sub-GeV WIMPs. The NEWS-G detector will be described in Section 7.1.

- **Skipper-CCD** is a technology used for low-energy detection, in particular for WIMP-electron scattering. It makes use of a silicon Skipper-Charge-Couple-Device that is divided into pixels. When a particle interaction occurs, electron-hole pairs are created and the charges are moved, pixel-by-pixel, to the readout located at the extremity of the Skipper-CCD. This technology reaches a very low threshold of the order of eV with sub-electron-noise precision, however there are limited to small masses of kg-scale. The 2D readout of the pixels enables background rejection. The detectors SENSEI and DAMIC-M use this technology.

The current status of searches for WIMP via the SI interaction is presented in Figure 2.6. No direct detection of WIMP is observed, so one places exclusion limits in the parameter space (σ_{SI}, m_χ), limits above which WIMP are excluded with 90% confidence level. For masses above ~ 3 GeV, the strongest constraints come from dual-phase liquid xenon detectors of the collaborations XENON, LUX-ZEPLIN (LZ), and PANDAX. This is mainly due to the large mass of xenon that enhances the SI interaction, to the liquid phase enabling ton-scale experiments, and to the efficient background discrimination coming from the S1 and S2 signals.

The exclusion limits are orders of magnitude less stringent in the sub-GeV region because of the limitations coming from the detection threshold. For this reason, the leading experiments in the region are using cryogenic bolometers that operate at a low threshold. The Migdal effect, if it turns to be demonstrated for nuclear scattering, would significantly extend the discovery reach of noble liquid detectors.

2.2.3 Background, mitigation strategies and limitations

We have not yet discussed the blue shaded area of Figure 2.6, whose upper limit is the so-called *neutrino floor*. Neutrinos also generate nuclear recoils via the coherent elastic neutrino-nucleus scattering (CEνNS), such signal being indistinguishable from a WIMP-induced nuclear recoil on an event-by-event basis [153]. There is no possible shielding for neutrinos and they consequently represent an irreducible background for direct detectors. There are many sources for the ambient flux of neutrinos and anti-neutrinos. We can classify the main ones into three groups [154]. First, the solar neutrinos that occur in some terminations of the *pp* chain, one of the nuclear fusion reactions in the Sun, for instance via the decay of ^{8}B produced in the chain. Second, the atmospheric neutrinos which are produced during collisions of cosmic rays with the Earth's atmosphere. Third, the diffuse supernova neutrino background arising from past supernova explosions. The limit in the plane (σ, m_χ) below which it is not possible to distinguish between a WIMP signal and a neutrino signal, at more than 90% confidence level, is called the *neutrino floor*. It depends on the target mass, the detection threshold, the exposure time, and the uncertainties on the neutrino fluxes. The neutrino floor could be lowered by a combination of multiple targets sensitive to the SD interactions [155]. The neutrino floor is then not a hard limit, and some authors propose to instead talk about *neutrino fog* [156]. While the neutrino background can be reduced thanks to annual and diurnal modulations [157, 158], directional detection remains the standard approach to overpass it, as we will see.

Neutrons also induce nuclear recoils that can be identified as WIMP events. The main source of neutron background in the underground laboratory of Modane, as we will see in Chapter 5, is the rock contamination with radioactive elements. Other particles participate to the background, for instance α produced in the detector materials or surrounding β and γ particles. Several background mitigation strategies can be developed to reduce the background: operating in an underground laboratory, shielding the detector, using high-purity materials, *etc* [137]. The *fiducialization*, which consists in defining a smaller active volume than the total detection volume, is also a powerful tool to eliminate background events that mainly occur close to the surface. In MIMAC, as in other detectors, we extensively use active rejection strategies: we combine several observables, during the data analysis, to reject events incompatible with a nuclear recoil signature.

A background-free experiment is not achievable. A crucial question directly arises from this statement: how to be sure that a measured WIMP-like event is not due to background? A first answer is a comparison between multiple experiments with several strategies of detection. A second one is a comparison to simulations. However, simulations rely on assumptions and sometimes do not correctly describe phenomena, as for instance the well-documented discrepancy between theory/simulations and measurements for the ionization quenching factor that we will frequently mention in this work (*c.f.* Chapter 7). The previously discussed case of DAMA/LIBRA's claim for WIMP detection is enlightening about the difficulty of the dark matter identification. On another basis, we can mention the recent measurements of excess in XENON1T data [159]. While this excess is observed on electronic recoil events, and thus has no connection with WIMP, it is instructive to show that the measurement of a significant excess, with respect to simulations, is not sufficient to claim for a detection. At the time of writing, the doubt exists whether the excess is correlated with DM detection or is due to tritium background.

The ultimate identification of a DM particle must be validated by a signature that is distinguishable from the background without any ambiguity. This is the purpose of directional detection. If a direct detector measures a WIMP-like signal, directional detectors would adapt their experimental conditions (in particular gaseous TPCs whose target can easily be changed) to validate or reject the detection claim. Let us now enter into the details of directional detection and we refer to [125] for a comprehensive review.

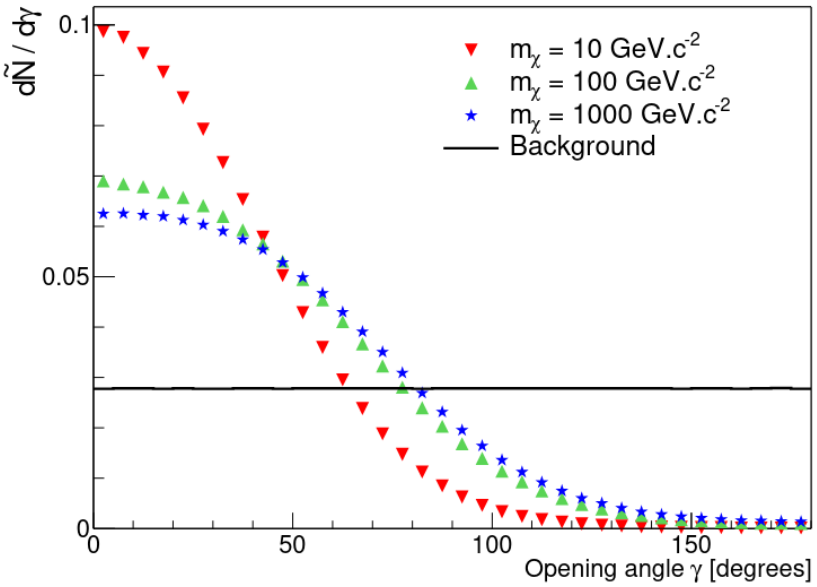

Figure 2.7: Normalized 1D angular distribution of WIMP-induced ^{19}F recoils as a function of the opening angle for recoil energies in the range $[5, 50$ keV$]$. Calculations were made in the case of a Maxwellian velocity distribution. The solid black line corresponds to the isotropic background. Figure extracted from [160].

2.3 Directional detection

2.3.1 The smoking gun

The relative motion of the Earth through the static DM halo would result in a "wind" of WIMP as opposed to the direction of motion. We will see that this specific feature, which cannot be mimicked by the background, leads to several unique signatures for WIMP identification. We have seen in Eq. (2.19) that the double-differential event rate in an Earth-based detector is proportional to the Radon transform of the velocity distribution of the WIMP in the halo. The Radon transform of a Maxwellian WIMP velocity distribution, truncated at the escape velocity $v_{\rm esc}$, can be expressed in the lab frame as [134]:

$$\hat{f}(v_{\rm min}, \hat{\mathbf{r}}) \;=\; \frac{1}{N\sqrt{2\pi\sigma_v^2}} \left[\exp\left\{ -\frac{(v_{\rm min} + \hat{\mathbf{r}}\cdot\mathbf{v}_{\rm lab})^2}{2\sigma_v^2} \right\} \;-\; \exp\left\{ -\frac{v_{\rm esc}^2}{2\sigma_v^2} \right\} \right] \tag{2.26}$$

where N is a normalization factor and where $v_{\rm min}$ is defined by Eq. (2.17). The velocity of the lab with respect to the center of the galaxy can be expressed as [125]:

$$\hat{\mathbf{r}}\cdot\mathbf{v}_{\rm lab} \;=\; \hat{\mathbf{r}}\cdot\mathbf{v}_{\rm c} + \hat{\mathbf{r}}\cdot\mathbf{v}_{\rm S} + \hat{\mathbf{r}}\cdot\mathbf{v}_{\rm E,\,rev.} + \hat{\mathbf{r}}\cdot\mathbf{v}_{\rm E,\,rot.} \tag{2.27}$$

as a vectorial sum of the rotation of the galaxy expressed by the local circular velocity $\mathbf{v}_{\rm c}$, the motion of the Sun in the galaxy $\mathbf{v}_{\rm S}$, the Earth rotation around the Sun $\mathbf{v}_{\rm E,\,rev.}$, and Earth self-rotation $\mathbf{v}_{\rm E,\,rot.}$. The WIMPs are then mainly entering an Earth-based detector from the direction to which is pointing $\mathbf{v}_{\rm lab}$, which corresponds roughly to the direction of the Cygnus constellation.

The Radon transform of the distribution velocity Eq. (2.26), and consequently the event rate, has a *dipole feature* related to the favoured WIMP velocity. Let us make use of the azimuthal symmetry of the recoil directions around $\mathbf{v}_{\rm lab}$ to rewrite, without loss of information, $dR/d\Omega$ as $dR/d\cos\gamma$, where γ is the opening angle between $\hat{\mathbf{r}}$ and $-\mathbf{v}_{\rm lab}$. We can then obtain the 1D angular distribution of the WIMP-induced recoils by integrating over an energy range. Figure 2.7 illustrates the recoil angular spectrum for three different WIMP masses and a ^{19}F target, when the recoil energies are in the range $[5, 50$ keV$]$. One can see that the angular distribution is always maximal for $\gamma = 0$, so for recoils coming from the Cygnus direction. The dipole feature, *i.e.* the anisotropy of the distribution, increases when the WIMP mass decreases, due to the finite energy range over which the event rate

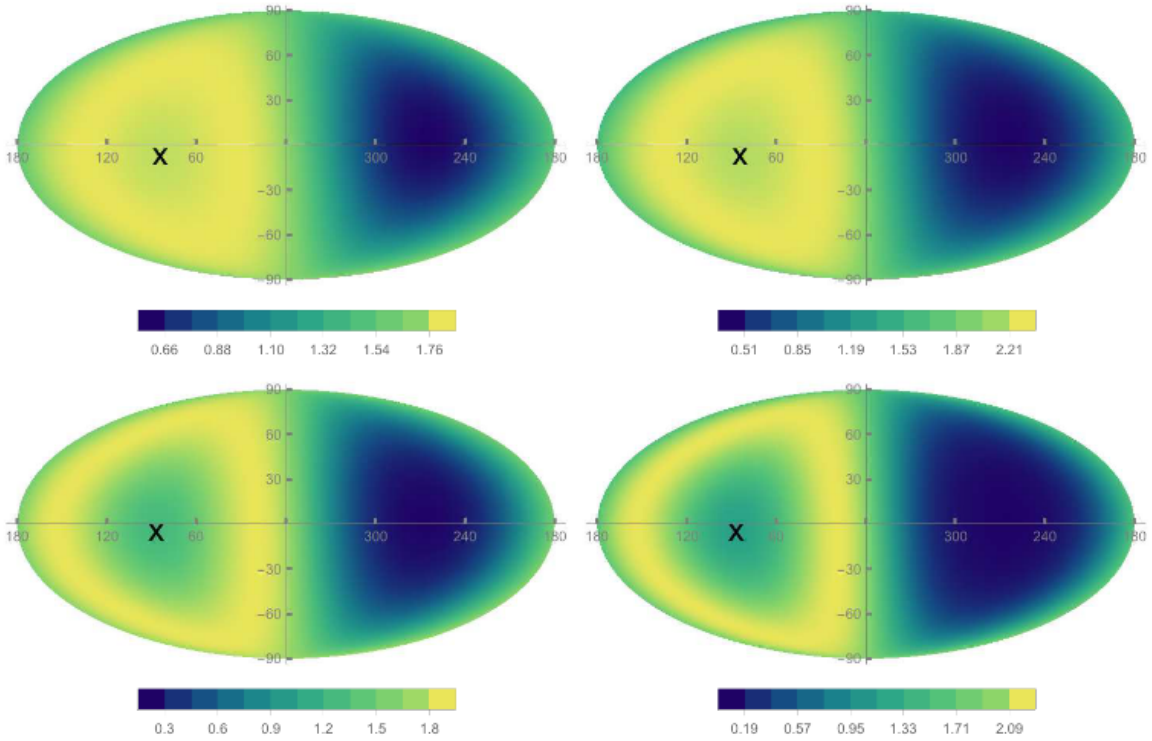

Figure 2.8: Mollweide projection maps of the differential recoil rate in Galactic coordinates. All panels are computed for recoil energy of 5 keV, a WIMP mass of 100 GeV, and an escape velocity of 544 km/s. The black cross represents the direction of $\mathbf{v}_{\rm lab}$. The top panels are computed for $v_c = 180$ km/s on May 30 with $\sigma_v = 225$ km/s (left) and $\sigma_v = 173$ km/s (right). The bottom panels are computed for $v_c = 312$ km/s on June 2 with $\sigma_v = 225$ km/s (left) and $\sigma_v = 173$ km/s (right). The values of the rate shown in colors are expressed in unit of $10^{-5} \times (\frac{\rho_0}{0.3\ \rm GeV}) \times (\frac{\sigma_{SD}}{10^{-40}\ \rm cm^2})\ \rm kg^{-1} \cdot day^{-1} \cdot keV^{-1} \cdot sr^{-1}$. Figure extracted from [125].

is integrated. Finally, the angular distribution can be approximated by a Gaussian distribution with zero mean value.

Another feature of the directional signature of WIMPs arises in the case $v_{\rm min} > v_{\rm lab}$, so for large WIMP mass and low recoil energy. We see in Eq. (2.26) that in such case the Radon transform can have two maxima: one for $-\hat{\mathbf{r}}\cdot\mathbf{v}_{\rm lab} = v_{\rm min}$; the other for an opening angle γ such that $\cos\gamma = v_{\rm min}/v_{\rm lab}$. In this situation, the recoils no longer exhibit a dipole feature, but a *ring-like feature*, as illustrated in Figure 2.8. In other words, the majority of the low-energy recoils are distributed in a ring around $\mathbf{v}_{\rm lab}$, the ring properties depending on the WIMP mass and the velocity distribution. A statistically significant detection of the ring-like feature requires about 5 times more events than the detection of the dipole feature [161]. The ring-like feature, which concerns only low-energy recoils, is not reproducible by the background and can then be used as a secondary signature for DM identification. On the other hand, the directional detection of WIMP accompanied by the observation of a ring-like feature would constrain the properties of the WIMP halo model.

Let us discuss a third directional signature of WIMP, the so-called *aberration feature*. Due to the Earth motion around the Sun, the direction of arrival of WIMPs in an Earth-based detector varies within a one-year period. The observation of an annual modulation of the directional recoil rate would confirm the galactic provenance of WIMPs and would determine the properties of the WIMP velocity. The detection of about 10^3 events with a directional detector would be sufficient to observe the aberration feature [162]. The observation of such directional annual modulation requires 10 times fewer events than the non-directional one [125].

The dipole feature is the dominant directional signature of WIMPs. The ring-like feature and the aberration feature can be used as additional probes for DM, improving the evidences for WIMP identification, and they are also valuable to constrain the properties of the WIMP halo. None of those features can be reproduced by the background [125], providing multiple unambiguous signatures that are considered as a smoking gun in the search for WIMP.

2.3.2 Beyond the neutrino floor

Before discussing a way to overpass the irreducible neutrino background, let us introduce the principle of *head-tail* recognition. Directional detectors not only measure the direction of a WIMP-induced nuclear recoil, $\hat{\mathbf{q}}$, they can also determine the sense of the recoil, *i.e.* they distinguish between $+\hat{\mathbf{q}}$ and $-\hat{\mathbf{q}}$. A nuclear recoil produces ion-electron pairs all along its track. It is convenient to talk about the *head* and the *tail* of a track, where the tail corresponds to the first electron-ion pair produced by the recoil. Due to the way the nuclear recoil deposits its energy in a medium, described by the stopping power introduced in Section 4.2, there is an asymmetry in the charge distribution along the track. We will present in Chapter 8 a procedure to observe this asymmetry, even for low energy recoils in the keV-range. Measuring the charge asymmetry enables head-tail recognition (*i.e.* sense recognition).

We have already discussed the three main sources of ambient neutrino fluxes. The fluxes of atmospheric and diffuse supernova neutrinos can be considered isotropic and constant over time [163]. They will then not exhibit any directional feature. The situation is however different for the solar neutrino flux: it is anisotropic and it evolves in time due to the eccentricity of the Earth's orbit. The triple-differential recoil rate for coherent neutrino-nucleus scattering (νNS) is given by a convolution between the double-differential νNS cross-section and the solar neutrino directional flux [125]:

$$\frac{d^3R}{dE_R\, d\Omega_R\, dt} = \mathcal{N} \int_{E_\nu^{\min}} \frac{d^2\sigma^{\nu NS}}{dE_R\, d\Omega_R} \times \frac{d^3\Phi_\nu}{dE_\nu\, d\Omega_\nu\, dt}\, dE_\nu\, d\Omega_\nu \tag{2.28}$$

where $\mathcal{N}$ is the number of target nuclei per unit mass and $E_\nu^{\min} = \sqrt{m_N\, E_R/2}$ is the minimum neutrino energy required to produce a recoil of energy E_R. An analytical calculation of the triple-differential rate is provided in the case of solar neutrino in [163].

The double-differential recoil rate of WIMPs, Eq. (2.19), can be extended to the triple-differential recoil rate by considering a period Δt and by explicitly stating the time dependency of $\hat{\mathbf{r}} \cdot \mathbf{v}_{\text{lab}}$ in the Radon transform. One can then compare the angular recoil rates of WIMPs and solar neutrinos, after integrating over the exposure time and the detection energy range, in order to determine the overlap between the angular distributions and thus to determine the ability to detect a WIMP, with 90% confidence level at 3σ, even inside a significant neutrino background.

The use of directional detection to overpass the neutrino floor is illustrated in the two panels of Figure 2.9 in which the exclusion potential is computed for two different experimental situations. The left panel compares several readout strategies (with and without directional information, with and without head-tail recognition) whereas the right panel uses 3D directional information for evaluating the effect of angular resolution on the discovery potential.

Few comments are required at this stage. First, one can see that directional information improves by about one order of magnitude the sensitivity for WIMP searches. Second, directionality mainly improves over non-directional strategies for light-WIMP with masses below 30 GeV. Third, head-tail recognition improves the discovery potential. Fourth, the neutrino floor can significantly be overpassed when directional information is measured, even when partially measured as in the 1D case. We will demonstrate in Chapter 8 that MIMAC achieved a better than 15° angular resolution for recoils down to a few keV and that it distinguishes between the head and the tail of a nuclear recoil.

2.3.3 WIMP identification

The physical results of a directional detector can be separated into two types. The first one consists in setting an exclusion limit, *i.e.* to demonstrate that measured recoils are sufficiently anisotropic so that they cannot be due to background. The second type consists in discovering a WIMP, that is correlating the recoil directions to the expected incoming WIMP direction, with more than 90% confidence level at 3σ. The difference between the two types is mainly a matter of statistics.

Non-parametric statistical tests can be used to reject an isotropic background without any assumption on the properties of the DM halo. This model-independent approach is possible by considering that the incoming direction of WIMPs is known. In such a case, the mean angle $\langle \cos\theta \rangle$ between the measured nuclear recoil and the incoming WIMP direction will be positive for WIMP-induced recoils, and zero for isotropic background. In the background-free limit, 10 recoil events are sufficient to claim

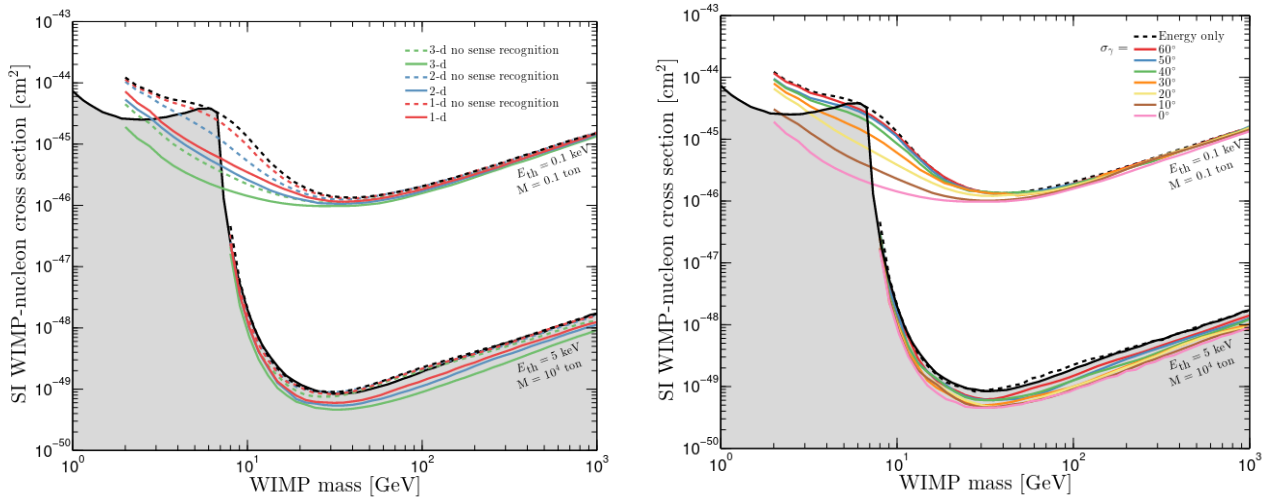

Figure 2.9: Exclusion potential as a function of the WIMP mass for a detector using Xe target and an exposure time of one year. Two sets of detection parameters are shown: (E_{th} = 0.1 keV, M = 0.1 ton) and (E_{th} = 5 keV, M = 10^4 ton). The neutrino floor for the Xe target is represented as the upper limit of the gray shaded area. Black dashed lines correspond to energy-only detection without directional information.
Left: Exclusion potential for several readout strategies (energy only, 1D, 2D, 3D, with and without head-tail recognition) assuming perfect angular resolution and 100% head-tail recognition in the background-free limit.
Right: Exclusion potential for a 3D detector with sense recognition for an angular resolution, σ_γ, varying between 0° and 60°.
Figures extracted from [163].

the discovery of a non-background event at 95% confidence level for a 3D detector with head-tail recognition, and about 100 recoils without head-tail recognition [164]. The same authors also showed that $\sim$ 30 events are sufficient, once again for an ideal detector in the background-free limit, not only to identify non-background events, but to demonstrate that the median recoil direction is correlated with the solar motion, hence demonstrating the Galactic origin of the signal [165].

While such results played an important role in comforting the interest in directional detection, they have later been extended to account for detector performances and background. Julien Billard *et al.* have developed likelihood statistical tests to determine the discovery potential of directional detection [160, 166, 167]. In their approach, the uncertainties on the astrophysical inputs, such as the halo properties or the local DM density, are included as nuisance parameters in the likelihood function in order to decrease the dependency of the results on these uncertainties. They have demonstrated that the discovery potential of a directional detector is affected, in order of priority, by (1) the energy threshold, (2) the background contamination, (3) the head-tail recognition efficiency, (4) the angular resolution, and (5) the energy resolution [166].

The most impacting effect, the energy threshold, is balanced by two competing phenomena. The first one is statistics: the higher the energy threshold, the fewer events are detected. The second one comes from the fact that the heavier the WIMP, the more anisotropic the recoil, so the easier to discriminate from the background. However, the loss of events dominates the influence on the discovery potential over the enhancement of anisotropy [166]. The conclusion is that directional detectors must decrease their energy threshold to improve their discovery potential.

Figure 2.10 presents the influence of some experimental conditions on the discovery potential of a 30 kg $\cdot$ year CF_4 directional detector with an energy range of [5, 50 keV]. The figure compares the effects of head-tail recognition, angular resolution and background. The solid black line corresponds to the ideal case of a detector accessing the full directional information in the background-free limit. One can see with the red curve that the introduction of background significantly reduces the discovery potential for low-mass WIMPs. From this analysis, we also conclude that only 5 events are sufficient to claim a 3σ discovery at 90% confidence level, for a WIMP mass of 5 GeV and a SD cross-section of $\sim 10^{-4}$ pb, with perfect head-tail recognition and angular resolution, an energy threshold at 5 keV, and in the absence of background. If one adds 300 background events isotropically distributed and flat

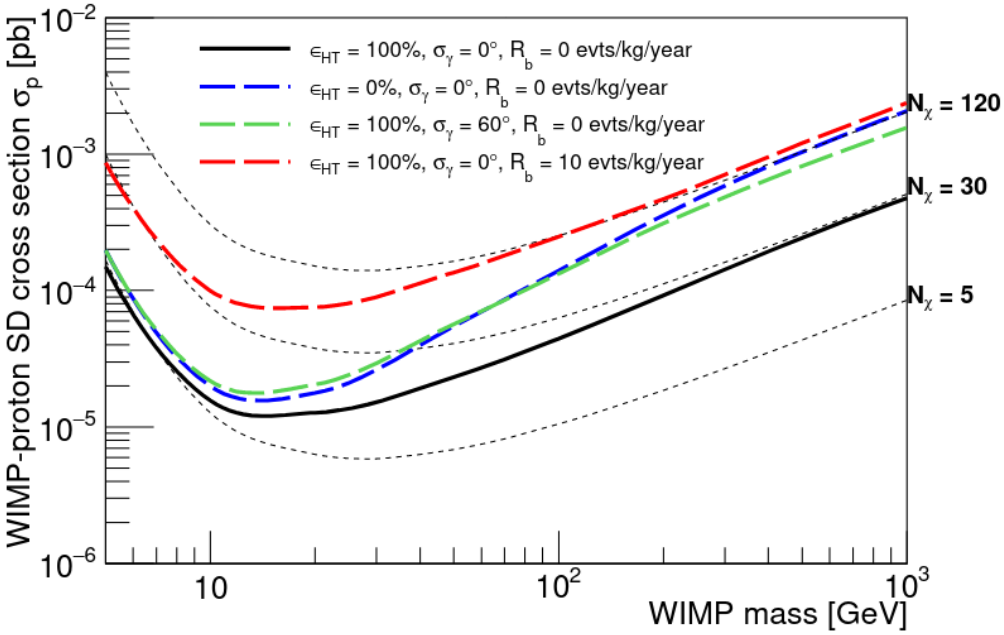

Figure 2.10: Influence of some experimental conditions on the 3σ discovery potential of directional detection at 90% confidence level. Estimations for a 30 kg $\cdot$ year CF_4 directional detector with an energy range of [5, 50 keV]. The dashed black lines correspond to iso-number of WIMP events. Figure extracted from [125].

in energy, then the required number of events increases to about 30. It has been shown that a MIMAC-like detector based on a fluorine target, with reasonable directional performances and a conservative background of 10 events/year/kg could discover WIMP down to a SD cross-section of order $\sim 10^{-4}$ pb and could set an exclusion limit down to $\sim 10^{-5}$ pb [168].

There is no hard limit on the requirements for a directional detector. In this work we aimed for $< 20°$ angular resolution and $> 80\%$ efficiency in the head-tail recognition for recoils in the keV-range. The most sensitive requirement remains the energy threshold: one should lower it as much as possible. Decreasing the energy threshold is challenging because, instead of an energy measurement issue, it is rather difficult to reconstruct the directional information for short tracks (sub-millimeter). In this perspective, this thesis dedicates special attention to the proton: as the lightest target, it is the less affected by quenching effects and the one having the longest tracks for a given energy. Moreover, kinematics favour the energy recoil on light targets for low-mass WIMPs, the ones that are less constrained experimentally and for which the neutrino floor is limiting non-directional detection. The MIMAC detector is then using a multi-target gas mixture, based on ^{1}H and ^{19}F (that are sensitive both to the SI and the SD channels), for searching for light WIMPs.

2.4 State of art of directional detection

In this section, we present a review of the current status of directional detection and we refer to [169] for more details. The key parameter for reconstructing the direction of the recoil is its track: in principle, the longer the track, the more accessible the directional information. In solid, nuclear recoils of less than 100 keV induce track lengths of less than 100 nm. We will see that directionality could be achieved in solid thanks to nuclear emulsions. However, most of the directional detectors operate in gases, usually at low pressure (< 100 mbar), with expected track lengths of the order of (sub)-millimeter. The price to pay is the reduction of the target density, requiring large detection volumes ($\geq$ m^3) to probe the WIMP parameter space. Gaseous directional detectors are based on Time Projection Chambers (TPC), whose working principle is extensively detailed in Chapter 4. For the moment it is enough to say that in a TPC, an interaction produces electron-ion pairs that drift towards a readout plane under the influence of a constant electric field. If this plane has a 2D granularity, and it is sampled at large frequency (50 MHz in the MIMAC detector), the combination of the constant drift velocity and

the sampling time enables reconstruction of the track in 3D. This reconstruction is performed at the readout plane, so after diffusion of the primary charges on their way towards the readout plane. Before describing the main directional projects, let us discuss two competing approaches used in directional gaseous TPC: the negative ion drift (NID) and the electron drift (ED).

2.4.1 Electron or negative ion drift

With MIMAC we are interested in the drift of primary electrons. An alternative approach for directional detectors relies on the drift of negative ions that are formed by the attachment process. In this case, one must use an electronegative gas with a large electron capture cross-section. For instance, in the SF_6 the electron capture occurs in less than a micron of drift [170], so in a few nanoseconds depending on the drift velocity, forming a metastable SF_6^{-*} anion that will evolve through one of the processes:

$$SF_6 + e^- \rightarrow {SF_6}^{-*} \rightarrow \begin{cases} SF_6 + e^- & (\text{auto} - \text{detachment}) \\ {SF_6}^- + \text{energy} & (\text{stabilization}) \\ {SF_5}^- + F & (\text{decomposition}) \end{cases} \tag{2.29}$$

In NID TPCs, the primary electron is quickly attached to a gas molecule, and the anion drifts under the influence of the electric field. The avalanche is still initiated by the electron, achieving $> 10^3$ gains [170], although larger amplification electric fields are usually required compared to ED TPCs. The supporters of NID detectors put forward the following arguments:

- **Fiducialization**. Since the metastable anion can decompose into other anion species, all of them having a specific drift velocity, the detected time difference between these *minority carriers* enables the localization of the interaction along the drift direction, so the fiducialization of the detector. This method proposed and validated a decade ago [171, 172] is an interesting feature of NID detectors.

- **Diffusion**. The ions are less affected by diffusion than the electrons and diffusion can sometimes be reduced down to the thermal limit in NID detectors.

- **Electronics**. Due to the different drift velocity between ions and electrons, the NID detectors are usually sampled around 1 MHz which simplifies the electronics compared, for instance, to the 50 MHz of the MIMAC detector.

These advantages must however be moderated. Concerning the diffusion, we will see in this thesis that we can achieve a 15° angular resolution down to 1 keV_{ee} proton recoils in a 25 cm drift chamber exploiting the ED technology event though the measurements are affected by diffusion. Actually, we even support the opposite argument: diffusion is required to access directionality on sub-millimeter tracks that otherwise would be detected as point-like events [173, 174].

While the minority carriers are definitely interesting for fiducialization, they are a direct consequence of the intermediate processes described in Eq. (2.29) whose cross-sections, and thus their relative occurrences, depend on the energy of the primary electron. The presence of such intermediate processes could possibly alter the directional information at low energy and deteriorate the energy resolution. For instance, the anion lifetime for the auto-detachment process, of the order $(10 - 68)$ μs for the SF_6^- [170], means that a primary electron is continuously captured and detached by gas molecules until it arrives at the readout plane.

2.4.2 Review of directional detectors

DRIFT was the pioneer of directional detectors and it exploits NID in a gas mixture of CS_2, CF_4 and O_2 with relative partial pressures of $(30 : 10 : 1)$ Torr [175]. The CS_2 is an electronegative gas that enables the drift of CS_2^- ions. The CF_4 is used for the fluorine target. The presence of O_2, another electronegative gas, acts as a minority carrier to fiducialize along the drift direction. The DRIFT-IId detector has a total volume of 1 m^3 and is composed of two chambers of 50 cm drift, back-to-back, sharing a common cathode. The readout is made of MWPC (Multi-Wire Proportional Counters), with

a grounded anode plane of 20 μm wires, sandwiched between two perpendicular grid planes of 100 μm wires. The pitch is 2 mm in both directions of the 2D readout plane [172]. The readout is sampled at 1 MHz. DRIFT-IId achieved a full fiducialization of a 0.8 m^3 volume [172], leading to very efficient background discrimination of surface events and an almost background-free operation. The detector operated for more than a decade in the Boulby mine and, to the author' knowledge, the project is now ended as the team dedicated efforts to the CYGNUS project (that we will present below). The DRIFT collaboration has demonstrated head-tail recognition down to 38 keV [176], as a statistical description and not as an event-by-event determination. The DRIFT collaboration has placed exclusion limits down to 0.160 pb in the SD channel for a WIMP mass of 80 GeV and it has set constraints down to a WIMP mass of 9 GeV [175].

MIMAC is the detector studied in this work but, for completeness, we summarize its main features so that it can be compared to other directional detectors. MIMAC is a TPC based on the drift of electrons in a gas mixture 70% CF_4 + 28% CHF_3 + 2% i-C_4H_{10} at 50 mbar chosen for its drift and gain properties while having a large amount of fluorine targets. The current prototype has two chambers of 3 L with 25 cm drift, connected by a common cathode. Another bi-chamber prototype of 60 L is currently tested and should serve as an elementary brick to be duplicated 16 times by for building a 1 m^3 detector in the near future. The charge amplification is performed thanks to a Micromegas of gap 512 μm which a 2D pixelated anode, with a strip pitch of 424.3 μm in both directions, sampled at 50 MHz. The Micromegas enables measurement of the energy on the grid whereas the 3D track is reconstructed from the pixelated anode. MIMAC achieved a rejection power of around 10^5 for rejecting electron background events [177] and it measured nuclear recoils from the Radon progeny that can be used as a benchmark for directional detectors [178]. In this configuration, its detection threshold is around 5 keV. Recently, the team has worked on another mixture of 50% i-C_4H_{10} + 50% CHF_3 at 30 mbar, where both proton and fluorine can be used as targets. This mixture is dedicated to high-gain operations, with a directional detection threshold of 1 keV, and was used to reconstruct mono-energetic neutron spectra at 8 keV and 27 keV [179] with a better than 15° angular resolution on proton recoils. A MIMAC prototype ran for almost 6 years in the underground laboratory of Modane.

NEWAGE is a collaboration making use of the electron drift in pure CF_4 at 100 mbar. The chamber has 41 cm drift and an active area of about 31×31 cm^2 [180]. The charge amplification is performed by means of GEMs (Gas Electron Multipliers) and the readout plane is made of micro-pixels (μ-PIC) with a pitch of 400 μm sampled at 100 MHz. The collaboration has developed low-alpha-emitting micro-pixels [181], reducing by about a factor of 100 the contamination from radioactive isotopes. Both the charge and the track are read from the μ-PIC: the charge waveform is recorded from grouped signals of the cathode strips. The track is determined from the measurement of the Time-over-Threshold of all strips hit by an event [182]. The collaboration measured an angular resolution of 48° for recoils in the range [50, 100 keV] with a detection threshold around 50 keV [180]. They also measured an electron rejection power around 8×10^5. Recently, the NEWAGE collaboration has set an exclusion limit down to 50 pb in the WIMP-proton SD channel for WIMP mass of 100 GeV [180]. In 2007, the NEWAGE collaboration published the first direction-sensitive exclusion limit [183]. In parallel, the collaboration also investigates a possible use of SF_6 gas for NID. A special NEWAGE detector for NID achieved 3D track reconstruction with a spatial resolution of 130 μm with absolute z-reconstruction by the use of minority carriers [184].

DMTPC is an electron drift TPC filled with CF_4 at a pressure varying between 40 and 100 mbar. A m^3 detector has been built based on two TPCs back-to-back and optically isolated. As a difference with previous detectors, the amplification region, and the corresponding readout plane, are located at the center of each chamber, separating the total drift into four independent regions of 27.5 cm in order to reduce the influence of diffusion [185]. Each amplification region is made of a grounded mesh at 435 μm from a biased anode. The amplification planes are segmented into four quadrants to reduce their capacitance and, consequently, the intrinsic noise. The readout exploits the scintillation channel: once primary electrons, produced by ionization, arrive at mesh, the avalanche produces light by scintillation which is read by 4 CCD cameras [186]. Each CCD is made of 1024×1024 pixels, binned 4×4 to increase the signal-to-noise ratio, leading to a 2D imaging with bins of 642×642 μm^2 size [187]. In addition, the optical readout, which sits outside of the active volume, also has three PMTs

measuring secondary scintillation with nanosecond time resolution. It then provides an independent measurement of the energy and the time profile of the signal can be used to determine the z-coordinate of the interaction. Finally, the ionization in the amplification region is also measured in two ways: from a current-sensitive preamplifier on the mesh; and a charge-sensitive preamplifier on the anode [187]. DMTPC demonstrated a 50% efficiency in head-tail recognition at 50 keV [187]. The angular resolution was measured in 2011 to 40° for 80 keV nuclear recoils [188]. The track-detection threshold has been simulated to 25 keV [186]. To the author' knowledge, there is a single published exclusion limit obtained in a 10 L detector at the surface with a 80 keV threshold, leading to an upper limit of 2 nb on the WIMP-proton SD cross-section for a WIMP mass of 115 GeV [188].

CYGNO is a recent project of the CYGNUS collaboration that exploits the optical channel in an electron drift TPC. A first prototype of 7 L has demonstrated the performance of the detector and a 50 L is currently being installed in the Grand Sasso underground laboratory [189]. The TPC is filled with 60%He + 40%CF_4 at atmospheric pressure, where both helium and fluorine are used as targets. In the LEMOn prototype, the amplification is made by a triple-GEM with a transfer gap of 2 mm between the GEMs. The scintillation produced in the amplification region is read by two independent systems. The first one is an sCMOS camera divided into 2048×2048 pixels that makes use of recent developments in optical readout to obtain a low noise of around two photons per pixel [190]. This camera is located at the edge of the TPC, at the opposite side of the amplification region, such that, by taking into account the aperture of the lens equipping the camera, each pixel covers an active area of 125×125 μm^2 of the GEM plane [190], providing a high-granularity 2D imaging of the track. In parallel, the time profile of the scintillation signal is measured by a PMT with 5 ns risetime, located at the GEM surface, that is used to reconstruct the z-component of the track. The charge measurement is performed both from the sCMOS camera and from the PMT. The detection threshold has been measured to 2 keV [191]. While CYGNO is still in the early development phase, it represents a promising approach for low-threshold directional searches.

NEWSdm is a recent directional detector using a very different technology that the ones described above since it exploits a solid target made of AgBr crystals dispersed in a polymer. A nuclear recoil generates a track of excited AgBr crystals along its path. After chemical development and fixation, excited crystals form silver clusters of a few nanometer diameters. These clusters can be distinguished by a microscope as black grains [192]. Light elements, as C, N, O, and H can be contained in nuclear emulsions, providing a wide range of targets [193]. The readout is performed by an automated scanning system that analyses the target volume, after the exposition, to identify the silver grain. A resolution of 10 nm has been achieved [193]. This resolution enables to search for carbon recoils down to 30 keV [192]. In the microscope analyse, the scattering of a polarized light enables to reconstruct the Z-position of the track. A 65% efficiency in head-tail recognition for carbon recoils of 100 keV has been achieved [194]. The presence of ^{14}C in the polymer substrate introduces a background that can however be reduced by operating at low temperature ($-50°C$). One of the interests of nuclear emulsion detectors is the ability to scale to a large mass. However, since the microscope analysis is performed after the exposition, directional information could be washed out by too many rotations of the Earth, limiting the exposition time. A 10 g · month test-run has been performed at the Gran Sasso underground laboratory and a 10 kg · year is planned [194, 195]. It has to be noted that, due to their large density, nuclear emulsion detectors lose partially the directional information [196].

Some properties of directional detectors are listed in Table 2.1 for a brief comparison. We have chosen to only present directional detectors that have published experimental results. In the past few years, new approaches for directional detection have been proposed, for instance in liquid argon by columnar recombination [197] or exploiting quantum defects in solid-state elements like diamond [198]. This recent development demonstrates the increasing interest in directionality but the proposed technologies are not mature enough yet to be presented on an equal footing with conventional directional detectors.

2.4.3 Outlook

In the past fifteen years, several direction-sensitive exclusion limits have been established by directional detectors. In parallel, the detectors improved their directional performance, reduced their energy

Experiment	Volume [m^3]	Type	Channel	Target	Threshold [keV]	Location	Status
DRIFT	1	Gaseous NID-TPC CS_2:CF_4:O_2, 30:10:1, 55 mbar	Ionization	F	20 [172]	Boulby	Ended
MIMAC	0.006	Gaseous ED-TPC 70%CF_4+28%CHF_3+2%i-C_4H_{10}, 50 mbar 50%i-C_4H_{10}+50% CHF_3, 30 mbar	Ionization	F H, F	5 [177] 1 [179]	Modane	Running
NEWAGE	0.04	Gaseous ED-TPC CF_4, 100 mbar	Ionization	F	50 [180]	Kamioka	Running
DMTPC	1	Gaseous ED-TPC CF_4, [40, 100 mbar]	Scintillation	C, F	25 [186]	SNOLAB	Running (?)
CYGNO	0.05	Gaseous ED-TPC 60%He+40%CF_4, 1000 mbar	Scintillation	He, F	2 [191]	Gran Sasso	Installation
NEWSdm	10 g · month (exposure)	Nuclear emulsion AgBr	/	C, N, O, H	30 [192]	Gran Sasso	Running

Table 2.1: Status of directional detectors.

thresholds, and increased their scales. This technological development was a long but mandatory process and we are currently entering into a new area: directional detectors perform well enough to probe a competing parameter space (σ, m_χ), and they could overpass the neutrino floor in the near future. The detectors described in the previous section are all able to quickly adapt targets and working conditions (for instance the gas mixture and the pressure for gaseous TPCs). This ability plays an important role in the complementarity between detection strategies: if a non-directional detector detects a signal, directional detectors would have to confirm, or to deny, the WIMP origin of a signal with such characteristics (mass, cross-section, event rate). Adapting the working conditions allows then to optimize the probed parameter space.

The CYGNUS workshop [199] was gathering for years most of the groups working on directional detection in order to share experiences and, after demonstration and comparison between several technologies, to build a large common detector with optimum configuration based on current knowledge. Part of the members of this workshop decided to create the CYGNUS collaboration aiming to build a large-scale directional detector of 1000 m^3 [200]. The physical goal of such a detector is to achieve full 3D track reconstruction down to $1-3$ keV with efficient electron-recoil discrimination. The CYGNUS collaboration has compared charge readout technologies based on a joined study of performances and costs. They conclude that the best cost-efficiency compromise for a large-scale detector is to use a strip readout [200] comparable to the one described in this thesis. They propose to work with NID, based on a 755:5 He:SF_6 gas mixture, so at atmospheric pressure, in which the SF_6 is used for NID and helium is the main target. A 1000 m^3 detector filled with this mixture and operating for 6 years corresponds to 1 ton · year exposure and could set exclusion limits down to a SI cross-section of $\sim 10^{-45}$ cm^2 for a WIMP mass of 10 GeV [201], a sensitivity close to the neutrino floor computed on fluorine.

The CYGNUS collaboration is promising in terms of experience sharing, readout technologies comparison, and the spread of the directional strategy of detection. The MIMAC team has however decided not to join these efforts due to the CYGNUS choice of an electronegative gas mixture. Our experience on NID let us skeptical about the possibility to use this technology to achieve directional detection at a large scale. In parallel, we have demonstrated that TPCs based on electron drift achieve high directional performances for recoils in the keV-range [179].

Summary

Observations leading to the DM hypothesis indicate that DM would form haloes surrounding galaxies. If DM is a WIMP, the relative motion of the Solar system within the DM halo would induce a "WIMP" wind in an Earth-based detector, with a velocity of around 300 km/s, the WIMPs coming roughly from the direction of the Cygnus constellation. The properties of the Milky Way DM halo are inferred from local observations and recent measurements motivate an anisotropic and triaxial halo containing a

substructure. Direct detection is a strategy aiming to detect a WIMP interaction happening within the active volume of a detector. In particular, a WIMP can produce an elastic collision with a nucleus through two interaction channels, SI (spin independent) and SD (spin dependent), the SD channel being accessible only for nuclei with non-zero spin content. A WIMP-nucleus scattering results in a nuclear recoil inside the active volume of the detector, with kinetic energy below 10 keV/nucleon, providing a signature for direct searches. The velocity distribution of the WIMPs in the DM halo is a key element of the WIMP-nucleus event rate. Directional detectors are interested in the double-differential event rate, that is the recoil event rate per unit energy and per unit solid angle, whereas non-directional detectors are only concerned with the event rate per unit energy.

Extensive direct WIMP searches are carried out trying to detect rare events of order $\mathcal{O}(1)$ event/year/kg for nuclear recoil energy in the keV-range. Background mitigation strategies are then crucial in order to observe an excess over background. Other direct detection strategies are also investigated, for instance using the annual modulation of the WIMP signal, or exploiting the WIMP-electron scattering. The hypothetical Migdal effect for nuclear scattering receives increasing interest for searching for sub-GeV WIMPs since it would produce an electronic signal above the nuclear recoil energy, up to a few keV. Many direct projects have been built, exploiting complementary detection approaches based on scintillating crystals, bolometers, (dual-phase) noble liquid, bubble chambers, gaseous TPC, skipper-CCD, etc. These detectors are currently probing a large region in the (σ, m_χ) parameter space. However, they are limited by the background, in particular by the irreducible neutrino background since no detector can be shielded against neutrinos. The theoretical limit beyond which a WIMP signal cannot be statistically distinguished from a neutrino signal is called the neutrino floor and it is the ultimate limit for non-directional detectors. Note also that if a WIMP-like signal is observed in an experiment, determined as excess over background according to simulations, non-directional detection would not be able to prove that this signal is indeed due to a WIMP.

Directional detection has been introduced to cope with these issues. The relative motion of an Earth-based detector in the WIMP halo provides several signatures for unambiguous WIMP identification. The most significant one is the dipole feature in the recoil event rate, related to the motion of the Earth in the galactic WIMP halo. The directional features of the WIMP event rate are not reproduced by any of the known background. In particular, the neutrino background can be discriminated even beyond the neutrino floor. Moreover, fewer WIMP events are required to set exclusions limits when a detector has access to the directional information than when it has not. If a directional detector is able to measure not only the direction of a nuclear recoil, but also the sense of the recoil (head-tail recognition), its discovery potential increases. An ideal directional detector in the background-free limit only requires 5 WIMP events to identify a WIMP of mass 5 GeV for a SD cross-section of 10^{-4} pb. The discovery potential of a directional detector is affected, in order of priority, by (1) the energy threshold, (2) the background contamination, (3) the head-tail recognition efficiency, (4) the angular resolution, and (5) the energy resolution.

Directional detectors must be able to measure the direction of a nuclear recoil having track lengths in the millimeter-range in low-pressure gas mixtures, or of order ~ 100 nm in solids. This challenging measurement required years of technological development. Currently, directional detectors demonstrate their ability to access directional information in the keV-range, validating the directional strategy of detection of WIMP. In gaseous TPC, two main approaches are studied: the drift of electrons produced by ionization, or the drift of negative ions (NID) that attach the primary electrons. NID is less affected by diffusion and the presence of minority carriers, each of them having a different drift velocity, enables localizing the z-coordinate of the interaction. However, NID is affected by intermediate processes such as the auto-detachment and, for the moment, does not provide better directional performances than the electron drift method. The main directional detectors are DRIFT, MIMAC, NEWAGE, DMTPC, CYGNO, and NEWSdm, all of them making use of different technologies. The main limitation of directional detectors is their small scale since low-pressure is required for gaseous TPC in order to detect long enough track. The proto-collaboration CYGNUS aims to build a 1000 m^3 detector to directionally probe WIMPs down to the neutrino floor. In parallel, directional detectors continue to demonstrate their ability to investigate a unique and unambiguous signature for WIMP searches.

Chapter 3

Solar axions in large extra dimensions

Who needs the WIMP if we can have the axion?

Elena Aprile – XENON spokesperson [202]

While the Standard Model (SM) of particle physics is one of the most successful scientific theories, it also encounters some puzzling issues. One of them is the so-called *strong CP problem*: why does QCD (Quantum Chromodynamics) preserve the CP-symmetry (charge parity symmetry), as observed experimentally, although there is no theoretical motivation for preserving such a symmetry in the SM? In 1977, Roberto Peccei and Helen Quinn proposed a new global $U(1)_{\mathrm{PQ}}$ symmetry [203] whose breaking gives rise to a pseudoscalar particle, the *axion* [204, 205]. When the axion relaxes to the minimum of its potential, it dynamically compensates the CP-violating term of QCD and consequently solves the strong CP problem. In Section 3.1, we will introduce the axion and we will see that, if it exists, the axion would be a stable particle, feebly coupled to the SM particles, with a mass typically around 10 μeV, and non-relativistic when produced non-thermally. The axion is hence a viable non-baryonic candidate for cold Dark Matter [206–208] even if this interesting feature was not the initial purpose of its prediction. The axion is also the prototype of a generic class of bosons, called Axion-Like Particles (ALPs) and already discussed in Section 1.3, arising in multiple SM extensions [80, 81]. In this sense, the axion is a well-motivated particle and its study also benefits a wide class of particles involved in Physics beyond the SM.

In this work, we are interested in axions propagating in large extra dimensions (LED). In this

framework, the fundamental scale of quantum gravity can be lowered near the TeV-scale, hence solving the mass hierarchy problem, without violating experimental constraints [209, 210]. In the original scenario, the SM particles are constrained to live on a 4-dimensional Minkowski brane whereas singlets under the SM gauge group can propagate into the bulk of dimension $(4+n)$. The weakness of gravity at large distances is explained by the propagation of gravitons in the bulk. The n extra dimensions are compactified and large compared to the electroweak scale, up to the micrometer range, which allows for experimental tests of the theory. We will describe the LED framework in Section 3.2 and its multiple theoretical motivations. The axion being a singlet under the SM gauge group, it may propagate in the extra spatial dimensions. We will see that the phenomenology of the axion drastically changes in such a case. As an example, let us mention here that the axion would be seen as an infinite superposition of massive states, called a Kaluza-Klein (KK) tower, when observed from our 4D brane.

KK axion modes up to the kinematic limit would be produced in astrophysical objects. The Sun appears as a particularly interesting source due to its proximity and its relatively well-known characteristics. In Section 3.3, we revise the processes for producing KK axions in the Sun by considering their coupling to photons. Let us mention an interesting feature of the KK axions produced by the Sun: part of them would be sufficiently non-relativistic to be trapped into the solar gravitational field. These orbiting axions accumulate over cosmic times and consequently increase the present KK axion flux in a detector on Earth by about 3 orders of magnitude compared to the direct flux of axions emitted by the Sun. The phenomenology of the trapped KK axions is presented in Section 3.4. The decay of these trapped KK axions into photons could be a new X-rays source in the solar system and has been proposed as an explanation for the coronal heating problem [211] and the non-thermal distribution of the solar X-rays measurements [212].

To the best of our knowledge, a single paper was describing the phenomenology of solar trapped KK axions [211] and was used to set the basis of experimental searches for KK axions [213–217]. In [218], in collaboration with Mar Bastero-Gil from the Granada University, we have revised the model and updated the astrophysical constraints, leading to significant consequences for KK axions searches. This chapter is dedicated to the introduction of the concepts of KK axions and their production in the Sun and it significantly relies on our article [218]. Chapter 9 will discuss the constraints applying to KK axions and will describe possible experimental searches with MIMAC.

3.1 Introduction to the axion

3.1.1 The strong CP problem and the Peccei-Quinn mechanism

The QCD Lagrangian contains a θ-dependent term that violates the CP symmetry, where θ can be seen as an angle determining the vacuum of the theory [219]. The physical observables related to θ require working in a basis where the quark mass matrix is real and diagonal, leading to an additional contribution to θ from the weak sector. We thus introduce the effective parameter $\bar{\theta} = \theta_{\rm QCD} + \theta_{\rm weak}$ so the CP-violating term of the Lagrangian is given by:

$$\mathcal{L}_{\not{CP}} = \bar{\theta}\,\frac{\alpha_s}{8\pi}\,G^a_{\mu\nu}\tilde{G}^{\mu\nu}_a \tag{3.1}$$

where α_s is the QCD equivalent to the fine-structure constant, $G^a_{\mu\nu}$ is the gluon field-strength tensor, and $\tilde{G}^{\mu\nu}_a$ its dual. A CP-violation in the QCD sector would yield a non-zero neutron electric dipole moment (nEDM). However, the nEDM is experimentally probed and not yet observed, leading to a constraint $|d_n| < 3.0 \times 10^{-26}\,e$ cm (90% C.L.) [220] that converts into $|\bar{\theta}| \lesssim 10^{-11}$. In the SM, there is no constraint on $\bar{\theta}$ so the strong CP problem is the fine-tuning problem of why $\bar{\theta}$ is so unnaturally small. In other words, the strong CP problem asks why does QCD seem to preserve the CP-symmetry?

The Peccei-Quinn solution to the strong CP problem consists in introducing a global chiral symmetry $U(1)_{\rm PQ}$ under which the full SM Lagrangian would be invariant. An exact $U(1)$ symmetry would enable chiral transformation to set $\bar{\theta}$ to zero. However, such an exact symmetry is not allowed [203]. The $U(1)_{\rm PQ}$ symmetry would be spontaneously broken at an energy scale f_a and, since the symmetry is anomalous, would lead to a pseudo-Nambu-Goldstone boson called the axion [205] and hereafter noted a.

After the symmetry breaking, the effective Lagrangian must include additional terms to remain $U(1)_{\rm PQ}$ invariant [221]:

$$\mathcal{L}^{\rm eff} \;=\; \mathcal{L}_{\rm SM} \;+\; \left(\frac{a}{f_a}\xi + \bar{\theta}\right)\frac{\alpha_s}{8\pi}\,G^a_{\mu\nu}\tilde{G}^{\mu\nu}_a \;-\; \frac{1}{2}\partial_\mu a\,\partial^\mu a \;+\; \mathcal{L}_{\rm int.}\big[\partial^\mu a/f_a;\Psi\big] \tag{3.2}$$

where $\xi \sim \mathcal{O}(1)$ is a model-dependent parameter associated with the chiral anomaly of the Peccei-Quinn current, and where $\mathcal{L}_{\rm int.}$ is a possible term accounting for interaction with any field Ψ of the theory.

One of the interests of the Peccei-Quinn mechanism is the modification of the QCD vacuum by the additional symmetry. The vacuum expectation value of the axion field $\langle a\rangle$ is determined from the effective potential:

$$\left\langle \frac{\partial V_{\rm eff}}{\partial a} \right\rangle \;=\; -\frac{\xi}{f_a}\,\frac{\alpha_s}{8\pi}\,\langle G^a_{\mu\nu}\tilde{G}^{\mu\nu}_a\rangle\Big|_{\langle a\rangle} \;=\; 0 \tag{3.3}$$

showing a minimum at $\langle a\rangle = -\frac{f_a}{\xi}\bar{\theta}$ [221]. It is then possible to rewrite the Lagrangian in terms of a physical axion field, $a_{\rm phys.} = a - \langle a\rangle$, which exactly compensates the CP-violating term. In other words, the $\bar{\theta}$ parameter is absorbed in a redefinition of the axion field.

The PQ mechanism thus solves the strong CP problem by introducing a new global symmetry that, once broken, gives rise to a new field, the axion, with a vacuum expectation value that systematically and dynamically compensates the CP-violating term of QCD.

3.1.2 Axion phenomenology

Without loss of generality, we can write the axion-dependent part of the effective Lagrangian after the breaking of the PQ and the electroweak symmetries, at leading order in f_a, as [84]:

$$\mathcal{L}_a = \frac{1}{2}(\partial_\mu a)^2 + \frac{a}{f_a}\frac{\alpha_s}{8\pi}\,G_{\mu\nu}\tilde{G}^{\mu\nu} + \frac{1}{4}\,a\,g_{a\gamma\gamma}F_{\mu\nu}\tilde{F}^{\mu\nu} + \frac{\partial_\mu a}{2f_a}\,j^\mu_a \tag{3.4}$$

where $F_{\mu\nu}$ is the electromagnetic field-strength tensor, $\tilde{F}^{\mu\nu}$ its dual, and j^μ_a is an axial current based on interactions with SM fermions and that we will neglect in the following since we restrain our analysis to hadronic axions that are not coupled to fermions at tree-level. In other words, we consider the general case of hadronic axions instead of model-dependent extensions. The coupling of the axion with the gluon field allows for mixing between the axion and the mesons. The first main consequence of this mixing is the coupling to photons introduced in Eq. (3.4). As a second consequence, the mixing gives rise to the axion mass that can be calculated from QCD [84]:

$$m_a = 5.70(6)\,\mu{\rm eV}\,\left(\frac{10^{12}{\rm GeV}}{f_a}\right) \tag{3.5}$$

Since the axion mass is related to this mixing, the axion would be a massless particle for energies above the QCD scale, so in the Early Universe [219]. Finally, we can rewrite the effective Lagrangian for hadronic axions as:

$$\mathcal{L}_{\rm eff} = \frac{1}{2}(\partial_\mu a)^2 - \frac{1}{2}\,m_a^2\,a^2 + \frac{g_{a\gamma\gamma}}{4}\,a\,F_{\mu\nu}\tilde{F}^{\mu\nu} \tag{3.6}$$

The coupling to the photon is expressed as [84]:

$$g_{a\gamma\gamma} = \frac{\alpha_{em}}{2\pi f_a}\left[\frac{E}{N} - 1.92(4)\right] \equiv \frac{\alpha_{em}\xi_{em}}{2\pi f_a} \tag{3.7}$$

where α_{em} is the fine-structure constant, E and N are the color and the electromagnetic anomaly coefficients, respectively, and we have defined ξ_{em} that embeds the model-dependent part of the expression. The ratio E/N is model-dependent and is equal to zero for hadronic models.

The Lagrangian Eq. (3.6) contains the most general terms that, apart from model-dependent parameters of $\sim \mathcal{O}(1)$, are always involved in the axion phenomenology. The Lagrangian could be

extended to couplings to electrons and nucleons but they will not be considered in this work, except when explicitly stated.

According to its coupling to the electromagnetic field tensor, the axion can decay into two photons with a lifetime given as:

$$\tau_a = \frac{64\pi}{g_{a\gamma\gamma}^2 m_a^3} \tag{3.8}$$

We will later present the constraints on the coupling to photons but we can already mention that the axion lifetime would be bounded as $10^{30} \lesssim \tau_a \lesssim 10^{45}$ days. The axion is then a stable non-baryonic massive particle that only feebly couples to SM gauge fields. It has then the properties of a DM particle. Let us now discuss the axion production mechanisms to determine if it is an appropriate DM candidate.

Axion production in the Early Universe

The axions could be produced thermally. When the universe cools down to a temperature $T \simeq f_a$, axions can be produced via the interactions between quarks, gluons, and photons [222]. For instance, the Primakoff process converts a photon into an axion in the field of a light quark: $\gamma + q \leftrightarrows a + q$. After the QCD confinement at $T = \Lambda_{\rm QCD}$, axions get massive and also interact with pions. A thermal population of axions is then produced until they decouple from the QCD plasma, depending on f_a. The thermal production of axions is analogous to the neutrino's one [223] and the thermal axions would then contribute to the so-called hot dark matter.

Besides the thermal production, axions could also be produced in the Early Universe by the re-alignment mechanism, also called misalignment mechanism, leading to a non-relativistic population having properties of cold dark matter. The realignment mechanism is a direct consequence of the PQ symmetry. After the spontaneous breaking of the PQ symmetry, the axion field relaxes to a minimum of its potential which fixes the value of the angular parameter to a random initial state $\theta_i \in [-\pi, \pi)$. The Universe continues to cool down until the QCD epoch where QCD effects explicitly break the PQ symmetry, providing the axion mass. At this point, there is a minimum in the axion potential that solves the strong CP problem, let us say for an angle $\theta_{\rm CP}$. However, there is no reason for $\theta_{\rm CP}$ to coincide with θ_i [219]. The axion field then rolls down towards $\theta_{\rm CP}$ and overshoots it, leading to damped oscillations around the CP-conserving minimum of the potential. These coherent oscillations, which are due to the realignment of the axion field, behave as cold dark matter. It is possible to determine the present energy density of the axions produced by the realignment mechanism by solving the equation of motion of the field and accounting for the expansion of the universe. Note that one must distinguish between two scenarii: if the PQ symmetry breaking happens before the inflation, then the initial value θ_i is the same everywhere and the description above remains valid. If the PQ symmetry breaking happens after the inflation, θ_i can take different random values in non-connected patches of the universe. So one can perform the overall calculations with the average value $\sqrt{\langle\theta_i^2\rangle} = \pi/\sqrt{3}$ [219]. The axion matter density would be given by [223, 224]:

$$\Omega_a h^2 \simeq \begin{cases} 0.7 \left(\frac{f_a}{10^{12}\ \text{GeV}}\right)^{7/6} \left(\frac{\theta_i}{\pi}\right)^2 & \text{pre} - \text{inflation model} \\ 0.3 \left(\frac{f_a}{10^{12}\ \text{GeV}}\right)^{7/6} & \text{post} - \text{inflation model} \end{cases} \tag{3.9}$$

Since the axion density given by the realignment mechanism is roughly proportional to f_a, the lighter the axion, the larger the relic density. In both scenarii, an axion mass of the order of 10 μeV could account for the total observed CDM density [219]. However, such estimations are crude. In the pre-inflation scenario, the non-thermal relic density depends on the parameter θ_i, which is unknown and usually set to unity. In the post-inflation scenario, there are additional sources of non-thermal production due to the inhomogeneities in the axion field since θ_i differs in multiple patches of the universe. In this case, the axion field forms topological defects [224], such as axion strings and walls, that later decay producing additional non-relativistic axions. The axion mass could then be significantly larger than 10 μeV while still accounting for the observed CDM density.

Bounds on the axion

A cosmological bound on axion can be derived from the above discussion. If a too large axion density was created, it would have "overclosed" the universe. By considering only the realignment mechanism[1], an upper bound on $f_a < 10^{12}$ GeV is found [225]. Once again this bound is a crude estimate that can be strengthened or relaxed, for instance depending on the details of the realignment mechanism.

Another kind of bounds on the axions comes from astrophysical concerns. If they exist, the axions would also be produced in astrophysical objects such as stars or supernovae, opening exotic channels for energy loss and then accelerating the evolution of the astrophysical object. If the axion coupling to photons or any other SM particles is too large, the production of axions in the astrophysical objects would become too significant, altering the measured observables of such objects. The two main corresponding astrophysical bounds come from observations of the Horizontal Branch (HB) stars and from the supernova SN 1987A [226]. The lifetime of the HB stars, which are in their helium-burning phase, can be inferred from observations of globular clusters where the stars are assumed to have all the same age. The comparison of observations to simulated lifetimes constrains axion production. In the case of supernovae, the axion emission would remove part of the energy used for late-time neutrino emission. In other words, the more axions are produced, the shorter is the neutrino signal.

Combining the multiple observations, the scale of the PQ symmetry breaking is constrained from astrophysical (lower limit) and cosmological (upper limit) considerations, with the usually quoted bounds [225, 227]:

$$10^9\,\mathrm{GeV} \lesssim f_a \lesssim 10^{12}\,\mathrm{GeV} \tag{3.10}$$

which can be converted into a mass range:

$$10^{-5}\,\mathrm{eV} \lesssim m_a \lesssim 10^{-2}\,\mathrm{eV} \tag{3.11}$$

This brief introduction to the axion phenomenology should provide enough elements for extending the study to large extra dimensions. For more detail, we refer to the comprehensive and recent introduction to axion [219]. At this stage, we have shown that the axion is a pseudoscalar involved in the PQ mechanism for solving the strong CP problem and that the axion is also an appropriate CDM candidate.

3.1.3 The Axion-Like Particle (ALP) and its cosmological bounds

Before moving to extra dimensions, let us discuss a generic extension of the axion phenomenology. An ALP is a boson, scalar or pseudoscalar, that arises from the breaking of a global $U(1)$ symmetry. In this sense it is a class of particles; the axion being an ALP. However, the ALPs do not necessarily solve the strong CP problem. The relation between the mass and the scale of the symmetry breaking, Eq. (3.5), is thus not fixed in the case of the ALP: the two parameters are independent. The phenomenology of the ALP is anyway close to the one of the axion, in particular when the ALPs are pseudoscalars so they also are good CDM candidates. In this sense, the extensive study of the axion can be used as a prototype for the wider case of ALPs.

The main interest in grouping similar particles into the ALP class is that a detector searching for axions is usually also sensitive to the ALPs. For instance, detectors exploiting the axion-photon coupling could be sensitive to any ALP ϕ including the following term in its Lagrangian:

$$\mathcal{L} = -\frac{g_{\phi\gamma\gamma}}{4}\,\phi\,F_{\mu\nu}\tilde{F}^{\mu\nu} \tag{3.12}$$

Similarly, the astrophysical and cosmological considerations described above can, to some extent, be applied to most of the ALPs [228].

We will see in Chapter 9 that the MIMAC detector can search for axions with a mass in the keV-range. Although this is not the mass of the QCD axion, we will see that this is the appropriate mass

[1] This approximation considers that axions are not thermally produced for $f_a > 10^8$ GeV although extensions of the calculation accounting for interactions with quarks and gluons defined a new bound for thermal production around $f_a > 10^{12}$ GeV [222].

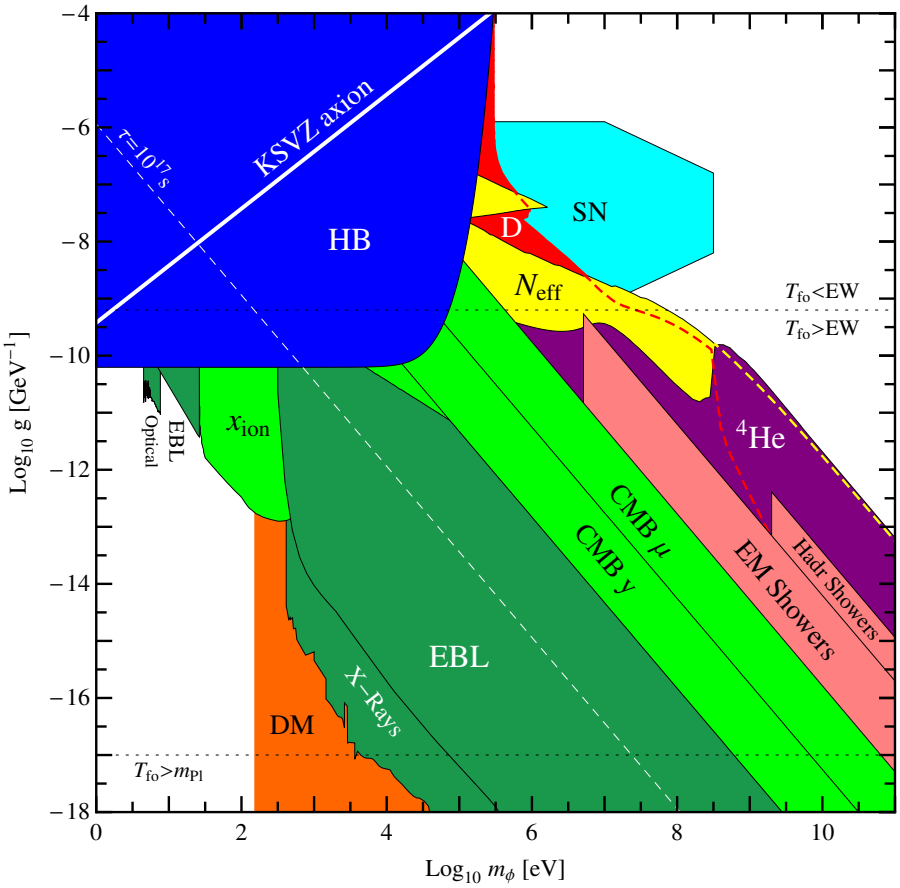

Figure 3.1: Cosmological and astrophysical bounds on the ALPs depending on their mass and their coupling g to the electromagnetic field-strength tensor. The bounds are obtained assuming a standard cosmology and a standard thermal production of the ALP relic density. Figure extracted from [85] and we refer to it for the meaning of the acronyms.

range for solar axions propagating in extra dimensions. At the same time, MIMAC could also search for ALPs. However, the parameter space ($g_{\phi\gamma\gamma} - m_\phi$) is significantly constrained by cosmological and astrophysical considerations, as one can see in Figure 3.1. In the keV-range, the most stringent limit is the one labelled "EBL" in the figure, standing for Extragalactic Background Light. The ALPs produced in the Early Universe could decay into two photons and would then contribute to the photon flux coming from outside the galaxy, *i.e.* the EBL. In order to compute the photon flux due to ALP decays, one must consider the expansion of the universe, which redshifts the emitted photons, and account for possible absorption of the emitted photons by the intergalactic medium. This additional predicted flux due to the ALP decays, computed at present time, should not exceed the measured EBL.

In Chapter 9, we will derive the EBL constraint for Kaluza-Klein axions and we will demonstrate that it significantly relaxes compared to the four-dimensional case. For the case of ALPs, on the contrary, the work of Cadamuro and Redondo [85] presented in Figure 3.1 seems to exclude the parameter space that could be probed by MIMAC. In their work, they consider the probability for a photon to be absorbed via photoionization on the atoms of the intergalactic medium. We propose to update the calculations by also including the probability of the Compton scattering, whose cross-section is larger on hydrogen for photon energies $\gtrsim 2$ keV. After a Compton scattering, the photon will remain in the medium but with lower energy. For simplicity, we consider the extreme case for which the photon no longer contributes to the EBL after a Compton scattering. While not physical, this assumption simplifies the derivation and determines the maximal influence that the Compton scattering can have on the EBL constraint.

Let us determine how much the ALP would contribute to the EBL spectrum. We follow the procedure of [229] to compute the energy flux of photons, F_E, in a general cosmological background.

Since only photons produced after recombination would contribute to the EBL, the ALPs have gone out of equilibrium and the number density redshifts as $n_\phi \propto a^{-3}$, with a the cosmic scale factor. The differential energy flux is given by [85]:

$$I_E = \frac{d^2 F_E}{dE\, d\Omega} = \frac{\bar{n}_\phi(z_0)}{2\pi H(z_0) t_0}\, x\, e^{-x} \tag{3.13}$$

where the subindex "0" refers to quantities evaluated at present time, $H(z_0)$ is the Hubble parameter evaluated at present time, where $\bar{n}_\phi$ is the number density if the particle did not decay, and where we defined:

$$x \equiv \Gamma_{\phi\gamma\gamma} t_0 \left(\frac{2E_0}{m_\phi}\right)^{3/2} \tag{3.14}$$

In the previous expression we have assumed that the decay into photons is the only decay channel. We now match the ALP density with the present DM abundance. In this sense, our derivation differs from the one of Cadamuro and Redondo since they assume a thermal production of ALPs. We approximate $H_0 t_0 \simeq 2/3$ to get:

$$E\, I_E \simeq \frac{3\, E_0\, \rho_{DM}(z_0)}{4\pi m_\phi}\, x\, e^{-x} \tag{3.15}$$

Following the approach of [85], the photons can interact with hydrogen in the intergalactic medium, so we include a survival probability that must be multiplied to the Eq. (3.15):

$$P(z) = e^{-\sum_i \kappa_i(z,E)} \tag{3.16}$$

$$\kappa_i(z,E) = \int_0^z \frac{dz'}{H(z')\,(1+z')}\, n_H(z')\, \sigma_i(E) \tag{3.17}$$

where $E = m_\phi/2 = E_0(1+z)$ is the photon initial energy, and where $\kappa_i(z,E)$ is an absorption factor describing either the photoionization (κ_P), either the Compton scattering (κ_C), and where $n_H(z')$ is the hydrogen density at redshift z'. We approximate the interaction cross-section from [230] by the expression:

$$\sigma_i \simeq \bar{\sigma}_i \left(\frac{10\,\mathrm{keV}}{E}\right)^{\alpha_i} \tag{3.18}$$

in which we take $\bar{\sigma}_P = 4.57 \times 10^{-27}\,\mathrm{cm}^2$ and $\alpha_P = 3.5$; $\bar{\sigma}_C = 6.4 \times 10^{-25}\,\mathrm{cm}^2$ and $\alpha_C = 0.2507$. We arrive at the expression:

$$\kappa_i(z,E) = \frac{\bar{\sigma}_i\, n_{H0}}{H_0} \left(\frac{10\,\mathrm{keV}}{E_0}\right)^{\alpha_i} \frac{2}{3-2\alpha_i} \left\{ \left(\frac{m_\phi}{2E_0}\right)^{(3/2-\alpha_i)} - 1 \right\} \tag{3.19}$$

where [231]:

$$n_{H0} = 1.8 \times 10^{-7}\ \mathrm{cm}^{-3} \left(\frac{\Omega_\mathrm{b} \mathrm{h}^2}{0.019}\right) \tag{3.20}$$

Finally, the spectral intensity function is obtained by collecting all factors and dividing by the present wavelength:

$$\begin{aligned} I_\lambda &= \frac{3\, E_0\, \rho_{DM}(z_0)}{4\pi m_\phi \lambda_0}\, x\, e^{-x}\, e^{-\sum_i \kappa_i(z, m_\phi/2)} \\ &\simeq \left(7 \times 10^8\ \mathrm{photons \cdot cm^{-2} \cdot s^{-1} \cdot sr^{-1} \cdot \AA^{-1}}\right) \left(\frac{2}{\mathrm{m}_\phi \lambda_0}\right) \mathrm{x\, e^{-x}\, e^{-\sum_i \kappa_i(z, m_\phi/2)}} \end{aligned} \tag{3.21}$$

This spectral intensity function can then be computed for given values of $g_{\phi\gamma\gamma}$ and m_ϕ and compared to EBL measurements, for instance to [232], to derive the EBL constraint on ALPs.

In Figure 3.2, we present the spectral intensity functions that we obtain for two ALP masses, for multiple ALP-photon couplings, and by including or not the absorption processes. We remind that in this derivation we have assumed for simplicity that a photon interacting via Compton scattering will no longer contribute to the EBL. This is thus a best-case scenario for relaxing the EBL constraint.

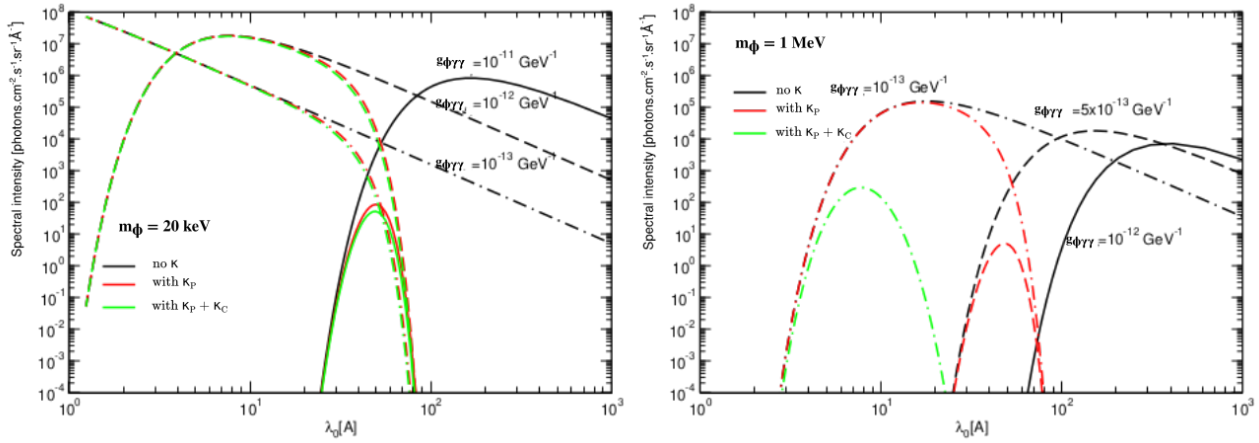

Figure 3.2: Spectral intensity functions from ALP decays for an ALP mass of 20 keV (left) and 1 MeV (right). Multiple values of the ALP-photon coupling have been taken, as indicated in the figure. The black lines are obtained without absorption, the red ones are obtained by only including the photoionization, and the green ones are obtained by including both photoionization and Compton scattering, under the strong assumption that after a Compton scattering the photon no longer contributes to the EBL spectrum.

Even in this best-case scenario, no significant contribution is observed when including the Compton scattering for an ALP mass of 20 keV. In other words, the mass range probed by MIMAC for searching for KK axions, which roughly is [1, 20 keV], cannot be used at the same time for searching for ALPs because the region is excluded by EBL observations. For larger masses, the Compton scattering can dominate over the photoelectric effect, and it must be included in the derivation of the EBL constraint. We then point out that the EBL constraint derived in [85] is too restrictive for large masses. However, our derivation is too conservative due to our assumption on the Compton scattering. It is anyway sufficient for our purpose since, even being conservative, we obtain "negative" results.

To summarize the discussion above, axion detectors are usually also sensitive to ALPs. In this thesis, we study the Kaluza-Klein axions which have a specific phenomenology for escaping the main cosmological constraints as we will see in Section 9.1. We then wonder if we could also search for general ALPs at the same time. While the region of interest for KK axions is $\sim \mathcal{O}(1 - 20$ keV), we have seen that this mass region is significantly constrained for ALPs by measurements of the EBL for an ALP-photon coupling covering several orders of magnitude. However, it is still worth setting experimental limits on this region of the parameter space since the cosmological bounds rely on assumptions, for instance concerning the relic density of ALPs. As discussed in Section 1.3, keV-ALPs receive increasing experimental interest since they could play a role in the explanations of some puzzling observations.

3.2 Large extra dimensions

3.2.1 Do we live in a 4D world?

It sounds tempting to answer yes to this question. But this point must be considered seriously since so far there is no experimental argument for ruling out the existence of extra dimensions. The original idea of considering more than 3 spatial dimensions is probably due to Gunnar Nordström in the 1910s who tried to unify his relativistic theory of gravitation with Maxwell's theory of electromagnetism [233,234]. While his theory has quickly been rejected, as well as the famous similar attempts of Kaluza and Klein in the 1920s based on general relativity, the idea of extra spatial dimensions came back in the 1980s, being motivated in particular by string theories and quantum gravity.

In 1998, Arkani-Hamed, Dimopoulos, and Dvali proposed the framework of the large extra dimensions [209], also called the ADD scenario from their names, in which extra spatial dimensions would exist. The ADD framework stabilizes the mass hierarchy by lowering drastically the fundamental scale of quantum gravity, sometimes down to the TeV-range, without violating experimental constraints, as we will see below. In such a paradigm, the SM fields are confined into a (1+3)-dimensional subspace,

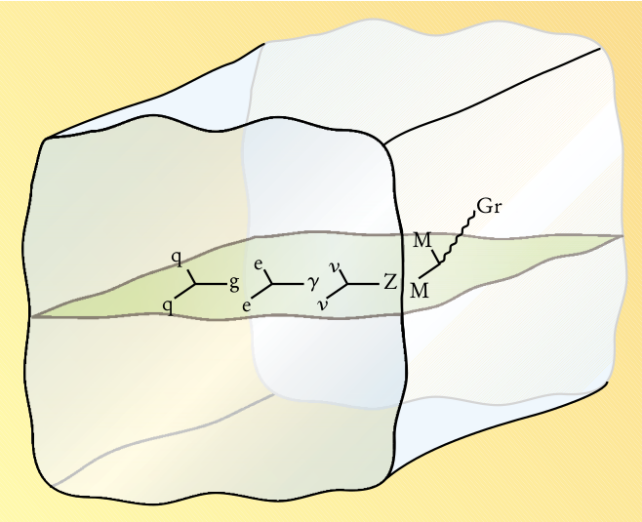

Figure 3.3: Schematic representation of our brane, here the green plane, embedded into a higher-dimensional bulk. The SM fields are confined to the brane but singlets under the SM gauge group could propagate into the bulk, such as the graviton *Gr* in this example. In this example, the extra dimension is not compactified but in the ADD scenario it would be curled up. Figure extracted from [235].

called *brane*, that constitutes our observable world. This subspace is part of a $(1{+}3{+}n)$-dimensional space, called *bulk*, having n extra dimensions that are compactified. In this theory, the bulk is a Minkowski space (we talk about *flat* extra dimensions) in which can only propagate singlets under the SM gauge group, for instance gravitons, right-handed neutrinos, or axions.

In this picture, the extra dimensions are compactified on a $\mathbb{Z}_2$ orbifold with an orbifold action $\mathbf{y} \to -\mathbf{y}$. In other words, they are curled up on a high-dimensional torus with a compactification radius R. For simplicity and conceptual reasons we consider all the extra dimensions to have the same R. The graviton would be free to propagate in all dimensions and the fundamental gravitational scale, M_*, can be much lower than the Planck scale, M_P, due to the extra dimensions volume suppression. They are related to each other via the expression [209]:

$$M_P = \left(2\pi R M_*\right)^{n/2} M_* \tag{3.22}$$

One can interpret the above formula as if gravity was "diluted" in the bulk compared to the other interactions that are confined to the brane. In order to solve the mass hierarchy problem, one would like to set $M_* \simeq M_{EW}$ so to lower the fundamental scale of quantum gravity near the electroweak scale. This matching influences the parameters of the theory, ruling out the possibility of a single extra dimension, but it gives extra dimensions of sizes lower than the millimeter for $n \geq 2$. This radius being large compared to other extra dimensional theories, the ADD scenario is referred to as *large* extra dimensions (LED). How large can it be? The size of the extra dimensions, described by R, influences many observables and is consequently constrained from multiple measurements. For instance, Newton's law evolving in $1/r^2$ would be extended to $1/r^{(2+n)}$ for $r < R$. The ADD framework has first been received with disbelief since it alters the laws of nature at the millimeter scale [235] but it is compatible with laboratory, astrophysical, and cosmological observations. A considerable review of the limits on R can be found in [236]. We list in Table 3.1 the most striking bounds on R obtained from tests of Newton law, colliders, and astrophysical considerations.

The results quoted as "neutron stars" set the most stringent limits on R for $n < 5$. They are obtained from the hypothetical γ rays production due to the decay of higher-dimensional gravitons trapped in a neutron star gravitational field. However, we here suppose the existence of axions, and it has been shown that gravitons would mainly decay into axions if they exist [240], a process that would alter the derived limits. In addition, the branching ratio of higher-dimensional gravitons decay into photons could be drastically lowered if another brane exists as pointed out by the founders of the ADD model [210]. For those reasons, we do not consider the limits on R derived from neutron stars in this thesis.

n		1	2	3	4	5	6
R_{max} [keV^{-1}]	Pendulum	2.2×10^{5}	/	/	/	/	/
	Colliders	/	2.5×10^{4}	6.2×10^{-1}	3.1×10^{-3}	1.2×10^{-4}	1.5×10^{-5}
	SN 1987A	2.5×10^{12}	4.9×10^{3}	5.8	1.9×10^{-1}	2.5×10^{-2}	6.1×10^{-3}
	Neutron star	2.2×10^{5}	7.9×10^{-1}	1.3×10^{-2}	1.7×10^{-3}	5.1×10^{-4}	2.2×10^{-4}

Table 3.1: Limits on R from torsion-pendulum experiments [237], from colliders (CMS) [238] and from the duration of the neutrino signal of the supernova SN 1987A and neutron-star excess heat [239].

The framework of LED quickly received considerable attention because the authors succeeded in developing realistic mechanisms to stabilize the size of the extra dimensions [241] and to localize the SM fields to the brane [209,242]. Large extra dimensions naturally solve the mass hierarchy problem and it can be embedded in string theory [242–244] while preserving gauge coupling unification [245,246]. At the same time, their scenario proposed new models for addressing modern issues such as the inflation [247,248] or the baryon asymmetry [249]. They also provided a mechanism for accounting for the proton stability (lifetime $> 10^{32}$ years) by assuming that the quarks and leptons are localized as slightly different positions in the extra dimensions, suppressing the coupling between them [250].

The ADD's claim that the electroweak scale is the only fundamental scale seems, at first glance, incompatible with the usual need for intermediate scales to address phenomenological issues such as the neutrino oscillations or the strong CP problem. However, the potential propagations of right-handed neutrinos and axions in the bulk give rise to a higher-dimensional seesaw mechanism without a heavy mass scale [251,252] and, as we will see, to an experimentally allowed breaking of the PQ symmetry near the electroweak scale preserving axion invisibility.

At this point we can reconsider the question raised at the beginning: yes, we do live in a 4D world because we are composed of SM particles. But there are multiple motivations for assuming that other particles evolve in a world having more than 4 dimensions. Gravity, which we experience continuously, could be a higher-dimensional phenomenon.

3.2.2 Axion in large extra dimensions and the Kaluza-Klein (KK) decomposition

The axion, as a singlet under the SM gauge group, may propagate into $\delta \leq n$ extra dimensions. In such a case, the 4-dimensional axion scale f_{PQ} can be much larger than the fundamental axion scale $\bar{f}_{PQ}$ of the overall theory:

$$f_{PQ} = \left(2\pi R M_*\right)^{\delta/2} \bar{f}_{PQ} \tag{3.23}$$

This relation tells us that the fundamental scale $\bar{f}_{PQ}$ could be very low, perhaps in the TeV range, while letting the experimentally constrained 4-dimensional scale f_{PQ} in the range of Eq.(3.10) that bounds the QCD axion. Without introducing any other fundamental besides M_* and the compactification radius R, *i.e.* taking $\bar{f}_{PQ} = M_*$, we see that if the axion propagates in the same number of extra dimensions as gravity, the 4-dimensional axion scale f_{PQ} must be at the Planck scale and thus disagree with the experimental constraints of Eq.(3.10).

Let us now study how the axions are propagating in the bulk by following the approach of [210, 240,253,254]. Since our observables and any detector are confined to the brane, we are interested in developing an effective four-dimensional theory of the axion. In other words, we want to describe the higher-dimensional axion as seen from our brane. Let denote $\mathbf{y} = (y_1, y_2, \ldots, y_\delta)$ the coordinates of the axion in each extra dimension $\delta \leq n$ in which it propagates, so that the coordinates of the axion can be written $x^M \equiv (x^\mu, \mathbf{y})$ where M is a spacetime index that runs over the $(4+\delta)$ dimensions. The $(4+\delta)$-action is given by:

$$\mathcal{S}_{(4+\delta)} = \int d^4x\, d^\delta \mathbf{y} \left\{ \frac{1}{2} M_*^\delta (\partial_M a)(\partial^M a) + \frac{\xi_{em}\alpha_{em}}{8\pi \bar{f}_{PQ}}\, a\, F_{\mu\nu}\tilde{F}^{\mu\nu}\, \delta^{(\delta)}(\mathbf{y}) \right\} \tag{3.24}$$

We now need to compactify the extra dimensions in order to get the effective 4-dimensional theory.

Since the axion field is compactified on a $\mathbb{Z}_2$ orbifold, one has:

$$a(x^\mu, \mathbf{y}) = a(x^\mu, \mathbf{y} + 2\pi R) \quad \text{and} \quad a(x^\mu, \mathbf{y}) = a(x^\mu, -\mathbf{y}) \tag{3.25}$$

The extra dimensions have a periodicity given by the orbifold action, so we know from quantum mechanics that the axion momentum in these extra dimensions is quantized. One can therefore Fourier expand the field without loss of generality:

$$a(x^\mu, \mathbf{y}) = \sum_{\mathbf{n}=0}^{\infty} a_{\mathbf{n}}(x^\mu) \cos\left(\frac{\mathbf{n}\,\mathbf{y}}{R}\right) \tag{3.26}$$

yielding an infinite superposition of modes; this procedure is called a Kaluza-Klein (KK) decomposition.

In this equation, $a_{\mathbf{n}}(x^\mu) \in \mathbb{R}$ are the KK modes, $\mathbf{n} = (n_1, n_2, \ldots, n_\delta)$ is a δ-dimensional vector that labels the KK modes, and the sum runs over all extra dimensions $\sum_{\mathbf{n}=0}^{\infty} \equiv \sum_{n_1=0}^{\infty} \sum_{n_2=0}^{\infty} \cdots \sum_{n_\delta=0}^{\infty}$. The next step is to plug this KK decomposition into the $(4+\delta)$-action and to integrate over the δ extra dimensions to get the effective 4-dimensional Lagrangian of the theory that describes the axion as seen from our brane:

$$\mathcal{L}_{\text{eff}}^{4D} = \frac{1}{2}\sum_{\mathbf{n}=0}^{\infty} (\partial_\mu a_{\mathbf{n}})(\partial^\mu a_{\mathbf{n}}) - \frac{1}{2} m_{PQ}^2 a_0^2 - \frac{1}{2}\sum_{\mathbf{n}\neq\mathbf{0}}^{\infty} \frac{\mathbf{n}^2}{R^2} a_{\mathbf{n}}^2 + \frac{\xi_{em}\alpha_{em}}{8\pi f_{PQ}} \left(\sum_{\mathbf{n}=0}^{\infty} r_{\mathbf{n}} a_{\mathbf{n}}\right) F^{\mu\nu}\tilde{F}_{\mu\nu} \tag{3.27}$$

with $r_0 = 1$ and $r_{\mathbf{n}\neq 0} = \sqrt{2}$ which are rescaling coefficients to ensure that the KK modes $a_{\mathbf{n}}$ have canonically normalized kinetic-energy terms [253].

This Lagrangian tells us that a single axion propagating in the bulk will be seen from our 4-dimensional brane as a sum of δ "infinite" superpositions of massive states with the same quantum numbers. The overall superposition of states is called a Kaluza-Klein tower. Saying that the KK tower is infinite is somehow a misuse of language since a cutoff truncates the tower. This cutoff can either be related to the quantum gravity scale M_*, or to the kinematic limit for KK axions produced in astrophysical objects such as the Sun. We call *KK axion* one of the excitation modes observed from our brane for an axion propagating in large extra dimensions. In other words, a single axion propagating in the bulk results in an "infinite" number of KK axions, all of them sharing the same quantum numbers but having different masses as we will see below.

We will now study the PQ mechanism in the case of KK axions. The authors of [253] obtain the effective potential of a KK axion mode $a_{\mathbf{n}}$ in the QCD vacuum given by:

$$V(a_{\mathbf{n}}) = \frac{1}{2}\sum_{\mathbf{n}\neq\mathbf{0}}^{\infty} \frac{\mathbf{n}^2}{R^2} a_{\mathbf{n}}^2 + \frac{\alpha_s}{8\pi}\Lambda_{\text{QCD}}^4 \left[1 - \cos\left(\frac{\xi}{f_{\text{PQ}}}\sum_{\mathbf{n}=0}^{\infty} r_{\mathbf{n}} a_{\mathbf{n}} + \bar{\theta}\right)\right] \tag{3.28}$$

where $\Lambda_{QCD} \sim 250$ MeV is the QCD scale.

The minimization $\frac{\partial V}{\partial a_{\mathbf{n}}} = 0$ gives the unique solution:

$$\begin{cases} < a_0 > &= \frac{f_{PQ}}{\xi}\left(-\bar{\theta} + \ell\pi\right), \quad \ell \in 2\mathbb{Z} \\ < a_k > &= 0, \quad \text{for all } k > 0 \end{cases} \tag{3.29}$$

We then realize that the ground state a_0 of the KK tower solves the strong CP problem. Eq. (3.29) tells us that the other KK modes, for $k > 0$, have vanishing vacuum expectation values and one can show that they are invariant under a PQ transformation [253], so they do not participate in the PQ mechanism. We then identify the ground state a_0 as the standard axion and the strong CP problem is still correctly solved by the bulk axion.

3.2.3 Phenomenology of the KK axions

The situation in large extra dimensions drastically changes compared to the standard axion: instead of a single particle, one now has to deal with an "infinite" number of axions! Besides, the phenomenology of the KK axions also have some specificities compared to the QCD axion. Let us first study the mass

of the KK modes. The axion mass matrix can be derived from the axion potential Eq. (3.5) and is given by [253]:

$$\mathcal{M}^2 \;=\; m_{\rm PQ}^2 \begin{pmatrix} 1 & \sqrt{2} & \sqrt{2} & \sqrt{2} & \dots \\ \sqrt{2} & 2+y^2 & 2 & 2 & \dots \\ \sqrt{2} & 2 & 2+4y^2 & 2 & \dots \\ \sqrt{2} & 2 & 2 & 2+9y^2 & \dots \\ \vdots & \vdots & \vdots & \vdots & \ddots \end{pmatrix} \tag{3.30}$$

where the authors have defined:

$$\begin{cases} m_{PQ}^2 & = \xi^2 \frac{\alpha_s}{8\pi} \frac{\Lambda_{QCD}^4}{f_{PQ}^2} \\ y & \equiv \frac{1}{m_{PQ} R} \end{cases} \tag{3.31}$$

The mass m_{PQ} is the expected mass that the axion would have in the four-dimensional case. Since the mass matrix is non-trivial, the KK modes are not the mass eigenstates so there is a mixing between the KK axions. The KK axion masses are given by:

$$m_{a_0} = \min\left(m_{PQ}\,,\, \frac{1}{2R}\right) \quad \text{and} \quad m_{a_{\mathbf{n}}} \simeq \frac{|\mathbf{n}|}{R} = \frac{\sqrt{n_1^2 + n_2^2 + \dots + n_\delta^2}}{R}\,. \tag{3.32}$$

In the phenomenologically interesting situations that we consider in this thesis, we have $m_{PQ} \ll 1/R$, so the mass of the fundamental mode of the KK tower is equal to the 4-dimensional Peccei-Quinn mass, $m_{a_0} = m_{PQ}$. It means that one can let $m_{PQ} \sim 10\,\mu$eV as in the standard case while having larger masses in the KK tower. We also see that the mass splitting of the KK tower is $\sim 1/R$. The differential mode multiplicity can reach very large values and is given by:

$$\frac{dN}{dm} = \frac{2\pi^{\delta/2}}{\Gamma[\delta/2]}\, R^\delta\, m^{(\delta-1)} \tag{3.33}$$

The last term of the Lagrangian Eq. (3.27) tells us that each individual KK mode couples to the electromagnetic field-strength tensor with the same coupling as in the 4-dimensional case, $\frac{1}{4} g_{a\gamma\gamma}$ defined in Eq.(3.7), up to a factor $r_{\mathbf{n}}$ that we will ignore for the rest of the discussion for simplicity. Since the KK axion are not mass eigenstates, as one can see from the mass matrix Eq. (3.30), they oscillate in a way that is similar to neutrino oscillations. However, the linear superposition of the KK modes "decohere" extremely rapidly [253] due to the axion oscillations, so it is sufficient to study the coupling of each KK axion to the photons instead of studying the coupling of the overall KK tower.

The lifetime of each individual KK mode is now given by:

$$\tau\left(a_{\mathbf{n}} \to \gamma\gamma\right) \;=\; \frac{64\pi}{g_{a\gamma\gamma}^2 m_{a_{\mathbf{n}}}^3} \;=\; \left(\frac{m_{PQ}}{m_{a_{\mathbf{n}}}}\right)^3 \tau^{\rm 4D}\left(a \to \gamma\gamma\right) \tag{3.34}$$

By considering the usual bounds of f_a from Eq. (3.10), we see that the lifetime of a KK axion of mass 10 keV is in the range $[10^{17},\ 10^{23}$ s]. We can now touch on the attractiveness of such a framework. The axion was first proposed to solve the strong CP problem and it has received considerable interest for more than four decades, both from theoretical and experimental aspects [81, 255]. In theories with large extra dimensions, the axion remains a compelling solution to the strong CP problem and a viable dark matter candidate, but its phenomenology changes. Instead of having one light particle, we must now consider an "infinite" number of massive states (the Kaluza-Klein axions), forming a continuum for large enough extra dimensions, with a large multiplicity of states. The ground state a_0 can be identified as the standard axion and its mass remains the same as in the four-dimensional case, whereas the mass of the other KK axions can take larger values depending on the compactification radius, so on the geometry of the extra dimensions.

As in the standard case, KK axions would be produced in astrophysical objects. We will show that the Sun would produce KK axions with masses distributed in the $(1-30)$ keV range. With such

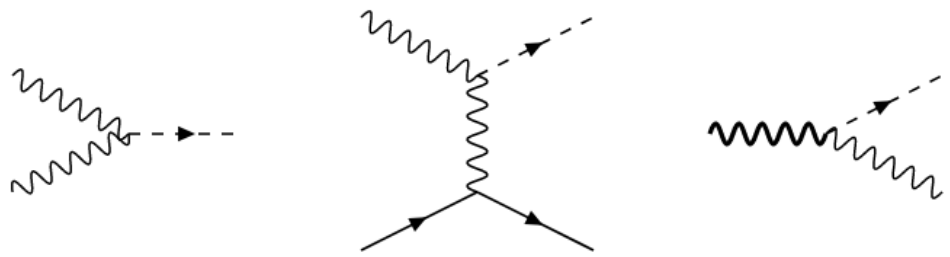

Figure 3.4: Feynman diagrams of the three dominant processes for production of hadronic KK axions in the Sun: the photon coalescence (left), the Primakoff effect (center), and the plasmon decay (right).

masses, the lifetime of KK axions could be of the order of the age of the universe and the photons obtained from its decay $a_{\mathbf{n}} \to \gamma\gamma$ would have impacts on cosmology and astrophysics, and would open a new channel for experimental searches. Moreover, as we will demonstrate, part of the KK axions produced by the Sun would be trapped in its gravitational field.

3.3 Production of hadronic KK axions in the Sun

In hadronic models, KK axions are produced in the Sun via three dominant processes whose Feynman diagrams are shown in Figure 3.4. The Primakoff process $\gamma + Ze \to Ze + a$ converts a photon into an axion in the electrostatic field of a nucleus or an electron. The second process is the coalescence of two photons $\gamma\gamma \to a$, which is kinematically suppressed for small masses (as for the QCD axion) but turns out to be significant for producing KK axions with masses in the keV-range. In the thermal environment of the Sun, photons acquire a thermal "mass" and a longitudinal component. This phenomenon opens up a third production process from the decay of a transverse plasmon $\gamma_T \to \gamma_L + a$. It is worth mentioning at this stage that the phenomenology of solar KK axions is almost exclusively driven by the process of photon coalescence since it produces non-relativistic KK axions that are susceptible of being trapped in the gravitational field of the Sun, as we will see in the next section.

3.3.1 Primakoff process

The Primakoff transition rate for KK axions produced in the Sun is derived in [254, 256]

$$\Gamma_{\gamma\to a}^{\text{Primakoff}} = \frac{g_{a\gamma\gamma}^2 T\kappa^2}{32\pi^2}\,\frac{|\mathbf{k}|}{\omega}\int d\Omega \frac{|\mathbf{k}\times\mathbf{p}|^2}{(\mathbf{k}-\mathbf{p})^2((\mathbf{k}-\mathbf{p})^2+\kappa^2)} \tag{3.35}$$

where T is the temperature at production, $\mathbf{p}$ is the axion momentum, $\mathbf{k}$ the photon one, and ω the photon energy; κ is the Debye-Hückel screening scale, given in general by $\kappa^2 = (4\pi\alpha/T)\sum_j Z_j^2 n_j$, where n_j is the number density of charged particles. For small momenta, it can be expressed as:

$$\Gamma_{\gamma\to a}^{\text{Primakoff}} = \frac{g_{a\gamma\gamma}^2 T\kappa^2}{32\pi}\left(\frac{8p^2}{3(\kappa^2+m^2)} + \mathcal{O}(p^4)\right) \tag{3.36}$$

where $p = |\mathbf{p}|$ and m is the axion mass. The differential axion flux at Earth, integrating over a standard solar model, is given by

$$\Phi_a^{\text{Primakoff}} = \frac{1}{4\pi d_{ST}^2}\int_{\text{Sun}} d^3\mathbf{r}\,\Gamma_{\gamma\to a}^{\text{Primakoff}}\,\frac{E^2}{\pi^2}\,f_a^{eq}(E) \tag{3.37}$$

where d_{ST} is the Earth-Sun distance, E the axion energy, and $f_a^{eq}(E) = (e^{E/T}-1)^{-1}$ is the Bose-Einstein axion distribution function. The authors of [254] arrived at the expression for the differential axion flux at Earth:

$$\Phi_a^{\text{Primakoff}} = \left(4.20\times10^{10}\ \text{cm}^{-2}\,\text{s}^{-1}\,\text{keV}^{-1}\right) g_{10}^2\,\frac{E\,p^2}{e^{E/1.1}-0.7}\left(1+0.02m\right) \tag{3.38}$$

where $g_{10} = g_{a\gamma\gamma} \times 10^{10}\,\text{GeV}$ is the dimensionless coupling to photon, and E, p, and m are given in keV.

3.3.2 Photon coalescence

Let us review the production of axions from the photon coalescence process $\gamma\gamma \to a$ in a thermal environment as such of the Sun. We start with the Boltzmann equation for the axion distribution function, f_a, including only production from the inverse decay [86]:

$$\begin{aligned}\frac{df_a(E)}{dt} &= \frac{1}{2E}\int \frac{d^3k_1}{(2\pi)^3 2\omega_1}\frac{d^3k_2}{(2\pi)^3 2\omega_2}(2\pi)^4\delta^4(k_1+k_2-p)|M_\gamma|^2 f_1^{eq}(\omega_1)f_2^{eq}(\omega_2)(1+f_a(E)) \\ &\simeq f_a^{eq}(E)\,\frac{1}{2E}\int \frac{d^3k_1}{(2\pi)^3 2\omega_1}\frac{d^3k_2}{(2\pi)^3 2\omega_2}(2\pi)^4\delta^4(k_1+k_2-p)|M_\gamma|^2\Big(1+f_1^{eq}(\omega_1)+f_2^{eq}(\omega_2)\Big) \\ &= \Gamma^{\text{Coal.}}_{\gamma\gamma\to a}(T) f_a^{eq}(E) \end{aligned} \tag{3.39}$$

where E is the axion energy, p its momentum, and ω_i are the photon energies, with $E = \omega_1 + \omega_2$. In the second line we have used:

$$f_1^{eq}(\omega_1)f_2^{eq}(\omega_2)(1+f_a^{eq}(E)) = f_a^{eq}(E)\cdot\Big(1+f_1^{eq}(\omega_1)+f_2^{eq}(\omega_2)\Big) \tag{3.40}$$

for the Bose-Einstein distribution functions. Performing the momentum integrals, the thermal inverse decay rate, $\Gamma^{\text{Coal.}}_{\gamma\gamma\to a}(T)$, is given by [85, 86]:

$$\Gamma^{\text{Coal.}}_{\gamma\gamma\to a}(T) = \Gamma_{a\gamma\gamma}\frac{m^2-4\omega_P^2}{m^2}\left(\frac{m}{E}\right)\left(1+\frac{2T}{p}\ln\frac{1-e^{-(E+p)/2T}}{1-e^{-(E-p)/2T}}\right) \tag{3.41}$$

where $\Gamma_{a\gamma\gamma}$ is the standard axion decay rate into photons at $T = 0$, and ω_P the plasma frequency that can be expressed as:

$$\omega_P^2 = \frac{4\pi\alpha n_e}{m_e} \tag{3.42}$$

n_e being the electron number density and m_e its mass. Finally, for the number of axions per unit volume, per unit time, and per unit energy, we make use of $dp/dE = E/p$ to obtain:

$$\frac{dN_a^{\text{Coal.}}}{dE} = \Gamma^{\text{Coal.}}_{\gamma\gamma\to a}(T)\,\frac{pE}{2\pi^2}\,f_a^{eq}(E) \tag{3.43}$$

We will apply approximations for later analytical calculations in order to simplify the expressions, as done in [254]. Neglecting the temperature corrections and the plasma frequency, with is of the order of 0.3 keV in the solar interior, Eq. (3.41) simplifies into:

$$\Gamma^{\text{Coal.}}_{\gamma\gamma\to a} \;\simeq\; \Gamma_{a\gamma\gamma}\frac{m}{E} \tag{3.44}$$

Integrating over a standard solar model (in this thesis we use the Saclay solar model [257]), we obtain the differential flux at Earth for axions produced by the coalescence of two photons:

$$\begin{aligned}\Phi_a^{\text{Coal.}} &\simeq \frac{1}{4\pi d_{ST}^2}\int d^3r\frac{dN_a^{\text{Coal.}}}{dE} \;=\; \frac{R_\odot^3}{4\pi d_{ST}^2}4\pi\Gamma_{a\gamma\gamma}\frac{pm}{2\pi^2}\int_0^1 d\bar{r}\bar{r}^2 f_a^{eq}(E) \\ &= \Big(7.45\times10^{11}\ \text{cm}^{-2}\,\text{s}^{-1}\,\text{keV}^{-1}\Big)\,g_{10}^2\,m^4\,p\int_0^1 d\bar{r}\bar{r}^2 f_a^{eq}(E)\end{aligned} \tag{3.45}$$

where g_{10} is the dimensionless coupling described before, and m and p are given in keV. Still, when performing the integral, this expression slightly differs from the one derived by Di Lella *et al.* [254]

$$\Phi_a \simeq \Big(1.68\times10^{9}\ \text{cm}^{-2}\,\text{s}^{-1}\,\text{keV}^{-1}\Big)\,g_{10}^2\,m^4 p\left(\frac{10}{0.2+E^2}+1+6\times10^{-4}E^3\right)e^{-E} \tag{3.46}$$

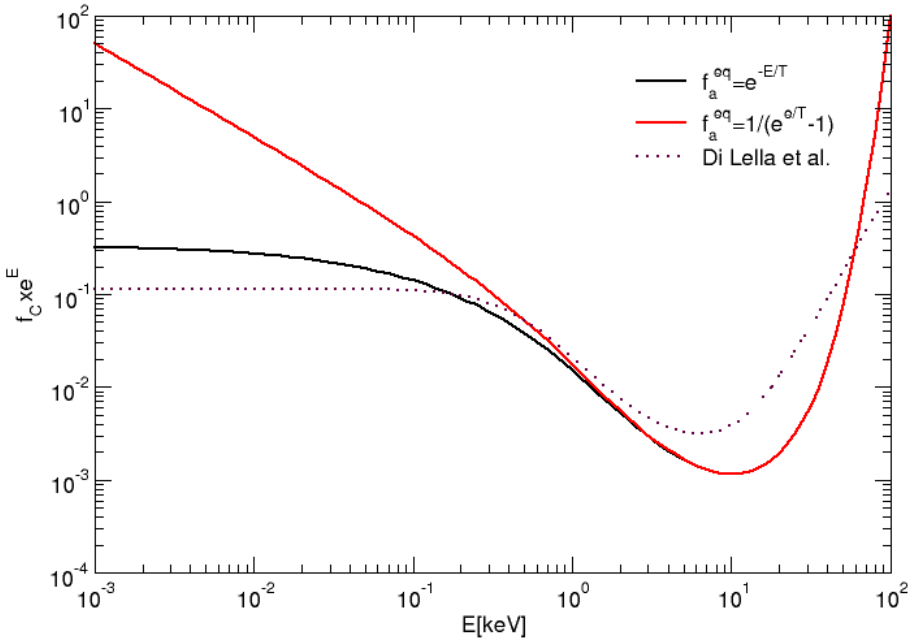

Figure 3.5: Energy dependency of the coalescence rate. We plot $f_C(E)\, e^E$ where $f_C(E) = \int_0^1 d\bar{r}\bar{r}^2 f_a^{eq}(E)$. The solid black line is obtained with a Maxwell-Boltzmann distribution, and the solid red line with a Bose-Einstein distribution. The dotted purple line shows the approximation derived in [254].

For comparison, Fig. 3.5 shows the energy dependency of the coalescence rate in Eq. (3.45) and (3.46). For example, in the energy range of interest, $E \sim \mathcal{O}(1-10)$ keV, the approximations applied by Di Lella *et al.* would overestimate the flux of photons by about 25% after integrating in the case $\delta = 1$.

3.3.3 Plasmon decay

In the thermal environment of the Sun, the excitations of the electromagnetic field follow non-trivial dispersion relations. These excitations, either longitudinal or transverse, are called "plasmons". The presence of plasmons in the solar interior opens up the possibility of producing KK axions by decay of a transverse plasmon, $\gamma_T \to \gamma_L + a$, since this process becomes kinematically allowed. In a thermal plasma, transverse and longitudinal photons have different dispersion relations:

$$\omega_T^2 = \omega_P^2\left(1 + \frac{k_T^2}{\omega_P^2 + k_T^2}\frac{T}{m_e}\right) + k_T^2 \;\simeq\; k_T^2 + \omega_P^2\,, \tag{3.47}$$

$$\omega_L^2 = \omega_P^2\left(1 + 3\frac{k_L^2}{\omega_P^2}\frac{T}{m_e}\right) \;\simeq\; \omega_P^2 \tag{3.48}$$

where $k_{T,L}$ are the transverse and longitudinal 3-momenta, and ω_P is the plasma frequency defined previously. In the Sun, $T \lesssim 1.3$ keV and $T/m_e \lesssim 0.0025$, so the dispersions relations can be well approximated by the second equality in Eqs. (3.47) and (3.48). In the expression Eq. (3.47), the dispersion relation is similar to the one of a massive particle, so the transverse photon can be viewed as a photon with a thermal "mass" ω_P.

We will compute the rate of production of axions with momentum p and energy E from:

$$\frac{dN_a^{\text{Decay}}}{dE} = \Gamma^{\text{Decay}}_{\gamma_T \to a\gamma_L}(T)\frac{pE}{2\pi^2} f_a^{eq}(E) \tag{3.49}$$

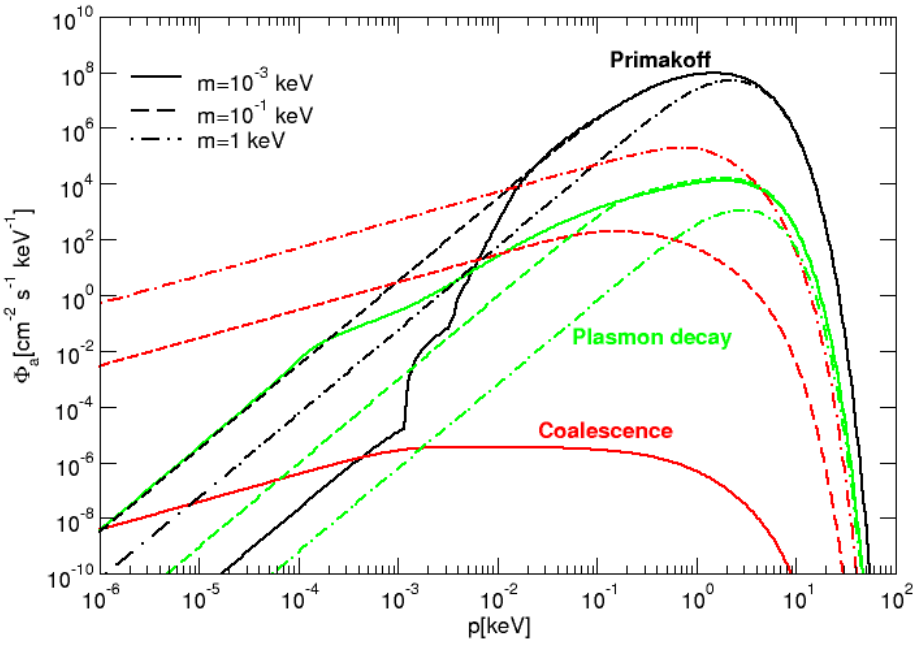

Figure 3.6: Differential flux at Earth for individual axions versus the axion momentum, for different production channels: black lines for Primakoff, red lines for Coalescence, and green ones for Plasmon decay. We have taken $g_{10} = 10^{-2}$, and different values of the axion mass as indicated in the plot.

where

$$\Gamma^{\rm Decay}_{\gamma_T \to a\gamma_L}(T) = \frac{1}{2E}\int \frac{d^3k_T}{(2\pi)^3 2\omega_T}\frac{d^3k_L}{(2\pi)^3 2\omega_L}(2\pi)^4\delta^4(k_T - k_L - p)|M_{\gamma_T\to a\gamma_L}|^2(1+f^{eq}(\omega_T)) \tag{3.50}$$

and the transition amplitude is given by [258]:

$$|M_{\gamma_T\to a\gamma_L}|^2 = g^2_{a\gamma\gamma}\frac{|(\mathbf{e}_T\times\mathbf{k}_T)\cdot\mathbf{k}_L|^2}{k_L^2}\frac{\omega_P^4}{k_L^2+\omega_P^2} \tag{3.51}$$

in which $\mathbf{e}_T$ is a polarization vector such that $\mathbf{e}_T\cdot\mathbf{k}_T = 0$.

The details of the derivation of the plasmon decay rate are presented in Appendix A. As it will be discussed in the next section, we are interested in non-relativistic KK axions so we restrict our analysis to the limit $p/k_T \ll 1$, for which we get:

$$\Gamma^{\rm Decay}_{\gamma_T\to a\gamma_L} \simeq \frac{g^2_{a\gamma\gamma}}{24\pi}\frac{\omega_P^4\,k_T}{k_T^2+\omega_P^2}\left(\frac{p}{E}\right)^2 \tag{3.52}$$

We now have all the elements to give the expression for the differential flux at Earth for KK non-relativistic axions produced by plasmon decay:

$$\Phi_a^{\rm Decay} \simeq \left(2.0\times10^{12}\ {\rm cm}^{-2}\,{\rm s}^{-1}\,{\rm keV}^{-1}\right)\ g_{10}^2\int_0^1 d\bar{r}\bar{r}^2\,\frac{\omega_P^4\,k_T}{k_T^2+\omega_P^2}\,\frac{p^3}{E}\,f_a^{eq}(E) \tag{3.53}$$

The differential fluxes at Earth for Primakoff, Coalescence, and Plasmon decay are shown in Fig. 3.6, for different values of the axion mass as indicated in the plot. The Primakoff differential rate has been computed with the transition rate in Eq. (3.35), including the thermal photon mass and using the approximation $\kappa \simeq 7T$ [254] for the Debye-Hückel screening scale; for Coalescence we use Eq. (3.45),

and that of plasmon decay has been computed with the full thermal decay rate given in Eq. (A.28). We have plotted the fluxes with respect to the axion momentum instead of energy to stress their behavior at low momentum. Primakoff is the main production channel for axions up to $m \sim O(10\text{ keV})$ and $p \sim E$. However, it will be suppressed with respect to Coalescence in the limit of small momentum $p \ll E$. Same happens with the plasmon decay channel: in both case the rate is proportional to p^2 which suppresses the production of non-relativistic KK axions.

We could also consider the production due to the conversion of thermal photons in the presence of the large-scale solar magnetic field [259–261]. However, given the profile of the solar magnetic field, the conversion is mainly efficient near the resonance for $m \sim O(10-100)$ eV [261]. Because we are interested in keV axions, this channel for us will be subdominant when compared to coalescence or Primakoff.

3.4 Gravitationally trapped KK axions

Part of the KK axions produced in the Sun will be sufficiently massive and non-relativistic to be trapped in the solar gravitational field. Those KK axions will start orbiting the Sun and they will accumulate over the Sun history. The large astrophysical times involved in this picture would result in a significant amount of trapped KK axions which overpasses by several orders of magnitude the amount of KK axions instantaneously emitted by the Sun. This scenario of trapped KK axions was first proposed by DiLella and Zioutas [211] to explain some astrophysical issues as the heating of the solar corona, but also as a window for possible detection of KK axions in a TPC. Recently, the phenomenological implications of such "stellar basins" of massive particles have been studied in more detail yielding striking consequences on direct and indirect detection [262, 263].

The article from DiLella and Zioutas about trapped KK axions [211] pioneered the domain and its results (obtained by simulations for a given set of parameters) have been used as a reference for all searches for KK axions [214, 216, 217]. This article is almost 20 years old and, to the best of our knowledge, no additional theoretical work has been conducted about trapped KK axions. In this section, we study the number density of trapped KK axions which is the key element for the phenomenology of the solar KK axions.

3.4.1 KK axion orbits

We first study the trajectory of a KK axion produced in the Sun. Since the energy and the angular momentum are conserved, the KK axion moves in the plane perpendicular to the angular momentum vector, so we here place our analysis in the (x, y) plane with x and y chosen accordingly. The Lagrangian of a point particle of mass m in the solar gravitational field is given by:

$$\mathcal{L} = \frac{m}{2}\left(\dot{x}^2 + \dot{y}^2\right) - m\Phi(r) \tag{3.54}$$

Outside the Sun, the gravitational potential evolves as:

$$\Phi(r > R) = -\kappa\frac{R}{r} \tag{3.55}$$

where $\kappa = GM/R$, with G the gravitational constant, M the solar mass, and R the solar radius. Inside the Sun, the gravitational potential depends on the density. It can be determined from the Poisson equation based on a solar model, such as [257], which indicates that the potential is about 5 times larger in the center compared to the surface. Under the assumption of a constant density, the gravitational potential inside the Sun can be approximated to $\Phi(r < R) \simeq -\frac{\kappa}{2}\left(3 - (\frac{r}{R})^2\right)$.

The equations of motion (EoM) are derived from the Lagrangian by applying the Euler-Lagrange equations and we obtain:

$$\begin{cases} \ddot{x} + \omega^2 x\, f(\bar{r}) = 0 \\ \ddot{y} + \omega^2 y\, f(\bar{r}) = 0 \end{cases} \tag{3.56}$$

where we have defined $\omega^2 = GM/R^3$, $\bar{r} = r/R$ is the radius normalized to the Sun radius, and $f(\bar{r}) = (1/\bar{r})^3$ outside the Sun. Inside the Sun, the approximation of a constant density leads to

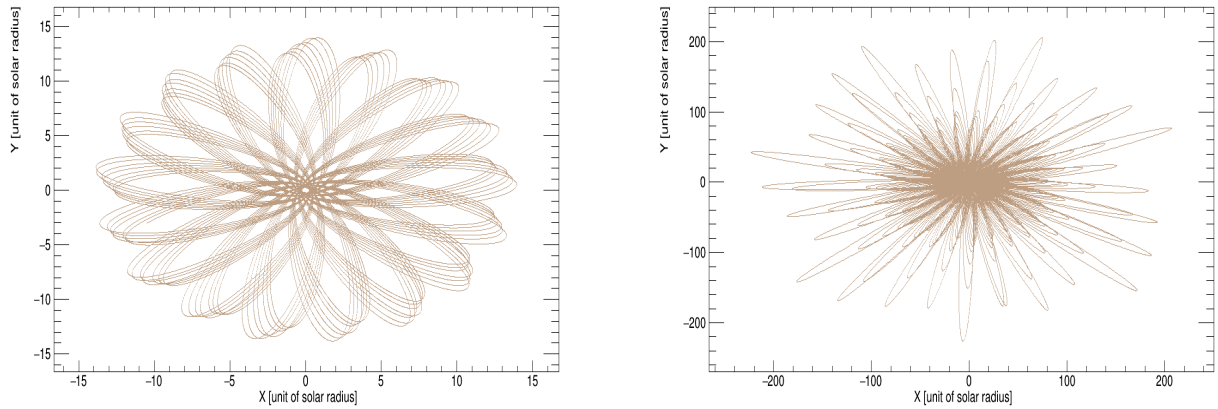

Figure 3.7: Examples of the trajectories for an axion produced inside the Sun at $\bar{r} = 0.3$. In the right plot, the axion has an incident velocity 1% larger than in the left plot and its orbit crosses the Earth located at $\bar{r} = 215.7$.

$f(\bar{r}) = 1$ and finer results are obtained numerically by considering a solar model. For instance, with the Saclay solar model [257], we get:

$$f(\bar{r}) \simeq -\frac{1}{\bar{r}}\left(0.47 - 142.06\bar{r} + 779.17\bar{r}^2 - 1859.87\bar{r}^3 + 2320.54\bar{r}^4 - 1481.77\bar{r}^5 + 382.60\bar{r}^6\right) \tag{3.57}$$

In Figure 3.7, we present two examples of the axion orbits around the Sun by solving numerically the EoM Eq. (3.56) with the gravitational potential determined numerically via Eq. (3.57). As long as the initial velocity of the axion is lower than the escape velocity, the particle gets trapped in the gravitational field and starts orbiting the Sun. However, for a too low initial velocity, the orbit remains close to the Sun and never reaches the Earth which is located at $\bar{r} = 215.7$. In the figure, we see that a 1% difference in the initial velocity significantly changes the maximal radius reached by the trajectories. Note also that the maximal distance will be influenced by the initial polar angle at production.

The conservation of the energy E and the angular momentum L allows to write the radial velocity as:

$$\dot{r}^2 = \frac{2\big(E - m\Phi(r)\big)}{m} - \Big(\frac{L}{mr}\Big)^2 \tag{3.58}$$

Bounded trajectories are obtained by the setting the condition $\dot{r} = 0$, which can be expressed as:

$$v_{r,0}^2 + r_0^2\dot{\phi}_0^2\Big\{1 - \big(\frac{\bar{r}_0}{\bar{r}}\big)^2\Big\} = \frac{2GM}{R}\Big(\bar{\Phi}(\bar{r}_0) - \frac{1}{\bar{r}}\Big) \tag{3.59}$$

where the subscript "0" refers to the initial conditions and where $\bar{\Phi}$ is the potential normalized by its value at the surface such that $\Phi(r < R) = -\frac{GM}{R}\bar{\Phi}(\bar{r})$. In terms of the initial kinetic energy per unit mass, $\tilde{E}_K = (v_{r,0}^2 + r_0^2\dot{\phi}_0^2)/2$, and using $a^2 = v_{r,0}^2/(2\tilde{E}_K)$, we have:

$$\tilde{E}_K(\bar{r}_0) = \frac{GM}{R} \cdot \frac{\bar{\Phi}(\bar{r}_0) - \frac{1}{\bar{r}}}{1 - \frac{1}{2}\big(\frac{\bar{r}_0}{\bar{r}}\big)^2\big(1 - a^2\big)} \tag{3.60}$$

Bounded orbits at a radial distance r are obtained for particles produced inside the Sun with kinetic energy per unit mass in the range $(\tilde{E}_K^{\min}, \tilde{E}_K^{\max})$ depending on the initial angular momentum. To reach the Earth, for particles produced at the Sun surface, their kinetic energy must be in the range $[0.995363, 0.995374]$ in units of GM/R; for those produced at half the Sun radius we have instead $\tilde{E}_K \in [1.952736, 1.95274]$.

3.4.2 Number density of trapped KK axions

We have now all elements to determine the number density of trapped KK axions in orbit around the Sun. The number density of trapped KK axions as a function of the distance to the Sun represents a

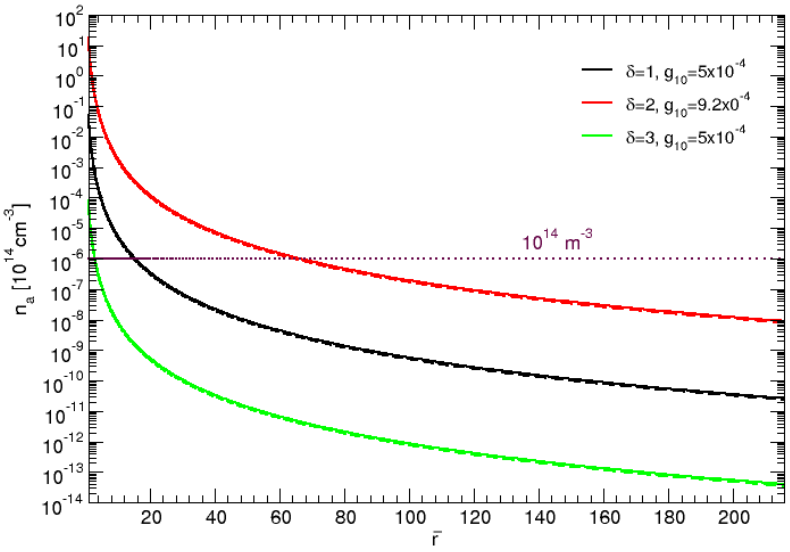

Figure 3.8: Number density of trapped KK axions for model parameters as indicated in the plot versus the radial distance in units of the solar radius. We have taken $R_1 = 2 \times 10^5$, $R_2 = 10^3$, $R_3 = 1$, all given in keV^{-1}. Solid lines are obtained with (3.62), while dashed lines correspond to (3.63), the difference being hardly visible since they overlap. The dotted line indicates the value obtained in [211] for $n_{KK}^{(T)}(t_\odot, 1\,\text{A.U.})$ and $\delta = 2$, $g_{10} = 9.2 \times 10^{-4}$.

crucial quantity for the determination of the event rate in a detector and also for some astrophysical constraints as presented later in Chapter 9. Since the Primakoff process and the plasmon decay are suppressed for low-momenta, it can be shown [211] that the amount of trapped KK axions is about 3 orders of magnitude larger for the production via the coalescence of two photons than for the other processes. For this reason, we only consider the coalescence of two photons in the following calculations.

The details of the calculations of the number density are presented in the article [218] and we here only sum up the procedure and the results. The derivation starts by determining the energy range required for bounded trajectories, as explained in the previous section. The next step is to integrate the Boltzmann equation over momenta for which the trajectories are bounded at a distance r to the Sun. Finally, we integrate over the KK tower and time, taking into account the potential decay of the axions. We arrive at the following expression for the number density of trapped KK axions:

$$n_{KK}^{(T)}(t,r) = \left(2.2 \times 10^{14}\text{cm}^{-3}\right) g_{10}^2 \frac{2\pi^{\delta/2}}{\Gamma[\delta/2]} \int dm\, (Rm)^\delta m^5 \frac{1 - e^{-t_\odot \Gamma_{a\gamma\gamma}}}{t_\odot \Gamma_{a\gamma\gamma}} \int_0^1 \bar{r}_0^2 d\bar{r}_0 \frac{1}{e^{E/T} - 1} \frac{m}{E} I_v[\bar{r}, \bar{r}_0] \tag{3.61}$$

where $g_{10} = g_{a\gamma\gamma} \times 10^{10}\,\text{GeV}$, $\bar{r}$ is the distance to the Sun normalized by the solar radius, m, R^{-1}, T and E are given in keV, and the product $t_\odot \Gamma_{a\gamma\gamma}$ must be dimensionless; the second integral must be performed over a solar model. Finally, $I_v[\bar{r}, \bar{r}_0]$ is the integral over velocities (in the plane of the trapped orbit) of the probability density for an axion of energy E to be at radius $\bar{r}$. In [218], we give two expressions for the quantity $I_v[\bar{r}, \bar{r}_0]$ depending on which expression we use for the probability density:

$$I_v^0(\bar{r}_0,\bar{r}) = \frac{1}{4\pi\bar{r}^4}\sqrt{2\left(\bar{\Phi}(\bar{r}_0) - \frac{1}{\bar{r}}\right)} \tag{3.62}$$

$$I_v^1(\bar{r}_0,\bar{r}) = \int_{\bar{v}_{\min}}^{\bar{v}_{\max}} d\bar{v}\bar{v}^2 \frac{1}{10\pi^2} \frac{\left(2\bar{\Phi}(\bar{r}_0) - \bar{v}^2\right)^{7/2}}{\left(\bar{v}^2 - 2\left(\bar{\Phi}(\bar{r}_0) - \frac{1}{\bar{r}}\right)\right)^{1/2}} \tag{3.63}$$

in which $\bar{\Phi}(\bar{r}_0)$ is the gravitational potential normalized by its value at Sun surface, and $\bar{v}$ is the velocity normalized by $(GM/R_\odot)^{1/2}$. The expression Eq. (3.62) differs by a factor of 2 compared with the one that we published in [218]. We have meanwhile discovered a mistake coming from the integral (B.13) of the cited paper, for which we integrated over the entire range whereas only positive velocities are allowed[2].

The number density behaves as $1/r^4$ as pointed out in [211]. For $\delta = 2$, $g_{10} = 9.2 \times 10^{-4}$ and $R = 10^3\,\mathrm{keV}^{-1}$ (set of parameters used in [211]) we obtain

$$n_{KK}^{(T)}(t_\odot, R_\odot) \simeq 0.15 \times 10^{16}\,\mathrm{cm}^{-3} \tag{3.64}$$

$$n_{KK}^{(T)}(t_\odot, 1\,\mathrm{A.U.}) \simeq 0.79 \times 10^{6}\,\mathrm{cm}^{-3} \tag{3.65}$$

which is about 50 times lower than the number density at Earth obtained in [211]. Possible explanations of such a difference are difficult to point out since very few details are given in the article about how the simulation works. In Figure 3.8 we show the trapped number density for different choices of parameters, and we have compared the number density of trapped KK axions computed with the different probability densities (solid and dashed lines): the difference is hardly visible since the two almost overlap. In other words, using Eq. (3.62) or Eq. (3.63) is equivalent, as expected since they are two alternate derivations of the same quantity.

Since the number density plays a crucial role in phenomenology, we aim to cross-check the analytic calculations with a Monte Carlo (MC) simulation, both approaches using a different philosophy. The backbone of the simulation is to produce a given amount of KK axions in the Sun and to follow the trajectory of each of them by solving the EoM. In this way, one knows the position of each KK axion at any time and one can compute the number density at a distance r. The number of KK axions of mass m produced by the Sun evolves in time as:

$$\frac{dN_a(t,m)}{dt} = -\Gamma_{a\gamma\gamma}(m)\, N_a(t,m) + P_a(m) \tag{3.66}$$

where $P_a(m)$ is the solar production rate. It implies that, at present time $t = t_\odot$ and summing over the mode multiplicity, one obtains:

$$N_a\big(\delta, R, g_{10}, t_\odot\big) = \frac{2\pi^{\delta/2}}{\Gamma[\delta/2]}\, R^\delta \int_0^\infty dm\, m^{(\delta-1)}\, \frac{P_a(m)}{\Gamma_{a\gamma\gamma}(m)} \left(1 - e^{-t_\odot \Gamma_{a\gamma\gamma}(m)}\right) \tag{3.67}$$

We have already seen that the coalescence mechanism is the main source of trapped axions. The solar axion production, per energy and time unit, through the coalescence process is given by:

$$P_a(m,E) = \frac{g_{10}^2}{32\pi^2}\, m^4 \sqrt{E^2 - m^2} \int_{Sun} dr\, \frac{r^2}{e^{E/T(r)} - 1} \tag{3.68}$$

in which the integration is over a solar model. The present total number of KK axions susceptible of being trapped is then given by

$$\begin{aligned} N_a\big(\delta, R, g_{10}, t_\odot\big) = \frac{2\pi^{\delta/2}}{\Gamma[\delta/2]}\, R^\delta \int_0^\infty dm\, \frac{m^{(\delta-1)}}{\Gamma_{a\gamma\gamma}(m)} \left(1 - e^{-t_\odot \Gamma_{a\gamma\gamma}(m)}\right) \\ \times \int_m^\infty dE\, \frac{g_{10}^2}{32\pi^2}\, m^4 \sqrt{E^2 - m^2} \int_{Sun} dr\, \frac{r^2}{e^{E/T(r)} - 1} \end{aligned} \tag{3.69}$$

[2]The expression (B.13) in [218] must be replaced by $I_v(\bar{r}_0,\bar{r}) = R_\odot^3 \left(\frac{GM}{R_\odot}\right)^{3/2} \int_{\bar{v}_{min}}^{\bar{v}_{max}} d\bar{v}\bar{v}^2 N_\delta \delta(f_T) = \frac{1}{4\pi\bar{r}^4}\sqrt{B(\bar{r},\bar{r}_0)}$.

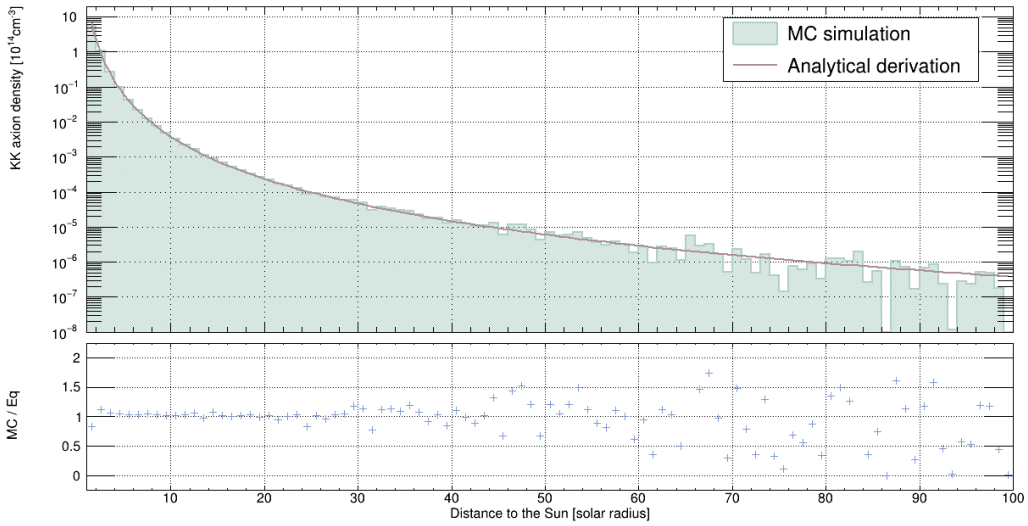

Figure 3.9: Comparison of the numbers density obtained from the MC simulation and from the analytical derivation. We have taken $\delta = 2$, $R = 10^3\,\mathrm{keV}^{-1}$ and $g_{10} = 9.2 \times 10^{-4}$, which are the parameters cited in [211].

The principle of the MC simulation is to generate n_{MC} KK axions of mass m and energy E, to follow them in their trajectories around the Sun, and to count the proportion that will be located in a $1\,\mathrm{cm}^3$ box at distance r to the Sun. Since the solar axion production is isotropic this box can be located at any position in the (ϕ, θ) plane. We then scale n_{MC} according to Eq. (3.69) to get the present number density of KK axions.

The randomness of the MC comes from the choice of the initial conditions in the EoM solver: r_0 is taken randomly in the distribution of Eq. (3.68); θ_0 and ϕ_0 are randomly chosen in a way to construct an isotropic angular distribution; and the duration of the integration, t_{rand}, is taken randomly in a power law distribution such that t_{rand} is large compared to the orbit period.

A comparison between the MC simulation and the analytical derivation is presented in Figure 3.9. For $r < 40\,R_\odot$ the two approaches differ by less than 20%. For larger r the statistics of the MC becomes too low and we observe significant statistical fluctuations. This 20% difference is small and is likely due to numerical uncertainties and approximations made in both approaches. The MC simulation agrees on the order of magnitude obtained by the analytical derivation and thus it cross-checks the calculations. The code of the MC simulations is provided on a public repository [3].

Let us conclude this chapter with some considerations about the trapped KK axions:

- We will determine the event rate $a \to \gamma\gamma$ in an Earth-based detector in Chapter 9. At this point, we can already say that, since KK axions accumulate over cosmic times, the event rate of trapped KK axions is about 3 orders of magnitude larger than the event rate for the direct KK axions emitted continuously by the Sun.

- Some calculations can easily be adapted to the standard axion without extra dimensions. For instance, the number density of trapped ALP can be determined from Eq. (3.61) by setting $\delta = 1$, by rescaling the results by $1/(2R)$, and by removing the integral over the masses. In other words, for $\delta = 1$, the KK axions can be seen as a sum of individual axion, up to a normalization factor.

- Since the number density of the trapped KK axions evolves as $1/r^4$, only a tiny fraction of them would reach the Earth.

- The trajectories of the trapped KK axions are repeatedly crossing the Sun. We have checked that the probability of reconverting the KK axion into a photon, via the three mechanisms described in Section 3.3, is negligible. However, if one considers a non-zero axion-electron coupling, that is for non-hadronic axions, we will show in Chapter 9 that the situation changes and that part of the KK axions would be reabsorbed by the Sun.

[3] https://github.com/BeaufortC/KKaxionDensity

Summary

The axion is one of the most studied particles for physics beyond the Standard Model. It is a pseudoscalar that arises from the breaking of a global $U(1)$ symmetry called the Peccei-Quinn symmetry. After the breaking, it modifies the structure of the QCD vacuum such that the CP-violating term of QCD is continuously and dynamically compensated. In this sense, the axion solves the strong CP problem since it enables CP-conservation in the QCD sector. Besides this feature, the axion would be a massive and stable particle, feebly coupled to the SM gauge fields, and it would be produced in the Early Universe via several mechanisms, in particular the realignment mechanism that is a direct consequence of the PQ symmetry breaking, and that produces non-relativistic axions. The axion is then a motivated candidate for cold dark matter.

The axion is a member of a wide class of bosons called ALP sharing similar phenomenology as the standard axion although they do not necessarily solve the strong CP problem. In most cases, the ALPs may also be good candidates for dark matter. Detectors searching for axions are usually also sensitive to ALPs, increasing the interest in axions searches. The ALPs are coupled to the photons and they can decay into two photons. If the decay is too large, one would then observe an ALP contribution to the photon flux coming from outside the galaxy, called the EBL. The measurements of the EBL flux set stringent limits on ALPs with masses in the keV-range, which is the mass range that can be probed by MIMAC. We have updated the EBL constraint by including possible Compton scattering of the photons emitted after an ALP decay. We have made the calculations in the best-case scenario and it turned out to be not sufficient to relax the EBL constraint on keV ALPs. The region of interest of the MIMAC detector searching for ALPs thus appears as excluded by cosmological considerations.

However, the situation changes drastically if one considers that the axion can propagate into extra spatial dimensions. In the ADD framework proposed in the 90s, the SM fields are confined into a 4D brane whereas any singlet under the SM gauge group, as the axion or the graviton, could propagate into a $(4+n)$-dimensional Minkowski space called the bulk. The n extra dimensions are compactified with a radius R up to the micrometer. For this reason, the extra dimensions are called *large*. This framework fulfils all experimental constraints from laboratory experiments, astrophysics, or cosmology. The motivations for the ADD scenario consist in solving the mass hierarchy problem while proposing mechanisms for gauge coupling unification, inflation, proton stability, baryon asymmetry, etc.

An axion propagating in the bulk, that is in the extra dimensions, would be seen from our 4D world as an "infinite" superposition of massive states called Kaluza-Klein axions. The ground state still solves the strong CP problem and is associated with the QCD axion whereas the other states have larger masses, in the keV-range for KK axions produced in the Sun. The phenomenology of the KK axions differs then significantly from the QCD case: they are numerous, more massive, and with a lifetime that can be comparable to the age of the universe.

In the Sun, hadronic KK axions would be produced by three mechanisms: the Primakoff effect, the coalescence of two photons, and the plasmon decay. The Primakoff effect dominates the other ones. However, non-relativistic KK axions are suppressed by Primakoff and plasmon decay, so only the coalescence mechanism produces non-relativistic KK axions. This difference is crucial because, in such a case, the KK axions could be sufficiently non-relativistic to be trapped into the solar gravitational field. They would then orbit around the Sun and accumulate over cosmic times. We have derived the number density of KK axions orbiting the Sun and it evolves as $1/r^4$, with r the distance to the Sun. The $a \to \gamma\gamma$ event rate of trapped KK axions in an Earth-based detector is about 5 orders of magnitude larger than the event rate of direct production of KK axions in the Sun.

Part II

The MIMAC project: a directional detector for low-mass WIMP and higher-dimensional axion searches

Chapter 4

Gaseous μ-TPC in a nutshell

> Journalist: *The wire chambers led to the Nobel Prize in Physics. What did this bring to you?*
> G.C.: *Free coffee whenever I entered a bar, a lot of visibility in the streets of Paris because of the television [...] a lot of travelling and even a dozen pairs of shoes that were offered by fans.*
>
> Georges Charpak – 2009 [264]

Time Projection Chambers (TPCs) are widely used for about 50 years for tracking particles and for rare events detection [265]. These detectors measure the energy of a charged particle entering the active volume and some of them reconstruct the particle track in 3D. A large active volume is filled with a gas or a liquid and is placed into a constant electric field, and sometimes into a magnetic field. A charged particle entering the volume produces charges via ionization, the charges then drift towards a readout plane that localizes them in 2D. The third coordinate, being longitudinal to the electric field lines, is reconstructed from the drift velocity of the charges combined with the time of arrival at the readout plane. A breakthrough in the development of TPCs was the introduction of micropattern detectors [266] as readout planes, the combination being called μ-TPCs. They are manufactured by microelectronics technologies yielding high position resolutions of order $\sim \mathcal{O}(100 - 500)$ μm.

In this work, we focus on the MIMAC detector [267], a gaseous μ-TPC in which the micropattern detector is a Micromegas [268]. MIMAC stands for MIcro-TPC MAtrix of Chambers since it can assemble several μ-TPC chambers to achieve a large volume detection of 1 m^3 or even more [269, 270]. The MIMAC project started at LPSC in 2007 in collaboration with CEA-Saclay and the IRSN of

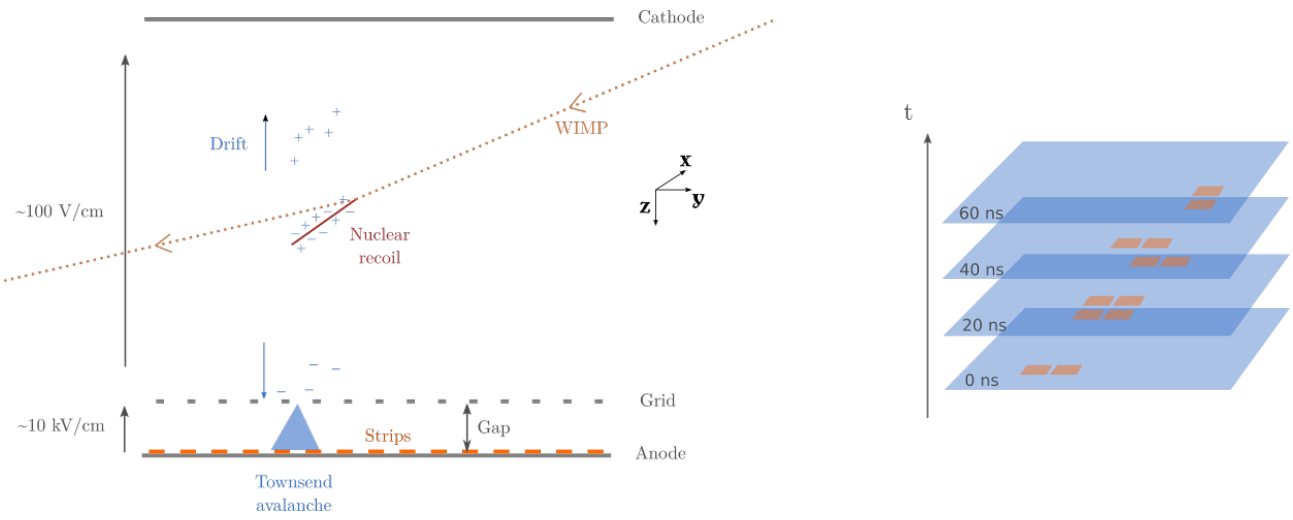

Figure 4.1: Schematic of the MIMAC detection principle. Left: description of an event. Right: the reconstruction of the track in 3D from the pixelated anode measurements.

Cadarache. In 2011, the CPPM of Marseille joined the project. This chapter introduces the physical processes involved in particle detection with MIMAC. Section 4.1 describes the elements that compose the detector. The physics of the primary electrons cloud is presented in Section 4.2, from the ionization process to the diffusion. Finally, we dedicate special care to the signal formation in Section 4.3 whose specificities are studied in several chapters of this thesis.

4.1 Introduction to MIMAC

We start with a brief description of the principles of particle detection with MIMAC. This section is intentionally let short to offer an overview of the detector while additional technical details will be presented in Chapter 5.

4.1.1 Welcome to the matrix

A MIMAC chamber consists of a two-stage structure: (1) a drift area corresponding to the active volume in between a cathode and a grid; (2) an amplification area in between a grid and an anode. The cathode and the grid are polarized in order to have a drift electric field of order $\mathcal{O}(100$ V/cm) and an amplification electric field of order $\mathcal{O}(10$ kV/cm). The grid enables the separation of the two regions of the detector. Due to the geometry of the electric field, the electrons easily pass through the grid. The anode is pixelated: it is composed of strips in two directions, leading to 65 536 pixels distributed on the readout plane. The chamber is filled with a low-pressure gas mixture.

The basic principles of MIMAC are presented in Figure 4.1. A WIMP entering the active volume could make an elastic collision on a nucleus of the gas, consequently inducing a nuclear recoil. The moving nuclear recoil ionizes the gas, producing electron-ion pairs. Due to the drift electric field, the ions drift towards the cathode and the electrons drift towards the grid. Once an electron reaches the grid, it enters the amplification area, also called *gap*, and it sufficiently accelerates to ionize the gas. It leads to a Townsend avalanche where one primary electron at the grid will generate about 10^4 secondary electrons at the end of the avalanche. The secondary electrons are collected on the anode while the secondary ions are collected on the grid. On the grid we measure the energy of the particle; on the anode, that is pixelated, we reconstruct in 3D the track of the particle.

The MIMAC chamber has 25 cm of drift maintained at a uniform electric field thanks to a field cage. The electric field lines are oriented along the Z-axis of the detector. We are using a bulk Micromegas [271] with a large amplification gap of 512 μm dedicated to low-pressure measurements. The Micromegas anode is pixelated and it contains 256 strips in both X and Y directions with a pitch of 424.3 μm, covering a total area of $10.8 \times 10.8\,\text{cm}^2$ [272]. A strip is fired when the current induced by

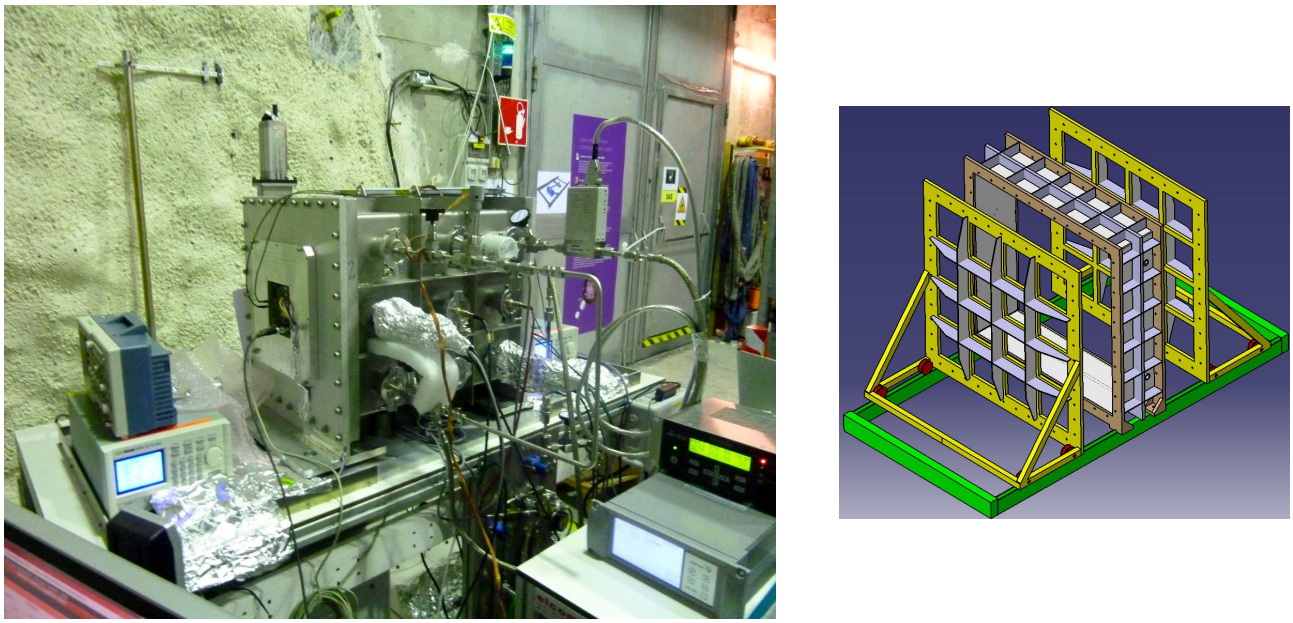

Figure 4.2: The matrix of chambers. Left: picture of the bi-chamber module. Right: the frame assembling 16 bi-chamber modules into a matrix.

the moving charges exceeds a threshold that is automatically calibrated before detector polarization in order to remain above the strip intrinsic noise [273].

MIMAC measures simultaneously the signal induced on the grid and the one induced on the pixelated anode by two independent but synchronized readouts, both sampled at 50 MHz (20 ns) by a self-triggered electronic system. On the grid, we use a charge-sensitive preamplifier that integrates the charge over time and which is digitalized via a Flash-ADC with one value per *timeslice*, which corresponds to a time sample of 20 ns. The ionization energy of the particle, as we will later see, is proportional to the amplitude of the Flash signal. In parallel, a set of 8 specially designed 64-channel MIMAC ASIC [274] reads the pixelated anode and measures in 2D the position of the activated strips for each timeslice of 20 ns.

The MIMAC chamber described above has a volume of 3 L. It is possible to increase its dimensions although one quickly reaches limitations due to charge loss, diffusion, or Micromegas manufacturing. Another approach to increase the active volume consists in duplicating the MIMAC chamber. Two chambers set back-to-back via a common cathode make the so-called *bi-chamber module*, as shown in the left panel of Figure 4.2. This module is then duplicated 16 times and assembled into a matrix: the MIMAC detector. The right panel of Figure 4.2 shows a representation of the matrix. The majority of the measurements presented in this work have been obtained in a single chamber. For this reason, when not specified, MIMAC refers to a single chamber detector in this thesis.

4.1.2 Gas mixture

The choice of gas mixture depends on the physical purpose of the experiment. One of the main advantages of gaseous detectors is to easily change the mixture or the experimental conditions to adapt the detector to some specific particle searches. For instance, for WIMP searches one will favour an odd nucleus (as H or ^{19}F) to open the spin-dependent channel and consequently increase the probability of WIMP-nucleus interactions. The mixture, and in particular its pressure, will also be adapted to the energy of the searched particles: the larger the energy, the longer the track. A compromise must be found to optimize some properties: large enough gain to detect all charges, intermediate electron drift velocity to properly describe the time component, and long enough recoil tracks to reconstruct the 3D.

We here introduce some properties of the main gases used in this work:

- The CF_4 represents an interesting gas for the detection of a WIMP with mass above $\sim$ 10 GeV thanks to its relatively large number of fluorine atoms. Another advantage of the CF_4 is to act

as a quencher. It means that it absorbs the photons produced during the avalanche which allows to operate in a proportional regime.

- The CHF_3 also has several fluorine atoms but it has an electron drift velocity about 30 times lower than the one in the CF_4, according to the simulation tool `Magboltz` [275]. We then use the CHF_3 to reduce the electron drift velocity in order to optimize the time description of the track.

- The i-C_4H_{10}, called *isobutane*, is introduced to increase the gain of the detector since it has a low W-value, the mean energy required to form an electron-ion pair, of 23.4 eV [276, 277]. In other words, adding isobutane to the mixture increases the number of secondary charges produced in an avalanche. The isobutane also plays the role of quencher.

In this work we mainly present results obtained in two gas mixtures:

- The *Mimac gas* is composed of 70% CF_4 + 28% CHF_3 + 2% i-C_4H_{10} at a pressure of 50 mbar and it is dedicated to WIMP searches via detection of fluorine nuclear recoils. For the last ten years, most of the MIMAC results have been obtained in this mixture. In particular, this mixture enables an efficient discrimination between nuclear recoils and electrons [177]. The density of the *Mimac gas* is 1.74×10^{-4} g $\cdot$ cm^{-3}.

- The *High-gain gas* is composed of 50% i-C_4H_{10} + 50% CHF_3 at a pressure of 30 mbar and is mainly used to search for low-energy protons recoils (< 10 keV) or electrons. This mixture leads to a high gain ($> 3 \times 10^4$, depending on the polarization applied on the grid) that increases the sensitivity to low-energy nuclear recoils and electrons. It is also dedicated to low-mass WIMP searches due to the large amount of hydrogen, the lightest odd nucleus target. The density of the *High-gain gas* is 8.15×10^{-5} g $\cdot$ cm^{-3}.

4.1.3 Glossary

We here introduce some vocabulary commonly used in the thesis.

- **Gap**. The gap is the distance between the grid and the anode, so it is the thickness of the amplification region. It is a key element of the detector since it defines the gain and its size influences the amount of detected ionic signal as we will later see. In this work we mainly use a gap of 512 μm compared to the gap of 256 μm commonly used in previous MIMAC works.

- **Gain**. The gain is the number of secondary electrons produced in a single avalanche. It depends on the gap, the voltages applied, and the gas mixture.

- **Flash**. The Flash refers to the signal measured on the grid. It corresponds to the integral of the charge induced on the grid which is digitized by the Flash-ADC. It has one value per timeslice and it is expressed in ADC-units.

- **Derivative**. It is the derivative of the Flash: $D[i] = F[i] - F[i-1]$. The derivative is more sensitive to the arrival of charges than the Flash so it is the appropriate tool for data analysis.

- **Timeslice**. A timeslice is the time sample of the detector. The electronics read the signal induced on the grid and on the anode every timeslice. Since the electron drift velocity is constant, one can convert a timeslice into a distance in the drift region. In this work, we always operate with a timeslice of 20 ns.

- **Primary electrons**. They are the electrons produced during the ionization process in the drift area. They are produced all along the track of the moving charged particle.

- **Secondary electrons**. They are the electrons produced in the avalanche process. Every single primary electron that enters the amplification area (that crosses the grid) will generate secondary electrons.

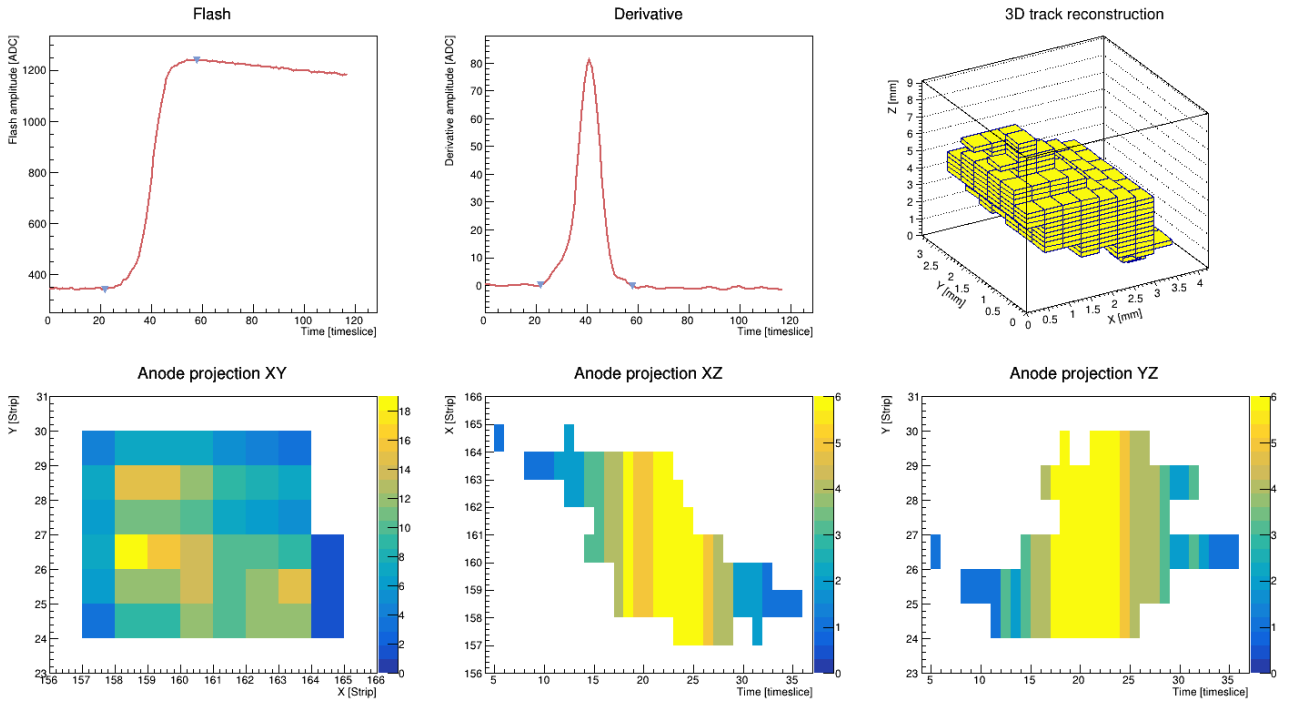

Figure 4.3: Example of the measurements of a proton recoil with a kinetic energy of 8.6 keV induced by a collision with a 27 keV neutron. The measurements were performed in the *High-gain gas* with a gap of 512 μm and an amplification electric field of 9.96 kV/cm.

- **Cluster**. A cluster is a group of primary electrons that is separated from the rest of the primary electrons cloud. A nuclear recoil track will typically not have any cluster (due to the large density of charges during the ionization process) whereas a muon will produce many clusters along its track.

- **Track**. A track is the distribution of the primary electrons along the trajectory of a charged particle passing through the detector. By extension, we sometimes refer to *track* to describe the signal on the anode, although some additional processes, such as diffusion for instance, modify the measured signal compared to the initial track produced by the charged particle.

- **Coincidence**. We talk about coincidence when one strip X and one strip Y, at least, have been fired during the same timeslice. This is a condition to localize in 2D the position of the charges.

As an illustration of some concepts presented above, Figure 4.3 shows a typical example of the measurement of a proton recoil produced by an elastic collision with a neutron. The Flash signal is well defined with a single peak on the Flash derivative. For this reason, no cluster is observed. The three bottom panels show the measurements of the pixelated anode on the three planes (X-Y), (X-t), and (Y-t). As already explained, the time is converted into a distance by means of the electron drift velocity to determine the relative length of the Z coordinate. It is then possible to combine the anode projections to reconstruct in 3D the track of the particle, as shown in the top right panel.

4.2 The primary electrons cloud

A charged particle passing through a TPC leaves a track of electron-ion pairs along its path. This primary electrons cloud corresponds to the picture of the particle and it drifts towards the amplification region before being detected by the MIMAC readout. The physical processes involved in the creation and the evolution of the primary electrons cloud must be precisely understood and controlled in order to optimize the information retrieved from the measurements.

4.2.1 Ionization process

The ionization is the process in which electrons are ejected from an atom. They can be directly ejected by the interactions with the charged particle, or via intermediate processes such as collisions with previously ejected electrons. The description of the energy loss by a charged particle in matter was a major topic in the previous century and is still under debate in the low energy region, as we will see. In first approximation, the maximum energy transferred by a particle of mass M to an electron during the ionization process is given by [278]:

$$T_{\max} \simeq 2m_e c^2 \beta^2 \gamma^2 \qquad \text{for} \quad 2\gamma \mathrm{m_e} \ll \mathrm{M} \tag{4.1}$$

where $\beta = v/c$ and $\gamma = 1/\sqrt{(1-\beta^2)}$ is the Lorentz factor. We then see that in most of the situations studied in this work, that is for recoil energies below 30 keV, the energy transfer to the electrons remains below the binding energies of the electrons of the atoms of the gas. For this reason, electrons ejected by collisions between the charged particle and the atom will usually not be able to ionize afterwards. We must also point out that in this low-energy region, the charged particle ranges are short (in this thesis we main study millimeter tracks) so we can consider that they are completely stopped in the detector. In other words, they release their entire kinetic energy into the active volume of gas of the detector.

The mean energy required to form an electron-ion pair, from all ionizations, is called the W-value and is hereafter denoted W. The mean number of electrons produced by a charged particle on a distance Δx is then given by:

$$\langle n_e \rangle = \left\langle \frac{dE}{dx} \right\rangle \frac{\Delta x}{W} \tag{4.2}$$

where $\left\langle \frac{dE}{dx} \right\rangle$ is the average total energy loss per unit path length of the charged particle. When the encounter with the gas atoms are random, $\langle n_e \rangle$ follows a Poisson distribution with variance $\langle n_e \rangle$ and a relative fluctuation of $\frac{1}{\langle n_e \rangle}$ [279]. The number of primary electrons is then subject to statistical fluctuations that limit the energy resolution of a detector.

However, the ionization process along the trajectory of the particle are not completely independent from each other. An empirical factor, called the Fano factor and denoted F, has been introduced to cope with the difference between the observed fluctuations and the expected ones from the Poisson distribution. The effect of the Fano factor is to reduce the dispersion of the distribution. When $F = 1$, the distribution is Poissonian and is sub-Poissonian when $F < 1$. The Fano factor is very challenging to measure experimentally since one must be able to deconvolve the energy resolution observed from effects due to statistical fluctuations in the avalanche and the electronics. For gases, its value usually lies between $F \simeq 0.1$ and $F \simeq 0.3$ [280, 281].

The statistics of the ionization process set an upper limit on the energy resolution achievable for a gaseous detector. When $\langle n_e \rangle$ is large enough, the detector response can be approximated by a Gaussian. In this case, the Fano factor can be included in the overall energy resolution of the detector. However, the situation changes at very low energies, when only a dozen of pairs or less are created, and the Fano factor must directly be accounted for in the ionization process. MIMAC measures signals in this low-energy region, an example will be presented in Section 5.4, and it seems sensitive to the fluctuation of the number of primary electrons. We then require an accurate description of the discrete distribution of charges produced by the ionization process.

To account for the Fano factor, and consequently for the dependence between successive ionizations, the distribution of the number of charges can be described by a Conway-Maxwell-Poisson (COM-Poisson) distribution [282] that depends on two parameters: λ and ν. The cited article proposes several approaches to rely on the parameters (λ, ν) to the physical values $(\langle n_e \rangle, F)$. The distribution of the number of electrons created during the ionization is expressed as a COM-Poisson distribution:

$$P(n_e = x \,|\, \lambda, \nu) \;=\; \frac{\lambda^x}{(x!)^\nu \sum_{s=0}^{\infty} \frac{\lambda^s}{(s!)^\nu}} \tag{4.3}$$

A COM-Poisson distribution with $\langle n_e \rangle = 7$ and $F = 0.25$ is compared to a Poisson distribution with $\langle n_e \rangle = 7$ on Figure 4.4. One can see two main differences. First, the COM-Poisson distribution

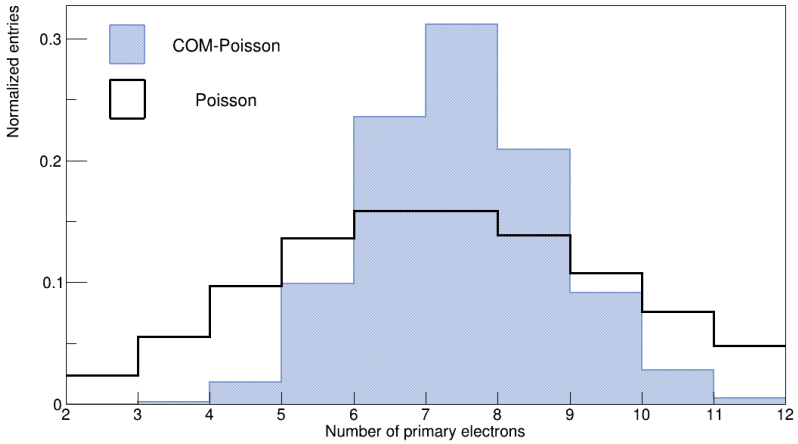

Figure 4.4: Comparison between a Poisson distribution with $\langle n_e \rangle = 7$ and a COM-Poisson with $\langle n_e \rangle = 7$ and a Fano factor of $F = 0.25$.

presents a better resolution since it takes into account the Fano factor. Second, it becomes more asymmetric than the Poisson distribution. The lower the values of $\langle n_e \rangle = 7$ and F, the larger the discrepancies between a COM-Poisson and a Poisson distribution.

Let us now discuss the W-value. It depends on the composition of the gas, and on the mass and energy of the incident particle. The W-value value remains constant above a few keV for electrons and above a few MeV for alpha particles [283]. However, at lower energies it depends on the energy of the incident particle. For electrons, the energy dependence of the W-value is typically described by [284]:

$$W(E) \;=\; \frac{W_a}{1 - U/E} \tag{4.4}$$

where W_a is the asymptotic W-value at large energy, and U is a constant with a value close to the average energy of sub-excitation electrons. At low energy, the W-value quickly increases. For instance in methane, the asymptotic value is 27.1 eV but it reaches 37 eV for electrons energy of 51 eV and 55 eV for electrons energy of 21 eV [276]. This energy dependency of the W-value should be kept in mind while discussing low-energy ionization.

Measurements of the W-value in gases are usually performed with experiments in which particles of known kinetic energies are sent in a gas, and one measures the current induced by the ionization to convert it into the number of charges produced [276, 277, 285, 286]. These experiments are performed at low pressure, $\mathcal{O}(1 - 50)$mbar depending on the energy of the incident particle. It also has to be noted that in such experiments the signal is not amplified by an avalanche nor any other multiplication process.

Corrections of eventual energy losses are also applied, in particular when measuring W-value for ions. For instance, they can be used to correct the effect of energy loss before entering the active volume, diffusion, and recombination by extrapolating measurements to $p \to 0$ and $p/E \to 0$ [287, 288] where E is the electric field strength and p is the pressure. For these reasons, standard W-value measurements are independent of the pressure such that the W-value can be considered an intrinsic property of a gas. However, a discussion remains about how to extrapolate W-value measurements to the operating conditions of μ-TPCs: with a non-zero gain (from avalanche processes) and larger pressure than in the experiments used to measure the W-value. We point out measurements with non-zero amplification in which the measured W-value varies both with the gain of the detector and with the pressure [289], the variations being attributed to secondary effects happening in the avalanches.

The W-value of a gas mixture can be determined from additivity rules that describe how the energy transfer is distributed among the gas components. We here only describe some additivity rules of *regular* mixtures in which no energy transfer is allowed between an excited state of one component with the ground state of another component. The simplest one, called the reciprocal Bragg additivity

Gas	W-value [eV]	Total ionization cross-section [10^{-16} cm^{-2}] evaluated for an electron kinetic energy of 85 eV
CF_4	34.3 [292]	5.080 [293]
CHF_3	28.1 [294]	4.634 [293]
i-C_4H_{10}	23.4 eV [276]	11.8 [295]

Table 4.1: W-value and total ionization cross-section of the main gases used in this work

rule, states that:

$$\frac{1}{W} = \sum_i \frac{C_i}{W_i} \tag{4.5}$$

where the sum is over all the gas components and where C_i is the concentration fraction of the i-th component. However, this simple expression does not take into account the fact that the energy loss processes depend on the ionization cross-sections. Several models have been established to determine the proportion of energy dissipated into component i, for additional details we refer to [290, 291]. We here cite another expression:

$$W = \frac{\sum \sigma_i C_i W_i}{\sum \sigma_i C_i} \tag{4.6}$$

where σ_i is the total ionization cross-section of component i evaluated at a sufficiently high electron energy compared to the ionization threshold energy. Table 4.1 lists the C_i and W_i tabulated for the main gases used in this thesis. We use Eq. (4.6) to determine the W-value of our gas mixtures: the *Mimac gas* has a W-value of 32.2 eV compared to 24.7 eV for the *High-gain gas*.

4.2.2 Ionization Quenching Factor

The amount of energy released by a nuclear recoil ionizing the atoms of the active volume of detection appears "quenched" compared to an electron of the same kinetic energy. This different behavior in ionization between electrons and nuclei is described by the Ionization Quenching Factor (IQF) and it plays a crucial role in many direct dark matter experiments. We refer to [296] for a clear introduction to quenching effects.

A nuclear recoil or an ion moving in a medium looses its energy by colliding with the electrons and the nuclei of the medium. The energy is released through three processes: (1) the production of electron-ion pairs called ionization, (2) scintillation, in which photons are emitted in the de-excitation of quasi-molecular states or by Bremsstrahlung, and (3) heat produced by the additional motion of the nuclei and the electrons. The energy is transferred both to electrons and to nuclei, producing a cascade of collisional processes by the secondary ions. Detectors usually only have access to one or two of these processes and the total kinetic energy of the recoil needs to be inferred, for instance by converting the observed ionization into kinetic energy. This is the case for MIMAC since it only measures the ionization energy.

The energy loss is directly related to the stopping power ($-dE/dx$), *i.e.* the energy loss per unit distance. It is convenient to separate the stopping power into two components, an electronic one and a nuclear one:

$$\left(\frac{dE}{dx}\right)_{\text{tot}} = \left(\frac{dE}{dx}\right)_{\text{elec.}} + \left(\frac{dE}{dx}\right)_{\text{nucl.}} \tag{4.7}$$

The nuclear contribution is related to the collisions of two nuclei described by a two-body scattering in the presence of a screened Coulomb potential. The nuclear stopping power is then the integral of the energy loss via all collision processes weighted by the probability of such processes. Determining the electronic stopping power is pretty complex since the moving ion and the electrons of the gas continuously change charge state during the motion of the ion [297]. In 1963, Lindhard *et al.* [298] described the case of a moving ion that loses all its energy in a detector, and they define the quenching

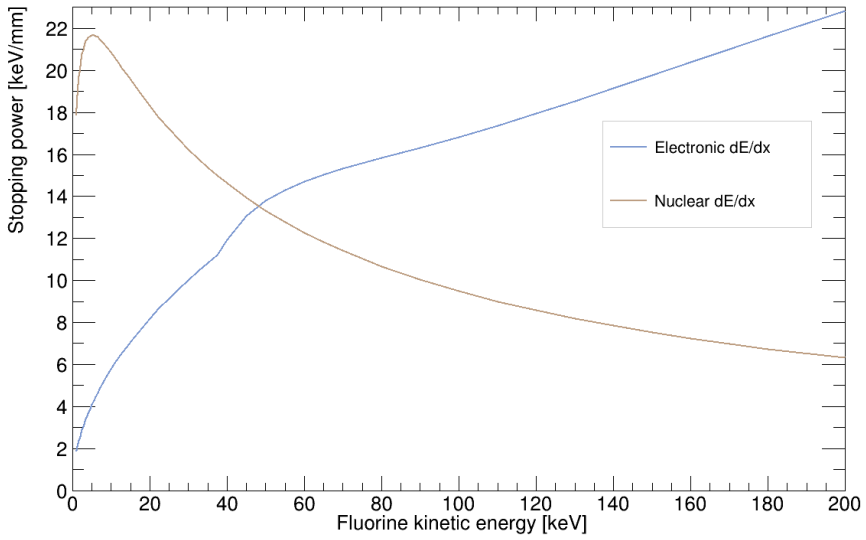

Figure 4.5: The electronic and nuclear stopping powers for fluorine ions in the *Mimac gas* at 50 mbar according to `SRIM`.

factor as the proportion of energy loss given to the electrons compared to the total energy loss:

$$q_f(E_K) \;=\; \frac{\int_0^{E_K} dE \left(\frac{dE}{dx}\right)_{\text{elec.}}}{\int_0^{E_K} dE \left[\left(\frac{dE}{dx}\right)_{\text{elec.}} + \left(\frac{dE}{dx}\right)_{\text{nucl.}}\right]} \tag{4.8}$$

The nuclear and electronic stopping powers for fluorine ions in the *Mimac gas*, simulated with the `SRIM` toolkit [297], are presented in Figure 4.5. One can see the typical tendency that the nuclear contribution dominates over the electronic contribution in the low energy region. The quenching factor then decreases at low energy.

The above description is based on theoretical arguments and cannot be not trivially extrapolated to experimental conditions. For this reason, an alternate definition of the quenching effect is commonly used in the literature: an effective quenching factor is defined as the conversion from the measured energy to the kinetic energy. In this work, we will almost exclusively discuss detectors measuring the ionization signal, as MIMAC or NEWS-G. To emphasize the difference with respect to the Lindhard quenching, we call Ionization Quenching Factor the fraction of energy released as ionization by a moving ion or a nuclear recoil. The IQF is defined as:

$$\text{IQF}\ (E_K) \;=\; \frac{E_{\text{ioniz}}}{E_K} \tag{4.9}$$

where E_K is the kinetic energy of the particle, and E_{ioniz} is the measured ionization energy. Note that an ion and a moving nucleus have the same IQF [297] due to the continuously changing state of charge during the ionization process. For simplicity, we usually refer to "ion" in this section although the statements also hold for a nuclear recoil. The IQF depends on the ion properties (mass and energy) and on the medium properties (composition and density). It must then be determined for each detection configuration in order to reconstruct the kinetic energy from measurements of the ionization energy.

The Lindhard theory models the stopping power of ions in matter under a semiclassical approximation. While complementary models have been developed on this basis (see [297] for details about several models), they do not describe low-energy ions for which the semiclassical approximation usually fails [296, 299]. `SRIM` code computes the quenching effects by following the approach of the Lindhard theory but using advanced calculations of the interatomic potentials based on a solid-state model in order to determine a *universal* screening function that has been compared to hundreds of experimental data [297]. While this method remains the most precise on a general basis, it has been developed for higher energies ($\sim$ MeV/amu) than those treated in this thesis. Also, it has to be noted that `SRIM` and

the Lindhard theory do not take into account the gas density when computing quenching factors, while we have previously observed that the IQF in the keV-range depends also on the gas pressure [300].

In Chapter 7, we will describe the multiple experimental approaches used for measuring the IQF and we will also detail all steps leading to an IQF measurement with Comimac. We will show that deviations to simulations and the Lindhard theory are commonly observed for energies below 50 keV in gases, crystals, and noble liquids. For instance, we will show a measurement having 33% difference for protons of 2 keV in 100 mbar of methane. For those reasons, it is important to perform IQF measurements for each gas mixture and pressure. Finally, let us mention that quenching effects behave differently for the three channels: ionization, scintillation, and heat. For instance, measurements in a germanium detector indicate that the heat quenching factor remains constant between 20 keV and 100 keV while the IQF varies by almost a factor of 2 in the same range [301].

4.2.3 Drift of electrons

The charges produced in the active volume will drift under the influence of the electric field. We here only describe the motion of the electrons. The electrons will quickly lose their kinetic energy due to the collisions with the gas molecules. However, they will be accelerated by the electric field and they can acquire energies of a few eV in between two collisions, depending on the strength of the field and the gas mixture. The motion of the electrons is stochastic since, due to their small mass, their direction and their energy can greatly change during collisions. On average, the distribution of the primary electrons cloud in their transportation towards the grid, $n(x, y, z, t)$, can be described by a Gaussian diffusion process:

$$n(x, y, z; t) \;=\; \frac{n_0}{\sqrt{8\pi^3}} \; \frac{e^{-\frac{x^2+y^2}{4D_t\, t}}}{\sqrt{4D_t^2\, t^2}} \; \frac{e^{-\frac{z^2}{4D_l\, t}}}{\sqrt{2D_l\, t}} \tag{4.10}$$

where D_t and D_l are respectively the transverse and the longitudinal coefficients. The standard deviations of the distribution are given by $\sigma_l = \sqrt{2D_l\, t}$ and $\sigma_t = \sqrt{2D_t\, t}$. It is convenient to make a change of variables to express the standard deviations in terms of the drift velocity of the electrons, v_d, which remains constant since the electric field is constant. We then introduce $\tilde{D}_l = \sqrt{2D_l/v_d}$ and $\tilde{D}_t = \sqrt{2D_t/v_d}$. Finally, we note $L = v_d t$ the longitudinal distance travelled by the electrons (along the electric field line) during a duration t, in order to rewrite Eq. (4.10) as:

$$n(x, y, z; L = tv_d) \;=\; \frac{n_0}{\sqrt{8\pi^3}} \; \frac{e^{-\frac{x^2+y^2}{2\tilde{D}_t^2\, L}}}{\tilde{D}_t^2\, L} \; \frac{e^{-\frac{z^2}{2\tilde{D}_l^2\, L}}}{\tilde{D}_l\, \sqrt{L}} \tag{4.11}$$

The parameters of Eq. (4.11) depend on the experimental conditions. We use the simulation tool `Magboltz` [275] to determine them. It is a Monte Carlo simulation that transports a single electron over a sufficiently large number of collisions to explore the entire phase space. `Magboltz` presents a good agreement with experimental data [302] as we will see in Section 5.4. For the *High-gain gas* at 30 mbar with a drift electric field of 100 V/cm, the simulations predict:

$$\begin{cases} v_d = 14.6 \ \mu\text{m/ns} \\ \tilde{D}_l = 420 \ \mu\text{m}/\sqrt{\text{cm}} \\ \tilde{D}_t = 328 \ \mu\text{m}/\sqrt{\text{cm}} \end{cases} \tag{4.12}$$

One can see an asymmetry in the diffusion coefficients: the primary electrons cloud will be more enlarged along the Z-direction than along the X and Y directions. We can estimate the effect of diffusion by simulating a primary electrons cloud with `SRIM` and by transporting randomly each charge according to Eq. (4.11). An example is presented in Figure 4.6. At first glance, one can observe that diffusion blurs the signal from the initial track.

We point out that some of the primary electrons can be attached by gas molecules during their drift towards the grid. The created molecular negative state has some lifetime that can cover many orders of

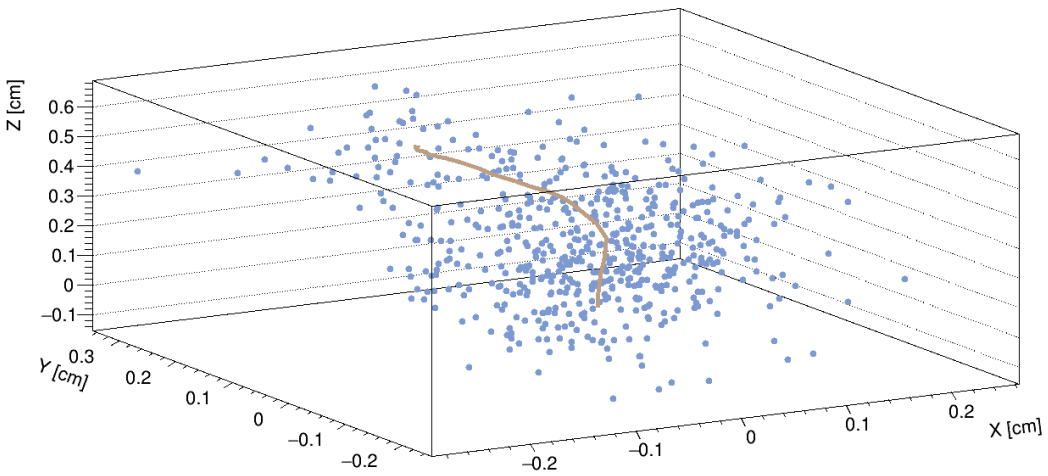

Figure 4.6: Illustration of the effect of diffusion. A primary electrons cloud of a 20 keV proton in the *High-gain gas* at 30 mbar, obtained from a `SRIM` simulation, is represented as a brown line. Each primary electron is affected randomly by diffusion over 5 cm according to Eq. (4.11) and the parameters given in Eq. (4.12). The primary electrons after the drift are shown as blue dots.

magnitude depending on the electron affinity of the molecule. The metastable state eventually evolves into a stable situation through the following processes [303]:

$$AX + e^- \longrightarrow AX^{-*} \longrightarrow \begin{cases} AX + e^- \\ A + X^- \\ AX^- + \text{energy} \end{cases} \tag{4.13}$$

The second process of Eq. (4.13) is called the resonant dissociative attachment (RDA) and dominates in the experimental situations we are interested in [304]. Due to the slow kinematics of negative ions compared to electrons, the RDA results in the loss of a primary electron. The attachment is then a statistical process that deteriorates the energy resolution of the detector.

The probability for an electron to survive after drifting over a distance x is given by $\exp(-x/\lambda)$ where λ is the mean attachment length. The average collected charge after drifting over a distance L, from an initial charge Q_0, is given by:

$$\frac{Q}{Q_0} = \frac{\lambda}{L}\left(1 - e^{-L/\lambda}\right) \tag{4.14}$$

The CF_4 is a gas with a relatively large electron capture cross-section. It has been shown that electron attachment can be the dominant process that deteriorates the energy resolution in CF_4 [305].

The influence of the attachment depends on several parameters: the electron affinity of the gas molecules, the electric field, and the drift distance. Note that the oxygen particularly attaches the electrons: a few hundred of ppm of oxygen in the gas mixture is sufficient to attach, and lose, some primary electrons, as presented in Figure 4.7. Gas contamination with oxygen is frequent due to surface out-gasing in the detector. The detector must then be let at vacuum for several days before each experiment in order to reduce the gas pollution.

4.3 Signal formation

Once a primary electron reaches the grid, it enters the amplification area where it produces an avalanche. To do so, it must cross the grid. We define the *transparency* as the fraction of primary electrons that enter the amplification area. The grid is a 2D meshing composed of stainless steel wires of 18 μm diameter with a pitch of 45 μm. The grid wires occupy then 13% of the area of the detector

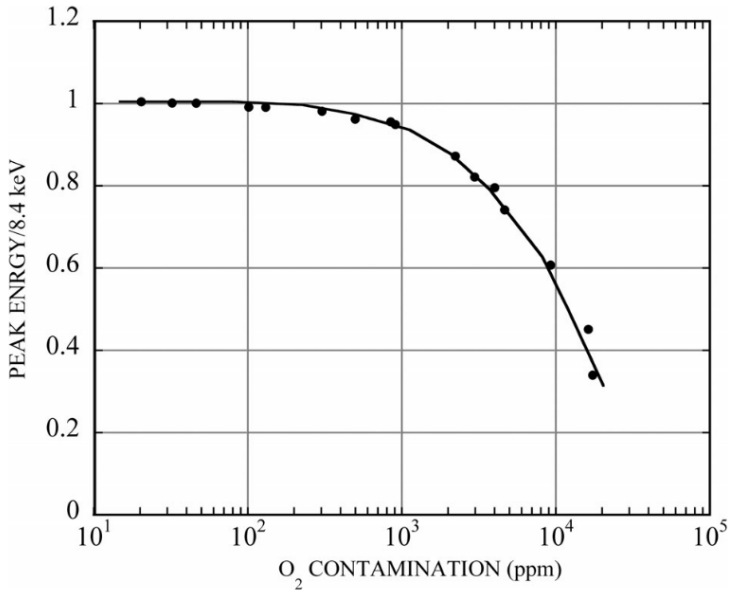

Figure 4.7: Influence of the concentration of oxygen in the loss of primary electrons for a drift up to 1 cm in a mixture of Xe + 10% CH_4. Figure extracted from [304].

in the (X-Y) plane, so the optical transparency is 87%. However this is not the total transparency of the grid because the electron trajectories depend on the electric field. The geometry of the electric field lines is influenced by $\xi = E_{\text{amp.}}/E_{\text{drift}}$, the ratio of the electric field in the amplification region over the one in the drift region. The larger ξ, the more electrons avoid the grid wires, so the larger the transparency [268]. For each gas mixture, one must then find the best compromise for the values of the electric fields: (1) $E_{\text{amp.}}$ determines the gain of the detector; (2) E_{drift} must be large enough to collect all charges but sufficiently small to describe the Z-component of the track in multiple timeslices; (3) the field ratio ξ must be adjusted to optimize the grid transparency to electrons. As we will see in Chapter 6, the grid transparency can be estimated by `SimuMimac`. We obtain 98.5% transparency in the *Mimac gas* at 50 mbar with $E_{\text{amp.}} = 11.1$ kV/cm and $E_{\text{drift}} = 152$ V/cm, which are the conditions used in [173, 174].

4.3.1 The avalanche

The number of primary electrons is too small to produce a detectable signal. It is then necessary to amplify this signal by proportionally increasing the number of electrons. This is the role of the avalanche. In the amplification region, the electric field is large enough to accelerate the electrons to energies up to $\mathcal{O}(100$ eV). During a collision with a gas molecule, the accelerated electron will be able to eject another electron from the molecule which will also be accelerated until it ionizes the gas. The number of secondary electrons then grows exponentially. The variation of the number of electrons over a path ds is given by:

$$dN = N\,\alpha\,ds \tag{4.15}$$

where α is called the first Townsend coefficient and it characterizes the intensity of the avalanche. α must be measured for each gas mixture and each electric field, but it can also be simulated, for instance using `Magboltz`. The amplification factor, also called *gain*, is given by:

$$G = \frac{N}{N_0} = \exp\left\{\int ds\,\alpha(s)\right\} = e^{\alpha d} \tag{4.16}$$

In the last step we have considered the case of a Micromegas where the electric field is constant in the whole amplification region, so is the first Townsend coefficient. We have also introduced $d = 512$ μm the gap. In all the situations presented in this work, the detector operates in a proportional regime where

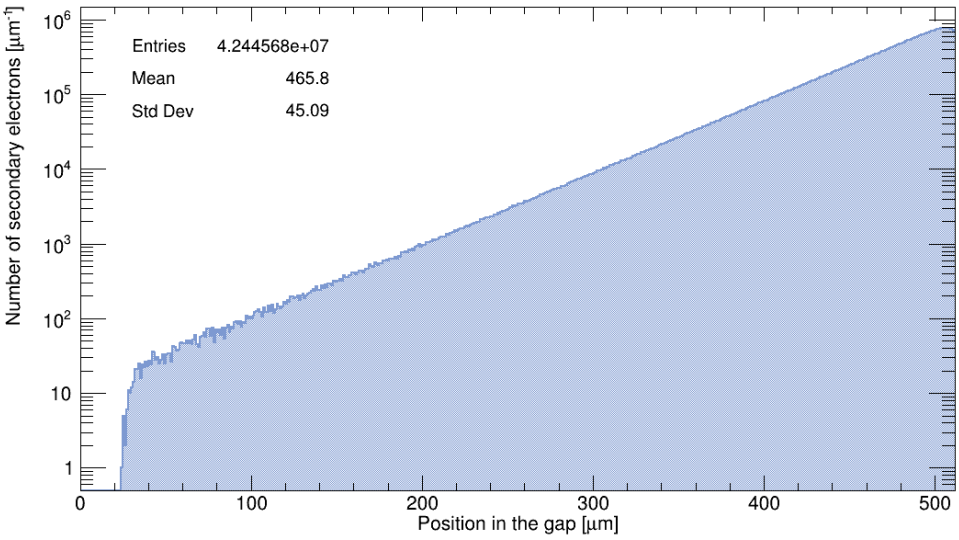

Figure 4.8: Z-position of the secondary electrons once they are produced in the avalanche. Simulation of 1000 avalanches with `SimuMimac` in the *High-gain gas* at 30 mbar with −480 V on the grid.

the number of secondary charges is proportional to the number of primary charges, the proportional factor being the gain. In this work, the gain typically varies between 10^4 to 5×10^4.

The avalanche is a statistical process that suffers some variations. The number of secondary electrons produced during the avalanche follows a Polya distribution [283], whose probability distribution is given for large gain as:

$$P(G) = \frac{1}{\bar{G}} \frac{(\theta+1)^{(\theta+1)}}{\Gamma(\theta+1)} \left(\frac{G}{\bar{G}}\right)^{\theta} \exp\left\{-(\theta+1)\frac{G}{\bar{G}}\right\} \tag{4.17}$$

where $\bar{G}$ is the mean gain, Γ is the Euler function, and θ is the Polya parameter describing the statistical fluctuation of the avalanche process. The standard deviation of the distribution is given by $\sigma^2 = \bar{G}^2/(\theta+1)$. The parameters of the Polya distribution can be determined by measuring the response of the Micromegas detector to a single primary electron, as in [306].

We have used `SimuMimac` to simulate 1000 avalanches in the *High-gain gas* at 30 mbar with −480 V on the grid. The Z position at which the secondary charges are produced is presented in Figure 4.8. We can see that it follows an exponential distribution, as expected from Eq. (4.16), so that half of the secondary electrons are produced in the last 50 micrometers. The avalanche process also has some spread in the transverse direction, so in the (X-Y) plane of the MIMAC detector. We have simulated that the transverse distribution of secondary electrons at the anode follows a Gaussian distribution with a standard deviation of order ~ 100 μm. Finally, we have also fitted the Polya distribution Eq. (4.17) to the 1000 avalanches simulated and we obtained $\bar{G} = 4.4 \times 10^4 \pm 2.8 \times 10^3$ and $\theta = 4.78 \pm 0.71$. The largeness of the uncertainties of the fit function is due to the small statistics (1000 events).

The fluctuations in the avalanche process influence the resolution of the detector by being quadratically added to the fluctuation of the number of primary electrons. The energy resolution is then:

$$R_{\text{stat.}} = 2.35 \sqrt{\frac{F + (1+\theta)^{-1}}{\langle n_e \rangle}} \tag{4.18}$$

where F is the Fano factor and $\langle n_e \rangle$ is the mean number of primary electrons. Other phenomena, like gas impurities or electronic noise, deteriorate the total energy resolution of the detector.

One challenge is to ensure the stability of the avalanche process. The electrons accelerated in the amplification area interact with the gas molecules but they do not necessarily ionize the gas. In some cases, the electrons excite the gas molecules resulting in the emission of photons. Those photons can

produce a photoelectric effect, leading to the introduction of an electron at almost any distance in the amplification area, and thus initiating a new avalanche. For this reason, one must control the production of the photons in the avalanche in order to remain in a proportional regime. One solution consists in absorbing the photons before they produce a photoelectric effect. Polyatomic molecules present excited states that will be able to absorb the photons. For instance, the methane efficiently absorbs photons between 7.9 eV and 14.5 eV [304], an interesting range for photons produced in the avalanche. A gas that absorbs photons to stabilize the avalanche is called a *quencher*. Usually, the quenching efficiency of a gas molecule increases with its number of atoms: for instance the isobutane, i-C_4H_{10}, is a quencher.

4.3.2 The Ramo-Shockley theorem

We will now discuss how the signal is formed in the detector. This point is crucial for understanding the work presented in this thesis. At first glance, one could think that the signal is induced once a charge touch an electrode. This is however not the case: the signal is induced during the entire time the charge is moving. In other words, the motion of a charge induces, quasi-instantaneously, a signal on an electrode. The current induced by a moving charge is given by the Ramo-Shockley theorem [307, 308]:

$$i = q\,\mathbf{v}\cdot\mathbf{E}^w(\mathbf{r}) \tag{4.19}$$

where q is the charge of the moving particle, $\mathbf{v}$ is its instantaneous velocity, and $\mathbf{E}^w(\mathbf{r})$ is the *weighting field* at position $\mathbf{r}$. The weighting field is defined as the electric field at coordinates $\mathbf{r}$, if the moving charge is removed and if all electrodes are grounded except the one in which we compute the signal, whose potential is set to 1 V. In MIMAC, the grid is a single electrode. On the contrary the strips of the anode are independent electrodes. It means that we have 513 electrodes: one for the grid and one for each strip.

The grid is one large and almost plane electrode and it is located sufficiently far away from the anode to consider the system as an ideal plane capacitor. In this approximation, the weighting field on the grid is constant in the whole gap:

$$\mathbf{E}^w_{\text{grid}}(\mathbf{r}) \;=\; \mathbf{E}^w_{\text{grid}} \;=\; \frac{1}{d}\,\hat{\mathbf{z}} \tag{4.20}$$

where d is the gap.

The weighting fields of the strips, however, are more complex since the strips are close enough to influence each other. Thanks to the symmetries of the detector, the weighing field of a strip is identical in the (X-Z) and the (Y-Z) planes. We have simulated in 2D the weighting field of the central strip of the detector using the `Garfield++` toolkit [309]. The results are presented in Figure 4.9. One can see that the weighting field is non-linear in both directions: in the transverse direction, the weighting field is maximal at the interface between two consecutive strips and it becomes negative on the following strips. An analytical expression for the weighting field of a strip is derived in [310] assuming that the strip has an infinite length along Y, a width w along X, and there is no gap between two consecutive strips. If $x = 0$ is the center of the strip located at $z = 0$, noting $z = d$ the gap, the z-component of the strip weighting field can be approximated as:

$$E^w_z(x,z) \;=\; -\frac{1}{2d}\left\{\frac{\sinh\left(\pi\frac{x-w/2}{d}\right)}{\cosh\left(\pi\frac{x-w/2}{d}\right)-\cos\left(\frac{\pi z}{2}\right)} \;-\; \frac{\sinh\left(\pi\frac{x+w/2}{d}\right)}{\cosh\left(\pi\frac{x+w/2}{d}\right)-\cos\left(\frac{\pi z}{2}\right)}\right\} \tag{4.21}$$

We are interested in the signal induced by an avalanche, so when a large number of ions and of electrons are produced. The Ramo-Shockley theorem can be generalized to multiple electrodes and charges:

$$i_k(t) = \sum_n q_n\,\mathbf{E}^w_k(\mathbf{r}_n)\cdot\mathbf{v}(\mathbf{r}_n) \tag{4.22}$$

where k labels the electrode (grid or strips), the sum is over all the moving charges, $\mathbf{v}(\mathbf{r}_n)$ is the velocity of the n-th moving charge, and $\mathbf{E}^w_k(\mathbf{r}_n)$ is the weighting field of electrode k at coordinates $\mathbf{r}_n$ of the

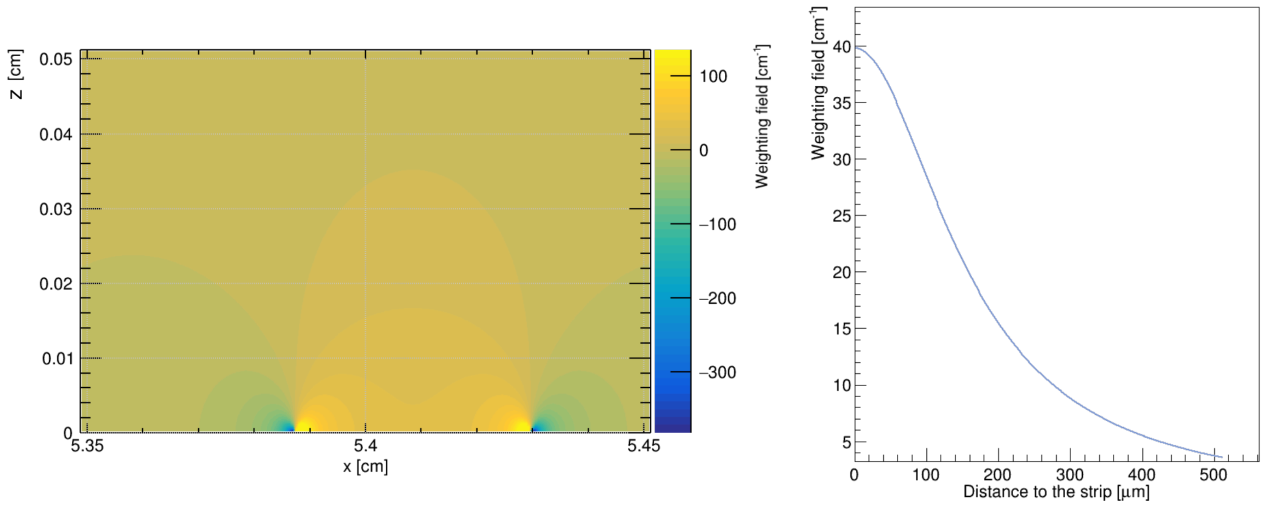

Figure 4.9: Weighting field of a single strip simulated with `Garfield++`. The left panel presents the 2D weighing field evaluated on the central strip of the detector. On the right panel, the weighting field is evaluated as a function of the distance Z to the strip for X chosen at the center of the strip.

charge n. The ions are moving towards the grid whereas the electrons are moving towards the anode. Since they move in the opposite directions and since they have an opposed charge, they induce both a signal of the same sign on the electrodes.

We will later discuss a possible space-charge effect: when the Coulomb fields of the charges in the gap locally distort the electric field and then influence the motion of the other charges as well as the avalanche development. We must point out that the Ramo-Shockley theorem remains valid even in presence of a space-charge [311, 312].

4.3.3 The ions and electrons ballet

The signal induced on the grid or on the anode strips is then composed of two contributions: one from the electrons and one from the ions. The electron velocity is two to three orders of magnitude larger than the ion velocity, as we will discuss later in Chapter 6. All the electrons are collected in less than 1 ns whereas the ions need typically 300 ns to reach the grid. The Ramo-Shockley theorem tells us that the ions then induce a tiny signal compared to the electrons, but for a longer time.

Dris and Alexopoulos [313] have estimated analytically the signal formed on the grid of a Micromegas by a single avalanche:

$$\begin{cases} f^g(t) &= \frac{qu_n}{d}\, e^{\alpha u_n t} &, \text{ for } 0 \leq t \leq d/u_n \\ g^g(t) &= \frac{qu_p}{d}\left(e^{\alpha d} - e^{\alpha u_p t}\right) &, \text{ for } 0 \leq t \leq d/u_p \end{cases} \tag{4.23}$$

where $f^g(t)$ is the electronic current induced on the grid, $g^g(t)$ is the ionic one, q is the elementary charge, u_n is the mean electron drift velocity in the gap, u_p is the mean ion drift velocity in the gap, d is the gap length, and α is the Townsend coefficient. This elegantly simple formula relies on several approximations: one-dimensional calculations, a constant Townsend coefficient, a mean ion mass produced in the avalanche, and the weighting field of the grid considered constant in the entire gap. In the above expression, we have added another simplification: we neglect the ionic signal when $t < d/u_n$, so when there are still electrons in the gap. We have validated in [179], and it will be presented in Chapter 6, that such approximations are reasonable and that the Dris and Alexopoulos model correctly describes the signal induced on the grid.

Figure 4.10 presents a typical example of the signal induced on the grid for a nuclear recoil. The electronic signal is sharp (less than 1 ns, so it can be assumed as instantaneous) and it corresponds then to the peaks in the figure. On the contrary, the baseline corresponds to the ionic signal. One can appreciate the different kinematics of both signals. In Figure 4.10 one can also observe the effect of

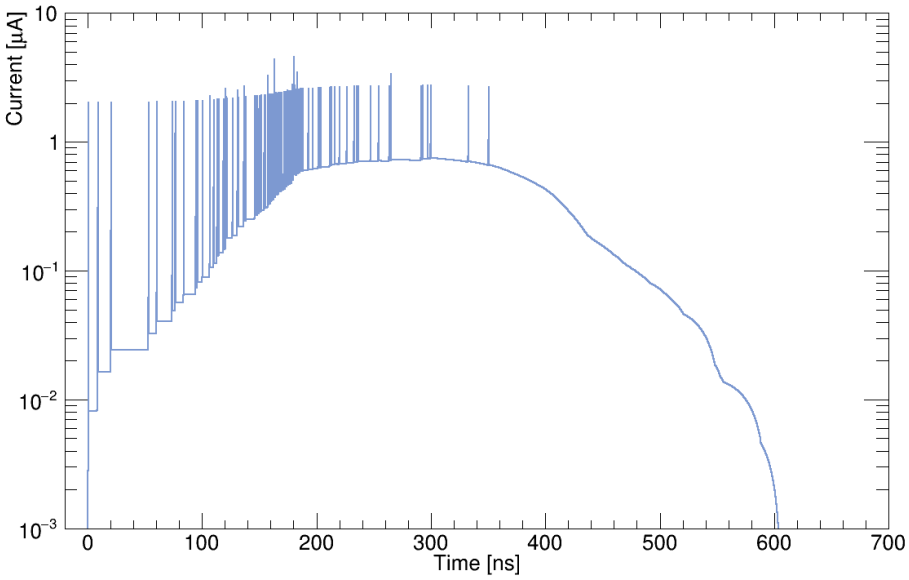

Figure 4.10: The signal induced on the grid which has been computed with the Dris and Alexopoulos model Eq. (4.23) for a 10 keV proton after 5 cm of drift in the *High-gain gas*. The primary electrons cloud has been obtained with `SimuMimac`.

diffusion: the time distribution of the electronic current is pretty Gaussian due to diffusion during the 5 cm drift of the primary electrons.

The signal induced on a strip by an avalanche can be determined in a similar way. Under the same approximations as before, in particular in neglecting the lateral development of the avalanche (assuming all secondary charges are produced at the same x position), we obtain:

$$\begin{cases} f^s(t) &= q u_n \, e^{\alpha u_n t} \, E_z^w(d - u_n t, x) &, \text{ for } 0 \leq t \leq d/u_n \\ g^s(t) &= q u_p \alpha \, e^{\alpha u_p t} \int_0^{d-u_p t} dz \, e^{\alpha z} \, E_z^w(d - z, x) &, \text{ for } 0 \leq t \leq d/u_p \end{cases} \tag{4.24}$$

where E_z^w is the strip weighting field given by Eq. (4.21), the grid is assumed to be located at $z = 0$, the strip at $z = d$, and x is the distance to the center of the strip. This formula relies on several approximations, the main one being the fact of neglecting the gap between two consecutive strips. It can be evaluated numerically. In Figure 4.11 we compare the signal induced on the grid and the signal induced on the strip aligned with an incoming primary electron, for a single avalanche. The electronic signals are pretty similar but the ionic ones are not. This is due to the z-dependency of the weighting field of the strips: as long as the ions move away from the anode, the signal they induce decreases. On the contrary, since the weighting field on the grid is constant, and since the velocity of the ions in the gap is constant, they induce a constant signal on the grid.

The Flash, which measures the signal induced on the grid, and the anode strips have detection thresholds: there is a minimal current below which they do not detect a signal. These thresholds are determined from the intrinsic electronic noise of the sensors. In general, the Flash threshold is lower than the strip threshold. For this reason, we can say that the Flash detects both the ionic and the electronic signal while the strips are mainly sensitive to the electronic signal. This simplified description is only valid at low gain (below 10^4) and we will later describe the importance of the ionic signal when operating at high gain.

Summary

The combination of a 2D micro-pattern readout with a TPC, called μ-TPC, allows to measure the energy released in ionization by a charged particle and to reconstruct at the same time its track in 3D with a spatial resolution of order $\sim$ 500 μm. As an example of such a μ-TPC, MIMAC uses

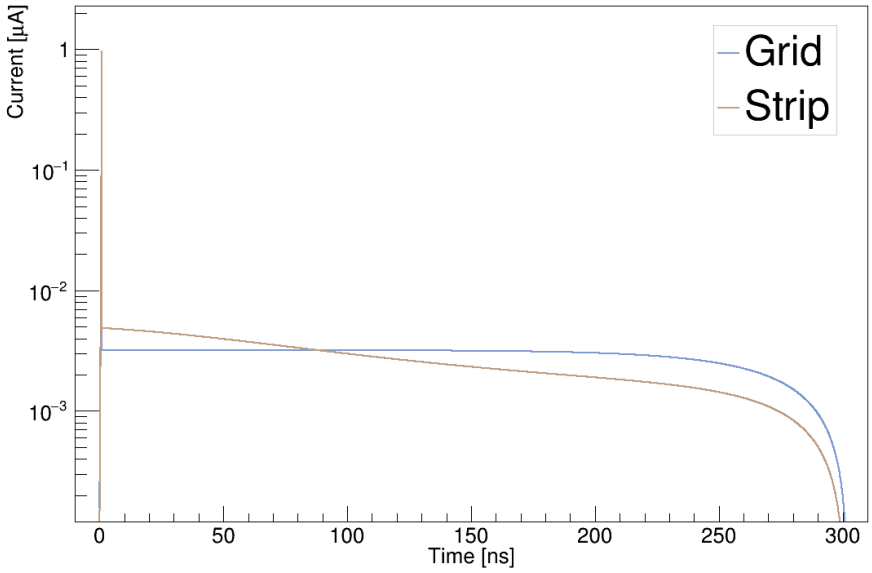

Figure 4.11: Comparison of the signal induced on the grid, obtained with Eq. (4.23), and the signal induced on a strip, obtained with Eq. (4.24) evaluated in $x = 0$, for a single avalanche.

a Micromegas to separate the volume into two regions: the primary charges are drifted in the drift region with $E_{\text{drift}} \sim 100$ V/cm; and they produce avalanches in the amplification region with $E_{\text{amp.}} \sim 10$ kV/cm. The secondary charges produced in the avalanche induce a signal on the Micromegas grid and on the Micromegas anode. Since the anode is pixelated, one has access to a 2D image of the charges and, when combined with the electron drift velocity and the sampling time, one can reconstruct the track in 3D. The choice of the gas mixture and the pressure is particularly important as a compromise between a WIMP target producing long enough tracks, a slow enough electron drift velocity allowing to reconstruct the 3D, a stable detector, and a large enough gain to access low energies.

Directional gaseous TPCs all depend on the ionization process that produces the primary electrons cloud. The number of primary electrons can be obtained from the W-value, the mean energy to produce an electron-ion pair. The electron W-value is constant above a few keV but it increases at low energies. The method to extrapolate W-value measurements to the working conditions of a gaseous TPC is still debated. The number of primary charges produced during the ionization is also affected by the Fano factor describing the dependency between successive ionizations. This number, which is central for directional detection, follows a COM-Poisson distribution than can be approximated by a normal distribution for large enough energies ($\simeq 1$ keV).

A charged particle deposits its energy in a medium through three competing processes: ionization, scintillation, and heat. The amount of energy released as ionization by a nuclear recoil appears as "quenched" compared to the ionization energy that an electron of the same kinetic energy would depose. The phenomenon is described by the Ionization Quenching Factor (IQF) which depends on the gas, the pressure, the incident particle and its kinetic energy. For instance, a proton of 2 keV in 100 mbar methane produces 45% less ionization energy than an electron of the same kinetic energy. Significant deviations are observed between simulated/theoretical quenching factors and the measured IQF.

During their drift towards the readout plane, the primary electrons experience diffusion that enlarges the primary cloud up to one order of magnitude. The diffusion is a Gaussian process, with an anisotropy between the longitudinal (along Z in MIMAC) direction and the transverse ones (X and Y). While diffusion distorts the directional information, it can also be a tool for accessing it for sub-millimeter tracks. Once at the grid, a primary electron will produce a Townsend avalanche due to the important electric field. The avalanche develops exponentially in the gap and the number of secondary charges produced can be described by a Polya distribution. In MIMAC we usually operate with a gain of around 3×10^4.

Each moving charge in the amplification region induces a signal both on the grid and on all the anode strips. According to the Ramo-Shockley theorem, this signal is proportional to the charge velocity, so it is about 1000 times larger for electrons than for ions. It also depends on the weighting field of the electrode, which can be considered constant for the grid, but is non-linear for the anode strips. The signals measured by the detector are then a complex interplay between an electronic contribution, abrupt and fast (< 1 ns), and a slow ionic contribution that extends for about ~ 300 ns since the ions must travel the entire gap before being collected on the grid. The large number of ions accumulated in the gap at high gain significantly contributes to the measured signal above the detection threshold.

Chapter 5

The MIMAC strategy of detection

What has the dark matter problem taught me, in the past 40 years, about the practice of science? I think that the central lesson is that science is essentially a social activity. This may seem obvious or trivial, but for me, it has been a profound, although gradual, realization.

Robert Sanders [14]

The MIMAC detector measures the ionization energy released by a charged particle and it reconstructs at the same time its track in 3D. The ionization energy is measured on the grid whereas the track reconstruction is performed from the pixelated anode. We make use of a bulk Micromegas [271], presented in Figure 5.1, that defines the amplification region by a single piece having a good mechanical resistance. The grid is placed on studs to ensure that its distance to the anode remains constant in the whole area, leading to an excellent homogeneity of the gain.

In the previous chapter we have described the main physical processes involved in particle detection with a μ-TPC. In the current chapter we introduce the different elements of the MIMAC detector to

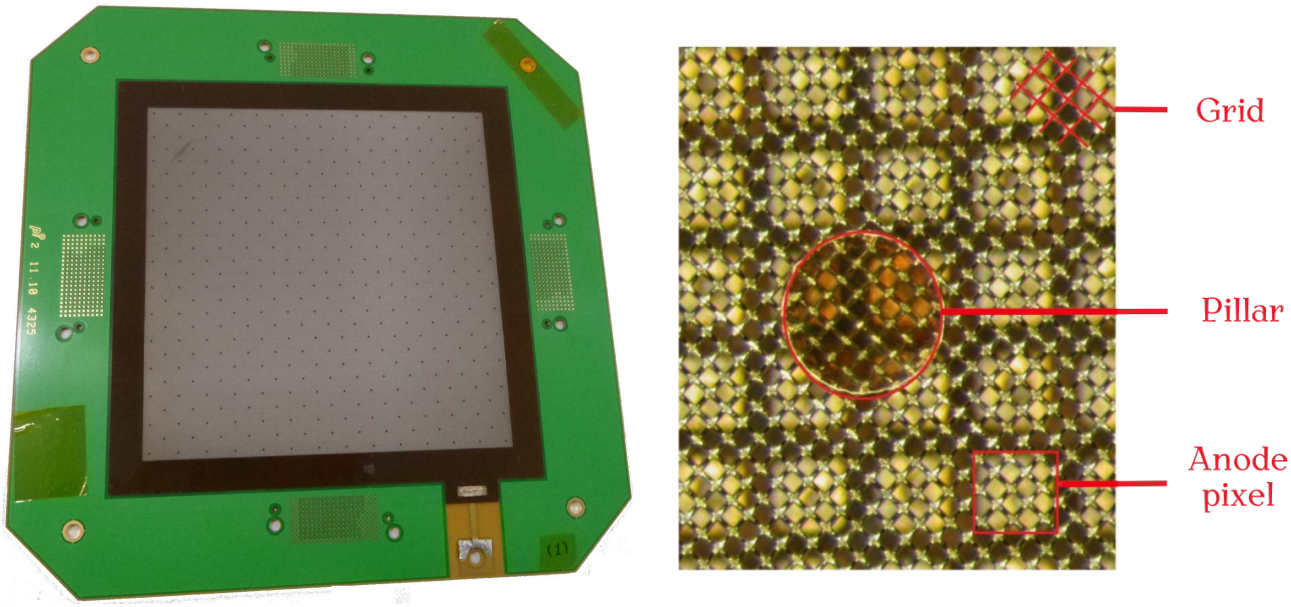

Figure 5.1: The bulk Micromegas.
Left: picture of a Micromegas with a gap of 512 μm and an active area of 10.8×10.8 cm^2. The dotted areas at the center of each edge correspond to the location where the connectors are placed. They allow to read the 512 strip channels with minimal cross-talk.
Right: zoom on the Micromegas. The grid wires are visible in the foreground and the anode pixels can be observed in the background. The picture also shows a stud that maintains the grid at a constant distance from the anode. Picture extracted from [314].

detail the strategy of detection. We start by presenting the measurement of the energy in Section 5.1 and several approaches for the energy calibration of the detector. Section 5.2 is dedicated to the 3D track reconstruction by means of the pixelated anode. We also give a description of the fast selft-triggered electronics that represent one specificity of the MIMAC detector. We then discuss in Section 5.3 how the observables from the grid and from the anode can be combined to identify the particles and discriminate the background. In Section 5.4 we introduce recent developments of a new detector to achieve a m^3 active volume in the near future. We also demonstrate the possibility to determine the absolute Z-position of the track thanks to the cathode signal. Section 5.5 concludes this chapter by presenting some facilities used for validating the MIMAC strategy of detection.

5.1 Measurement of the energy

5.1.1 Charge sensitive preamplifier

The ionization energy of an event is measured thanks to a charge-sensitive preamplifier (CSP). The role of this CSP is to integrate the current induced on the Micromegas grid over time. The CSP output is digitalized by a Flash-ADC over a 12-bit resolution range, so having 4096 channels. The signal is sampled at 50 MHz meaning that a value of the integrated current is converted into ADC channel every 20 ns. The CSP, coupled with the Flash-ADC, gives the total charge induced on the grid as a function of time.

The CSP is characterized by two time constants: the rise time, τ_C, corresponding to the time required for charging the CSP; and the decay time, τ_D. The rise time plays a crucial role in the time resolution of the CSP. Ideally, τ_C should be smaller than the time separation between the primary electrons in order to resolve them individually. However, the sampling time of 20 ns limits the resolution of the acquisition system. The decay time constant, τ_D, must be larger than the signal duration in order to collect all charges without influence from the CSP decay. On the contrary, a too long τ_D could lead to a pile-up, *i.e.* the CSP would start to integrate the current of a new event before being completely discharged.

The properties of the CSP can be determined experimentally. We make use of a pulse generator coupled to the grid via a 10 pF capacitor. The generator sends short pulses of voltage that can be approximated by a Heaviside function with a width smaller than 20 ns. The voltage pulses induce a current $i_{\text{ind.}}$ on the grid via the capacitor, following the relation:

$$i_{\text{ind.}}(t) \;=\; C\,\frac{dV}{dt}(t) \tag{5.1}$$

The transfer function of the CSP, as well as the characteristic times, are then determined by fitting an analytical model to the measured signal. We typically measure $\tau_C \sim 60$ ns and $\tau_D \sim 30$ μs [131].

One can also use the same approach to measure the linearity of the CSP by varying the pulse amplitude in order to probe the entire range of the Flash-ADC. We measure a linear response, always having an offset that corresponds to the electronic noise of the system. This offset usually lies below 0.3% of the total range of the Flash-ADC [131]. However, it must be measured and taken into account for accurate analyses.

We are interested in the ionization energy, *i.e.* a measure of the number of electron-ion pairs produced during the ionization process. The ionization energy is proportional to the number of secondary charges produced during the avalanche, so it is proportional to the charge induced on the grid. We define the ionization energy, in unit of ADC channel, as the amplitude of the Flash-ADC signal:

$$E_{\text{ioniz.}} \;\equiv\; F_{\max} - F_{\min} \tag{5.2}$$

Another possible definition of the ionization energy is the integral of the Flash signal. In our work we have not observed any noticeable difference between those two definitions. In the present thesis, the ionization energy will systematically be defined as the amplitude of the Flash. An illustration of this definition is presented in Figure 5.2.

5.1.2 Ballistic deficit

The Flash signal is affected by the time response of the CSP. While the charging time remains below a few timeslices, having thus only a small influence on the measurements, the self-discharge of the CSP can result in a significant loss of signal due to the continuous discharge of CSP while it still integrates the current induced by the moving charges. The signal loss due to the self-discharge of the CSP is called the *ballistic deficit*.

The Flash signal at the timeslice t_i, $F[t_i]$, is described by the convolution of the integrated current, $Q[t_i]$, with the transfer function of the CSP. We here only consider the self-discharge phenomenon so the transfer function is approximated by an exponential decay:

$$F[t_i] \;=\; Q[t_i] * \frac{e^{-t_i/\tau_D}}{\tau_D} \tag{5.3}$$

This expression can be deconvolved to extract recursively the integrated current [315]:

$$Q[t_i] = \begin{cases} F[t_i] & ,\ \text{for i} = 1 \\ Q[t_{i-1}] + F[t_i] - F[t_{i-1}]\, e^{-\Delta T/\tau_D} & ,\ \text{for i} > 1 \end{cases} \tag{5.4}$$

In this formula, Δt corresponds to the sampling time and $\tau_D = RC$ is the decay time that is directly related to the values of the resistor and the capacitor of the CSP. For each preamplifier, we measure the value of R and C to determine the decay time. We then apply the deconvolution formula Eq. (5.4) to correct the signal from the CSP self-discharge. An example of this deconvolution is presented in Figure 5.2 in which the measured Flash signal is shown in blue whereas the brown curve corresponds to the deconvolved signal. The ballistic deficit is defined, at each timeslice, as the ionization energy loss due to the CSP self-discharge. We can make three comments at this stage. First, we see that the ballistic deficit increases with the duration of the signal: the longer the signal, the more charges are integrated during the discharge of the CSP. Second, if not corrected, the ballistic deficit results in an energy loss. Third, after correction of the ballistic deficit the signal must follow a plateau once all primary charges have been collected. This is a way to check that the deconvolution is efficiently working.

In the measurements presented in this thesis, the ballistic deficit is systematically corrected.

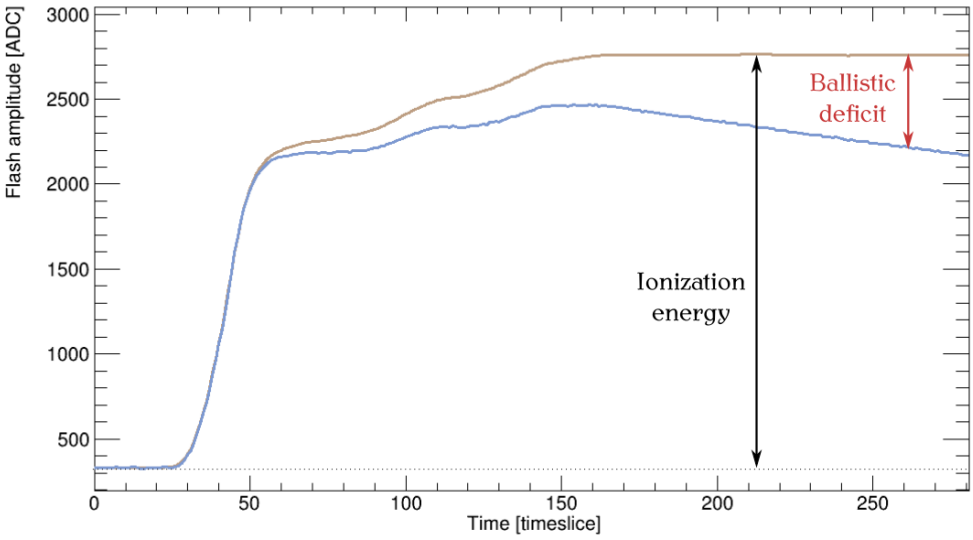

Figure 5.2: Description of the ballistic deficit for a measurement of a 12 keV electron sent by Comimac in the *High-gain gas* at 30 mbar. The blue curve corresponds to the Flash measurement. The brown curve is obtained after deconvolution of the response of the CSP with $\tau_D = 16$ μs. The ballistic deficit is defined, for each timeslice, as the amplitude difference between the Flash measurements and the deconvolved signal. We also represent the ionization energy as defined in Eq. (5.2).

5.1.3 Calibration

We defined the ionization energy as the amplitude of the Flash signal given in ADC-channel unit. The next step consists in converting the digital unit into a physical ionization energy, that is to convert the ADC unit into keV. This is done via an energy calibration.

An energy calibration compares the detector response to a reference particle of known energy. In gaseous detectors that measure the ionization energy, the reference particle is the electron. Unlike the ions, whose ionization energies are affected by the IQF, the ionization energy released by an electron is proportional to its kinetic energy. This relation remains valid as long as the non-linearity of the W-value can be ignored, so for kinetic energies above a few hundreds of eV. We have two different approaches, sometimes used simultaneously, to calibrate the detector.

Calibration with photoelectrons

The first approach relies on X-rays that will be absorbed by a molecule of the gas, resulting in the emission of an electron from the core. The kinetic energy of the resulting photoelectron is the initial X-ray energy minus the binding energy, $E_{e^-} = E_\gamma - E_b$. The binding energies for core-electrons in gaseous molecules are measured experimentally [316]: 301.9 eV for CF_4, 694.1 eV for CHF_3, 290.48 eV for C_4H_{10}. In addition to the emitted photoelectron, the exciting molecule relaxes to the ground state via two possible mechanisms: either by the emission of a photon by fluorescence due to the transition of an electron; or by the emission of one or more electrons, called Auger electrons [304]. In both cases, the total energy emitted in those secondary processes is close to the binding energy. The Auger electrons will be merged into the primary electrons cloud and they cannot be resolved individually by the MIMAC detector. In the other case, the fluorescence photon accompanying the photoelectron will travel some distance before being absorbed; if this distance is large enough, it can be identified as a cluster. One must note that in both cases we measure an ionization energy equal to E_γ, the energy of the incident X-ray.

We want to send X-rays of known kinetic energy in the active volume of the detector. To do so, we make use of an X-ray generator from Amptek that irradiates three metal foils: aluminium, cadmium, and copper. The X-rays sent by the generator will eject electrons from the core of the atoms of the foils. The excited atoms then relax by the emission of a photon. This is the principle of fluorescence.

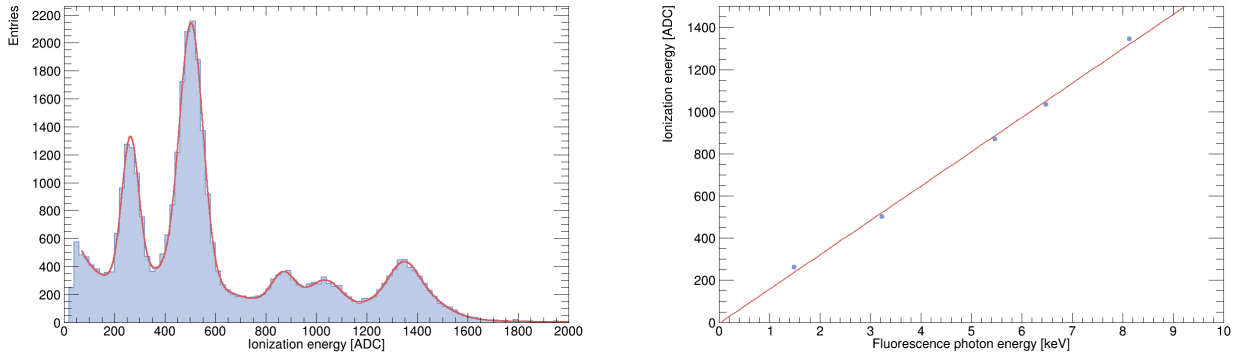

Figure 5.3: Calibration performed with the X-rays generator in the *High-gain gas* at 30 mbar.
Left: the measured spectrum fitted by a sum of Gaussian functions for each expected fluorescence line plus an exponential modelling the background.
Right: the corresponding calibration with the energies listed in Table 5.1. A linear fit function is also displayed in red showing an offset value of −4.5 ADC.

Material	Type	X-ray energy [keV]
Al	K	1.49
Cd	L	3.23
Cr	K	5.47
Fe	K	6.47
Cu	K	8.13

Table 5.1: Mean energies of the principal fluorescence lines of the calibration system, data from [317].

The system is connected to a MIMAC chamber and it has a curved geometry to ensure that only the fluorescence photons enter the active volume. A schematics including the connection between the X-rays generator and MIMAC is presented later in this work, in Figure 5.11. The energy of the initial X-rays is determined by the voltage applied to the generator, which can be as high as 20 kV, so one can excite the fluorescence lines of the atoms up to 20 keV.

The X-rays will excite the fluorescence lines of the three foils but also the ones of the surrounding materials since the MIMAC chamber is made of stainless steel. The mean energies of the fluorescence lines of such materials are listed in Table 5.1. A example of a calibration with the X-rays generator is presented in Figure 5.3 in the *High-gain gas* at 30 mbar. In the left panel, we present the measured spectrum as well as a fit function accounting for the expected energy and an exponential background. The three lines corresponding to the foils are the most visible and one can also observed the two peaks due to the stainless steel fluorescence. Depending on the resolution of the detector, the two peaks of the stainless steel are not always distinguishable. In the right panel, we present the corresponding calibration as well as a fit by a linear function having an offset of −4.5 ADC. We always obtain a non-zero offset that we attribute to the response of the electronic chain.

The calibration with photoelectrons is a pretty light and convenient tool. Such a system has been installed on a MIMAC bi-chamber that operated for six years in the Modane underground laboratory. A short calibration run was performed every week to control the gain stability of the detector.

Calibration with electrons produced by Comimac

Another calibration method consists in coupling a MIMAC chamber to a particle accelerator, called *Comimac*, which will be introduced at the end of this chapter. In a few words, Comimac sends electrons and ions of known kinetic energy into the active volume of the detector. We can then use the electrons as a reference to determine the calibration function of the detector.

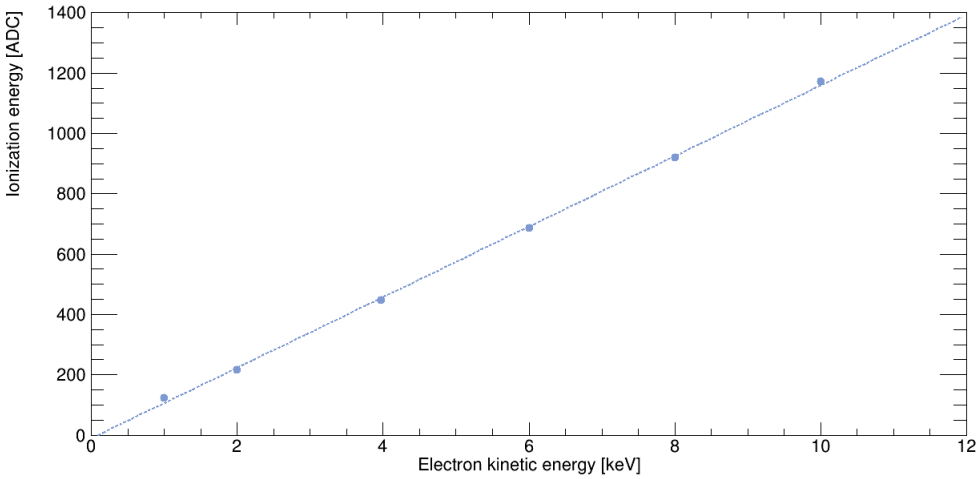

Figure 5.4: A calibration with Comimac electrons in the *Mimac gas* at 50 mbar. The data has been fitted by a linear function showing an offset value of −10.2 ADC.

There are some differences between a calibration with Comimac and with X-rays:

- The location of the events. Comimac sends all the electrons at the same position in the detector whereas X-rays can produce a photoelectric effect almost everywhere in the chamber. For this reason a calibration with X-rays incorporates volume effects.
- The event rate. The event rate with the X-rays generator can hardly be lower than 200 Hz whereas it is a free parameter with Comimac: we usually operate below 50 Hz. At a large rate, the detector could suffer a space-charge effect or some acquisition issues.
- The available energies. They are fixed by the choice of foils when using the X-rays whereas they can be chosen with Comimac.
- The *in situ* calibration. A calibration with Comimac must be performed before a measurement (and/or after) while the X-rays generator can be activated at any time when the detector is operating.

The works presented in this thesis have mainly been calibrated with Comimac. We have also compared a Comimac calibration with the X-rays generator [318] with less than 4% differences attributed to sensor effects, as we will see in Section 7.2.

Since the ionization energy of the electron is proportional to its kinetic energy, the calibration is supposed to be linear. A non-linear calibration could indicate a poor gas quality, a space-charge effect, a high-gain effect, *etc.*, so the origin of the non-linearity must be investigated. An example of calibration with Comimac electrons is presented in Figure 5.4. A linear function fits the data; it corresponds to the calibration function that converts the ionization energy measured in ADC into a kinetic energy measured in keV. The linear function presents an offset value of −10.2 ADC.

5.2 Track reconstruction in 3D

The reconstruction of the track in 3D is probably the most challenging part of the MIMAC strategy of detection since we are interested in the low-energy region, that is for nuclear recoils below 30 keV, whose track lengths are of the order of the millimetre. The pixelated anode is responsible for the 3D track reconstruction.

5.2.1 The pixelated anode

The pixelated anode covers an active area of 10.8×10.8 cm^2 and is segmented into 256 strips in each direction (X and Y). The anode is then composed of 65536 pixels of 200 μm width separated from

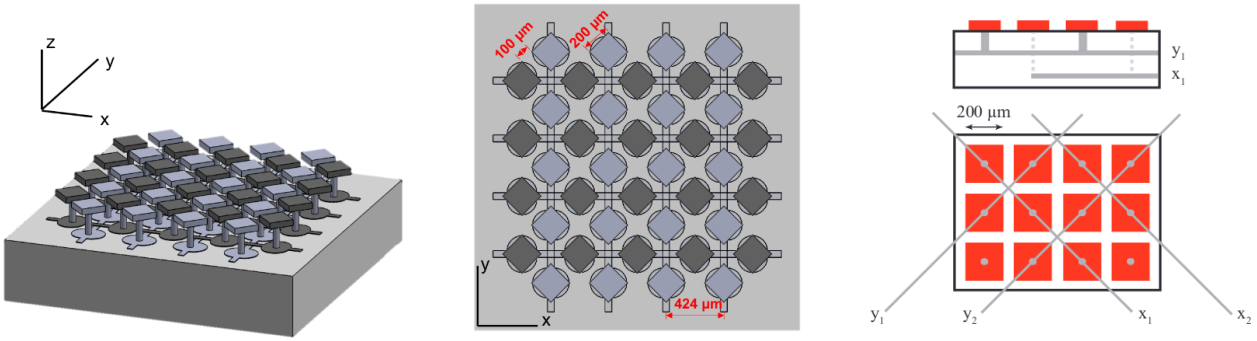

Figure 5.5: Diagrams presenting the pixelated anode. The strips are oriented along the X and the Y directions of the detector, leading to a succession of pads oriented diagonally to the (X-Y) plane. The strips X and Y are located at two different depths to optimize the anode space. The two left figures are extracted from [128] whereas the figure on the right is extracted from [319].

each other by 100 μm of insulator, so the strip pitch is equal to 424.3 μm. The pixels are electronically connected to the strips through 100 μm diameter metallized holes that have been filled to ensure a uniform surface. The strips X and Y are located at two different depths, the X strip being below the Y strip, in order to optimize the geometry. Figure 5.5 illustrates the geometry of the pixelated anode in order to clarify the description.

The pixelated anode must be interfaced with the readout electronics. The anode is placed on a PCB of 5 mm thickness presenting particular features to ensure the leak tightness of the detector. A PCB interface is then added to distribute the signals to the electronic card. The signal of each strip must be brought to the readout electronics with minimal cross-talk. This step is achieved by means of connectors with springs that are located at the center of each edge of the boards [319].

At each timeslice, the electronics determine which pixels have been fired by the signal induced by the motion of charges. A pixel is fired if the current induced by the moving charges overpasses a current threshold that is automatically calibrated, for each strip, as the digital value above the intrinsic electronic noise of the strip determined before detector polarization. The pixels then give binary information, activated or not, instead of measuring the induced charge over a timeslice. In other words, we have a 2D picture of the activated pixels every 20 ns.

The Z-coordinate is provided by the combination of the constant electron drift velocity and the time sampling. For instance, in the *Mimac gas* at 50 mbar with a drift electric field of 150 V/cm, `Magboltz` predicts a drift velocity of 22.9 μm/ns. The longitudinal resolution of the detector is then equal to $v_d \Delta t = 452$ μm, which is comparable to the transverse resolution of 423.4 μm that is given by the pitch of the strips. However, this reconstruction of the Z-coordinate only offers relative information and does not determine the absolute position of the interaction point along the Z-axis.

5.2.2 Readout electronics

The readout electronics developed for the MIMAC collaboration is crucial for the detector performances. Figure 5.6 presents a diagram of the main elements of the electronics.

ASIC 64-channel

The role of the ASIC (Application Specific Integrated Circuit) is to read the strip signals every 20 ns and to identify the ones that have been fired. Each ASIC reads 64 strip channels, so there are 8 ASICs in total, all of them covering a surface of 22 mm^2. Each channel has its own current preamplifier to amplify the signal by a gain of 15 before sending it to a current comparator. The comparator determines if the input current exceeds a threshold, in such a case the strip is considered as fired. The current threshold value is fixed thanks to a 5-bit DAC with a Least Significant Bit (LSB) of 200 nA [273]. It means that one can choose 32 values for the current threshold, ranging from 0 to 413.3 nA before the amplification stage, with a step of 13.3 nA. Usually the threshold lies around 3 DAC = 39.9 nA.

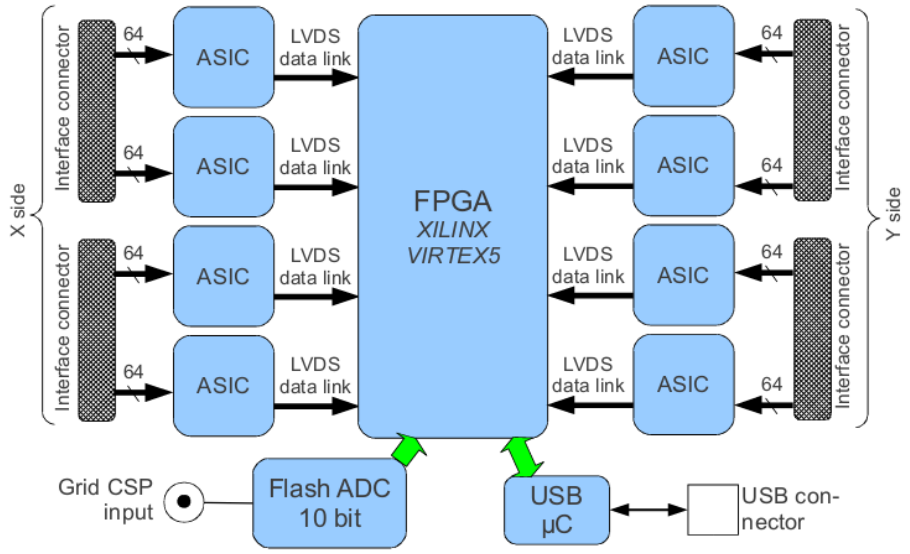

Figure 5.6: Block diagram of the acquisition chain of the MIMAC detector composed of 8 ASICs, an FPGA, a Flash-ADC, and a USB connection. Figure extracted from [273].

One of the main advantages of this technology, as explained above, is that the threshold value can be fixed for each strip. The threshold is automatically calibrated to remain 1 DAC unit (13.3 nA) above the intrinsic noise of the strip. We here insist on the fact that the strips are triggered when a current exceeds a threshold, not a charge. This difference is important because the fast (less than 1 ns) electronic signal induced by a single avalanche can be sufficient to activate a strip when operating at high gain ($> 10^4$). All ASICs use the same reference clock allowing synchronous sampling. The sampling is performed at 50 MHz whereas the serializing is performed at 400 MHz.

FPGA

The FPGA (Field Programmable Gate Array) coordinates the readout and stores the information for an event. The FPGA reads in parallel the data received from the ASICs and from the Flash-ADC, measured by two independent readouts, but re-synchronized by the FPGA. The signals from the strips and the Flash are continuously read at 50 MHz but they are stored only if a trigger condition is fulfilled. The FPGA checks the trigger condition and then determines if an event occurred. The trigger condition applies to the Flash signal:

$$F(t) - F(t - 320 \text{ ns}) > \mathrm{E}_{\text{thresh.}} \tag{5.5}$$

where $F(t)$ is the Flash signal. The trigger condition verifies if the slope of the Flash, computed at 320 ns difference, exceeds a threshold, $E_{\text{thresh.}}$, that is manually fixed in order to remain above the noise level. We usually operate with a threshold value of around 30 ADC. When this condition is fulfilled, the recording takes place: the FPGA sends to the acquisition software, via a USB connection, the information of the fired strips and the Flash amplitude for each timeslice. The information is then stored in a database, or directly in a text file depending on the acquisition software, according to an encoding procedure that minimizes the time of the writing operations.

The event stops when no longer primary charges arrive at the grid level. Once N_{postmax} timeslices have been recorded since the maximal amplitude of the Flash, the FPGA stops to save the data and the event is finished. The value of N_{postmax} is manually fixed depending on the physical purposes of the experiment. A large value, for instance $N_{\text{postmax}} = 1024$ timeslices, ensures that delayed charges are collected but it increases the probability of observing two independent events in the same time window. It also increases the *dead time*, that is the time during which the electronics are occupied to store the event and during which the detector cannot measure a new event. Currently, the mean dead time per event is around 800 μs. When searching for low-energy events, below 30 keV, we usually operate with $N_{\text{postmax}} = 64$ timeslices.

To localize the charge on the readout plane, we need at least one strip X and one strip Y fired during the same timeslice. This is what we call a *coincidence*. However, the pixels are either connected to a strip X or a strip Y. It means that in order to have a coincidence, we need a detectable signal induced on two pixels at least during the same timeslice. For isolated primary electrons, this condition is not necessarily fulfilled, in particular at low gain.

5.2.3 3D track reconstruction algorithms

A MIMAC event is composed, for each timeslice, of the amplitude of the Flash signal and a vector of activated strips along X and along Y. Knowing the drift velocity of the primary electrons, we then have a vector of coordinates, $(\mathbf{X}, \mathbf{Y}, \Delta Z)$, of the positions of the charges at the readout plane, so after experiencing diffusion and the avalanche. We have written $\mathbf{X}$ and $\mathbf{Y}$ to highlight the fact that for each timeslice we measure a vector of the activated strips in both directions. We also remind that the Z-component is only given relatively to the first activated timeslice; for this reason we write it ΔZ. From this point, we want to determine the track properties: lengths, curvature, angles, etc. We distinguish three main methods to retrieve the track information, all of them being illustrated in a measurement example in Figure 5.7.

Barycenter method

The simplest method, and sometimes the most reliable, to determine the properties of the track consists in reducing the amount of information retrieved from the pixelated anode. For each timeslice, we compute the barycenter of the activated strips along X and along Y, given as (for the X case):

$$x^b(t_i) = \frac{1}{N} \sum_{j=0}^{N} x_j(t_i) \tag{5.6}$$

where N is the number of activated X strips during the timeslice t_i. The barycenter method is motivated by the diffusion that tells us that the primary charges are gaussianly spread in the transverse direction. For this reason, the barycenter is the most probable position of the primary charge before the drift. With the barycenter method we obtain a coordinate vector $\left(x^b(t_i), y^b(t_i), \Delta Z(t_i)\right)$ with a single X and Y value per timeslice. We define three quantities from this vector:

- The **track duration** is defined as the time difference between the last timeslice with activated strips, $t_{\max}$, and the first one $t_{\min}$. The track duration corresponds then to the length of the track projected along the longitudinal axis of the detector, the Z-axis.

- The **straight length** corresponds to a 3D line drawn in between the two extreme activated timeslices. It is a convenient tool to discriminate the particles in an entire run as we will later see. Mathematically the straight length is defined as:

$$\mathrm{SL} = \sqrt{\left(\mathrm{x^b(t_{max})} - \mathrm{x^b(t_{min})}\right)^2 \; + \; \left(\mathrm{y^b(t_{max})} - \mathrm{y^b(t_{min})}\right)^2 + \left(\mathrm{\Delta Z(t_{max})} - \mathrm{\Delta Z(t_{min})}\right)^2} \tag{5.7}$$

- The **curvilinear length** corresponds to the sum of the 3D distance between two consecutive barycenters. The difference between the curvilinear length and the straight length tells us about the curvature of the track. We note N the number of activated timeslices, so that the curvilinear length is defined as:

$$\mathrm{CL} = \sum_{\mathrm{j=1}}^{\mathrm{N}} \sqrt{\left(\mathrm{x^b(t_j)} - \mathrm{x^b(t_{j-1})}\right)^2 \; + \; \left(\mathrm{y^b(t_j)} - \mathrm{y^b(t_{j-1})}\right)^2 + \left(\mathrm{\Delta Z(t_j)} - \mathrm{\Delta Z(t_{j-1})}\right)^2} \tag{5.8}$$

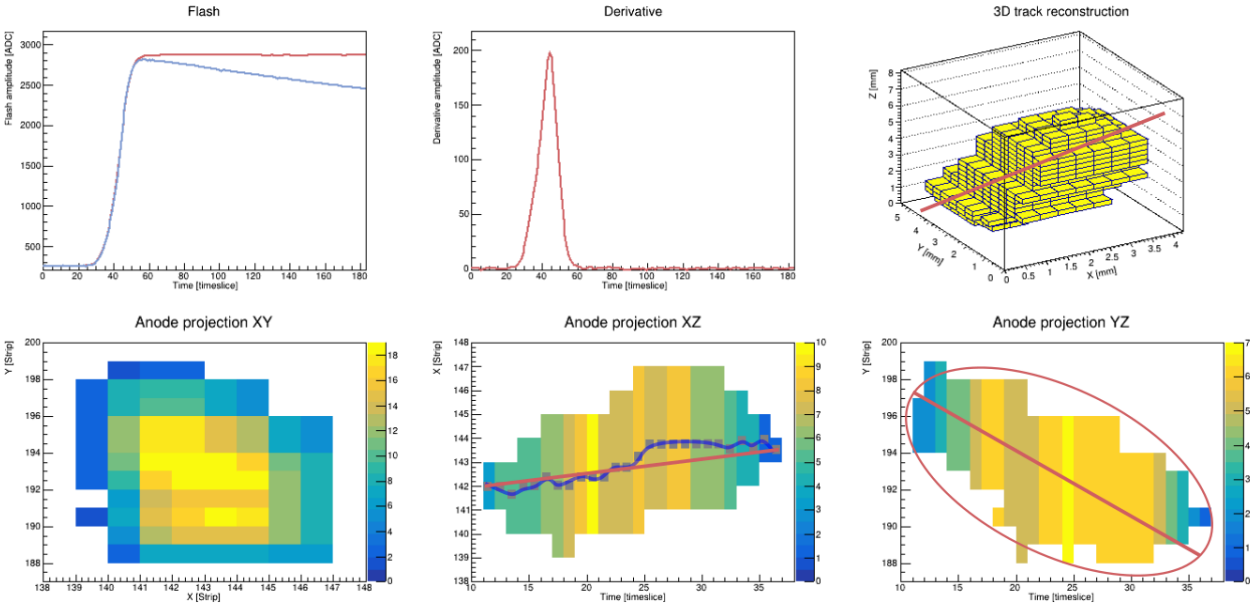

Figure 5.7: Presentation of the 3D track reconstruction methods on a measurement of a proton recoil with a kinetic energy 16.6 keV produced by scattering with a neutron of 27 keV. The 3D line fit method is presented as a red line in the upper right plot showing the 3D track reconstruction. For visual reasons the barycenter and the ellipse methods are represented in 2D projections. The barycenter method is presented in the bottom central plot: the curvilinear length is drawn in blue whereas the straight length is in red. The ellipse method is shown in the bottom right plot: the principal axis of the ellipse is determined by a robust fit method.

3D line fit

Another approach for reconstructing the track is to perform a linear regression in 3D. The parametric equation for a 3D line is defined thanks to 4 independent parameters:

$$\begin{cases} x = p_0 + p_1 \cdot t \\ y = p_2 + p_3 \cdot t \\ z = t \end{cases} \tag{5.9}$$

where t is a free quantity that parametrizes the line. We determine the best set of parameters p_i that minimizes the distance of each point of the vector $(\mathbf{X}, \mathbf{Y}, \Delta Z)$ to the 3D line. After this regression we can determine the straight length as well as the polar and the azimuthal angles. While this approach is the most direct method for accessing the track information, it is also the one with the largest uncertainties since the 3D fit can sometimes fail. For instance, for a Gaussian-like cloud, the initial conditions of the fit will bias the obtained 3D line, leading sometimes to a 90° error. This method must then be carefully used.

Ellipse

For a straight track or a short curved track, the primary electrons cloud at the Micromegas grid can be described by an ellipsoid. The properties of the track could then be obtained by fitting an ellipsoid to the data. We have realized that we obtain a better angle description and a more robust code when we decompose the problem into 2D situations: instead of fitting an ellipsoid to a 3D histogram, we fit two ellipses to the 2D projections in the (X-Z) and in the (Y-Z) planes. The properties of the ellipsoid can be reconstructed afterwards from the ellipse parameters. For instance, the polar angle of the ellipsoid, θ, can be expressed as a function of the polar angle of the (X-Z) ellipse, θ_x, and the one of the (Y-Z) ellipse, θ_y:

$$\tan^2\theta = \tan^2\theta_x + \tan^2\theta_y \tag{5.10}$$

An ellipse is defined by a second-order polynomial equation and a constraint:

$$ax^2 + bxy + cy^2 + dx + ey + f = 0 \qquad \text{for} \quad \mathrm{b}^2 - 4\mathrm{ac} < 0 \tag{5.11}$$

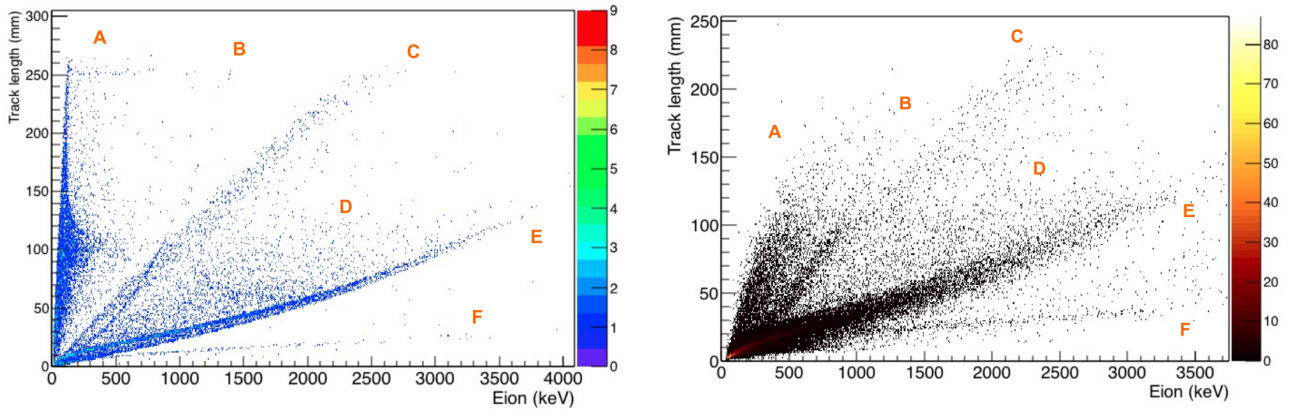

Figure 5.8: Straight length as a function of the ionization energy for nuclear recoils produced by a mono-energetic neutron field of 15 MeV. The gas mixture is composed of He + 5% CO_2 at 700 mbar and is dedicated to high energy measurements. The letters identify the branches of the expected particles. The branches B, E, and F correspond to nuclear recoils that released their entire kinetic energy in the volume, respectively for protons, ^{4}He, and ^{12}C/^{16}O that are not resolved individually. The other branches are explained by particles that escape the volume before releasing all their energy. Figures extracted from [321].
Left: simulation with the GEANT4 toolkit. Right: MIMAC measurements.

There are 5 parameters that, under a proper change of variables, can be related to physical properties: the two coordinates of the center of the ellipse, the lengths of the semi-major axis, and of the semi-minor axis, and the polar angle. We have implemented an ellipse fit of the data following the approach of [320]. This method is so far the one that gives the most accurate angle reconstruction for millimeter tracks.

5.3 Particle identification

Several types of particles can create a signal in the detector: cosmic particles such as muons, neutrons, and neutrinos; particles from radioactive decay as the radon progeny producing alphas, electrons, and nuclear recoils; or ambient background as photons and electrons. Each particle has its own signature and its identification is a crucial point for rare events searches. For the moment, we have decided to operate without any shielding to better understand the background since we are able to extract the nuclear recoils, that we are looking for, from the other particles.

The strength of MIMAC lies in the numerous observables it provides, leading to a precise particle identification as well as an efficient background rejection. The observables are constructed either from the Flash signal, either from the strips, or from a combination of them. We here do not list the observables used in MIMAC, since they are numerous and continuously optimized for the experiments, and we refer to [177] for a description of the main ones. As an example, the curvilinear length and the straight length presented in the previous section are two observables frequently used.

5.3.1 Particle signatures

The primary electrons cloud produced by muons, electrons, or nuclear recoils are all different and they depend on the stopping power introduced in Chapter 4. The signature of each particle in the MIMAC detector will then have specificities, the main differences being observed on the track length, the ionization energy per timeslice, or the charge density of the track. It is also possible to discriminate nuclear recoils of different masses. An example is presented in Figure 5.8 that compares predictions from GEANT4 simulations to measurements for the nuclear recoils produced by a mono-energetic neutron field of 15 MeV in a He + 5% CO_2 gas mixture at 700 mbar. The straight length as a function of the ionization energy enables clearly identifying branches: the lighter the recoil, the longer the track.

In Figure 5.9 we present some typical signatures of four types of particles that we frequently observe in the detector when operating at high gain ($> 10^4$). Figure 5.9a can be identified as a muon. The muon

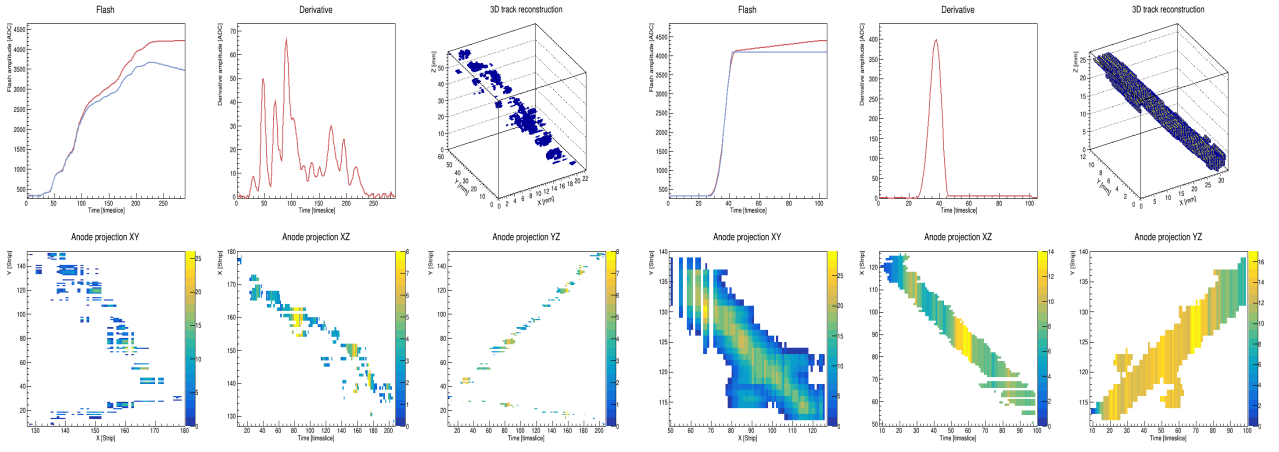

(a) Muon with the emission of a delta electron

(b) Alpha

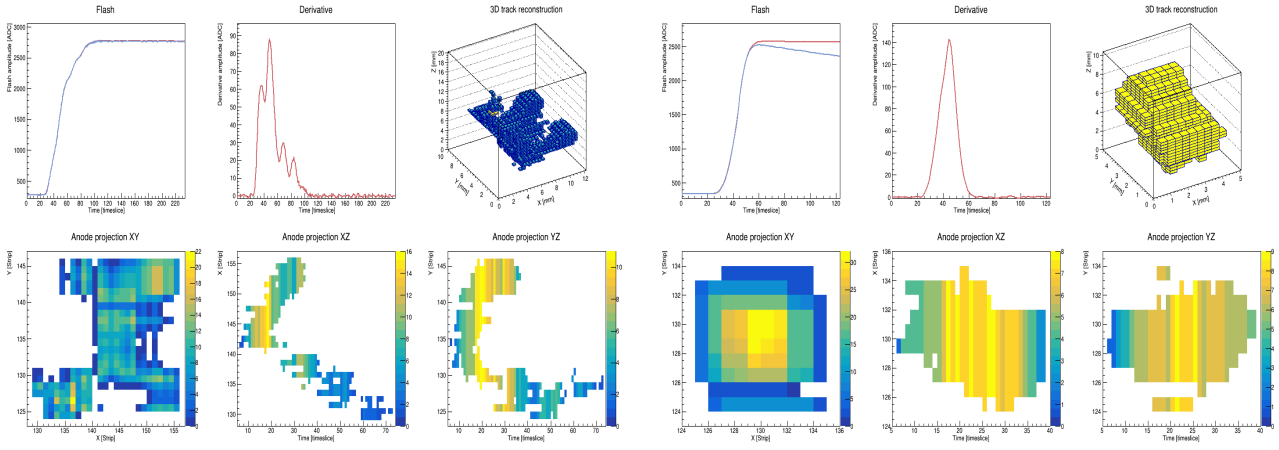

(c) Electron

(d) Proton

Figure 5.9: Typical signatures of four types of particles measured in the *High-gain gas* at 30 mbar.

tracks are long and straight, and they are composed of multiple clusters of small energy, as one can see on the derivative signal composed of many peaks. On the (Y-Z) projection one can observe a second track perpendicular to the main one. We identify it as an electron track and it is probably a delta electron ejected by the muon. Due to the kinematics, delta electrons are usually ejected perpendicularly to the muon trajectory. The muons dominate the background in our laboratory experiments but they can easily be identified due to their clustering and consequently they can be discriminated. An alpha particle is shown in Figure 5.9b. The decay of a radon progeny in the active volume or on a surface of the detector emits an alpha particle of a few MeV, that will saturate the Flash signal. The alpha tracks are typically thin, long, straight, dense, and homogeneous. An electron of 10 keV is presented in Figure 5.9c. Its typical signature is a curved and semi-dense track. Finally we present a proton track in Figure 5.9d that can be identified, as every nuclear recoil in the keV-range, from the dense and short track, with no hole on the strips and, as a consequence, a clear Flash signal with an almost Gaussian peak on the derivative.

5.3.2 Electron-recoil discrimination

We have presented the main characteristics of the signatures of different particles. The next step consists in implementing a systematic identification of nuclear recoils to reject background events. The main challenge is to discriminate the electrons, produced for instance by a gamma background, to the nuclear recoils in the low energy region, *i.e.* below 30 keV. The procedure for the electron-recoil discrimination is the following: (1) we apply some minimal cuts to remove the events that are

surely not recoils; (2) we define a set of discriminating observables and we apply cuts on them, either in a sequential way, either by the use of machine learning; (3) we estimate the performance of the discrimination.

The performance of the discrimination is evaluated by two quantities. The first one is the *rejection power*, *i.e.* the ratio between the total number of background events over the ones that pass the cuts. It determines the ability to reject the background. The larger the rejection power, the better the discrimination. The second quantity is the *acceptance*. It is defined as the ratio between the number of recoils that pass the cuts over the total number of recoils. It quantifies the proportion of recoils passing the cuts. A compromise must be found that maximizes the acceptance and the rejection power at the same time.

In the *Mimac gas* at low gain, we have shown that good electron-recoil discrimination was reachable with a rejection power of 10^5 [177] for fluorine recoils produced in a 565 keV mono-energetic neutron field. Recently, we have demonstrated that a similar rejection power could be obtained at high gain for proton recoils produced in a neutron field of 27 keV with an acceptance of about 50% [179].

Electron-recoil discrimination from machine learning

While the experimental details of the mono-energetic neutron measurement at high gain mentioned above will be presented in Chapter 8, we will now present the electron-recoil discrimination that we have performed. We here only need to mention that we have two sets of data: one that only contains background events, that we call "background only"; and another set that contains the same background plus of the neutron field. We call this second set of data "background + signal".

We start by applying some minimal cuts: (1) at least two timeslices with coincidences are required; (2) single cluster is detected on the Flash and its amplitude is larger than 96% of the total amplitude; (3) the straight length as a function of the energy, SL(E), must remain compatible with proton recoils, the cut on this quantity being determined empirically from the branches observed in a 2D histogram, as in Figure 5.8. These minimal conditions, which are always fulfilled for protons recoils, remove 97.6% of the events.

We make use of machine learning to discriminate the recoils from the background. To do so, we start by training an algorithm on a set of data composed both of "background only" and of "background + signal" where we tell the algorithm from which dataset comes the event. During this training period the algorithm has n variables whose behaviour will be observed in order to determine a cut in a n-dimensional space. Once the algorithm has found a way to separate the signal from the background, we give it a dataset that it has never seen. In this test phase, the algorithm classifies the events as signal or background, and we evaluate its performance (rejection power and acceptance). We also test a possible over-training effect, *i.e.* when the algorithm has too many degrees of freedom leading to an artificially too good rejection power on the training data but that cannot be extrapolated on the test sample.

We decide to make use of Boosted Decisions Trees (BDT). A decision tree is a series of binary cuts. For a single event, the tree tests all input variables and determines a succession of cuts that optimizes the discrimination. Several trees operate in parallel, all of them working on the same dataset, and the best cuts are chosen "democratically". The decision trees are *boosted* because weight is given to each event depending on the largeness of the classification error. The principle of the boost consists in giving more importance to the events for which the discrimination is difficult. We train, test, and apply the BDT on the data by means of the TMVA software [322]. The training and the test samples are both composed of 15000 events, half of them being background events, letting 46231 signal events to apply the BDT.

We have selected 12 observables for which we expect a different behaviour for electrons than for recoils. These observables are for instance the number of holes in the track divided by the energy, or also the asymmetry of the Flash derivative. The data are pre-processed to reduce the correlation between the 12 observables. This is done in two steps. We start by transforming each observable into a uniform distribution by using its cumulative distribution function. Then, this uniform distribution is transformed into a Gaussian of zero mean by applying the inverse error function. The second step

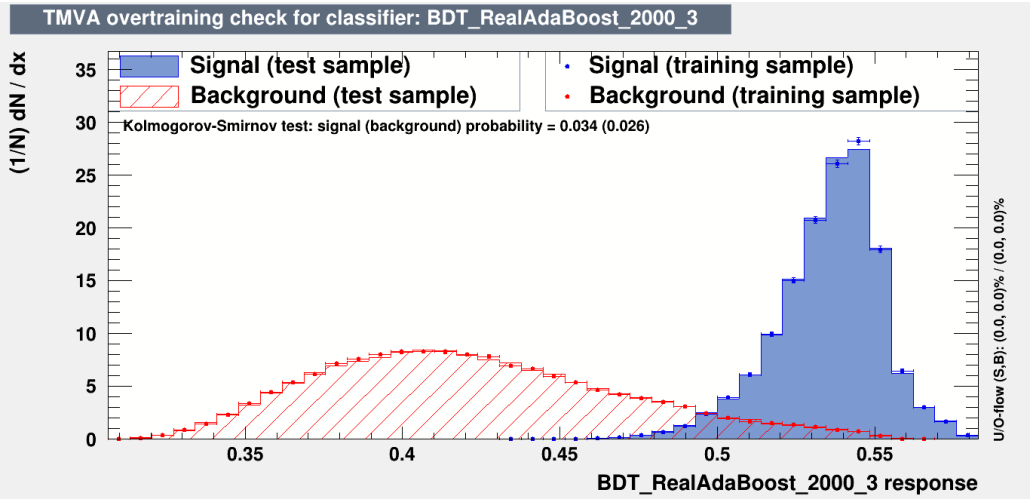

Figure 5.10: Response of the BDT on the train and the test samples.

of the pre-processing is a decorrelation which consists in diagonalizing the correlation matrix of the observables and then linearly transforming each variable from this diagonal matrix.

After such preparation, we train 2000 BDTs with a maximal depth of 3 and a boost of type RealAdaBoost proposed by the TMVA toolkit. These parameters have been determined empirically by comparing a dozen of configuration and by choosing the one that gives the best performance on the test sample.

For each event, the BDT determines a parameter, called *classifier*, that is supposed to be different for signal and background. The histograms of the classifier are presented in Figure 5.10 for the training and the test samples. The first remark is that the histograms for both samples are compatible, meaning that the BDT is not over-trained. We observe that for a classifier value above 0.57, the BDT will reject 100% of the gamma background. On the other hand, such a cut will also reject a certain number of recoils, although this number is not directly quantifiable because the signal run contains both recoils and background. By refining the analysis, we notice that a cut at 0.557 allows highlighting the proton branch on a histogram of the straight length as a function of the ionization energy.

Finally, we evaluate the performance of the electron-recoil discrimination. The rejection power can be determined on the BDT test sample and, including the minimal cuts, we obtain 8×10^4. The expected number of recoils can be roughly estimated from the event rate difference between the background run and the measurements in the neutron field. The comparison between this expected number and the effective number of recoils after application of the BDT (2300 events) gives an estimation of the BDT acceptance: about 50% of the proton recoils are kept. For directional analyses, the exclusion of recoil events does not represent an issue except that it decreases the statistics.

In this particular case, for the mono-energetic neutron measurement at 27 keV presented in Chapter 8, the electron-recoil discrimination was challenging. The two main reasons of this challenge was the low-energy measurements, with millimeter tracks and a few hundred of primary electrons, and the large background rate: we estimate that the nuclear recoils represent only 0.2% of the measured events. The BDT approach presented above is efficient and it determines the rejection power, but it can also introduce some bias on the energy or the angles, as we observed for a mono-energetic neutron field of 8 keV [179]. In such a case, it is sometimes preferable to implement a manual discrimination by determining empirically a succession of cuts.

5.4 MIMAC development

The MIMAC project aims to build a m^3 detector in the near future, based on a matrix of bi-chamber modules as detailed in Chapter 4. A first bi-chamber prototype operated for almost 6 years in the Underground Laboratory of Modane (LSM according to the French acronym), from June 2012 to February 2018. This operation was the first step to validate the MIMAC strategy of detection as well

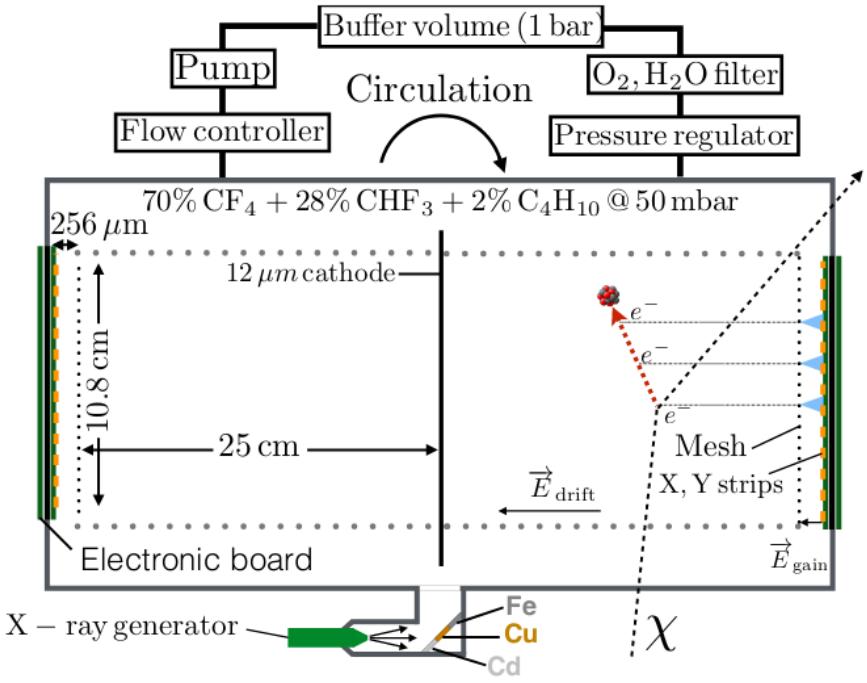

Figure 5.11: A schematics of the bi-chamber module operating at the LSM for almost 6 years. The two MIMAC chambers are joined by a common aluminized mylar cathode of 12 μm thickness. The chamber is connected to an X-rays generator used for calibration. A gas circulation system ensures the stability of the detector. Figure extracted from [178].

as the stability of the detector. A schematics of the bi-chamber module is presented in Figure 5.11.

Meanwhile, the MIMAC team has developed a new detector of $35 \times 35 \times 25$ cm^3 with 1792 strips based on resistive Micromegas technology and an improved radiopurity of the materials. This new detector, which is still under experimental validation at the time of writing, would be installed on the bi-chamber module. By duplicating 16 times the bi-chamber module into a matrix of chambers, the volume of detection would be equivalent to 1 m^3. When the time will come to build a large detector, the best directional technology should be used, whether it be the MIMAC technology or any other one. As an example, a 50 m^3 MIMAC-like detector would reach a 3σ sensitivity at 90% C.L. down to 10^{-5} pb for spin-dependent cross-sections [166].

5.4.1 MIMAC in the Underground Laboratory of Modane

The LSM is an underground laboratory "platform" of the LPSC. The LSM is located in a tunnel in between France and Italy, below 1700 m of rock that is equivalent to 4800 m of water. The rock significantly reduces the amount of cosmic particles that contribute to the background. The cosmic neutrons are completely stopped by the rock so the neutrons in the laboratory are only due to the natural radioactivity. The rock of the cavern presents natural contaminations to ^{238}U (0.84 ppm) and ^{232}Th (2.45 ppm) that have been measured by spectroscopy [323], corresponding to a fast neutron flux of 4×10^{-6} neutrons/s/cm^2 for neutron energies between 2 MeV and 6 MeV. These neutrons are produced by spontaneous fission or by nuclear reaction (α, n) on the wall of the cavern. The cosmic flux of muons is measured around 4 muons per day per m^2, so the rock reduces the flux by about 2×10^6. While the muons can be identified in the detector, they will also produce neutrons, called *cosmogenic neutrons*, by interactions with the detector materials or with the surrounding rock.

Since neutrons induce a similar signal than WIMPs, the neutron background must be under control. Quentin Riffard has studied in details [131] the neutron event rate in the LSM, as well as its anisotropies and the influence of the potential of discovery of a 1 m^3 MIMAC detector. He observed anisotropy in the cosmogenic neutron flux due to the shielding of the SEDINE experiment located close to MIMAC. He has also demonstrated that the cosmogenic neutron flux is 5×10^3 lower than the flux of neutrons

produced in the rock. The neutron event rate in a MIMAC detector containing 146 g of ^{19}F, without any shielding, would be 620 recoils/year. Finally, he has also shown that the anisotropies of the neutron background flux only affects in a negligible way the directional discovery potential of MIMAC.

Another source of contamination is the natural presence of radon in the laboratory air. The radon rate varies in time since it depends on the weather and the tunnel ventilation system. The LSM has installed a Radon Trapping Facility based on charcoal that reduces the radon level in the air by three orders of magnitude, from 20 Bq/m^3 down to 10 mBq/m^3 [324]. The decays of ^{222}Rn and ^{220}Rn, and consecutive daughters, produce α-particles of a few MeVs and nuclear recoils with kinetic energies around 100 keV, called Radon Progeny Recoils (RPR).

The RPR could be misidentified as WIMP-induced nuclear recoils so one must be able to discriminate them. We distinguish between volume events, for which the joined detection of the RPR and the α saturates the detector, from surface events, where the decay occurs on the cathode or the anode, with a possible detection of the RPR and the α in two consecutive chambers. These coincidence events led to the detection of RPRs in the bi-chamber module installed at the LSM [178], in particular the detection of ^{210}Pb and ^{214}Pb nuclear recoils with ionization energies of 45.85 ± 0.5 keV and 32.85 ± 0.28 keV, respectively, in the *Mimac gas* at 50 mbar. This analysis concluded that the MIMAC detector effectively identifies the RPRs and can then remove them from the background. The detection of tracks of RPRs can be used as a benchmark for directional detectors. We also note that `SRIM` predicts that all daughters of the radon depose more than 44 keV ionization energy in the *High-gain gas*. Although `SRIM` overestimates the IQF in gases (*c.f.* Section 4.2.2 or Chapter 7), the RPRs will likely saturate the detector in the High-gain configuration (with a maximal energy range around 20 keV), so the radon contamination should not impact the efficiency of our identification of WIMP-induced recoil.

The bi-chamber module has a gas circulation system that ensures the quality of the gas and then plays an important role in the stability of the detector. A buffer volume is filled with the detection gas mixture at a pressure slightly above the atmospheric pressure to avoid exterior contamination. The gas in the detector is continuously renewed via a circulation system going through the buffer volume. An oxygen filter traps the few oxygen impurities (of the order of ppm) of the circulation system in order to limit the attachment process already discussed. A charcoal filter at 258 K reduces the amount of radon. The low temperature of the filter also enables to condensate and eventually to stock the water vapour of the circulation loop. Thanks to this system, the bi-chamber module has operated for almost 6 years with gain variations remaining below 1.5%.

At the time of writing we prepare the bi-chamber module for a new run at the LSM. We have placed two 512 μm detectors, one of them using the new technology described in the following subsection, and we will operate in the *High-gain gas* at 30 mbar. This run aims to study the background in the underground laboratory in order to compare it with the background measured at the surface, for a description in 3D of the background below 20 keV.

5.4.2 Low-noise 35 cm detector

Directional searches for low-mass WIMPs (below 10 GeV) require to operate at high gain (above 3×10^4) with a low energy threshold (below 100 eV) and with low-radioactivity materials. For this purpose, the team has developed a new detector for MIMAC, called *low-noise* detector, based on the resistive Micromegas technology [325, 326]. A schematics of the low-noise Micromegas is represented in Figure 5.12. The anode is covered by a single thin resistive layer made of DLC with a surface resistivity $R_\square \simeq 100$ MΩ/sq. The resistive layer is deposited on an insulating volume, made of kapton and coverlay, in which are placed the copper strips, the Y strips being located deeper than the X strips. The signal is induced on the strips via capacitive coupling. The width of the strips is adapted, 130 μm for the X strips and 300 μm for the Y strips, to ensure that the current induced by a moving charge in the gap is of comparable order in both strips. However, since the Y strips are larger, they are more sensitive to an intrinsic electronic noise so the auto-calibration sets a detection threshold that is larger on the Y strips than on the X strips. The strip pitch and the characteristics of the grid remain unchanged with respect to the bulk detector.

The signal formation on the anode of a resistive Micromegas differs from the bulk case. The weighting field acquires a time dependence, so the Ramo-Shockley theorem Eq. (4.22) must be extended

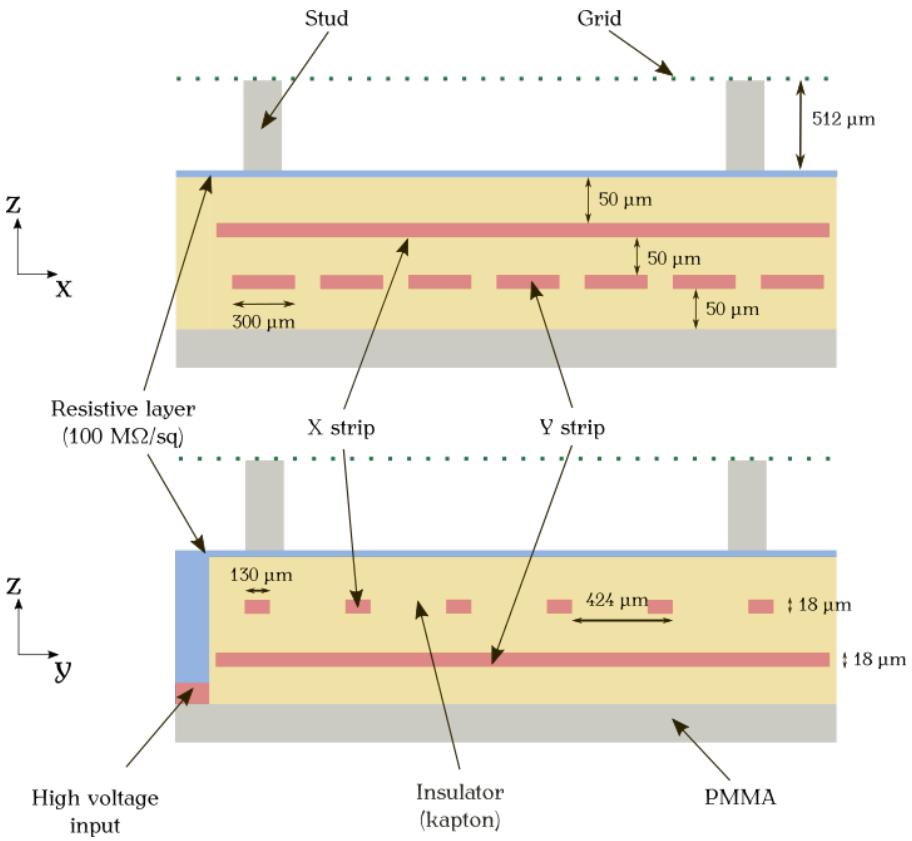

Figure 5.12: Schematics of the Micromegas of the *low-noise* detector. A thin resistive layer of DLC covers the anode and the strips are located inside an insulator. Since the Y strips are lower than the X strip, their widths are increased so that a moving charge in the gap induces a comparable current in both X and Y strips via capacitive coupling.

to an integral expression [327]:

$$i_k(t) \;=\; \sum_n q_n \int_0^t dt'\, \mathbf{E}_k^w\big(\mathbf{r}_n(t'),\, t-t'\big) \cdot \mathbf{v}\big(\mathbf{r}_n(t')\big) \tag{5.12}$$

There is another difference in the signal formation compared with the bulk case. The Ramo-Shockley theorem tells us that a moving charge in the gap induces a charge in the resistive layer. The propagation of the induced charge in the resistive layer can be described by the Telegraph equations with null-inductance [328]. It tells us that the induced charge will be spread in the layer, almost gaussianly, with a time constant $\tau \sim \mathcal{O}(1\ \mu\text{s})$ and the charge is eventually evacuated towards the high voltage (or the ground depending on polarization) entrance point, so at a corner of the anode. The charge density is sufficiently diluted during the spread in the resistive layer so that it has a limited influence on two consecutive strips.

The resistive anode presents several advantages for low energy searches compared to the bulk Micromegas:

- **Spark-resistant**. When the number of secondary charges in the gap exceeds the Raether limit, around 10^7, sparks can occur. The detector then gets out of the proportional regime and it can be damaged. Such a large number of charges can be obtained at high gain for a dense primary electrons cloud. In the new configuration, the charges are accumulated in the resistive layer, locally decreasing the electric field and consequently reducing the risk of developing sparks [325]. In other words, the *low-noise* detector can reach a larger gain than the bulk one.

- **Simplified design**. In this configuration, there is no connector on each strip compared to the bulk case which was a limiting factor for producing pixelated anodes larger than 10×10 cm^2. Note also that in case a spark occurs, which is rare as explained above, the spark intensity will

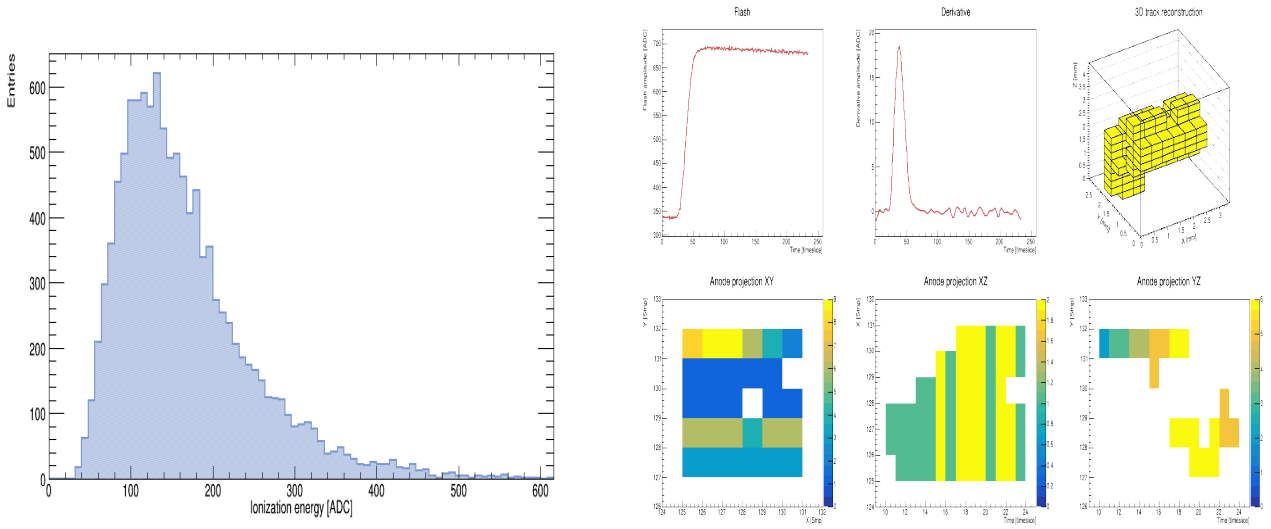

Figure 5.13: Measurements of 150 eV electrons sent by Comimac in the *High-gain gas* at 30 mbar when operating with the *low-noise* detector. The acquisition threshold was set to 28 eV. Left: energy spectrum. Right: example of a an event.

be attenuated before reaching the electronic board. For this reason, we have removed some protections on the electronic card, reducing consequently the intrinsic noise of the strips.

- **Radiopurity**. The radiopurity of the materials has been improved with respect to the bulk detector. The anode is made of layers of kapton and coverlay and it lies on a PMMA stand instead of PCB in the bulk detector.

- **Low threshold.** The intrinsic noise of the detector has been reduced in order to reach detection thresholds below 30 eV.

A first low-noise detector of 10.8×10.8 cm^2 has been finalized in 2017. To illustrate its performance, we present in Figure 5.13 the measurements of 150 eV electrons sent by Comimac in the *High-gain gas* at 30 mbar. One can see in the left panel that the energy spectrum is non-Gaussian due to the fluctuation of the number of primary electrons during the ionization process. For these measurements the acquisition threshold was set to 28 eV to remain above the electronic noise. The reconstruction of the tracks in 3D has been possible for half of the events, an example is presented in the right panel of Figure 5.13. The proper measurements of 150 eV electrons is an achievement of the *low-noise* detector since it requires operating at a very high gain ($\sim 10^5$) with a low detection threshold.

We also mention a change in the polarization of the detector. In the previous bulk technology, the anode was set to the ground while the grid and the cathode were biased to high voltages. In the *low-noise* detector, the grid is set to the ground, reducing the electronic noise on the Flash. In this way, one can also reduce the value of the high-voltage applied to the cathode and consequently limit the risk of electrical breakdown.

The development of the *low-noise* detector was the first step towards an upgrade of MIMAC. The resistive Micromegas technology has been used to build a larger detector with an active area of 35×35 cm^2 while keeping a 25 cm drift space. This new chamber has a volume of 30 L, and will lead to a m^3 detector when assembled into the matrix of chambers. The detector has a total of 1792 strips, 896 in both directions. To operate the 35 cm detector, the team has upgraded the electronics and the acquisition system. A picture of the electronic card associated to the 35 cm detector is shown in Figure 5.14. At the time of writing, the first prototype of the detector and the electronic card have been developed and they are currently being tested.

5.4.3 Cathode signal

As already discussed, a limitation of the MIMAC detector is the lack of event localization in the Z-direction. We only measure the time of arrival of the charges relatively to the first one, from which we

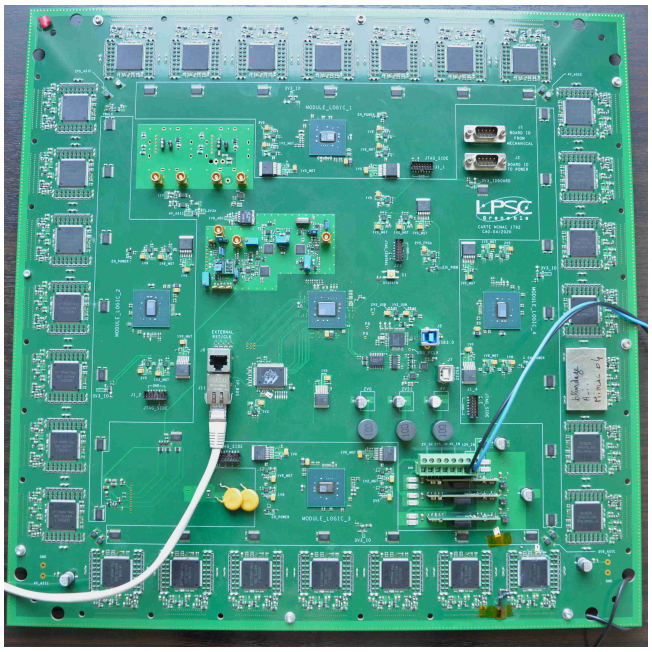

Figure 5.14: Picture of the electronic card of the 35 cm detector. 7 ASICs are located on each side and they are controlled by 4 side-FPGAs. A central FPGA is in charge of the synchronization and the communication with the acquisition software.

can reconstruct the track in 3D. Positioning the track in the volume, *i.e.* determining the Z-coordinate of the first interaction, would provide valuable information. It would for instance enable quantifying the influence of diffusion and fiducializing the volume to reject surface events such as the RPRs.

The cathode signal is one possibility to cope with this issue. According to the Ramo-Shockley theorem, the motion of the primary charges in the active volume instantaneously induces a signal on the cathode. The electrons drift towards the anode and once they reach the grid they produce avalanches inducing a signal on the grid and on the anode. Let us note Δt the time difference between the signal induced on the cathode and the Flash signal. We consider that the primary electrons quickly reach their maximal drift velocity, so the Z-coordinate of the interaction is proportional to the transit time of the electrons: $Z_{\text{initial}} = v_d \Delta t$. Knowing the drift velocity in the gas, the measurement of the cathode signal then enables the absolute localization of the track.

As a first step we must then measure the drift velocity of the electrons. The team developed an experimental setup, presented in Figure 5.15, in which an alpha source is placed on a rod at a known distance from the cathode. The rod can be moved to change the position of the source. We use a ^{241}Am source emitting alpha particles of 5.37 MeV, the source being collimated so that the particles are emitted parallel to the cathode. We measure the signal induced on the cathode by the primary charges and the one induced on the grid by the secondary charges. A measurement of the drift velocity in the *Mimac gas* has been performed by keeping the drift electric field constant while varying the Z-position of the alpha source. The team measured a drift velocity 12% lower than estimated by `Magboltz` for a reduced electric field of $E/N = 12.5$ Td [329]. The differences with respect to `Magboltz` are attributed to experimental conditions, in particular to impurities in the gas mixture or a lack of collimation of alpha particles. We consider the `Magboltz` prediction as the drift velocity that one would have in a metrological installation.

The *in situ* measurement of the drift velocity is an important element to determine the quality of the gas and properly reconstruct the Z-component of the track. The cathode signal is then a powerful tool for determining the Z-position of the event and for 3D track reconstruction.

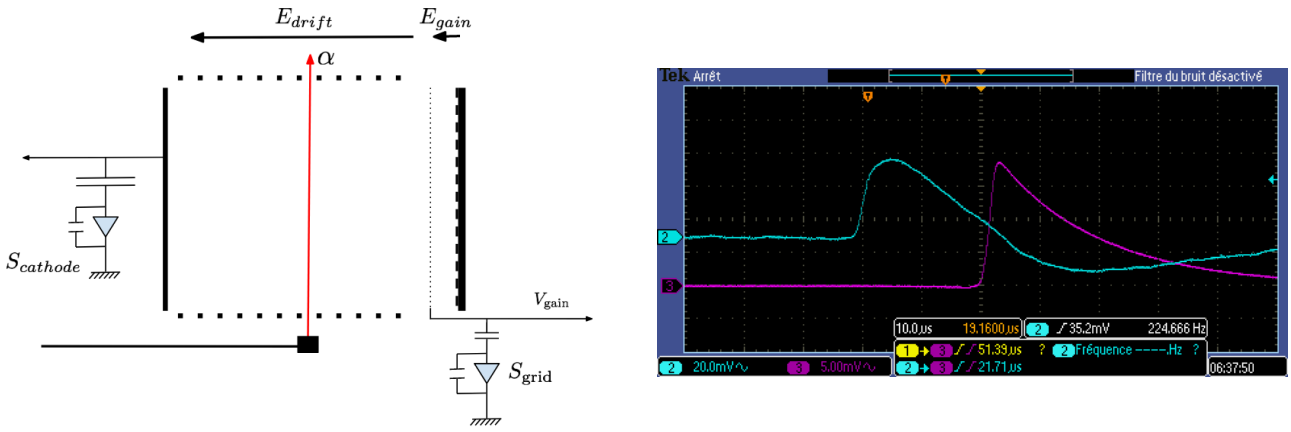

Figure 5.15: Left: schematics of the experimental setup to measure the drift velocity of the electrons from the cathode signal. An alpha source is placed at an adaptable but known distance from the cathode. Figure extracted from [131].
Right: oscilloscope screenshot showing the average of 512 signals. The cathode signal is in blue and the grid signal is in purple. A delay has been included to observe them in the same time window.

5.5 Facilities

We conclude this chapter by introducing three facilities used either to determine the performance of MIMAC, or to perform important measurements as for instance the IQF or neutron spectroscopy.

5.5.1 Comimac

Comimac definitely is the facility that underlies the work presented in this thesis. I had the chance to participate in about twenty measurement campaigns with Comimac, the richness of the data leading to the development and the validation of `SimuMimac`, and opening the window towards ALP searches and directionality in the low energy region.

Comimac is a table-top accelerator that produces ions or electrons of known kinetic energy from a few tens of eV up to 50 keV. It has been developed by the MIMAC team at the LPSC and a clear description of the facility can be found in [330]. Comimac uses an Electron Cyclotron Resonance Ion Source (ECRIS) that produces a plasma in its resonant cavity using a low-power microwave (5 W – 2.45 GHz). A voltage V_{ex} is applied to extract either electrons or ions (depending on the polarity) with kinetic energy given by $E_K = qV_{\text{ex}}$. While electrons can be obtained from any gas mixture placed in the source, the situation differs for ions depending on the species we are interested in. For instance for extracting protons, we usually place a 50% mixture of H_2 and He, the helium acting as a carrier gas to efficiently break the H_2 molecule: the electrons of the helium molecule will be excited by the cyclotron resonance and will acquire sufficiently high energy to break the H_2 molecule into protons.

In order to send the particles into a detector, Comimac is coupled with a MIMAC chamber having 5 cm of drift. The coupling is performed thanks to a 1.45 μm hole that ensures pressure independence between the Comimac facility ($\sim 10^{-5}$ mbar) and the MIMAC chamber. A picture of the experimental setup is presented in Figure 5.16. The particles enter the MIMAC chamber at the cathode level, always at the same position, and they are parallel to the Z-direction. Some focusing electrodes are placed after the ECRIS in order to align the ion (or electron) beam with the interface hole. These electrodes produce an electric field transverse to the beam direction in order not to alter the kinetic energy of the particles.

When applying a positive voltage several types of ions are extracted. For instance for a gas mixture of H_2 and He one expects to extract H^+, He^+, but also heavier species such as N^+ or H_2O^+ due to water vapor contamination and surface out-gassing in the source. According to the Lindhard theory [298] of quenching, the proton is the particle that releases the largest proportion of its kinetic energy through ionization. We thus identify the proton as the peak with the highest ionization energy. The identification of heavier species can be more difficult, for instance for separating ^{19}F from water

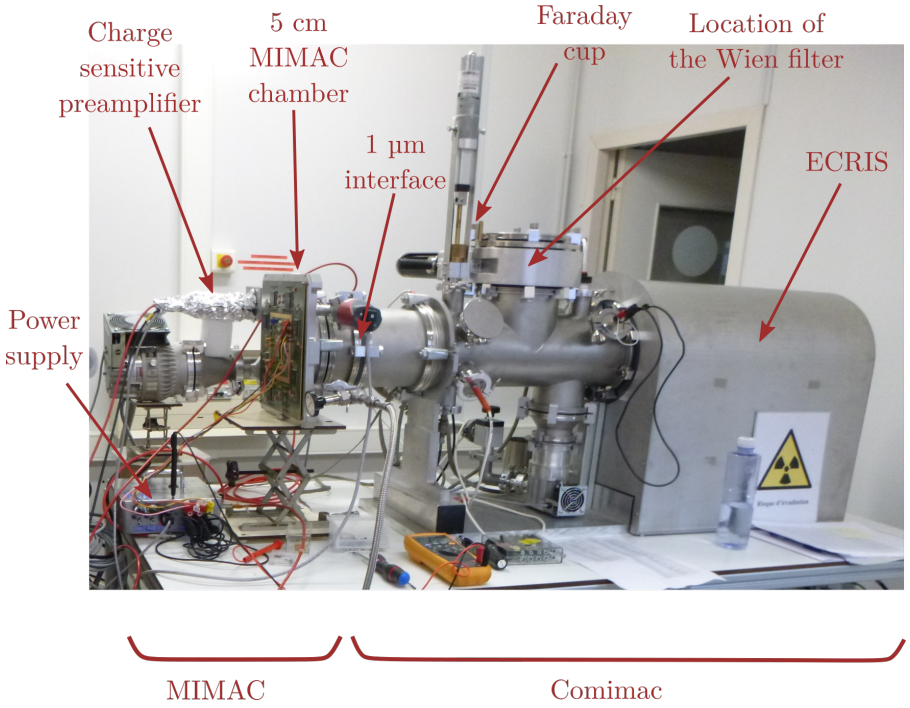

Figure 5.16: A picture of the experimental setup coupling a MIMAC chamber to Comimac. The ions and the electrons produced by Comimac enter the detector at the cathode level.

vapour. To cope with this issue, we can add a Wien filter to the facility. The Wien filter combines a magnetic field, produced by permanent magnets, and an electric field. The magnetic field will separate the species according to their charge over mass ratios, q/m. The electric field intensity is then tuned in order to align the desired ion specie with the hole that interfaces Comimac with a MIMAC chamber. An example of an energy spectrum obtained for 14 keV fluorine ions in the *Mimac gas* using a Wien filter is presented in the left panel of Figure 5.17. One can see a Gaussian peak with an energy resolution of FWHM/μ = 34%, demonstrating the purity of the ion beam sent by Comimac in the MIMAC chamber.

Energy loss in the Comimac interface

The MIMAC chamber is coupled with the Comimac beamline through a hole that has been drilled by a laser in a foil of stainless steel of thickness 13 μm. The ions and the electrons sent by Comimac pass through the hole and can lose part of their energy by scattering with the gas in the hole before reaching the active volume of detection. This energy loss must then be quantified in order to determine the kinetic energy of the particle when it enters the MIMAC chamber. We characterized the quality of the hole with a Scanning Electron Microscope (SEM) at the NanoFab technological platform of the Néel institute in Grenoble. We measured a circular hole of diameter 1.45 ± 0.06 μm.

With the hole properties in mind, the MIMAC team has performed simulations of the energy lost in the interface. The simulations are decomposed into two steps. Firstly, using a `Molflow+` [331] simulation to determine the profile pressure inside the hole. `Molflow+` is a Monte Carlo simulation tool developed by CERN for high vacuum studies. Secondly, using the obtained pressure profile as input for simulating the particle transport inside the hole. This second simulation is performed with `Casino` [332] for the electrons and with `SRIM` for the ions. In both cases, the initial kinetic energy of the particle is set to a value and it is compared to the kinetic energy of the particle once it escapes the hole. This way we can approximate the amount of energy loss in Comimac's hole.

The simulations show that the energy loss increases with the pressure in the MIMAC chamber and it also increases when the particle energy decreases. An example is presented in the right panel of Figure 5.17 for electrons and protons in 100 mbar of methane, a gas in which we performed an IQF measurement that will be presented in Chapter 7. One can see that the energy loss in this situation

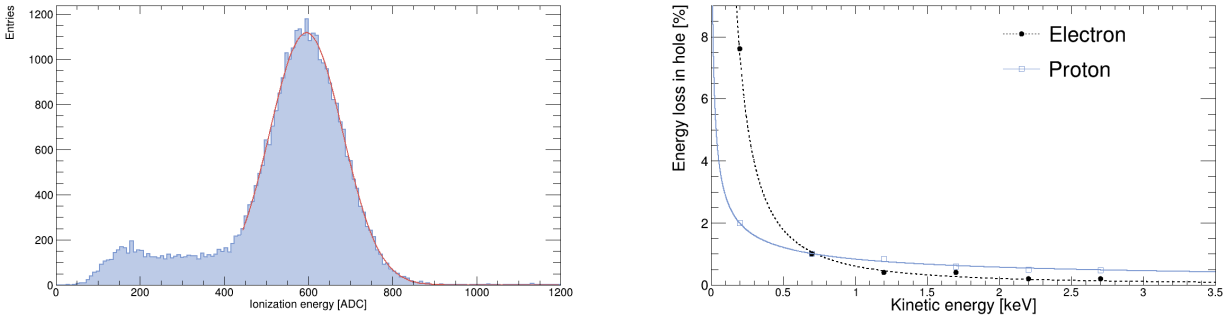

Figure 5.17: Left: energy spectrum of fluorine ions with kinetic energies of 14 keV sent by Comimac in the *Mimac gas* at 50 mbar while using the Wien filter calibrated to select fluorine ions. A Gaussian function has been fitted on the spectrum.
Right: simulations of the energy loss in the interface between Comimac and a MIMAC chamber in 100 mbar of methane for protons and for electrons.

remains below 1% for kinetic energies above 1 keV. However the situation changes at larger pressure: for 1keV electrons in methane the energy loss is 0.6% at 100 mbar, 1.6% at 300 mbar, and 5.4% at 1000 mbar.

The simulations also retrieve the energy distribution of the particle leaving the hole. When the energy loss is non-negligible, the energy spectrum shows a tail to the left of the peak. We observed such a behavior when sending Ne^+ ions in a mixture of Ne + 10% CH_4 at 1 bar, for which the simulations predict 6% loss at 1keV. The measured spectrum is similar to the ones in [333] that are typical of a lossy process. The lossy spectra that we measure can be fitted by the function described in the cited article which is a sum of a Dirac delta (the energy sent by Comimac) and an exponential tail (the loss in the hole) convolved with a Gaussian function (accounting for the resolution of the detector).

The simulations of the energy loss have not been performed yet in the *Mimac gas* nor in the *High-gain gas* but we expect the loss to be negligible since we operate at low pressure and since the energy spectra are Gaussian. Finally, we mention that Comimac can also generate fluorescence X-rays on the stainless steel of the interface with a mean value of 6.4 keV. Such photons can pass through the interface and produce a photoelectric effect in the active volume, leading to a peak at 6.4 keV in the energy spectrum.

5.5.2 LHI

The "Ligne expérimentale de Haute Intensité" (LHI) is a facility of the LPSC that produces an ion beam of known kinetic energy. The working principles of LHI are similar to the ones of Comimac. A gas is excited by a 8.5 GHz ECRIS, turning into a plasma, and the ions are extracted by applying a positive voltage. On the contrary of Comimac, LHI is a facility of a dozen meters large. The ion beam is sent to a high-resolution magnetic spectrometer separating the ion species according to the ratio q/m over a circular trajectory with radius $\rho = 0.7$ m with $B\rho = 0.23$ T $\cdot$ m. The resolution power of the spectrometer is larger than 100, meaning that two ions with mass difference $\Delta m = 1$, and a total mass around 100, can be separated. The relative error on the kinetic energy of the ion beam after the mass spectrometer lies around 1%. The ion beam is eventually coupled with a MIMAC chamber through a $\mathcal{O}(1\ \mu\text{m})$ interface as for Comimac.

Due to the geometry of LHI, in which the ion trajectory is curved by the mass spectrometer, it is not possible to send electrons to the detector. The energy calibration of the MIMAC detector is then performed with radioactive sources. The advantage of LHI is its separation power that enables the selection of an ion mass without any ambiguity. LHI is then the appropriate tool for measuring the IQF of fluorine, as done in [131], for which the separation between $^{19}F^+$ and H_2O^+ can sometimes be difficult on Comimac. In this thesis, we will present LHI data for track length measurements of fluorine ions. For the rest of the results produced with an ion beam, we work with Comimac since it is more convenient and that one can also send electrons during the same campaign.

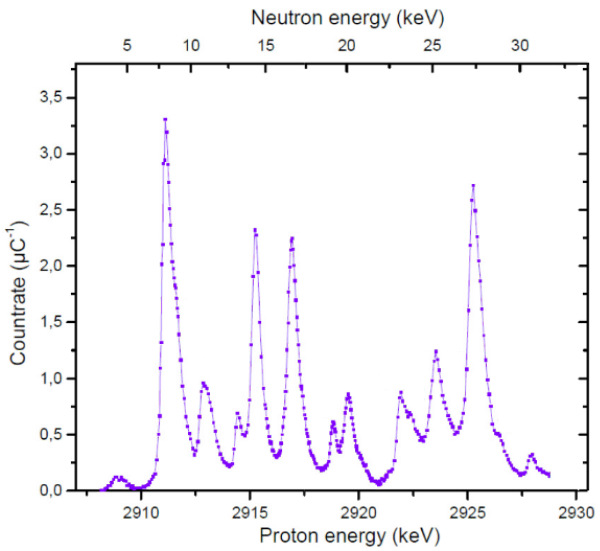

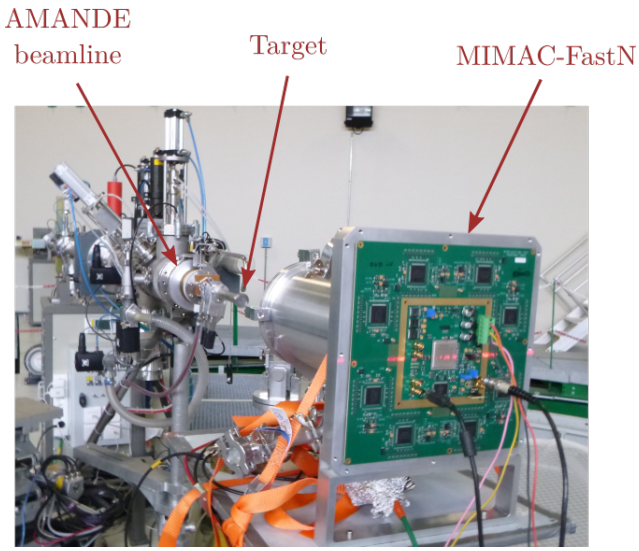

Figure 5.18: Left: the relative neutron fluence rate as a function of the incident proton energy. The fluence is expressed as the count rate in a Bonner sphere assumed to have a flat response in the neutron energy region, enabling comparison between the resonance peaks. Figure adapted from [336].
Right: experimental setup of a measurement on the AMANDE facility presented in Chapter 8

5.5.3 AMANDE

The AMANDE facility [334, 335] of the French Institute for Radiation protection and Nuclear Safety (IRSN) produces mono-energetic neutron field between 2 keV and 20 MeV. The neutron fields are produced either in a pulsed mode, either continuously, by the acceleration of protons or deuterons that will be sent to thin targets. In the work presented in Chapter 8 we use the nuclear reaction $^{45}\mathrm{Sc}\,(p,n)$ to produce neutron fields. The cross-section of this nuclear reaction has several resonances that can be activated depending on the energy of the incident proton beam, as presented in the left panel of Figure 5.18. The resonances are thin enough to produce mono-energetic neutron fields with kinetic energy of 8.12 ± 0.01 keV or 27.24 ± 0.05 keV [336]. The yield at 27 keV resonance is 90% of the yield of the resonance at 8 keV [337].

We place a MIMAC chamber specially designed for neutron spectroscopy, MIMAC-FastN [321], in front of the ^{45}Sc target such that the proton beam is parallel to the Z-axis of the detector. The neutrons are emitted within a solid angle depending on the distance between the Sc target and the detector. A picture of the experimental setup is shown in the right panel of Figure 5.18. The experiment is placed inside a "void" sphere of 6 m radius in which there are very few surfaces in order to reduce the flux of possible backscattered neutrons entering the detector.

The production of mono-energetic neutron field in the metrological installation AMANDE represents a valuable tool for a directional detector since the neutrons will induce a similar signal than WIMPs. The kinetic energy of proton recoil induced by an elastic collision with a neutron, E_p, can be expressed in the lab frame as:

$$E_p = E_n \ \cos^2\theta \tag{5.13}$$

where E_n is the neutron kinetic energy and θ the scattering angle, between the incident neutron and the proton recoil directions, having an angular distribution centred on 45 °. The reconstruction of the neutron energy spectrum with MIMAC, as presented in Chapter 8, thus requires precisely measuring the angle of the nuclear recoil and correctly determining its kinetic energy by applying the IQF. It then enables estimating the angular resolution of the detector and it represents the ultimate validation of the MIMAC strategy of detection for directional WIMP searches.

Summary

The MIMAC detector measures simultaneously the ionization energy of a charged particle and its track in 3D. The ionization energy is proportional to the charge deposited by the particle, the charge being measured by a charge-sensitive preamplifier (CSP) that reads the signal induced on the grid. The self-discharge of the CSP must be deconvolved to correct from the ballistic deficit. An energy calibration of the detector is performed, either by fluorescence X-rays, or by electrons of known kinetic energies sent by Comimac, in order to convert the measured charge into ionization energy.

The track is reconstructed in 3D from the signal of the anode. The anode is pixelated with 256 strips both in X and Y direction and the Z-component is reconstructed from a combination of the time sampling and the drift velocity. The fast self-triggered electronics of the detectors play a crucial role to read the 512 strips and the Flash-ADC, to synchronize them, to determine if a strip has been fired, and to store the information of an event. Several methods have been implemented to determine the properties of the 3D track from the anode signal: by using a barycenter method, by a 3D line fit, or by an ellipse fit.

The MIMAC observables built from the anode signal and the Flash allow to identify the detected particles. The identification is based on the stopping power of the particles. It is also possible to distinguish between several nuclear recoils of different masses by comparing the track lengths and the ionization energies. The discrimination of the electron background, with respect to WIMP-induced nuclear recoils, is usually the most challenging. We have developed a method based on BDT to reach rejection powers of 10^5 in the keV-range with an acceptance of 50%.

A bi-chamber MIMAC module has operated for almost 6 years in the Underground Laboratory of Modane, validating the stability of the detector, evaluating the background, and enabling the detection of radon progeny recoils. This 6 years operation was the first step toward the building of a m^3 detector. The second step was the development of a new detector, the *low-noise* detector, that uses a resistive anode Micromegas technology to increase the gain and the radiopurity of the materials. This detector is now validated and it enabled, for instance, to measure 150 eV electrons with 3D track and an acquisition threshold of 28 eV. This technology is currently extended to a 35×35 cm^2 detector with 1792 strips supposed to be the elementary brick of the m^3 detector. We also developed the measurement of the signal induced on the cathode at high energies in order to localize in 3D the position of the first interactions in the active volume.

The validation of the MIMAC strategy of detection is one of the purposes of this thesis. In this view, we make use of several facilities to test the detector and to measure its performance. In particular we frequently use Comimac, a table-top accelerator, to send electrons or ions of known kinetic energies in a MIMAC chamber. We sometimes use LHI for accurate measurements on ions of masses larger than 4 since LHI uses a high-resolution mass spectrometer to separate the ion species. The ultimate validation of the MIMAC strategy of detection is performed in a mono-energetic neutron field produced by the metrological facility AMANDE.

Chapter 6

SimuMimac: a numerical model for MIMAC at high gain

Some call this "the conclusions of Science". In reality, the ventriloquist's computer is merely expressing the political views of the scientists who ran the models.

Daniel Tanuro [338]

The comparison between measurements and theoretical predictions in a gaseous detector is usually not straightforward due to the successive physical processes involved in particle detection: the ionization, the drift of the primary charges, the avalanche, and the signal formation. Simulations are commonly used as an intermediate step between theoretical models and experimental data. While simulations correctly reproduced the track description of the MIMAC events for energies above 30 keV, the situation changed when we started to operate at high gain in order to probe low energies. For instance, we measured fluorine track lengths twice longer than predicted from simulations [173]. At that time, the simulation models that we used were neglecting a phenomenon that we did not identify

yet. The situation was very uncomfortable and unsatisfying. We describe in Section 6.1 such issues and the first hypothesis we developed to explain the behavior of the detector at high gain. We believed that the large number of ions accumulated in the gap could locally distort the electric field and influence the drift and the avalanche of electrons; in other words, they could build a *space-charge*. As far as we know, no simulation toolkit could include this hypothesis so we decided to develop our own simulation code.

Actually, we concluded that the detector did not suffer a space-charge effect. The explanation was simpler: at high gain, the detector gets more sensitive to the signal induced by the motion of the ions accumulated in the gap. At lower gain, the ionic signal is negligible compared to the electronic one, because of the detection threshold, and one could safely consider an instantaneous signal formation in the simulations. The happy end of the story will be presented at the end of the chapter when we will demonstrate that the new simulations agree with the measurements and that they provide valuable information.

This chapter presents `SimuMimac`, a simulation tool that models the signal induced both on the grid and on the anode strips, for a primary electrons cloud defined either manually, either from `SRIM` that is interfaced with `SimuMimac`. In this chapter, we follow the chronology of the events since we consider it as instructive. Section 6.2 details the implementation of the physical processes required for the simulations. In Section 6.3 we exclude the space-charge hypothesis for a gain lower than 10^5, leading to restructuring of the code. An overall description of `SimuMimac`, as well as an experimental validation, are provided in Section 6.4 with few technicalities.

I consider `SimuMimac` as my main contribution to the MIMAC project. Its development forced me to dig into the processes involved in particle detection with MIMAC, to question hypotheses, and to validate them one by one. It brought us to a better understanding of the operation of the detector at high gain. The description of the signal formation by `SimuMimac` led us to the deconvolution of the ionic signal on the grid, enabling to access directionality and head-tail recognition in the keV-range [179]. It will likely be a crucial tool for the deconvolution of the ionic signal on the strip, the last missing piece at high gain. Many efforts have been made to make `SimuMimac` easy to use so newcomers can quickly get started with it. Finally, since I wrote it from scratch, I have total control over it so I can quickly test hypotheses, which makes `SimuMimac` an essential tool for my everyday work.

The source code of `SimuMimac` is available on request.

6.1 The birth of `SimuMimac`

6.1.1 Evidence for a non-linear effect

Let us have a quick look at the difficult situation where we stood in 2019. We will describe the main puzzling measurements that led us to postulate a non-linear effect appearing at high gain.

Track depth

The team has used LHI to send fluorine ions of kinetic energy in the range $[6.3, 26.3\ \text{keV}]$ in a 10 cm MIMAC chamber filled with the *Mimac gas* at 50 mbar with an amplification electric field of 11.1 kV/cm leading to a high gain value that we measured around 2.6×10^4 for a W-value of 32 eV. The fluorine ions were sent parallel to the Z-direction of the detector and we note *depth* the ΔZ measured on the anode. The experiment aimed to measure in 3D the tracks of the particles and to determine the angular resolution in this energy range. We compared the measured track depths and widths to simulations. In the simulation we used `SRIM` to determine the primary electrons cloud, we transport all primary electrons towards the grid, and we later compute the avalanche, by using `Garfield++` [309]. Garfield++, which we will frequently mention in this chapter, is a toolkit for particle tracking simulations whose electron transport algorithm solves the second-order equations of motion based on the `Magboltz` gas tables. In these simulations, we did not include the signal formation since we thought, as in previous experiments, that the ionic contribution would be negligible.

While the measured track widths were compatible with the simulations [173], the track depths strongly disagreed: the measured depths were more than a factor 2 longer than predicted by the

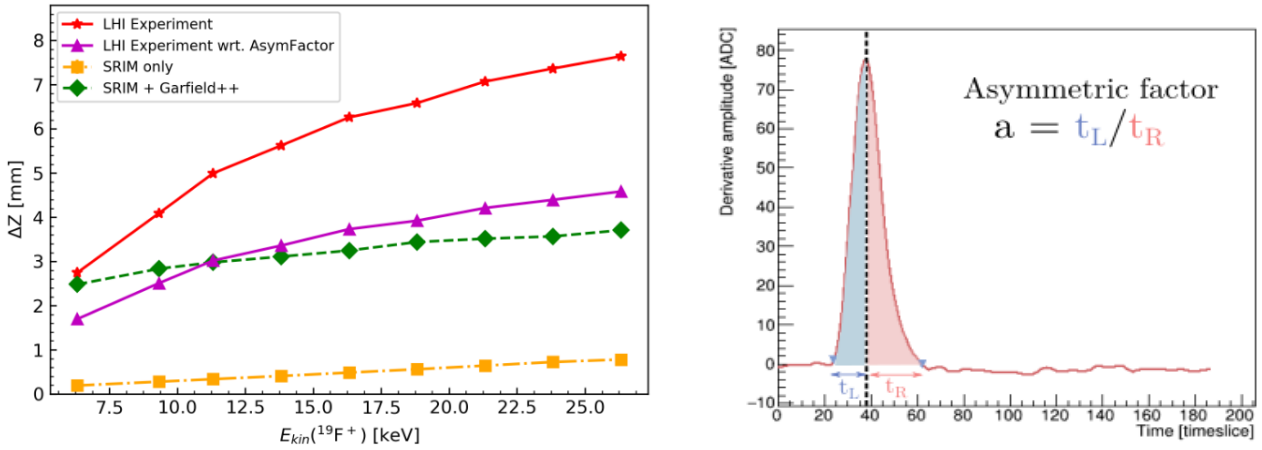

Figure 6.1: Left: track depths of fluorine ions send by LHI in a MIMAC chamber. The measured depths on the anode strips are shown in red. The measured depths multiplied by the asymmetric factor are shown in purple. A SRIM simulation is presented in orange and the green curve simulates the depth after 10 cm of drift.
Right: the definition of the asymmetric factor from the derivative of the Flash.

simulations for kinetic energies above 15 keV, as presented in the left panel of Figure 6.1. In the article, we postulated that a phenomenon was reducing the electron drift velocity, for instance a space-charge, resulting in an elongation of the measured track depths. In this case, the elongation should also be visible on the Flash: as the last charges to reach the grid will be more delayed, we expected the derivative of the Flash to be enlarged due to the slower effective velocity. We then defined the *asymmetric factor* as the ratio between the time duration of the falling part of the Flash derivated and the time duration of the rising part, *c.f.* the right panel of Figure 6.1 for a visual definition. Since the asymmetric factor accounted for a possible reduction of the drift velocity, we proposed an empirical correction of the measured depths: we multiplied them, event by event, with the asymmetric factor. The corrected depths are presented in purple in the left panel of Figure 6.1, and they are somehow of similar order to the simulated ones. With this correction we obtained a better than 15° angular resolution for fluorine kinetic energies above 10 keV [174]. However, the phenomenon behind this correction was not understood yet.

Gain curve

We had one more motivation to introduce the asymmetric factor as an empirical correction of an unidentified non-linear phenomenon: the gain curve. Since we suspected the elongation of the measured track depths to be related with a space-charge effect, we supposed the effect would increase with the gain of the detector. We then use Comimac to send particles of known energy in a MIMAC chamber, in multiple gas mixtures for electrons and ions, and we varied the gain while keeping constant the drift electric field. We measured the track depths both on the anode and on the Flash. In Figure 6.2 we present measurements in the *High-gain gas* for 5 keV electrons indicating clearly that the measured depths increase non-linearly with the gain of the detector. Interestingly, the asymmetry of the Flash derivative was also more pronounced. However, once multiplied with the asymmetric factor, the depths followed a plateau up to −540 V on the grid, except for the anode measurements at low voltages for which the gain is not sufficient to activate the strips. Recovering a plateau with the correction was an indication that the asymmetric factor quantified the non-linear phenomenon that we still did not understand.

Within the hypothesis of a space-charge effect, the intensity of the track elongation would depend on the density of the primary electrons cloud at the grid. The effect would then depend on the type of particle (electron or ion), its kinetic energy, the gain, and the drift distance of the primary electrons. In the Comimac experiment, we varied the gain whereas on LHI we varied the energy. To compare the measurements in both experiments, we used the value of the asymmetric factor. The range of the asymmetric factor measured during the LHI experiment is reported in Figure 6.2, so for the gain curve

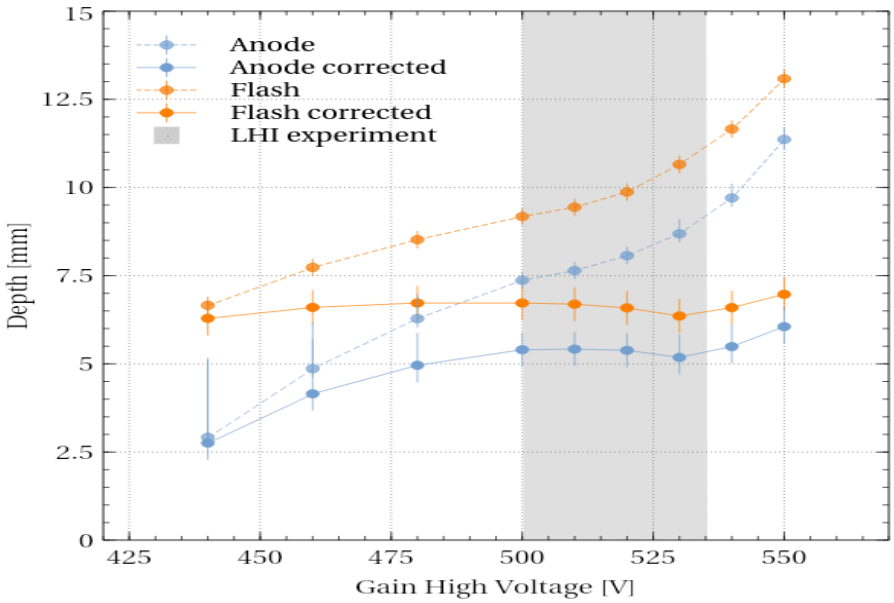

Figure 6.2: Measured ΔZ of 5 keV electrons sent by Comimac in the *High-gain gas* at 30 mbar for several voltages applied on the grid but keeping constant the drift electric field. The orange curves correspond to the measurements on the Flash, the blue ones are obtained from the anode strips. The dashed line corresponds to the measured depth multiplied by the asymmetric factor. The shaded gray area describes the region for which the asymmetric factor is comparable to the one measured during the LHI experiment.

measurements, in the shaded gray area: one can see that corrected depths in this range follow a plateau tendency, indicating that the asymmetric factor correction can be applied to the LHI measurements.

6.1.2 The space-charge hypothesis

Until spring 2020, we performed several measurements to better understand a possible non-linear effect in the detector and to draw its contours. We observed that the effect was correlated with the gain of the detector and the charge density of the primary electrons cloud, and that it could be corrected by the asymmetric factor. Today we can explain all of the puzzling measurements by taking into account the signal induced by the ions in the gap. However, at that time we neglected this hypothesis because it was commonly accepted that the contribution of the ionic signal was negligible on the strips, which actually is reasonable for Micromegas gap lower than 256 μm.

The hypothesis that for us was the most relevant to explain the puzzling measurements was a space-charge effect introduced by the large number of ions accumulated in the gap and slowly drifting towards the grid. We will see in the following section that about 20% of the ions slightly overpass the grid and accumulate close to the grid wires for a few microseconds. We supposed that these ions would locally distort the electric field, that they would screen the grid potential, and that their motion would induce a magnetic field, the combination of these effects reducing the electron velocity in the drift region.

Space-charge effect is usually considered in TPCs when operating at large event rates [339–342]: the slowly drifting ions are not all collected by the electrodes before the arrival of a new event, and their local distortions of the drift electric field influence the motion of the primary charges. In MIMAC the situation is different since we usually operate with rates below 100 Hz and since we are interested in low-energy events for which the number of ions produced during the ionization is negligible. Moreover, the secondary ions are collected on the grid, except for a small proportion that escapes into the drift region and that is called *ion backflow* [343]. We will later see that `SimuMimac` estimates the ion backflow between 2% and 3% depending on the voltages applied to the detector.

Our hypothesis was an event-based space-charge effect: a space-charge that is built within a single event and that resorbs before the following one. The ions produced by the avalanches of the first primary electrons influence the motion of the following primary electrons. The space-charge increases

with the number of secondary ions accumulated in the gap and depends on the balance between the rate at which the ions are collected on the grid and the rate of arrival of primary electrons. The denser the primary electrons cloud, the stronger is the space-charge effect. For simplicity in this chapter, we will write *space-charge* when talking about the event-based space-charge.

In the measurements where we observed the track elongation and the Flash-asymmetry, the energy calibration of the detector remained linear. For this reason, we assumed the space-charge effect to have no influence on the number of secondary charges produced in the avalanches. We supposed that the local distortions of the electromagnetic (EM) field only affect the time of arrival of the charges. For instance, the magnetic field induced by the motion of the ions close to the grid bends the trajectories of the primary electrons and consequently decreases their velocity.

6.1.3 The need for a new simulation tool

The minimal requirement for the simulation of a space-charge effect is an implementation that loops over time and, for each timestep, that computes the EM field distortions according to the position of each charge, before transporting them. As far as know, there is no simulation tool able to do so. In particular, we paid attention to *Garfield++* since it is widely used and validated for the drift and the avalanche of the electrons in the experimental conditions we are interested in. We observed three limitations with `Garfield++`:

- The particles are tracked one by one from the beginning until the end of their trajectory.
- The electric field is computed analytically from the voltages applied to the electrodes and cannot depend on the position of the charges. However, `Garfield++` can work with field maps computed by external software.
- From what we have seen, and we could have missed something, the transportation of low-energy ions (< 30 keV) at low pressure is not efficiently working. For instance, an ion placed in the gap moves towards the anode at 30 mbar of the *Mimac gas*, but towards the grid at 100 mbar. Also, we observed an inconsistent generation of primary electrons cloud in the interface with `SRIM` when the ion stops in the volume.

At first, we tried to adapt the `Garfield++` code but it required deeply modifying its structure. However, `Garfield++` presents several important advantages: the transportation of electrons is reliable and optimized, it has an efficient interface with `Magboltz` and it quickly computes the electric fields in 2D. We then opted for a hybrid implementation: we use `Garfield++` for setting the geometry, determining the gas properties, and computing the constant electric fields.

We have then started to develop our own simulation code based on `Garfield++` and entirely written in `C++` for speed performances. The code is interfaced with `SRIM` to generate the primary electrons cloud. The electrons are transported by a code greatly inspired by the one of `Garfield++`. For the drift of the ions we developed our own solver. The signal formation is based on an implementation of the Ramo-Shockley theorem. Finally, the most challenging point is the computation of the distortions of the EM field. After many attempts, we opted for a numerical calculation of the Coulomb field of the neighbour charges of the one that is transported, this approach appearing as the fastest and the most reliable of the ones we have tested. Due to the geometry of the detector, there is a symmetry between the X and the Y directions, we then decided to implement the code in 2D.

6.2 Modelling the detector

This section is dedicated to the technical details of the implementation of the main parts of the code. The short description of the code in the previous paragraphs should be enough for understanding the rest of the chapter, so the reader can skip this section if not interested in how to implement the physical processes of particle detection.

6.2.1 Geometry

The definition of the geometry of the detector and the gas properties is performed thanks to `Garfield++`. All the parameters of the geometry are free so one can easily adapt the code for any Micromegas. The grid wires and the anode strips are generated thanks to the class `ComponentAnalyticField`.

The properties of the gas are obtained from the class `MediumMagboltz` which has an interface with `Magboltz`. We then rely on it for the W-value, the Fano factor, and the electron-molecule scattering cross-sections that play a central role in the transportation (drift and avalanche) of the electrons.

6.2.2 The primary electrons cloud

We have implemented several approaches for generating the primary electrons cloud depending on the tests we were doing. We distinguish between manual generation and `SRIM` generation.

The manual generation consists in placing the electrons in the cloud. The first possibility is to define a uniform track in which electrons are evenly placed along the track. While this approach neglects the physics of the stopping power, it enables to compare simulations without statistical fluctuations in the ionization process. The track length, the number of charges, the Z-position, and the angle are free parameters. The second approach consists in generating a Gaussian cloud at the grid to model the diffusion in the transverse and the longitudinal directions. One can then save time by not transporting the electrons in the drift region.

The other possibility is to make use of `SRIM` to generate the primary electrons cloud. We developed an interface with `SRIM` so it can be automatically run inside the simulation by using the already defined properties of the gas. The `EXYZ.TXT` file outputted by `SRIM` contains the position of each collision as well as the electronic, η, and the nuclear, ν, energy losses. We compute the amount of energy released as ionization, for each collision, as $\eta/(\eta+\nu)$. This method then relies on the IQF determined by `SRIM` although we know it is overestimated (*c.f.* Section 4.2.2), inducing some bias in the simulation. The number of primary electrons produced in each collision is determined from a Poissonian distribution according to the energy loss and the W-value.

Another issue with `SRIM` is that it has been developed for tracking the primary ion and it does not give the information about secondaries. The DMTPC collaboration has developed a code called *retrim* [344], that determines the most probable secondary ionizations from the `SRIM` output. For the moment we have not included *retrim* in our modelling of the primary electrons cloud, meaning that we do not locate properly all charges. For the low energies that we consider, we expect this error to be negligible after diffusion.

The ionization process and the diffusion suffer from large statistical fluctuations. For this reason, a Monte-Carlo that generates a primary electrons cloud from `SRIM` must consider a large number of iterations (at least 200) to be statistically reliable. In our simulation code, the slowest part is the drift of the secondary ions in the amplification region, limiting the number of simulations we can run. To increase statistics and reduce statistical fluctuations we separate the simulations into two steps: we first transport the primary charges in the drift region; secondly, we simulate the avalanches and compute the induced signals. In the first step, the primary electrons clouds are generated with SRIM and we transport a large number of charges ($> 3 \times 10^4$) in order to reduce uncertainties inherent to stochastic processes. The second step of the simulation uses the results of the first step as input: the coordinates of each primary electron at the grid level are drawn from a 2D Gaussian distribution whose properties have been defined thanks to the results of the first step.

6.2.3 The ion motion

The motion of an ion in gas is described by the Langevin equation which is the Lorentz equation extended by a friction term modelling the collisions with the gas molecules:

$$m\frac{d\mathbf{v}}{dt} = q\big(\mathbf{E}+\mathbf{v}\times\mathbf{B}\big) - \frac{q}{\mu(E,p)}\mathbf{v} \tag{6.1}$$

where $\mu(E,p)$ is the mobility of the ion in the gas that depends on the electric field and the pressure. We then need to know the mass of the ion as well as its mobility, which is not straightforward.

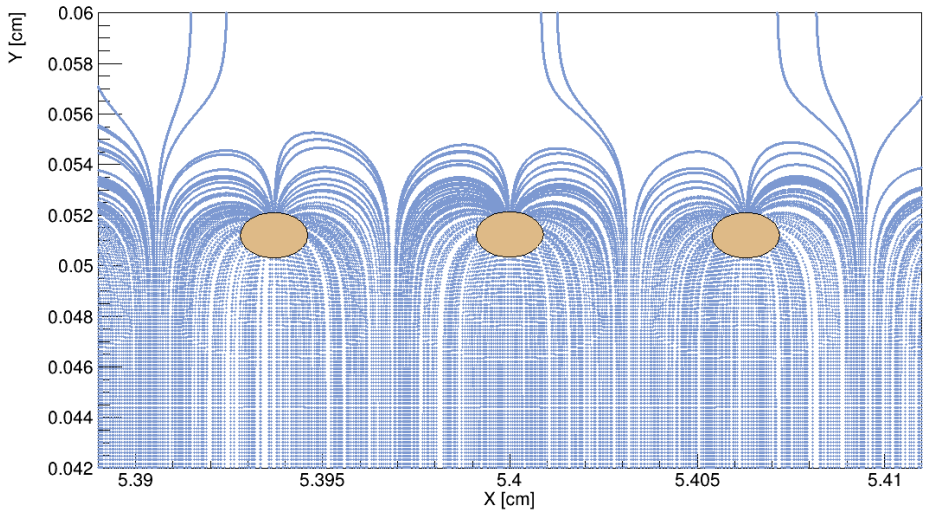

Figure 6.3: Trajectories of ions randomly distributed in the gap determined by solving Eq. (6.1). Simulations in the *High-gain gas* at 30 mbar with −510 V on the grid and a drift electric field of 85 V/cm. The yellow ellipses are the grid wires.

In the avalanche, several types of ions will be produced by the electrons. For instance in CHF_3, the ion CHF_2^+ will be produced in about 50% of the cases, depending on the energy of the electron, but one must also consider CF^+, CF_2^+, CF_3^+, H^+, *etc.* [293]. In CF_4, the ion CF_3^+ is produced in more than 80% of the cases [293]. In isobutane, the most probable ion is $C_3H_7^+$ produced in about 30% of the ionizations [295]. Here we had to decide whether we consider all types of ions by taking into account the partial cross-sections of electron impact ionization for each gas mixture. For simplicity, we decided to work with a single ion: the most probable one. In the *Mimac gas*, according to partial ionization cross-section and stoichiometry, the most probable ion is CF_3^+; it is CHF_2^+ in the *High-gain gas*.

Simplicity was not the only argument motivating this choice. For each ion, we need to plug its mobility into the Langevin equation. According to Blanc's law, the mobility of an ion in a gas mixture is related to its mobility in each of the gases [345]:

$$\frac{1}{K} = \sum_i \frac{f_i}{K_i} \tag{6.2}$$

where the sum is over all gases of the mixture and f_i is the mole fraction of each of them. However, there is a lack of experimental data to determine the ion mobility in our gases. The `LXCat` database [346,347] collects an impressive amount of data for electrons and ions swarm parameters, for instance mobility. Even in this database, we missed information about the mobilities of some ions (for instance CHF_2^+ in CF_4).

With the available data we observed two phenomena: the mobility is non-linear as a function of the electric field, but it usually changes by less than a factor 2 between the reduced electric fields in the drift region and the ones in the amplification region. The second observation is that the mobilities of the ions we consider are of comparable order. For instance, for a reduced electric field of $E/N = 400$ Td, the mobility of CHF_2^+ in CHF_3 is about 0.83 $cm^2/(Vs)$ whereas the mobility of CF_3^+ in CF_4 is about 1.12 $cm^2/(Vs)$.

Based on these observations, we decided to apply a significant simplification in the drift of the ions: we consider that a single ion species is produced (a single mass) and that it drifts with constant mobility that does not vary with the electric field. While the mass of the ion is set according to the most probable ion produced during the avalanches, the mobility value is a free parameter that must be adjusted to match the measurements, as we will see later.

The Langevin equation Eq. (6.1) can be solved numerically by a Runge-Kutta-Fehlberg (4,5) method (RKF45) thanks to the GNU scientific library (GSL) [348]. The timestep to solve the equation

has been adjusted manually: when larger than > 1 ns the solver is too coarse and the ions miss the grid; when smaller than < 0.1 ns the solver does not always converge.

A typical example of the ion trajectories, obtained by solving the Langevin equation with GSL, is presented in Figure 6.3. The ions have been randomly distributed in the gap and then drifted. The ion trajectories follow the electric field lines, for this reason they drift in straight lines (along $\mathbf{z}$) with a constant velocity. Close to the grid wires, the geometry of the electric field lines is more complex and we distinguish between three types of trajectories:

- The ions that are directly collected on the grid wires.
- The ions that overpass the grid up to ~ 30 μm before going back to be collected on the grid. The drift velocity of the ions significantly decreases when they overpass the grid, so it takes about one to two microseconds for them to be collected on the grid.
- The ions that escape the grid wires and that enter the drift region. This is the ion backflow already mentioned.

6.2.4 Drift and avalanche of the electrons

For the drift and the avalanche of the electrons we have used the code of `Garfield++` implemented in the class `AvalancheMicroscopic`. An adaptation has been made to drift the electrons over a single timestep in order to recompute the EM field at every iteration. Let us briefly describe the `Garfield++` code. The electron is followed from one collision to another with a collision frequency $\nu(E)$ given by `Magboltz` gas tables. In between two collisions, the trajectory of the electron is computed classically as if it were in vacuum. However, the electron velocity between two collisions is not constant, and the mean frequency collision depends on it. To cope with this issue, the transportation code relies on the *null-collision* method [349]. This method is a mathematical trick, without any approximation, that enables to operate with a mean collision frequency even in the velocity-dependent case.

The trick consists in using a trial collision frequency, ν', that is greater than the mean collision frequency. To exactly compensate for the fact that too many collisions will be considered, we let a part of the collisions $(1 - \nu(E)/\nu')$ for which there is no momentum transfer. In other words, when a null-collision happens the electron trajectory is not modified. The energy of the electron is however adapted, taking into account the acceleration induced by the EM field. The energy and the direction of the electron are then adapted depending on the type of collision, null or real, that it experiences. The choice of the null-collision frequency ν' is done randomly at each iteration, as long as it is larger than the real-collision frequency.

When the collision is real, the code determines the type of collision that happened according to `Magboltz` cross-sections. For instance, it can be an ionization, an excitation, photons or Auger electrons can also be produced, *etc.* We can then know when and where secondary ions or electrons are produced. The direction of the secondary particle is drawn randomly in a uniform distribution.

6.2.5 The local distortions of the electromagnetic field

A standard approach for space-charge simulations, for instance developed in [339], consists in solving the Poisson equation, according to the position of all charges, by the use of a Finite Element Method (FEM). However, we decided not to follow this approach that we judged too demanding in our case because (1) it would require a thin meshing according to how close the secondary charges are and according to the field geometry; (2) we need to recompute the field map at every timestep, so dozens of thousand times, which we believe incompatible with such a precision method. We instead decide to compute the distortions according to the Coulomb potential of the neighbour charges.

The moving charges modify locally the EM field. The question is to know if these modifications are significant enough to influence the motion of the other charges. We assume that only the ions contribute to the field distortions: the primary electrons are too few, and the secondary electrons are collected almost instantaneously (< 1 ns) on the anode. According to the superposition principle, the

total EM field is given by a uniform contribution, $\mathbf{F}^u$, and a distortion contribution $\mathbf{F}_d$:

$$\mathbf{F}(\mathbf{x},t) \;=\; \mathbf{F}^u(\mathbf{x}) + \sum_{k=\text{ions}} \mathbf{F}^d_k(\mathbf{x},t) \tag{6.3}$$

The uniform contribution is computed by Garfield++, we must then only compute the distortion term. Since the charges are in movement, we decide to determine the EM field they induce by applying the retarded potential of Lienard-Wiechert. In the approximation that the charges move with a constant velocity, the induced EM field can be expressed as [350]:

$$\begin{cases} \mathbf{E}(\mathbf{x},t) & = \frac{q}{4\pi\epsilon_0}\left(\frac{\mathbf{n}-\boldsymbol{\beta}}{\gamma^2\left(1-\boldsymbol{\beta}\cdot\mathbf{n}\right)^3 R^2}\right)_{ret} \\ \mathbf{B}(\mathbf{x},t) & = \frac{1}{c}\left(\mathbf{n}\times\mathbf{E}\right)_{ret} \end{cases}$$

where $\mathbf{x}$ is the position in which the field is computed, $\boldsymbol{\beta} = \mathbf{v}(\tau)/c$ is the reduced velocity of the charge, τ is its proper time, γ is the Lorentz factor, $\mathbf{n}$ is a unit vector in the direction $\mathbf{x}-\mathbf{r}(\tau)$, and $\mathbf{r}$ is the position of the charge. Finally, the subscript $_{ret}$ indicates that the expression must be evaluated at a retarded time τ_0 for which the light-cone condition is fulfilled: $x_0 - r_0(\tau_0) = |\mathbf{x}-\mathbf{r}(\tau_0)| \equiv R$.

The retarded time τ_0 embeds the notion of trajectory in the computation of the EM field. From an algorithmic point of view, we decide that this time corresponds to the previous timestep: if we evaluate the field at timestep t_i, then $\tau_0 = t_{i-1}$. In the following expression we note x_1 and x_2 the coordinates x and y, respectively, and the superscripts indicate the timestep. The non-vanishing terms of Eq. (6.4) can be expressed algorithmically as:

$$\begin{cases} E_x(\mathbf{x},t) & = E_1^i = \frac{q}{4\pi\epsilon_0}\left(\frac{\left(x_1^i - r_1^{i-1}\right)/R - v_1^{i-1}/c}{\gamma_{ret}^2 R^2\left[1-\frac{1}{cR}\left(v_1^{i-1}(x_1^i-r_1^{i-1})+v_2^{i-1}(x_2^i-r_2^{i-1})\right)\right]}\right) \\ E_y(\mathbf{x},t) & = E_2^i = \frac{q}{4\pi\epsilon_0}\left(\frac{\left(x_2^i - r_2^{i-1}\right)/R - v_2^{i-1}/c}{\gamma_{ret}^2 R^2\left[1-\frac{1}{cR}\left(v_1^{i-1}(x_1^i-r_1^{i-1})+v_2^{i-1}(x_2^i-r_2^{i-1})\right)\right]}\right) \\ B_z(\mathbf{x},t) & = B_3^i = \frac{1}{cR}\left[\left(x_1^i - r_1^{i-1}\right)E_2^i - \left(x_2^i - r_2^{i-1}\right)E_1^i\right] \end{cases}$$

with $1/\gamma_{ret}^2 = 1 - \left((v_1^{i-1})^2 + (v_2^{i-1})^2\right)/c^2$.

In principle, one must consider each ion in the sum of Eq. (6.3) but the computation complexity would be too large since we transport several millions of ions. However, since the EM field evolves in $1/r^2$ with r the distance between two charges, only the closest ions significantly contribute to the field. After several attempts we eventually have found a robust implementation of the phenomenon. We placed the ions into a C++ `unordered_multimap`, which is an unordered list that associates each element (in our case each ion) to a *key* that is unique but can be shared by several elements. This map is implemented in a hash table that groups all ions with the same key in order to quickly give access to their properties. We developed a key that gives information about the location of a charge: neighbour ions have the same key. To evaluate the EM field distortions at coordinate (x, y) we first compute the key associated with the position and we then sum over all ions sharing this key. If the number of considered ions is large enough we stop the field computation, otherwise we loop over the closest keys.

An example of the motion of the charges and the field distortions are presented in Figure 6.4. The electric field distortions reach a similar value than the field generated by the voltage applied to the grid. Locally, the electric field can be an order of magnitude larger when two charges are very close to each other.

6.2.6 Signal formation

The signal formation is computed according to the Ramo-Shockley theorem Eq. (4.22). Following the approximation of Dris and Alexopoulos [313], and after validation with Garfield++, we consider the

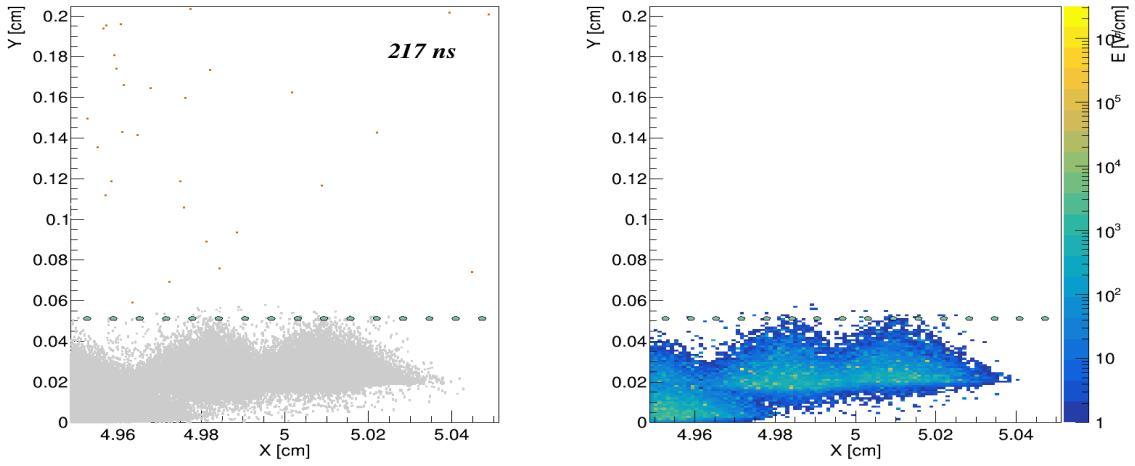

Figure 6.4: Simulation of the positions of the charges (left) and the electric field distortions (right) for a proton track generated by SRIM and drifted over 5 cm. In the left figure, the orange dots are electrons, the gray dots are ions, and the green ellipses are the grid wires. The simulation generates such a plot every 2 ns so one can produce a movie of the charge movement.

weighting field of the grid to be constant in the amplification region. On the contrary, the weighting fields of the strips are computed with Garfield++.

The induced current is computed each time a charge moves. In the code, ions are transported over a constant timestep but the time of flight of an electron is taken randomly following the null-collision method. For this reason, we have decided to store the signal in a C++ map that associates an element (the current) with a key (the time). The currents induced in the same time sample are summed.

6.3 The exclusion of the space-charge hypothesis

6.3.1 Reionization and relativistic avalanche

We here mention several issues that we have encountered while simulating the space-charge effect. We have not studied in details these issues since, as we will see, we have excluded the space-charge hypothesis at the same time. We anyway briefly introduce them in case someone is interested in developing a space-charge code.

When two charges are close enough to each other, the Coulomb field they experience can reach significant values. We distinguish two cases:

- When two ions are too close, they are repelled by the Coulomb interaction and they reach kinetic energies up to keV. For instance, a CF_3^+ ion can be accelerated up to 1 keV if it experiences an electric field of 3×10^5 V/cm, which happens when two ions are separated by 7 nm. This situation is rare since, according to Garfield++, the closest ions produced in avalanches are separated by $\sim$ 10 nm. It could anyway statistically happen and, in that case, the energetic ions are able to ionize the gas in the amplification area. We have called this process *reionization*. We used stopping power tables from SRIM to generate new primary electrons in the amplification region, distributed uniformly along the ion path as a first approximation. Reionization usually happens close to the anode, where the ion density is the largest, so the primary electrons it generates are usually collected on the anode before they could start an avalanche, otherwise the detector would get out of the proportional regime.

- When an electron in the avalanche process gets close enough to an ion, it can be sufficiently accelerated by the Coulomb field so that it must be treated relativistically. Let us consider that we must use relativistic formalism for an electron velocity $v \sim 0.1c$. We estimate that this velocity is reached when an electron approaches an ion at less than 3 nm. This distance being

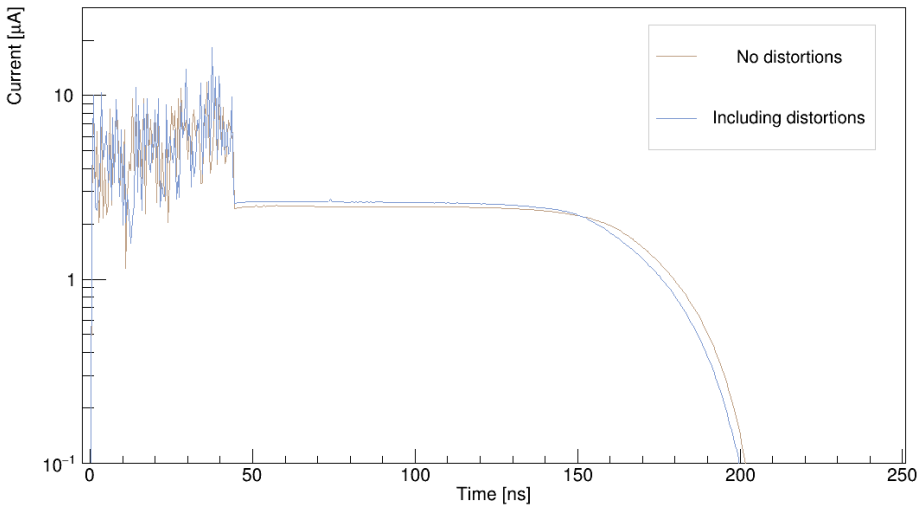

Figure 6.5: Current induced on the grid including or not the distortions of the EM by the ions space-charge. The primary electrons cloud at the grid is made of 50 electrons separated by 1 ns, all of them entering the amplification region at the same coordinate (worst-case scenario). Simulation in the *Mimac gas* with an amplification electric field of 11.1 kV/cm corresponding to an estimated gain of 5×10^4.

reasonable when millions of ions are in the gap, we have extended the `Garfield++` code to a relativistic formalism in the avalanche process based on the relativistic equations of motion:

$$m\frac{dU^\alpha}{d\tau} = \frac{q}{c}\,F^{\alpha\beta}U_\beta \tag{6.4}$$

with τ the proper time, $F^{\alpha\beta}$ the EM tensor and $U^\alpha = \left(\gamma c, \gamma \mathbf{u}\right)$ the 4-velocity of the electron. In that case, we approximate the energy of the electron to:

$$\epsilon(\tau) \;=\; \epsilon(\tau_0) + q\gamma(\tau_0)\,\mathbf{u}(\tau_0)\cdot\mathbf{E}\,d\tau + \frac{q^2}{2m}\,|\mathbf{E}|^2\,d\tau^2 \tag{6.5}$$

We have not fully validated the implementations of such phenomena since these developments correspond to the moment when we abandoned the space-charge hypothesis. Also, we have not taken the recombination into account: there is a non-negligible possibility that an electron recombines with an ion when they are close enough to each other.

6.3.2 Arguments to exclude the hypothesis

For two identical primary electrons clouds, we have not observed a significant difference in the duration of the signal simulated whether or not the EM field distortions are taken into account. For instance, we present in Figure 6.5 an example of the typical results we obtain. We have simulated a worst-case scenario in the *Mimac gas* with an amplification electric field of 11.1 kV/cm: we placed 50 electrons separated by 1 ns at the grid, all of them entering the amplification region at the same coordinate. As one can see in the figure, no significant deviation is observed and similar results are also obtained on the anode strips. According to the simulations, the gain is about 5×10^4. The presented figure has been produced by `SimuMimac` that models the signal formation, so one can see the long baseline produced by the ions explaining the 3D track distortions at high gain. However, as already said, we neglect at first the signal formation since we unfortunately thought the ionic contribution would be negligible. At that time, we were only looking at the time of arrival of primary electrons, which was not affected by the space-charge in our simulations.

These simulation results were not sufficient to rigorously exclude the space-charge hypothesis. First, as we have seen previously, the implementation of reionizations and relativistic avalanches was not fully validated. Second, one would need to systematically compare the signals for several configurations of

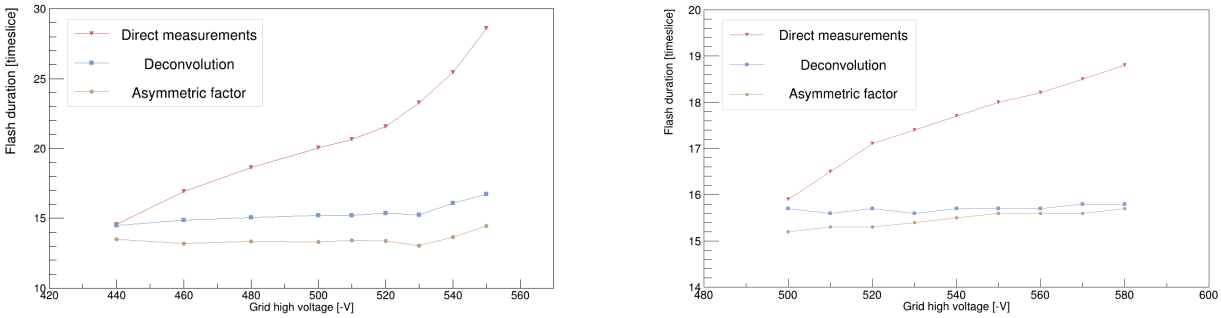

Figure 6.6: Gain curve obtained with Comimac for (left) 5 keV electrons in the *High-gain gas* at 30 mbar; (right) 10 keV protons in the *Mimac gas* at 50 mbar. The red curve corresponds to the measured duration whereas the brown one is obtained after multiplying by the asymmetric factor. The curve in blue is obtained by the deconvolution of the ionic contribution on the Flash and it corresponds then to the duration of the primary electrons cloud before the avalanche.

primary electrons cloud. We were limited by the time required to operate at such high-gain: for instance, the simulation producing the results of Figure 6.5 ran for about two weeks. Third, we do not entirely rely on simulations, in particular when they have not yet been validated experimentally.

Anyway, at this stage we started to seriously doubt about the space-charge hypothesis as an explanation of the measured 3D track elongations. This detailed work about the motion of charges in the detector led us to the explanation that the track elongation is due to the ionic contribution, as we will see and validate in the next section, and we had all elements ready to simulate it. Then, a second argument to exclude the space-charge hypothesis is that we do not need it to explain all our puzzling measurements.

Finally, we anticipate over Chapter 8 to present a third argument, an experimental one, to exclude the space-charge hypothesis. We will later see that it is possible to separate the electronic and the ionic currents from the Flash signal thanks to an analytical deconvolution. Since the electronic current is almost instantaneous (< 1 ns), its time distribution is equivalent to the time distribution of the primary electrons cloud at the grid. Without space-charge effect, the duration of the electronic current should remain constant as a function of the gain whereas it should increase in the presence of a space-charge. To test this behaviour, we perform once again a gain curve: we use Comimac to send particles of known kinetic energy in the detector while we vary the gain.

The results are presented in Figure 6.6 where, on the left, electrons of 5 keV are sent in the *High-gain gas* and, on the right, protons of 10 keV are sent in the *Mimac gas*. In both cases, the direct measurements of the duration show a non-linear tendency increasing with the gain while the duration of the deconvolved Flash follows a plateau, corresponding to a gain-independent duration. For completeness, we also present the effect of the empirical correction based on the asymmetric factor. On the left plot, one can observe a change of regime for high voltages stronger than -530 V. According to the simulations, the gain in such conditions exceeds 10^5. Up to this voltage, the duration of the electronic current remains constant so no space-charge effect is observed. Above it, the non-linearities could be explained by a space-charge effect although the validation of this hypothesis requires further investigation. Note that during the measurements in the *Mimac gas* we did not reach such a high gain: the simulations predict a gain of $\sim 5 \times 10^4$ for the maximal voltage tested of -580 V on the grid.

6.4 SimuMimac

We have seen that the space-charge effect can safely be excluded as a hypothesis for explaining the puzzling measurements presented at the beginning of the chapter. The simulation code can then be restructured:

- We no longer compute the EM field distortions. The electric field is now entirely given by `Garfield++`.

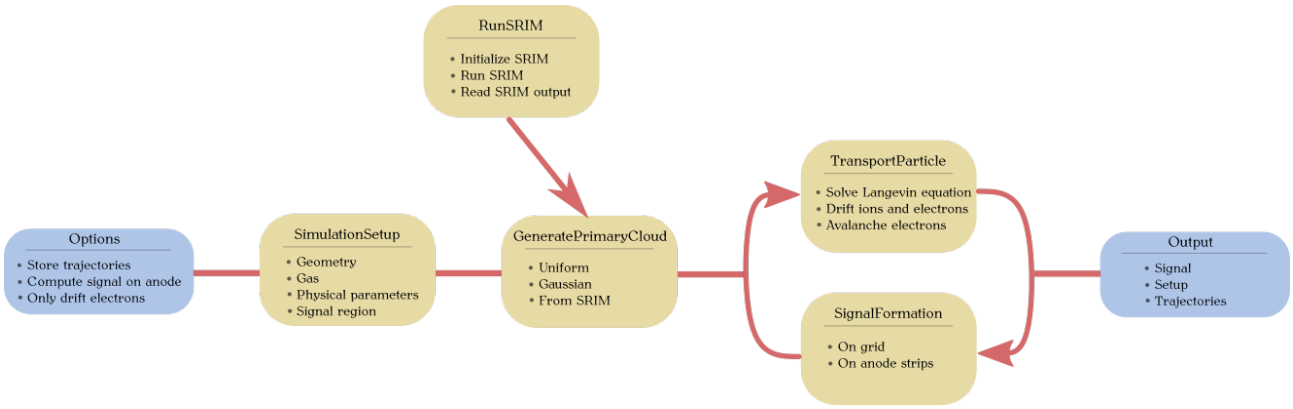

Figure 6.7: Flow diagram of SimuMimac. Each yellow box corresponds to a C++ class whose action is coordinated by the main program.

- We track the particles one by one since we can now assume that they do not interact with each other.
- We now model the signal formation that we have unfortunately neglected so far.

SimuMimac is the name of the simulation code after performing such modifications. As we will see, it efficiently reproduces MIMAC measurements at high gain. We must mention that, since we do not simulate a space-charge effect, Garfield++ has all the required abilities to model MIMAC. However, we prefer to work with SimuMimac since it is adapted to MIMAC: we only model the phenomena we are interested in. For this reason, the drift of the ions, including the signal calculation, is twice faster with SimuMimac than with Garfield++, although the transportation of electrons is slower. Besides, the main argument for using SimuMimac is that we have 100% control over the code and each development step has been validated. In this section we introduce SimuMimac and its abilities.

6.4.1 General description

One goal when developing SimuMimac was to implement a code easy to use, even by people not familiar with C++. In this sense, the main program is short and understandable, an example is presented in Appendix B. The user defines:

- The options: to store or not the trajectories of the particles; to compute or not the signal on the anode; to perform or not the avalanche of the electrons.
- The setup: geometry, gas, voltages, drifting ion properties, region of interest for the signal computation. A default value exists for all parameters.
- The primary electrons cloud type (uniform, Gaussian, from SRIM), its Z-position, and its angle with respect to the Z-axis.

Once this is done the simulation is ready and it can be run. It first transports all electrons (drift and avalanche) and it later transports all ions. Each time a charge moves in the amplification region the code computes the corresponding induced signal. The simulation stops when all charges have been transported. It outputs a text file that contains the current and the charge induced both on the grid and on the anode strips. It outputs as well a setup file that details all parameters of the simulation, and one can also generate plots of the trajectories. The plots are performed with ROOT [351], but this part of the code can be removed, since it is optional, if one wants to compile without ROOT.

A flow diagram of SimuMimac is presented in Figure 6.7. The code is organized into five classes that, in principle, should not be modified by the user except if he/she wants to include additional features. We briefly introduce the role of each class:

- **SimulationSetup** interfaces the main program with the other classes and manages the inputs and the outputs of the simulations.

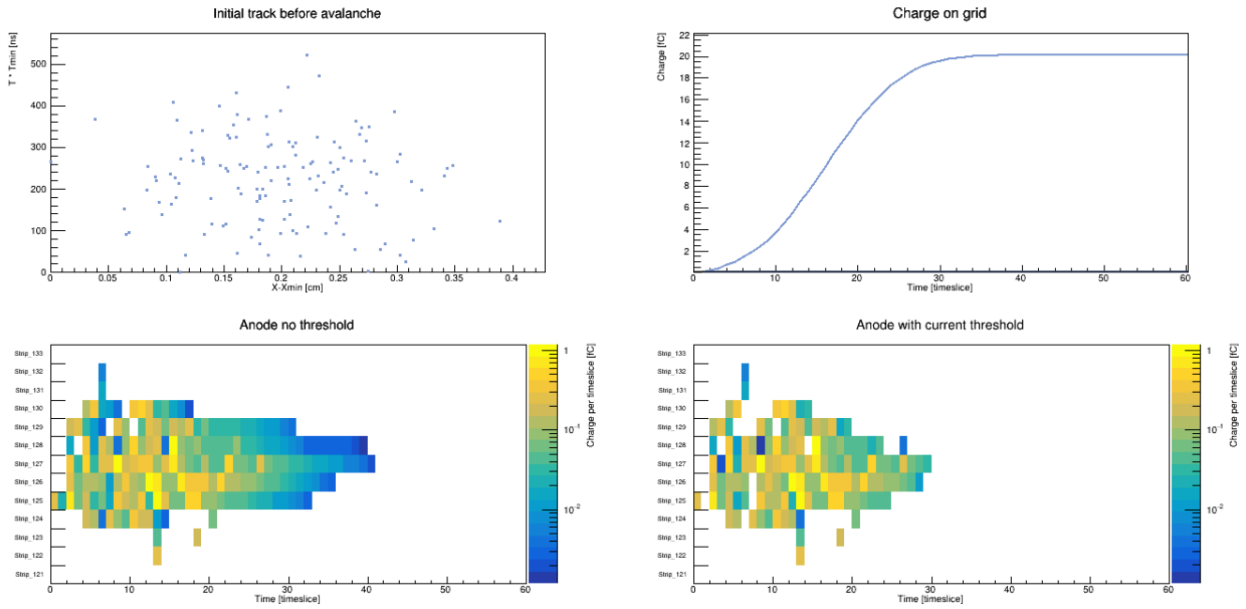

Figure 6.8: Example of SimuMimac results for the simulation of a Comimac experiment. A 7 keV proton track sent along the Z-axis has been generated by SRIM in the *High-gain gas* and it has drifted over 5 cm. The primary electrons cloud at the grid is presented in the upper left panel. SimuMimac has produced the avalanches and modelled the induced signals. The upper right panel shows the simulated Flash. The two bottom panels present the simulated signal on the anode. To account for the strip threshold, a current threshold has been applied on the bottom right panel. In this simulation, we worked with a amplification electric field of 6.05 kV/cm, for reasons explained in Section 6.4.3, so the charge must be scaled if one wants to compare it to physical values.

- **GeneratePrimaryCloud** creates the cloud of primary electrons according to the requirements set by the user.
- **RunSRIM** is in charge of the interface with SRIM and it is only used if required by GeneratePrimaryCloud. It initializes and runs SRIM according to the setup of the simulation. It also reads SRIM output to determine the properties of the primary electrons.
- **TransportParticle** manages the list of ions and electrons in the detector. It drifts the ions by solving the Langevin equation. It transports the electrons (drift and avalanche). It also stores the trajectories if the option has been activated.
- **SignalFormation** computes the signal (current and charge) induced on the grid and on the anode strips. It is then called for every displacement of a particle. It also formats the signal to save it into the output file.

Let us illustrate the working principles of SimuMimac with an example whose results are presented in Figure 6.8. We first initialize the setup to simulate the detector with a 512 μm gap Micromegas and filled with the *High-gain gas* at 30 mbar. Secondly, we generate a primary electrons cloud by running a SRIM simulation of a 7 keV proton entering the detector parallel to the Z-axis at the cathode level (5 cm away from the grid). Third, we transport all electrons towards the grid and we obtain the cloud shown in the top left panel of the figure. Fourth, we perform the avalanches before drifting the ions, computing meanwhile the signals induced by the motion of the electrons and ions in the amplification region. Finally, we analyse the output file. The current induced on the grid is integrated and digitalized at 50 MHz to reproduce the Flash signal, as shown in the top right panel. The charge induced on the strips is also digitalized at 50 MHz and shown in the bottom left panel. One can see the influence of the slow drifting ions that introduce a tail effect: a charge is continuously induced on a strip for about 300 ns, corresponding to the ion drift in the gap. However, the MIMAC strips have a current threshold that we have been modelled to obtain the bottom right plot.

As a drawback of SimuMimac, we must define manually two parameters of the simulations for which we do not have experimental values. One must adjust the mean mobility of the ions in the gap based on

an extrapolation from database values, as discussed previously in the chapter. The second parameter to fix is the strip threshold on the pixelated anode, *i.e.* the current above which the strips are fired. The values are adjusted manually for a reference run, and we later compare the tendencies of the simulated quantities to the measurements in order to quantify their agreement. We will give an example of it in the following subsection.

6.4.2 Validation on experimental data

We have validated each functionality of `SimuMimac` during the development of the code. Let us give a few examples of such tests. The diffusion during the drift of the electrons has been compared to the diffusion coefficients given by `Magboltz`. The avalanche has been compared to `Garfield++` and we also checked that we recovered the exponential ion distribution predicted by the Townsend theory, as well as the Polya distribution of the number of secondary charges. The drift of the ions has been validated by comparing the trajectories to the electric field lines geometry, and the amount of ion backflow agreed with the literature. The signal formation on the grid has been compared to the Dris and Alexopoulos model of Eq. (4.23) [179]. The overall simulation has been compared to `Garfield++`. However, such comparisons are necessary but not sufficient: the complete validation of `SimuMimac` must be performed on experimental data.

The main success of `SimuMimac` has been to reproduce the puzzling measurements detailed at the beginning of the chapter. We have simulated the fluorine track depths in the energy range $[6.3, 26.3\,\text{keV}]$ to compare with the LHI measurements. In order to reduce the statistical fluctuations due to diffusion, we proceed in two steps as described previously: we first drift a large number of charges ($> 3 \times 10^4$); then we randomly draw the coordinates of each primary electron at grid level from a 2D Gaussian distribution whose properties have been defined thanks to the results of the first step. This "two-step simulation" enables us to operate with low statistics for the `SimuMimac` simulation. The statistics depend on the computing time and vary between 20 simulated fluorine ions (at 26.3 keV) and 150 (at 6.3 keV).

The two free parameters of `SimuMimac`, the ion mobility and the strip threshold, are adjusted in order to have an agreement between the simulations and the measurements at 16.3 keV: we obtain a mean ion velocity of $1.7\,\mu$m/ns and a strip threshold of $0.56\,\mu$A. While the depth measurements, and their correction multiplying by the asymmetric factor, have already been presented in Section 6.1, we show in Figure 6.9 the comparison with the `SimuMimac` measurements. One can see that they agree, within the statistical uncertainty, over the entire energy range.

This agreement is a validation of `SimuMimac` on experimental data at high gain. On the other hand, it also shines light on this puzzling elongation. The measured depth appears as elongated (compared with the expected size of the primary electrons cloud before the avalanche) because of the contribution of the ionic signal. The large number of ions accumulated in the gap after the arrival of the last primary electron keeps inducing a detectable signal on the anode strips for several timeslices. This signal depends on the total number of ions located in the amplification area at the same time. In other words, it depends on the kinematics balance in the gap between the input charges (primary electrons starting an avalanche) and the output (ions being collected on the grid). For this reason, the influence of the ionic contribution increases with the charge density of the primary electron cloud, and thus with the kinetic energy of the fluorine ions. A detailed description of the phenomenon will be provided in Chapter 8.

The agreement between the measurements and the simulations for the depths corrected by the asymmetric factor is also an important validation of `SimuMimac` since the depths are determined from the anode strips whereas the asymmetric factor is obtained from the Flash. While some asymmetry on the Flash derivative is expected from the stopping power tendency of fluorine in the gas, the simulations show that the main component of this asymmetry is related to the ionic signal. Since we are more sensitive to the ionic contribution at large energies, it explains why the asymmetry of the Flash derivative gets more significant when the energy increases.

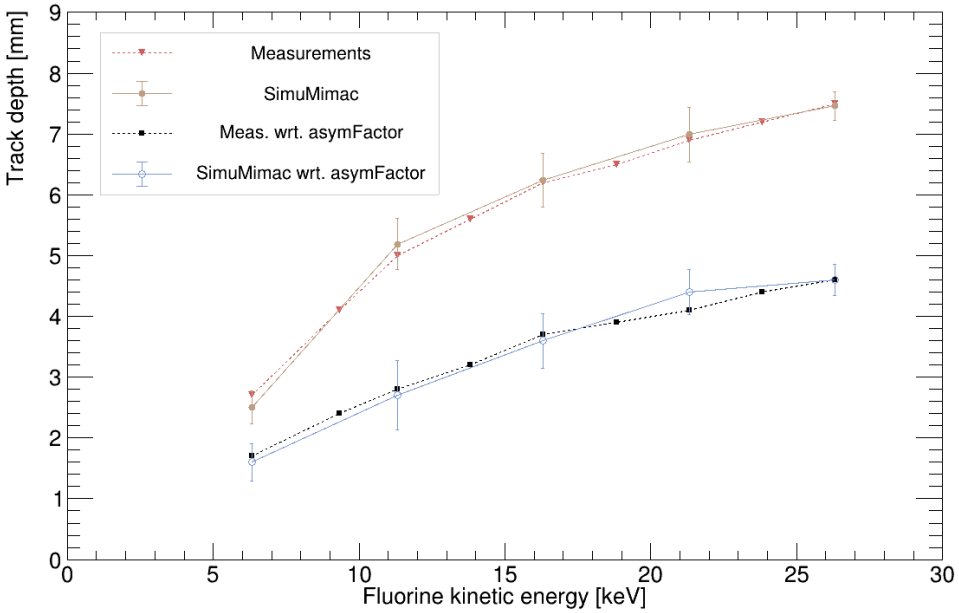

Figure 6.9: Fluorine track depths after 5 cm of drift in the experimental conditions of [173] described in Section 6.1. The depth measurements and their correction with respect to the asymmetric factor are respectively shown in red and black. The SimuMimac simulated depths are presented in brown and their correction by the simulated asymmetric factor are shown in blue. The error bars in the simulation results account for the statistical uncertainty at one sigma.

6.4.3 Approximations and limitations

For completeness we introduce the limitations of SimuMimac as well as the main approximations used in the code so that the user is aware of the validity domain of the simulations. We have already discussed the fact that two parameters are experimentally unknown and must thus be adjusted manually: the ion mobility and the strip threshold.

The main limitation of SimuMimac lies in the long computing time required to perform a complete simulation. The computing time mainly depends on the number of primary electrons, the gain, and the size of the signal region (related to the number of strips for which the signal is computed). For a signal region containing 12 strips, the simulation runs for about 3 min for 10^3 secondary ions; 500 min for 2×10^5 secondary ions. Since there is no space-charge effect, we often make use of a trick to speed up the code: we run the simulation at a very low amplification electric field ($\sim$ 6 kV/cm) and we normalize the obtained signals by a factor (that can be determined by the simulation) to scale them to the expected value. In doing so, one must adjust the ion mobility accordingly so that the ion drift velocity is not affected. Even with this trick, it takes about 5500 min to simulate a 20 keV proton track produced by SRIM and located at $z = 12.5$ cm away from the grid.

We have already discussed most of the approximations in the technical presentation of SimuMimac, yet we list them all at the same place:

- We assume that a single type of ion (single mass) is produced by the avalanches and that it has constant mobility.
- The primary electrons cloud for nuclear recoil is given from SRIM. In the simulation we neglect the secondary processes so all primary electrons are placed along the ion path. We also make use of SRIM IQF, which usually is overestimated in gases. We also consider that all primary electrons are generated with the same energy, although this approximation has little influence since the electrons quickly reach limit energy in the drift region.
- 2D simulations. We assume that the physical processes for particle detection with MIMAC experience a symmetry in the (X-Y) plane. This approximation is necessary to make use of Garfield++

to analytically compute the electric fields and the weighting fields. 3D track reconstruction and directional performances can thus hardly be simulated by SimuMimac.

- We assume that the weighting field of the grid is constant everywhere in the gap.
- In the avalanche we neglect the production of photons: the only secondary particles taken into account are electrons and ions.

6.4.4 A valuable tool for MIMAC prospects

SimuMimac is an experimentally validated tool to model the physics of the MIMAC detector and it quickly became an essential element in our studies. One of its main advantages is the possibility to evaluate independently the influence of each physical process (ionization, diffusion, avalanche, signal formation, *etc.*) leading to a better understanding of the detector, in particular at high gain.

The simulations also estimate some physical quantities, such as the ion backflow or the grid transparency. In the *Mimac gas* with -1320 V on the cathode and 5 cm drift, the proportion of ion backflow continuously increases when the absolute value of the grid voltage decreases: 2.0% at -570 V, 2.5% at -530 V, 3.0% at -440 V. Applying the electric fields of the LHI experiment described previously, the simulations evaluate the grid transparency to primary electrons around 98.5%. We have already discussed that SimuMimac can be used, after comparison to experimental data, to determine the ion mobility in the gap as well as the current threshold on the anode strips.

SimuMimac can be used to determine the optimal conditions (gas mixture, pressure, voltages, gap length) for an experiment depending on the physical quantities one wants to measure. It can also evaluate the benefits of eventual technical improvements such as reducing the strip pitch, changing the grid wires diameter, or decreasing the strip threshold. We will see in Chapter 8 that we have derived a formula for the deconvolution of the ionic signal; we used simulated data from SimuMimac to evaluate the efficiency and the bias introduced by such a method. It is also a convenient tool to push further our understanding of the detector and the physical processes.

Summary

A few years ago, we performed several puzzling measurements: we observed elongation of the measured track depths and an asymmetry of charge distribution, both being correlated with the gain of the detector. These measurements were not correctly described by our simulations and we published two papers to point out this situation. Previously our track measurements always agreed with simulations but the main difference this time was that we operate at high gain (around 2×10^4) with a large gap of 512 μm. At that stage, we believed the elongation to be the consequence of an event-based space-charge effect: the large number of ions produced by the avalanche of the first primary electrons would locally distort the electromagnetic (EM) field, in particular close to the grid wires, and consequently they would alter the motion of the successive primary electrons before they enter the amplification region. As far as we know, the simulation of this space-charge effect was not possible by standard simulation tools and we decided to implement our own code based on an extension of Garfield++.

For the geometry of the detector, as well as the gas properties, we relied on Garfield++. We have implemented our own interface with SRIM in order to generate the primary electrons cloud. We also developed a solver of the Langevin equation to describe the ion motion. To do so we made use of a significant approximation considering that a single ion type (ion mass) was produced in the avalanche and that it had constant mobility. The drift and the avalanche of the electrons were adapted from the source code of Garfield++. The most challenging part of the simulation was the computation of the local distortion of the EM field. At each timestep, and for each charge, we computed the EM field at its position as the sum of a uniform electric field, due to the applied voltages, plus a distortion EM field induced by the motion of the closest neighbour ions. We decided to proceed analytically based on a covariant formula of the Coulomb field induced by a moving charge. The EM field distortions were then taken into account in the motion of the charges.

We arrived at the important conclusion that the space-charge effect was not explaining the puzzling measurements at high gain. Our simulations were not showing any difference in the time of arrival of the primary electrons whether we include or not the EM field distortions. We have later validated experimentally such a conclusion: up to a gain of $\sim 10^5$ the time distribution of the primary electrons cloud at the grid level remains constant when the gain varies. Up to this moment, in the simulations, we had neglected the signal formation because we believed that the electronic contribution, which is almost instantaneous, was strongly dominant over the ionic one due to the detection threshold of the detector. However, this assumption is no longer valid when operating at a high gain in a gap of 512 μm.

We have eventually implemented the signal formation on the grid and on the anode strips by using the Ramo-Shockley theorem. Since we had shown that the space-charge effect was negligible, we have restructured the code in order not to compute the EM field distortions. The updated code is called `SimuMimac` and it models the physical processes involved in particle detection with MIMAC at high gain. `SimuMimac` is written in C++ and it makes use of `Garfield++` for the geometry of the detector, the gas properties, and computation of the fields. Several classes interact to simulate an event from ionization to signal formation, but the main program contains only a few lines and it can easily be used by someone not familiar with programming languages.

`SimuMimac` has been validated on experimental data. Its main success has been to reproduce the published puzzling measurements of the track elongations and the asymmetry of the time distribution of the charge deposition. It is then a very valuable and reliable tool to describe the MIMAC detector, evaluate some physical quantities as the proportion of ion backflow or the grid transparency, or estimate the influence of each process (ionization, diffusion, avalanche, signal formation) on the measured data.

Part III

Towards DM identification at the low-energy frontier

Chapter 7

Ionization Quenching Factor measurements in an SPC

The world had taken a deep breath and was having doubts about continuing to revolve.

Maya Angelou [352]

In Chapter 2, we have introduced the complexity of WIMP detection due to the large parameter space that the detectors must probe. In this searches for WIMPs, directional detection can be regarded as a complement to non-directional direct detection since it offers a strategy to unambiguously identify a WIMP although it is, for the moment, limited to small-scale detectors. Non-directional detectors however reach the ton-scale, so they are currently probing WIMP-nucleus cross-sections close to the neutrino floor, thus playing an important role in the exploration of the parameter space. The complementarity between the strategies of direct detection drove part of the MIMAC team to participate in the NEWS-G project: New Experiments With Sphere-Gas [353]. The NEWS-G detector will be presented in Section 7.1. It exploits the technology of SPCs (Spherical Proportional Counters), being an elegantly simple gaseous detector, to achieve low detection thresholds down to single electron with high-radiopurity materials at a reduced cost [354].

In Grenoble, we have an SPC of 30 cm diameter with multiple NEWS-G sensors enabling measurements in the frame of the collaboration. The comparison of the measurements in the SPC and in the MIMAC detector is enlightening concerning the physical processes happening in a gaseous TPC, such as the ionization, the diffusion, the avalanche, or the signal formation described in Chapter 4. The SPC can be coupled with Comimac, offering many possibilities for physical analyses. In this chapter, we present the measurement of the IQF of protons in methane, the discussion significantly relying on our paper [318]. We remind that the IQF is defined as the conversion between the measured ionization

energy, released by a moving ion in the active volume, to the kinetic energy, more detail can be found in Section 4.2.2. For the measurements, we use Comimac to send electrons and protons of known kinetic energies in the SPC. The experimental setup, the study of the systematic effects, and the calibration will be detailed in Section 7.2.

Direct detection is addressing the issue of searching for sub-GeV WIMPs since, as discussed in Section 2.4, the detection of light WIMPs is challenging due to the energy threshold and the difficult discrimination of the background. The recoil energy transmitted to a nucleus by such light WIMPs must be searched below the keV. The IQF then becomes a critical parameter since the proportion of kinetic energy released as ionization strongly drops in the sub-keV region. For energies below 50 keV, deviations from the predictions of the Lindhard theory [298] or simulation toolkits have been measured in multiple media: in gases [131, 300, 314, 355–358], noble liquids [299, 359], and crystals [360–362]. For this reason, one must perform an IQF measurement before a physical run searching for WIMPs. In Section 7.3, we present our measured IQF for protons in 100 mbar of methane and we discuss its implications for direct searches in gaseous detectors. We also discuss the multiple approaches used for IQF measurements.

7.1 NEWS-G: a non-directional detector in the low-mass region

7.1.1 Spherical proportional counter

The working principles of an SPC are similar in many aspects to the ones presented in Chapter 4 since it is a gaseous TPC. A schematic representation of the working principles is presented in Figure 7.1. A spherical vessel is filled with a gas mixture and it is grounded in order to act as a cathode. A small sensor is placed at the center of the sphere supported by a grounded metallic rod and the sensor is biased to a positive high voltage. As a first approximation, the electric field in the volume evolves as $1/r^2$ with r the distance to the center, dividing the inner volume into two regions: (1) the drift region with low electric field $\sim \mathcal{O}(10$ V/cm) in which the primary electrons from ionization will drift towards the sensor within typically ~ 100 μs ; (2) the amplification region with $E \sim \mathcal{O}(10$ kV/cm) in which the electrons are sufficiently accelerated to trigger a Townsend avalanche with gain typically $\mathcal{O}(10^4)$. The motion of the secondary electrons and ions produced in the avalanche induces a current on the sensor which is integrated by a charge-sensitive preamplifier (CSP) and digitized at 1.04 MHz. As for MIMAC, a WIMP entering the SPC can produce a nuclear recoil by an elastic collision on a nucleus, the nuclear recoil ionizes the gas and the primary electrons drift towards the central sensor before producing an avalanche whose signal is collected by the CSP.

The main advantages of the SPC are:

- The low-capacitance of the sensor, of the order of 0.1 pF [364], that allows for low electronic noise.
- The radiopurity of the materials. For instance, the SPC can be built in 99.99% pure copper and an additional layer of ultra-radiopure copper can be deposited in the inner surface of the SPC, limiting the activity of the detector below 0.6 μBq/kg [365].
- The simplicity of the design allowing for high-pressure operation and large detection volumes.
- A high energy resolution ($< 10\%$ at 5.9 keV [366]).
- The fiducialization by the analysis of the risetime of the pulse, that depends on diffusion, so on the radial position of the interaction [367].

The design of the sensor must address two contradictory effects [368]. First, the electric field must be large enough at large radii to collect all charges and reduce the attachment, requiring to operate with a large radius anode ball. On the contrary, to increase the electric field close to the sensor and then to operate in the high-gain mode, one must reduce the radius of the anode ball. The ACHINOS sensor has been introduced to cope with this issue. ACHINOS consists of 11 spherical anode balls of $r_A = 0.5$ mm radius, the balls being uniformly distributed around a central sphere. The balls are

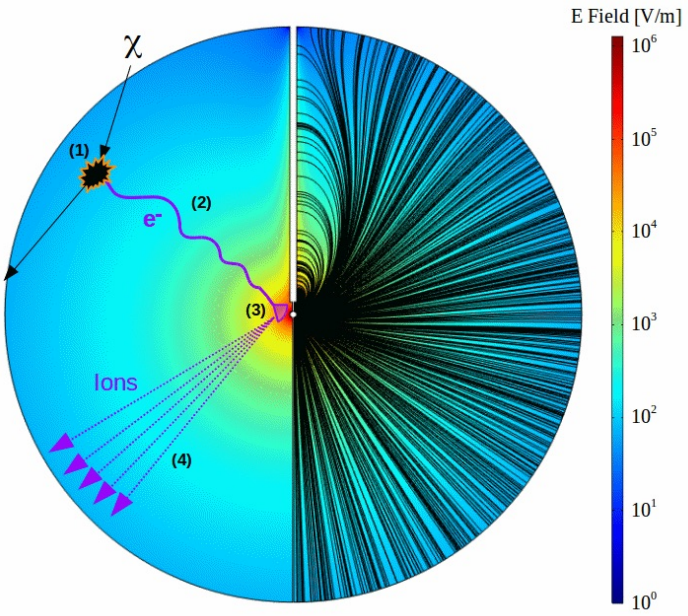

Figure 7.1: Working principle of an SPC. A sensor is placed at the center of the sphere by means of a rod. The electric field lines are represented on the right side of the sphere. A WIMP can scatter off a nucleus, whose motion produces a cloud of primary electrons by ionization (1). The primary electrons drift towards the sensor at the center of the SPC (2). Near the sensor, they generate avalanches (3). The ions produced in the avalanches drift towards the vessel (4). Figure extracted from [363].

located at a radius r_S from the center. With this geometry, the gain of the detector is governed by r_A whereas the electric field at large radii can be seen as a collective electric field from all anode balls and is governed by r_S [369]. In other words, ACHINOS presents specific features to increase the magnitude of the electric field at large radii and to operate the detector at high gain. A schematic representation and a picture of ACHINOS are shown in Figure 7.2. The 11 anode balls are separated into two hemispheres: 5 anodes near the rod, 6 anodes far from the rod, such that the signal of those two sets of anodes can be read independently. The support of ACHINOS is covered with a resistive DLC layer to reduce sparking rate and intensity, *c.f.* Section 5.4 for more detail on resistive sensors. The high-voltage is applied to all anode balls by means of insulated wires inside the grounded rod. An additional high-voltage can also be applied to the surface of ACHINOS to optimize the electric field configuration and reduce the inhomogeneities close to the rod [368].

7.1.2 A detector dedicated to sub-GeV WIMP searches

We have described above the specificities of the SPC for achieving low-energy detection. The NEWS-G collaboration has operated a prototype called SEDINE to demonstrate its ability for searching for light WIMPs (sub-GeV). SEDINE is a 60 cm diameter SPC made of pure copper. It has operated for 10 days at LSM in a mixture of Ne + 0.7% CH_4 at 3.1 bars. This run has set new constraints on WIMP down to 0.5 GeV [370]. We mention that, as a gaseous detector, the target can easily be adapted to optimize the kinematics depending on the probed WIMP mass. Recently, the NEWS-G detector has performed a run of 10 days at the LSM while operating in 135 mbar of methane (CH_4), thus exploiting the proton as a target. The results, which at the time of writing have not been published yet, set new constraints down to a WIMP mass of 0.15 GeV in the spin-dependent channel.

The direct search for light WIMP requires operating with a low detection threshold. NEWS-G aims for a sub-electron threshold, *i.e.* a detection threshold below the W-value of the gas mixture. The sensitivity to single electron has been demonstrated in a NEWS-G sphere filled with Ne + 2% CH_4 at 1.5 bar [364]. In this experiment, a monochromatic UV Laser illuminates the inner surface of the SPC to produce electrons. The current of the Laser is tuned to extract between one and about one hundred electrons. The Laser is pulsed at 10 Hz and is synchronized with the SPC in order to trigger the acquisition when at least one electron is generated. The data are adjusted by a function

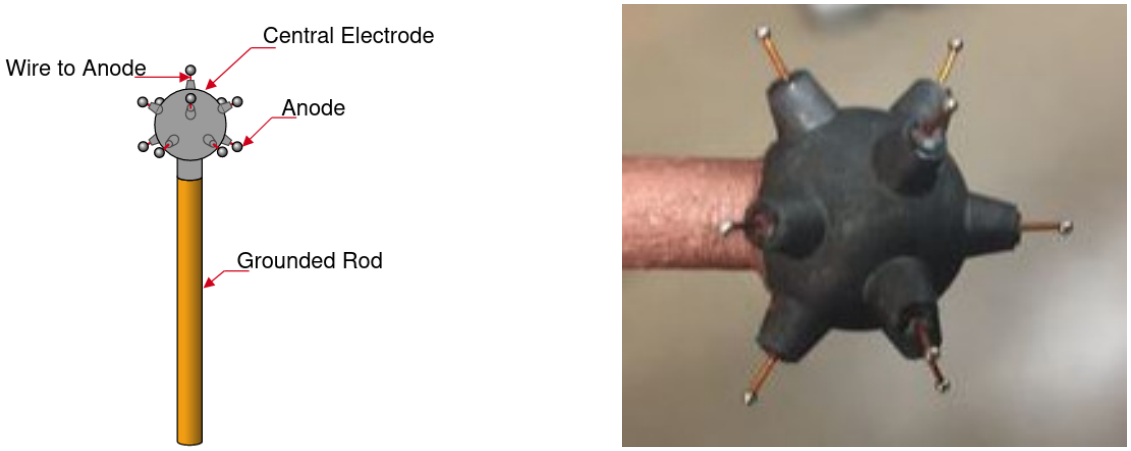

Figure 7.2: Left: schematics of the ACHINOS sensor. Figure extracted from [369].
Right: a picture of the ACHINOS sensor used for the measurements presented in this chapter. Credits: Jean-François Muraz.

that models the single electron response, accounting for statistical fluctuations in the avalanche. This analysis results in measurement precision of the order of 1% on the mean gain and its relative variance, demonstrating the ability for an SPC to achieve sub-electron thresholds.

At the time of writing, the NEWS-G collaboration finalizes the installation of an SPC of 140 cm diameter at SNOLAB [363], one of the deepest underground laboratories in the world [371]. This detector takes benefits of the recent development of the collaboration, such as the radio-purity of the detector materials and the shielding, and includes an *in-situ* calibration and a modelling of the detector response. The detector has been transported from the LSM where it has performed the 10-day campaign in methane described above. The detector will exploit multiple targets, using a mixture of Neon and methane, with an expected sensitivity down to ~ 50 $\mathrm{eV_{nr}}$ for the kinetic energy of a nuclear recoil, for setting constraints on WIMP masses down to 0.1 GeV. We have estimated that an exposure of 20 kg $\cdot$ days would probe an SI cross-section down to 10^{-38} cm^2 for a WIMP mass of 0.1 GeV and 2×10^{-41} cm^2 for a WIMP mass of 2 GeV. We mention that, beyond the searches for sub-GeV WIMPs, the NEWS-G detector is also involved in the detection of Coherent Elastic Neutrino-Nucleus Scattering (CEνNS). The SPC could also search, at the same time, for Kaluza-Klein axions by the detection of two photons of the same energy in a single time window [217], in a similar way as described in Chapter 9.

7.1.3 The complementarity between NEWS-G and MIMAC

The involvement of part of the MIMAC team in the NEWS-G collaboration is enriching in multiple aspects. First, NEWS-G is probing the sub-keV region in which the MIMAC detector is also interested. Second, we share and learn about methods for data analysis and detector improvement. Third, there is a complementarity between the two strategies of detection: the probability for NEWS-G to detect a WIMP signal is larger than for MIMAC, but then we would adapt our detector for probing similar parameter space with directionality in order to validate or reject the WIMP discovery. Finally, both detectors are gaseous TPCs measuring the ionization signal, and thus share similarities in the physical phenomena involved in particle detection.

The main differences between MIMAC and NEWS-G working principles, besides technological differences, are the following:

- The drift electric field is constant in MIMAC, leading to constant drift velocity, whereas the field in the SPC evolves roughly as $1/r^2$.
- The ions produced in the avalanche are collected on the grid in MIMAC, so they travel ~ 512 μm, whereas they are collected on the cathode in the SPC, except if they recombine before.

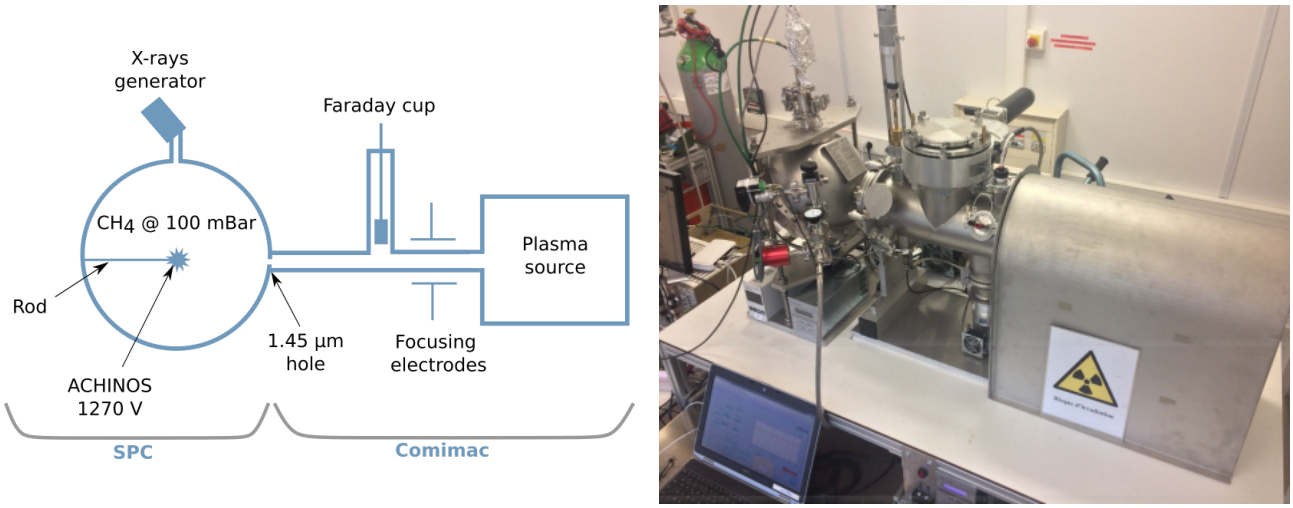

Figure 7.3: The experimental setup coupling the SPC to Comimac. The left panel presents schematics of the setup. The right panel shows a picture of the experiment.

- The weighting field of ACHINOS is non-linear and depends on the geometry of the sensor whereas the weighting field of the MIMAC grid can be considered constant.

These differences mainly affect the drift of the primary electrons cloud, the avalanche, and the signal formation. The comparison of the responses of the two detectors for a similar input particle, for instance an electron sent by Comimac, is then enlightening for a better understanding of the detectors. In the following section, we will give an example illustrating how the use of two complementary detectors teaches us about the physical processes involved in the electron calibration.

7.2 The SPC coupled with Comimac

7.2.1 Experimental setup

The results presented in this chapter have been obtained with an experimental setup coupling an SPC to Comimac, as presented in Figure 7.3. The SPC used in the experiment consists of a grounded 30 cm diameter vessel made of stainless steel filled with 100 mbar of CH_4. The ACHINOS sensor is placed at the center of the SPC by means of a grounded metallic rod and the sensor is biased to a positive high voltage (1270 V). The 11 anode balls are polarized to the same voltage and are read by a single CSP whose signal is digitized at 1.04 MHz. We define the measured ionization energy in ADU (Analog-Digital Units) as the amplitude of the signal given by the CSP after correction of the ballistic deficit. This ballistic deficit depends on the time constant of the CSP (measured to be 51.8 μs) which is small compared to the signal duration of a few hundred of microseconds. In other words, it means that the signal starts decaying before all the charges have been collected. We correct the ballistic deficit by deconvolving the CSP self-discharge following the approach described in Section 5.1.

The SPC is coupled to the Comimac facility, described in Section 5.5, by a circular hole of 1.45 ± 0.06 μm diameter, insuring pressure independence between the SPC and Comimac. The pressure in the SPC is monitored continuously with a pressure gauge and only suffers variations due to temperature changes (< 0.5 mbar). The SPC is also coupled to an X-ray generator that sends high-energy X-rays on thin layers of cadmium and aluminium. The excited atoms will emit fluorescence X-rays (1.49 keV for K_x-Al ; 3.23 keV for L_x-Cd [317]) that will produce photoelectrons of known energy at any radius inside the sphere. As we will later see, the fluorescence X-rays are used to cross-check the kinetic energy of the electrons sent by Comimac.

The data used for the electron calibration and the IQF measurements have been taken in a single day with the same charge of gas. The detector was stable during the measurements: the measured energy of a reference Comimac point (6 keV electrons) varied by less than 1% between the beginning and the end of the experiment. The number of events in the electron runs is always larger than 30×10^3

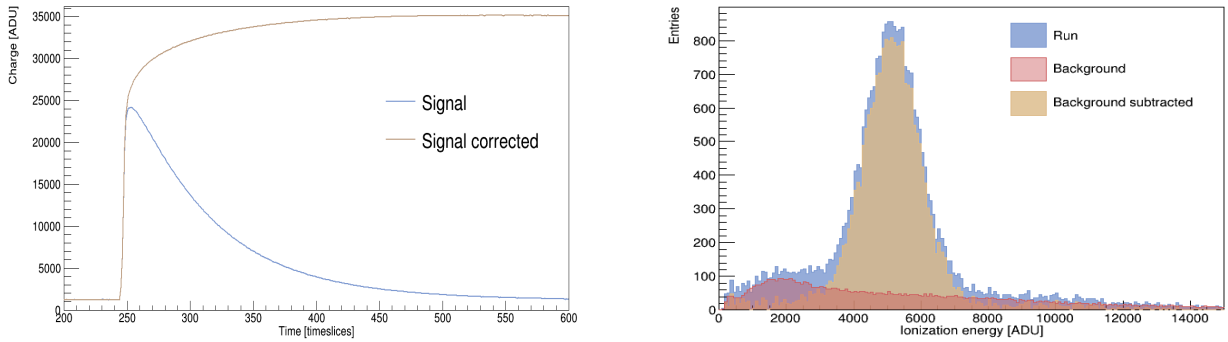

Figure 7.4: Examples of the treatment applied to the data. Left: correction of the ballistic deficit on the measured signal by applying the procedure described in [315]. Right: background subtraction for 1.5 keV electrons.

while for protons it varies between 3×10^3 and 13×10^3, the disparity depending on the proportion of heavier species sent by Comimac.

In the analysis, we do not apply any cut to the data: we keep all events. The only treatment applied to the data is the correction of the ballistic deficit and a subtraction of the background to the measured energy spectrum. An example of these manipulations is presented in Figure 7.4.

The main background contribution comes from cosmic rays creating particles in the atmosphere, like muons, that can produce signals in the SPC in the keV-range [372]. The background remains constant throughout the experiment with a high signal-over-background ratio. In these conditions, the background energy spectrum, measured in the same experimental conditions as for Comimac measurements, can be subtracted from the other energy spectra after time normalization. The background rate has been measured to 23 Hz, a rate that remains low compared to the Comimac rate that varied between 50 Hz and 200 Hz depending on the particle species sent (electrons or ions, respectively). The proportion of Comimac events affected by random coincidences with muons is around 2%. The right panel of Figure 7.4 shows an example of the background subtraction for the lowest energy point exploited in the analysis (1.5 keV electrons).

7.2.2 Study of systematic effects

The measurements of the IQF represent an experimental challenge and the systematic effects must be carefully studied. In this section, we detail the main systematic effects and the dedicated analyses we have performed in order to quantify them.

Energy loss in the Comimac interface

The hole that interfaces Comimac to the SPC has a diameter of 1.45 μm and a thickness of 13 μm. The particles sent by Comimac can interact inside the hole and some of them could then enter the SPC with a lower energy than before the hole. We have quantified the energy loss in Comimac's hole by means of simulations described in Section 5.5 whose results are presented in the right panel of Figure 5.17: for 100 mbar of CH_4 the simulated energy loss in the interface hole remains below 1% both for electrons and for protons in the considered energy range, *i.e.* for $E_K > 1$ keV. The percentage of energy loss obtained by simulations can be parametrized by a polynomial function $f(E_K) = \gamma\ E_K^{-\delta}$ with γ and δ determined by fitting the simulation results: $\gamma = 0.61$ and $\delta = 1.56$ for electrons, $\gamma = 0.83$ and $\delta = 0.54$ for protons in 100 mbar of methane. In our analysis, we use this parametrization to correct the kinetic energy of the particles, *i.e.* we subtract the amount of energy lost in the interface to the total kinetic energy given by Comimac. Such simulations can only give a first estimate of the energy loss, in particular since they rely on `SRIM` while we will later show some discrepancies between measurements and `SRIM` simulations. We thus decide to work with a conservative uncertainty of 100% on the value of the energy loss.

Comparison between Comimac electrons and fluorescence photoelectrons

We used the X-ray generator to produce photoelectrons of 1.49 keV and 3.23 keV [317] by fluorescence as explained in the previous section. According to CXRO database [373], 94% of the fluorescence X-rays of the cadmium travel 15 cm without interacting. For this reason, while this setup does not produce photoelectrons everywhere in the volume, it does produce them at all possible radii within the detector, and so we assume they will integrate any potential volume effects. On the contrary, the Comimac electrons are always sent at the same position: at the SPC surface through the hole. The range of the particles remains low: 7 mm for 5 keV electrons (according to `Casino`) and 1.4 mm for 5 keV protons (according to `SRIM`). Thus, comparing fluorescence photoelectrons and Comimac electrons is of particular interest for validating two assumptions: (1) that the electric field in the SPC is strong enough to collect all the charges, even from the surface; (2) that the kinetic energy of the electrons sent by Comimac is well determined.

We define $R \equiv (E_{\text{Comimac}} - E_{\text{X-rays}})/E_{\text{X-rays}}$, a ratio that quantifies the difference between the ionization energy measured for a fluorescence photoelectron and the one measured for a Comimac electron. We obtain $R(1.49 \text{ keV}) = 3.7\% \pm 0.5\%$ and $R(3.23 \text{ keV}) = 3.9\% \pm 0.5\%$, respectively for the aluminium line and for the cadmium line, indicating that we measure slightly more ionization energy for the Comimac electrons than for the photoelectrons, excluding energy losses in the interface between Comimac and the SPC as a possible explanation for the difference. The measurements with the X-ray generator have been performed with a fresh charge of gas compared to the other measurements but we applied the same working conditions. The different charge of gas has a non-negligible influence on the gain of the detector so we must scale the measured energies by comparing the position of the energy peaks in both datasets. This scaling brings an additional uncertainty that we propagate through our calculations.

From this analysis, we conclude that we efficiently collect the charges down to 1.49 keV, even the ones produced at the SPC surface and we validate the kinetic energy of Comimac. Due to the ACHINOS geometry, Comimac electrons mainly induce a signal on the anode ball aligned with the Comimac beam, while in the case of photoelectrons (having more heterogeneity in production position), a signal appears in several anode balls. Gain discrepancies between the anode balls [369] could explain the measured differences, in particular since the energy resolution deteriorates by about 13% for photoelectrons compared with Comimac electrons of the same energy. For the rest of the analysis, we will consider a conservative uncertainty of 4% on the kinetic energy sent by Comimac. Note that this uncertainty also embeds the energy loss for electrons in the Comimac's hole described above.

The event rate with the X-ray generator is $\sim$ 400 Hz, which is about 8 times larger than for Comimac electrons. The measured energy could depend on the rate, for instance, if the ions drifting towards the cathode build a space charge [339]. We have checked that in our conditions we are not sensitive to a rate effect. To do so, we have sent 15 keV electrons with Comimac and we have varied the event rate up to 360 Hz which is comparable to the rate obtained with the X-ray generator. We do not report any change in the measured energy up to this rate, from which we conclude that the X-ray measurements can be compared with the Comimac measurements.

7.2.3 Electron calibration

Electrons of known kinetic energies are sent in the detector by the Comimac facility. They are used to calibrate the detector by measuring the amplitude of the signal obtained for the Comimac electrons.

Figure 7.5 shows a superposition of the entire set of energy spectra obtained from Comimac electrons runs, after the background subtraction previously detailed. Each of the energy spectra presents the expected Gaussian shape and fits can be performed. The energy resolution, FWHM divided by the mean value, ranges between [13.2 % , 32.7 %]. This good energy resolution, as well as the unambiguous determination of a Gaussian peak in each spectrum, leads to small statistical uncertainties compared to systematic uncertainties. The avalanche gain of the detector is determined by the use of a pulse generator combined with a capacitor to inject a charge into the CSP. We obtain a gain of 1.5×10^4 using a W-value of 27 eV [277].

The electron calibration is shown in Figure 7.6 taking into account the correction of the energy

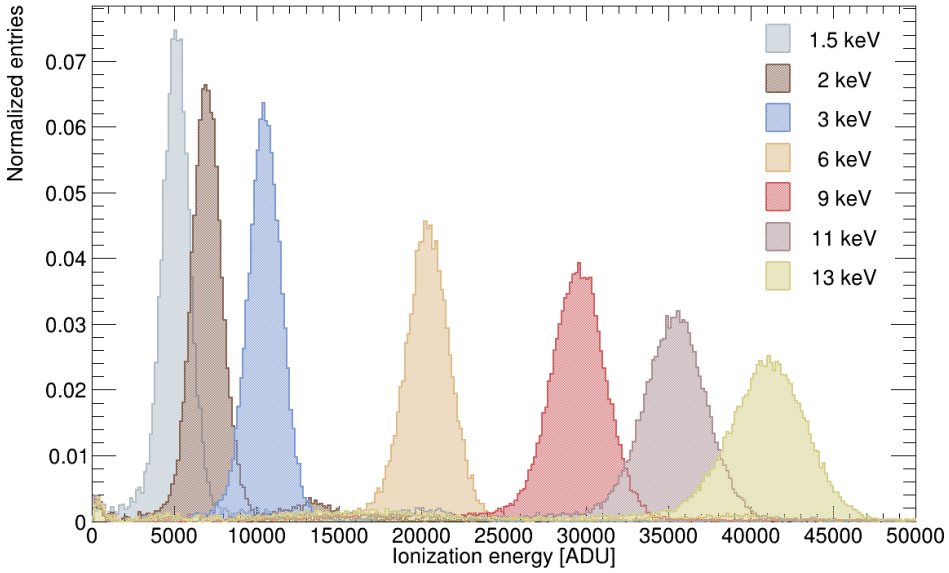

Figure 7.5: Complete set of energy spectra used for the calibration of the detector response. The kinetic energy is determined by the Comimac facility. The cosmic background has been subtracted but no cut is applied.

loss in the Comimac hole as detailed previously. The statistical uncertainties of the energy spectra are included in the error bars in Y. The error bars in X correspond to the uncertainty on the Comimac energy that embeds the 4% difference observed with X-rays and the uncertainty in the energy loss in Comimac's hole.

The calibration presents a non-linear tendency that can be well-fitted by a first-order polynomial function plus a decreasing exponential function. We have chosen to represent a linear function on the same plot, as a dashed line, this function passing through the first data point and having a small offset (-117 ± 15 ADU which is equivalent to -32 eV). This offset value corresponds to a linear extrapolation of the response of our acquisition chain. For this measurement, the SPC was coupled to a pulse generator and we varied the pulse amplitude to cover a detector response region from 3×10^3 ADU up to 26×10^3 ADU. In other words, the dashed line in Figure 7.6 represents the calibration expected from the response of the acquisition chain. This linear function highlights a departure from linearity above 4 keV that could be due to the high gain of the sensor. While the exact mechanism that introduces this non-linearity is not fully understood, it has already been observed in Proportional Counters operating at high gain [374, 375].

To understand the origin of such a phenomenon, we have performed an electron calibration with Comimac in a MIMAC chamber with a 256 μm gap filled with 100 mbar of methane. This analysis will be presented in Section 8.2, in Figure 8.8, while discussing a deconvolution of the signal induced on the grid by the moving ions in the amplification region. At this stage, it is sufficient to say that we also measured a deviation to linearity with the Micromegas, although opposed to the one observed with the SPC since we measured more ionization at large kinetic energies. We have demonstrated that this non-linearity was due to the specific case of signal formation in methane since, in this experimental configuration, the contribution of the ionic signal in the Micromegas grid significantly dominated the signal induced by the secondary electrons. We could recover a linear calibration by extracting the electronic signal from the measurements.

This analysis gives an example of the complementarity between NEWS-G and MIMAC. However, our understanding of the non-linearity in the MIMAC detector cannot directly be extrapolated to the SPC case due to the multiple differences previously described impacting the signal formation. We can postulate that the signal induced by the numerous ions produced in the avalanche, and drifting towards the SPC cathode, could alter the amplitude of the CSP signal at large energies. However, the validation of this hypothesis was out of the scope of our analyses.

We have reproduced our measurements at a lower ACHINOS voltage, 1230 V instead of 1270 V,

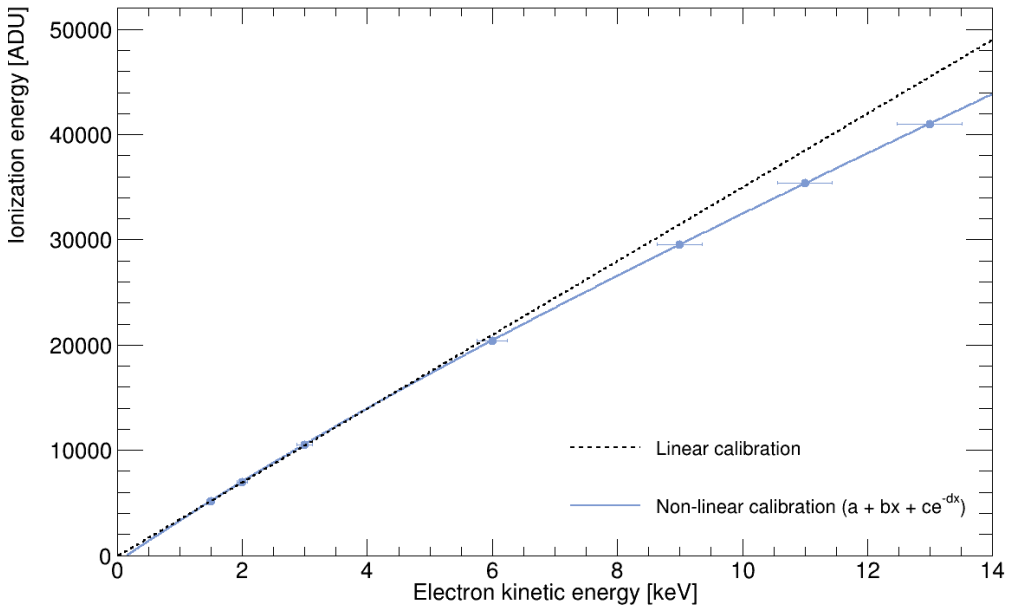

Figure 7.6: Electron calibration. The dashed line represents a linear calibration passing through the first data point and having an offset of −117 ADU. The solid blue line is a fit with a first-order polynomial function plus a decreasing exponential function. Error bars are drawn in X and Y but they are hardly visible in Y.

in order to better understand the influence of the high gain on the departure from linearity. The ratio of the ionization energies at the two voltages remains constant in the entire tested region (between 3 keV and 13 keV) with variations of less than 2%. This analysis indicates that we are operating in a voltage region where the deviation from linearity seems not to depend on the avalanche gain. In other words, this analysis demonstrates that, even though the phenomenon behind the non-linear calibration is not fully understood, one can still compare the ionizations released by an ion and by an electron to measure the IQF.

7.3 Measurements of the proton IQF in methane

7.3.1 Discussion about IQF measurements

Let us have a short break in the data analysis to discuss the complexity of measuring the IQF. Theoretically, the quenching factor in the Lindhard theory [298] is the ratio of energy given to the electrons of the medium over the total energy loss. In Section 4.2.2, we have introduced the IQF defined as the fraction of the kinetic energy released as ionization energy in a medium. The IQF is a more convenient definition for our experimental purposes, since it directly converts the measured ionization energy released by a moving ion into the total kinetic energy of the particle. Measuring the IQF requires then two elements:

- **The production of an ion of known kinetic energy** in the detection volume. Alternatively, since the IQF for an ion is the same than the IQF for a nuclear recoil [297], one can make use of an elastic collision for producing a moving nucleus of known kinetic energy in the active volume.
- **The measurement of the ionization energy**. The measured ionization, which is usually a digitized charge, must then be converted, thanks to a calibration, into an ionization energy to be compared to the incident kinetic energy. A calibration in an ionization TPC is usually performed using electrons as reference particles (an X-ray source will ultimately produce photo-electrons in the gas). However, to the best of our knowledge, it has not been demonstrated that an electron releases its entire kinetic energy into ionization. For experimental purposes, that is for using a detector calibration, the definition of the IQF is then updated: the IQF is expressed as the

ratio of the ionization energies released by an ion and by an electron of the same kinetic energy. Mathematically, it means $\mathrm{IQF(E_{nr})} = \mathrm{E_{ee}/E_{nr}}$ with E_{ee} the electron-equivalent energy and E_{nr} the nuclear recoil energy.

Several experimental procedures can be used to measure IQFs and we will introduce the main ones: using an accelerator as Comimac, using a neutron field, exploiting the thermal neutron capture, and making use of W-value measurements.

In this chapter, we present a measurement performed with Comimac, an original facility developed for IQF measurements. Besides the simplicity of the setup, the main advantage of Comimac is the ability to send ions and electrons in the exact same conditions, so the comparison of the measured ionization energies is a direct measurement of the IQF. In this approach, the IQF is not determined event-by-event, but is rather obtained by a comparison between the proton and the electron energy spectra. The kinetic energy of the particle is a free and known parameter that is determined by the extraction polarization. The only background is due to cosmic particles and natural radioactivity since we can select the ion species sent inside the detector.

Most of the experiments for measuring the IQF are exploiting neutron fields [360, 376–379]. In these experiments, a mono-energetic neutron field is produced by a nuclear reaction on a target. The neutron can make an elastic collision in the detector, generating a nuclear recoil whose ionization energy is measured by the detector. The kinetic energy of the nuclear recoil is determined from kinematics knowing the incident neutron energy and by measuring the scattering angle thanks to a coincident detection of the scattered neutron in a backing detector (BD). As an illustration, Figure 7.7 presents the experimental setup of [355] in which the IQF of neon nuclei in a neon gas is measured using an SPC of the NEWS-G collaboration. In this experiment, the BDs are liquid scintillators coupled with photomultiplier tubes whose pulse shapes can be used to distinguish between a neutron signal and a gamma signal. The data analysis requires several steps:

- **Discrimination of the background**. The production of the neutron field via the (p, n) nuclear reaction on the target also produces gammas. The gammas are discriminated in the BD thanks to the pulse shape of the signal and the time of flight between the target and the BD. In the SPC, they are discriminated from the rise time of the charge signal.

- **Identification of a coincidence event between the SPC and a BD**. This identification is done by comparing the trigger times in the BDs and the SPC. The comparison must take into account the drift time of the primary electrons depending on the radius of the interaction.

- **Determination of the scattering angle** from the distance to the triggered BD. The uncertainty on the reconstructed scattering angle includes both the uncertainty on the position of the interaction inside the SPC and the one on the incident direction of the neutron.

- **Reconstruction of the IQF**. In [355], the analysis performs a joint fit of all datasets from a likelihood function having 19 free parameters and 6 fixed parameters.

The measurement of the IQF using a neutron field is then a complex analysis requiring the control of multiple experimental parameters.

Another approach for measuring the IQF consists in exposing a detector to a thermal neutron field to produce a neutron capture [380]. After the capture, the excited atom can emit a photon of known energy, resulting in a nuclear recoil. Since the incident neutron must be thermalized, its kinetic energy can be neglected and the kinetic energy of the nuclear recoil is then determined from kinematics as $E_R = E_\gamma^2/2m$, with m the mass of the recoil. For instance, one could measure the IQF of deuterons by means of the nuclear reaction $^1\mathrm{H} + \mathrm{n} \rightarrow {}^2\mathrm{H} + \gamma$ that emits a gamma of energy $E_\gamma = 2.224$ MeV [381], resulting in a deuteron recoil of kinetic energy $E_R = 1.3$ keV. This method presents the advantages of the precision of the determination of the nuclear recoil energy, as well as the possibility of measuring the coincident gamma for discriminating the background.

Finally, let us mention a novel approach for IQF estimation that has been proposed in [382]. It relies on the W-value for electrons, W_e, and ions, W_i, and suggests the following relation $\mathrm{IQF(E)} = \mathrm{W_e(E)/W_i(E)}$. The advantage of this approach is the possibility of using numerous precise W-value

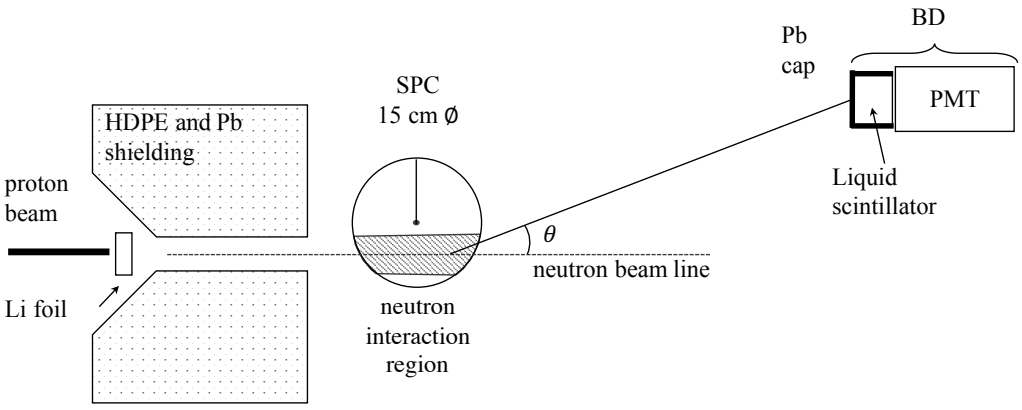

Figure 7.7: Scheme of the experimental setup reported in [355] to measure the IQF of neon nuclei in a neon gas using a neutron field and an SPC.

measurements. However, we have discussed in Section 4.2 that W-value measurements cannot easily be extrapolated to the experimental conditions of gaseous TPCs: having non-zero amplification and arbitrary pressure. From our understanding, this approach is misleading since it does not provide the IQF in experimental conditions, but rather an upper limit estimated in optimized conditions for W-value measurements but not for WIMP searches.

7.3.2 IQF results

We are now ready to present our measurements of the IQF of protons in methane. Protons of known kinetic energy are sent in the SPC by applying a positive extraction voltage on Comimac. The gas placed in the Comimac source, which turns into a plasma, contains a mixture of H_2 and He. For this reason, Comimac will send several types of ions: H^+, He^+, but also heavier species as N^+ or H_2O^+ due to water contamination and surface out-gassing in the source [330]. According to the Lindhard theory [298], the proton is the particle that releases the largest proportion of its kinetic energy through ionization. We thus identify the proton as the peak with the highest ionization energy, the peak being Gaussian and well separated from the others. The complete set of measured proton spectra is presented in Figure 7.8. We use a sum of two Gaussian as a fit function, modelling the proton and the helium peaks, with a fitting range starting in the tail of the helium peak in order to account for possible overlap between the peaks. In each spectrum, the relative amplitude of the peaks depends on the focusing parameters of the Comimac beam.

The breaking of the H_2 molecule into protons in the Comimac source depends on the amount of He in the source: it must contain enough He so that the electron cyclotron resonance (ECR) sufficiently ionizes the plasma to break the molecular hydrogen. In the experiment performed at 1230 V, we observed the presence of an additional ion that we identified as H_2^+ as presented in Figure 7.9. Its separation from the H^+ peak was only possible for kinetic energies above 9 keV. The presence of the H_2^+ contamination is not correlated with the gain of the SPC but only with the amount of He introduced in the Comimac source. While the contamination with H_2^+ in the source limited our IQF measurements at 1230 V, we do not observe this additional peak in the 1270 V campaign. Note also that the IQFs for protons agree between the two campaigns, at least down to 9 keV. We thus conclude that we have efficiently broken the H_2 molecule into protons during the 1270 V campaign, that is the data that we later use to parametrize the IQF.

We use the electron calibration as a reference for the kinetic energy, allowing us to write:

$$\text{IQF}\ (E_K)\ =\ \frac{f_{\text{calib}}(E_{\text{ADU}})}{E_K} \tag{7.1}$$

where E_K is the ion kinetic energy and $f_{\text{calib}}(E_{\text{ADU}})$ is the calibration function that converts the measured ionization energy, E_{ADU}, into the kinetic energy that an electron would require to produce such a signal. The main advantage of this approach is to compare directly the electrons and the ions produced in the same conditions.

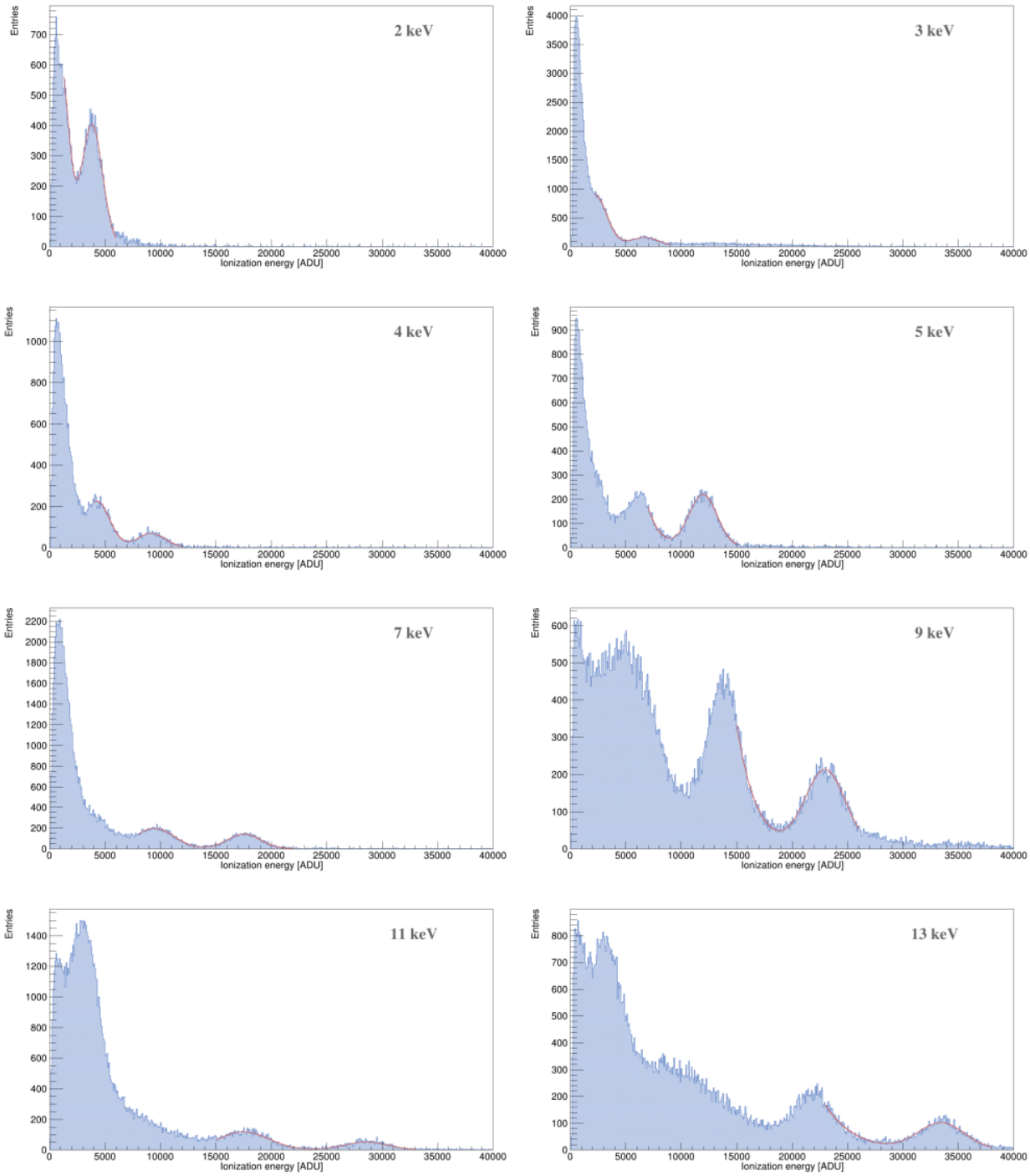

Figure 7.8: Complete set of proton spectra measured at 1270 V. The fit functions of two Gaussian, used for the analysis, are shown in red. In each spectrum, the proton peak can be identified as the one with the highest ionization energy. The second peak from the right corresponds to helium.

The measured IQF is presented in Figure 7.10. For comparisons, we show `SRIM` simulations and the prediction of the Lindhard theory with the parametrization described in [359]. Measurements at 1230 V and 1270 V are presented and they agree, at least down to 9 keV. We consider this agreement as evidence that the reported IQF values do not depend on the observed high-gain effects, although definite proof would require data with larger spreads in gain. The uncertainties account for the effects described previously as well as statistical uncertainties. The main contribution to the error bar is due to the 4% uncertainty on the Comimac kinetic energy. There was no calibration data for the ion recoils, so we assume that the uncertainty on the energy of the ions is the same as for the electrons.

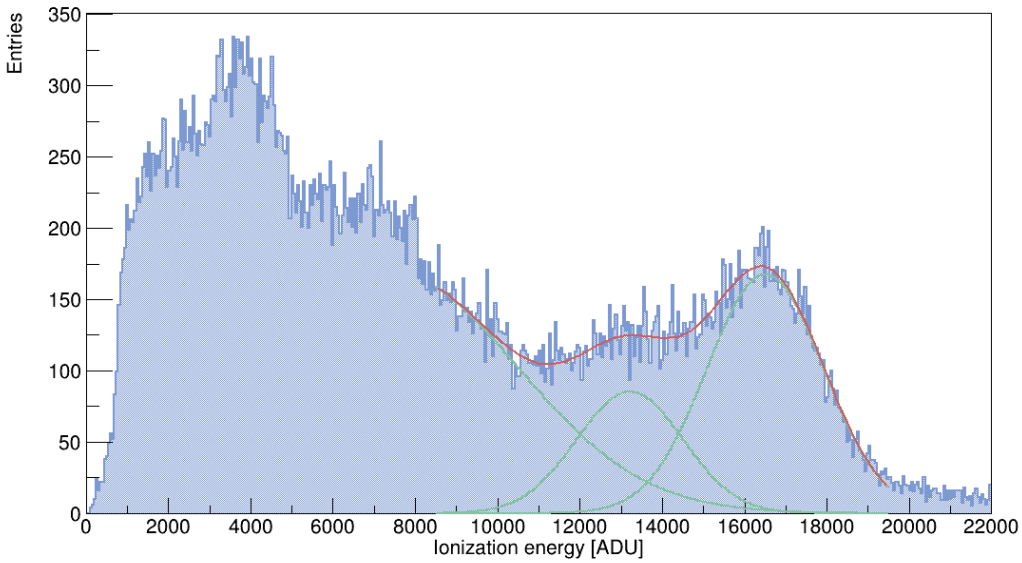

Figure 7.9: Example of a 9 keV proton spectrum at 1230 V showing the difficult separation between H_2^+ and H^+. The H_2^+ peak can be identified around 13000 ADU whereas the H^+ peak is around 17000 ADU. The presence of H_2^+ is related to the low amount of He introduced in the Comimac source during this campaign.

Following the approach of [359] we propose a simplified parametrization of the IQF for the proton:

$$\text{IQF}\ (E_K)\ =\ \frac{E_K^\alpha}{\beta + E_K^\alpha} \tag{7.2}$$

where we determine $\alpha = 0.70 \pm 0.08$ and $\beta = 1.32 \pm 0.17$ by fitting the experimental data. This fit function is also shown in Figure 7.10. To the author's knowledge, this work presents the first measurement of the IQF of protons in methane.

We observe a deviation from `SRIM`, in particular at low energy, that reaches 33% at 2 keV. Similar deviations with lower ionization energy than predicted by `SRIM` have already been observed in several gas mixtures [131, 300, 314, 356, 357]. The NEWS-G collaboration has recently measured a deviation from `SRIM` in the opposite direction (measuring more ionization energy) for neon nuclei in neon gas [355] with the setup described in the previous section by using a neutron field. It has to be noted that the `SRIM` quenching does not vary with the pressure whereas we have previously observed that the IQF in the keV-range depends also on the gas pressure [300].

7.3.3 Implications for WIMP searches

At this stage, and as often pointed out in the literature, we have enough elements to say that the IQF must be measured experimentally instead of being simulated by `SRIM`. In the direct DM community, `SRIM` is commonly used for track length simulations, as we are also doing in Chapter 6, and it is also sometimes used for determining the IQF while deriving exclusion limits. We here stress that the `SRIM` quenching is overestimated compared with measured IQF in gases, which would result in too optimistic exclusion limits.

Besides the mis-reconstruction of the kinetic energy of a nuclear recoil, an error on the IQF also influences the detection threshold. In the low-energy region, the IQF drops non-linearly to low values and then limits the detectable ionization energy. The NEWS-G collaboration is currently writing a paper setting WIMP exclusion limits from proton recoils in methane, down to a WIMP mass of 0.15 GeV requiring to search proton recoils with a kinetic energy below 100 eV. Since we did not measure the IQF below 2 keV, the NEWS-G collaboration decided to parametrize the IQF from W-value measurements [382], as introduced at the beginning of this section, but including a scaling factor of 0.85 accounting for the 15% difference between the W-value IQF and the Comimac measurements. With

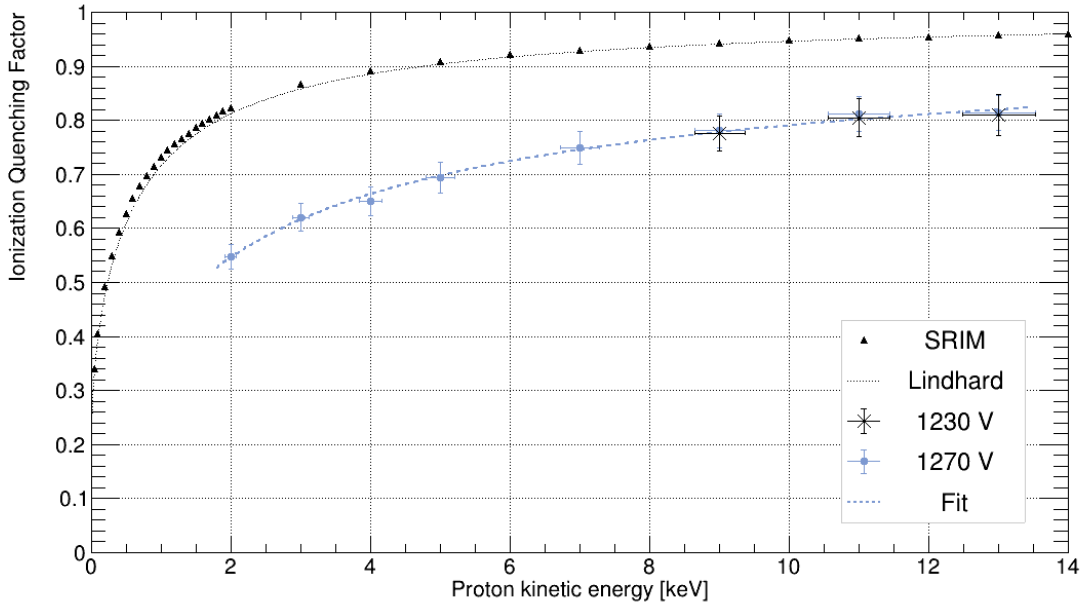

Figure 7.10: Ionization Quenching Factor for protons in 100 mbar of methane. The measurements at 1230 V and 1270 V are respectively presented with black crosses and blue dots. Comparisons with `SRIM` and with the Lindhard theory are also shown.

this normalization factor, the scaled IQF remains always equal or lower than our IQF measurements and its extrapolation; it is thus a conservative IQF.

There is however no experimental value below 510 eV for estimating the IQF from Comimac or the W-value method. Two parametrizations are then proposed below this energy: a Lindhard-like parametrization similar to Eq. (7.2) and a more conservative logarithm parametrization. The logarithm parametrization gives a null IQF below 150 eV, thus setting an irreducible limit for the detection threshold of the detector, whereas the Lindhard-like parametrization leads to an IQF of 11% at this energy. For comparison, the `SRIM` quenching is equal to 47% at 150 eV. We here see the drastic influence of the IQF for low-mass WIMP searches. While in one case, no ionization is detectable below 150 eV, relying on `SRIM` would predict a detection threshold at a kinetic energy below 50 eV.

Summary

The NEWS-G collaboration, including part of the MIMAC team, has developed an SPC for sub-GeV WIMP searches. The SPC is a spherical gaseous detector based on the TPC principles. A sensor is placed at the center of the sphere, providing an electric field evolving roughly as $1/r^2$, thus separating the volume into a drift region and an avalanche region near the sensor. This design has several advantages such as a low capacitance, a simplicity allowing for high-radiopurity at a reduced cost, and a high energy resolution. The collaboration has demonstrated that the detector can be sensitive to single electron signal, leading to a detection threshold down to ~ 50 eV in kinetic energy, allowing to search for WIMP masses down to ~ 0.1 GeV. The complementarity between the SPC and MIMAC is first related to the interplay between non-directional and directional detections in the WIMP identification process. The two detectors share many similarities, for instance in the ionization process, while some differences happen during the drift, avalanche, and signal formation. The comparison between MIMAC and SPC measurements thus offers instructive and valuable information for describing the physical processes involved in the detection.

The Ionization Quenching Factor (IQF) is a crucial quantity for WIMP searches in an ionization detector since it converts the measured ionization into the kinetic energy of the nuclear recoil. The IQF depends both on the properties of the moving nucleus (mass and energy) and on the detection medium

and its density. The measurement of the IQF is an experimental challenge and it is usually performed by exploiting a neutron field to produce nuclear recoils whose kinetic energies can be determined by a complex analysis. In this chapter, we present an IQF measurement performed by coupling an SPC to the Comimac facility. This simple experimental setup enables the direct comparison between the ionization released by an electron and the one released by an ion (that has the same IQF than a nuclear recoil), thus leading to the IQF measurement without applying any cut to the data.

We dedicate special attention to the systematic effects during the measurements. Some energy can be lost in the interface between Comimac and the SPC, although the measured energy spectra are Gaussian and well-resolved, and simulations indicate that it remains below 1% in the considered energy range. We also investigate a possible volume effect since the Comimac particles are sent at the surface of the SPC. We thus compare Comimac electrons to fluorescence photoelectrons produced by an X-ray generator irradiating metal foils, demonstrating that the charge collection at the surface is efficient. The electron calibration however presents a non-linearity that is probably related to signal formation but that is not yet fully understood. By comparing measurements at two different detection gains, we conclude that the IQF measurements are not affected by the calibration non-linearity.

We present measurements of the IQF of protons in 100 mbar of methane between 2 keV and 13 keV in the SPC. The measured IQF lies below the `SRIM` and the Lindhard quenching factors, the difference reaching 33% at 2 keV. Such a difference has often been pointed out in the literature and it has important consequences on WIMP exclusion limits: an overestimation of the IQF gives a too optimistic detection threshold and does not estimate properly the kinetic energy of the nuclear recoil. We conclude that the IQF must systematically be measured and that DM direct experiments should not rely on simulations for determining the IQF.

Chapter 8

Directionality in the keV-range

No one can predict the surprises that surely lie ahead as we attempt to shed light on nature's dark secret.

Vera Rubin [383]

In Chapter 2, we have described the privileged role played by directional detection to identify a WIMP-nucleus interaction event. Multiple directional features of the event rate for WIMP-induced recoils cannot be reproduced by the background, allowing a discovery potential beyond the neutrino floor, which is the irreducible background for direct detection with the residual neutrons. Directional information also enables the reduction of the number of events required for setting exclusion limits compared to non-directional detectors.

A WIMP typically transfers, at maximum, a recoil energy of 10 keV/nucleon so nuclear recoils must be searched in the keV-range, in particular for WIMP of mass below 100 GeV. In this low-energy region tracks are short, even in low-pressure TPCs. For instance in the *Mimac gas* at 50 mbar, `SRIM` predicts a track length of 4.6 mm for a 20 keV proton, and only 615 μm for a 20 keV fluorine. Measuring the directional information of millimeter-tracks is definitely challenging, in particular because it is comparable to the spatial resolution of a detector (remind that the MIMAC strip pitch is 424.3 μm). In [173] and [174] we claim that diffusion is a tool in such a case because it enlarges the primary electrons cloud, almost gaussianly, enabling track detection by several pixels and timeslices while preserving most of the directional information.

In order to fully describe the nuclear recoil track at low energy, directional detectors must be sensitive to any primary charge which requires to operate at high gain ($> 10^4$). In a Micromegas we boost the gain by increasing the voltage applied on the grid but also by operating with a large

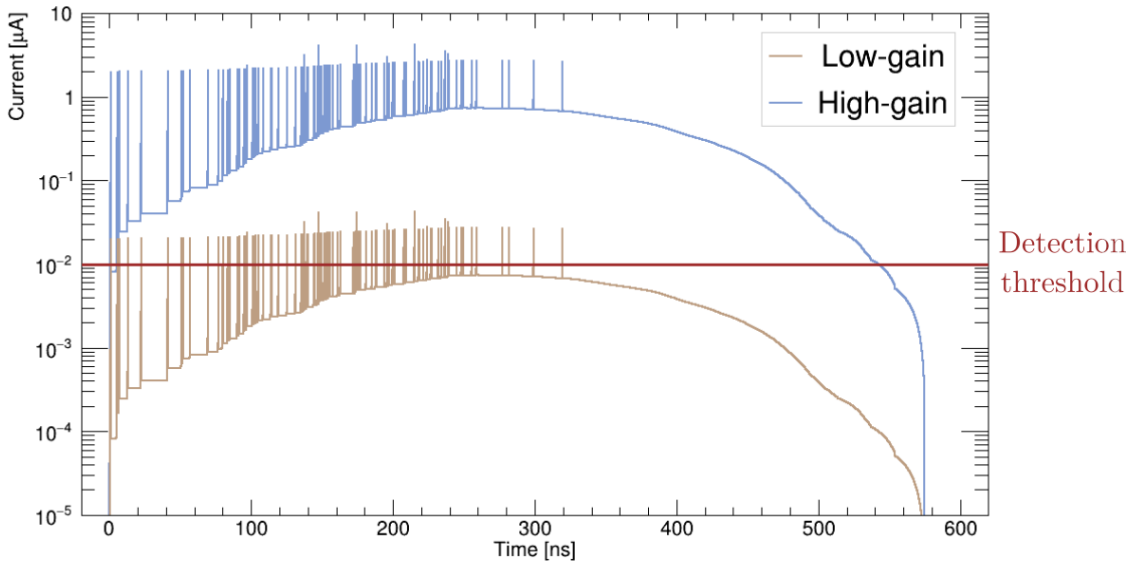

Figure 8.1: Influence of the gain on detection. The primary electrons cloud follows a typical distribution for a single event of 10 keV proton. The current is determined analytically from the Dris and Alexopoulos model described in Chapter 4. The peaks correspond to the electronic signal, with a typical duration of 1 ns, and the baseline is the contribution of the ionic signal. A signal is measured on the Flash when the current exceeds the detection threshold represented in red.

gap (512 μm) since it gives more distance for the avalanche to develop. As a drawback, in this configuration the detector gets more sensitive to the signal induced by the numerous ions accumulated in the amplification area. The interplay between the abrupt electronic signal and the blunt ionic one causes the distortions of the measured 3D tracks. This issue, while already discussed in Chapter 6, will be presented from another perspective in the preamble 8.1.

We have developed a model to analytically separate the electronic and the ionic contributions from the Flash signal (*c.f.* Section 4.1 for a reminder on the Flash signal). This deconvolution will be detailed in Section 8.2. We will see that the deconvolution gives access to the time distribution of the primary electrons cloud at the grid, so just before the avalanche. This valuable information provides a new approach for determining the ionization energy, by the integral of the deconvolved signal, and it also improves the MIMAC ability to distinguish between the head and the tail of the track, so to measure the sense of a nuclear recoil.

The performance of a directional detector can be evaluated thanks to a mono-energetic neutron field. A neutron of kinetic energy E_n and mass m_n induces a nuclear recoil with kinetic energy E_R on a target of mass m_A, given in the lab frame as:

$$E_R = 4\frac{m_n m_A}{(m_n + m_A)^2} E_n \cos^2\theta_R \tag{8.1}$$

where θ_R is the scattering angle between the incident neutron direction and the recoil direction. The equation simplifies to $E_R = E_n \cos^2\theta_R$ for proton recoil. Knowing the kinetic energy of a mono-energetic neutron source, the simultaneous measurements of the kinetic energy of a WIMP-induced nuclear recoil and of the corresponding scattering angle should satisfy Eq. (8.1). The angular distribution of proton recoils induced by neutrons is centred on 45°. Since a neutron induces a similar signal than a WIMP, the reconstruction of mono-energetic neutron spectra is the ultimate test for directionality. In Section 8.3, we evaluate the directional performance of MIMAC, on proton target, in the keV-range. To do so, we propose a new approach based on the deconvolution of the ionic contribution from the Flash, so this method is physically related to the interplay between the electronic and the ionic signals in the Micromegas.

The standard approach for measuring the direction of a nuclear recoil in MIMAC consists in exploiting the signal on the pixelated anode. The directional approach based on the Flash could then

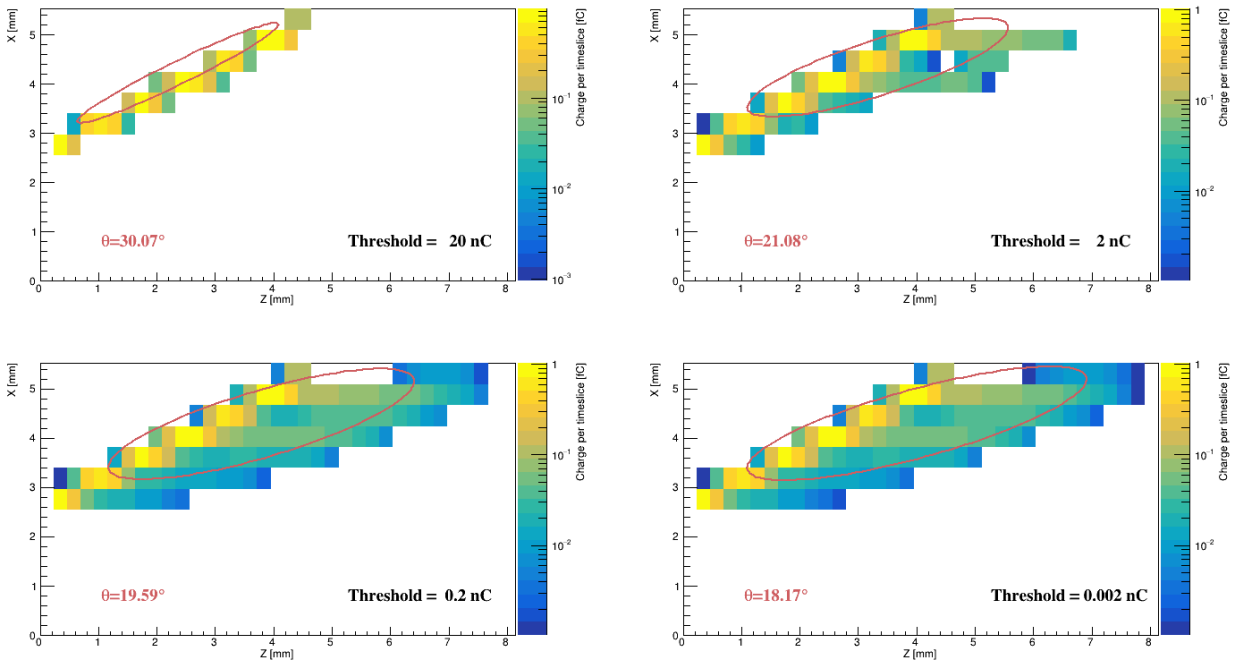

Figure 8.2: Polar angle reconstruction from the ellipse method for a uniform straight track having a 30° angle with respect to the Z-axis. The signal on the anode strips has been simulated with `SimuMimac` and we show four different configurations of strip thresholds. In this simulation, the larger the strip threshold, the lower the observed track is affected by the ionic signal.

be complemented by another method, based on the pixelated anode, providing redundancy to improve the MIMAC directional performance. In Section 8.4, we will present preliminary results which, even if further validation is still required at the time of writing, seem to provide directionality both on proton recoils and on carbon recoils. We will see that additional studies, both from experiments and simulations, are required to evaluate the validity of this method. The proposed method for directionality on the anode does not correct the ionic signal, but rather uses it as an additional information. At this stage, it is already possible to claim that the influence of the ions at high gain can be used as a helping and valuable tool for accessing directionality on millimeter-tracks. The work presented in this chapter relies on the article [179].

8.1 Preamble: influence of the ions at high gain and large gap

In the avalanche, as described in Section 4.3, most of the electron-ion pairs are produced close to the anode. All the electrons are collected on the anode in less than 1 ns whereas the ions need about 300 ns to reach the grid. The ions will then induce a tiny signal compared to the electrons, but for a longer time, as described by the Ramo-Shockley theorem Eq. (4.22). We illustrate the signal induced on the grid in Figure 8.1 using the Dris and Alexopoulos model Eq. (4.23). The peaks represent the electronic signal; the baseline is due to the ionic signal. The electronic noise defines the current detection threshold of the Flash signal. The brown signal of Figure 8.1 illustrates a situation that could happen when operating at low gain: the measured signal stops when the last primary electron enters the gap. The blue signal describes the situation at high gain: the detector gets more sensitive to the ionic contribution and still measures a signal more than 200 ns after the arrival of the last primary electron. We here stress that, for two identical primary clouds, the measurements differ depending on the gain of the detector.

Being sensitive to the ionic signal even after the arrival of the last primary electron results in an elongation of the measured track. In parallel, it also alters the track reconstruction from the anode since, at high gain, each avalanche will activate a single strip for a time up to $\sim$ 300 ns, depending on the charge density inside the gap. In other words, the first avalanches are feebly altered by the

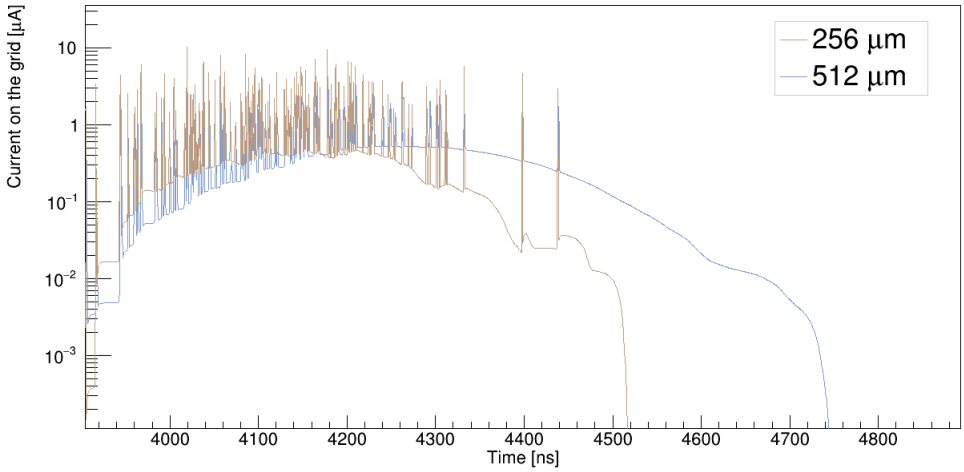

Figure 8.3: `SimuMimac` simulations of a 7 keV proton track in the *High-gain gas* at 30 mbar after 5 cm of drift. The simulations compare the currents induced on the grid for a gap of 256 μm and for a gap of 512 μm when the same voltage is applied on the grid.

ion accumulated in the gap, but the more primary electrons arrive, the more altered is the track. In general, the influence of the ions in the gap introduces a distortion of the track, leading to a bias in the reconstruction of the track angle (under-estimation of the polar angle).

The distortion of the measured track on the anode by the ionic contribution, and consequently the bias on the angle reconstruction, can be illustrated by `SimuMimac` and is presented in Figure 8.2. In this example, we have represented the enlightening situation of a homogeneous track of 140 primary electrons evenly distributed along a track of 5 mm making an angle of 30° with respect to the Z-axis. The track is placed at the grid level so it is not affected by diffusion. In this sense, the track is not physical but is an illustrative case. We use `SimuMimac` to model the signal induced on the anode strips and we reconstruct the angle thanks to the ellipse method introduced in Section 5.2. In this ideal case, one can increase the influence of the ionic signal by simply varying the strip threshold instead of varying the gain: the lower the strip threshold, the more sensitive the anode to the ionic signal. In the figure, we show the signal and the reconstructed angle for four different strip thresholds. The top left panel presents a case in which the anode is almost exclusively sensitive to the electronic signal and the ellipse method reconstructs the expected angle. However, one can see in other panels that a large contribution of the ionic signal results in an under-estimation of the reconstructed angle.

The MIMAC team has already been able to access directionality and reconstruct neutron spectra at intermediate energies (127 keV [384] and 27 keV [336]) when operating with a gap of 256 μm. The gap size changes drastically the influence of the ion flow, as one can see in Figure 8.3 where we compare the signal induced on the grid for two different gaps thanks to `SimuMimac`. One can see that the influence of the ionic signal increases with the gap of the detector since a larger number of ions accumulate at the same time in the amplification region because (1) the avalanche develops over a longer distance, producing more secondary charges; (2) the ions must travel a longer path before being collected on the grid; (3) the amplification electric field is smaller (since in the figure the same voltage is applied on the grid for both gaps) so the ion velocity decreases.

We are then facing a situation that, at first glance, appears as an issue: to search for low-mass WIMPs one must be sensitive to any primary electrons, so must operate at high gain with a 512 μm gap, while in these conditions the influence of the ion flow in the gap cannot be neglected and results in 3D track distortions. However, we aim to demonstrate in this chapter that, when controlled, the ionic contribution opens the window for low-energy detection since it acts as a magnification of the signal and it embeds physical information that could be used for directionality. We will show that the sensitivity to the ionic signal at high gain does not alter the measurement of the ionization energy released by a particle.

8.2 Deconvolution of the ionic signal on the Flash

8.2.1 Deconvolution procedure

The Flash signal can be seen as the time integral of a convolution between an electronic current, $f(t)$, and an ionic one, $g(t)$, having different kinematics. We aim to deconvolve the ionic contribution from the Flash measurements in order to extract the electronic current induced on the grid. The electrons produced in an avalanche, initiated by a single primary electron entering the amplification region, are collected in less than 1 ns. This value being significantly lower than the detector time sampling of 20 ns, the electronic current induced on the grid can be seen as the time distribution of the primary electrons cloud before the avalanche. In other words, the deconvolution of the ionic signal would provide gain-independent information on the primary electrons cloud.

The electronic and the ionic currents induced on the grid can be elegantly expressed by the Dris and Alexopoulos model Eq. (4.23). Starting from this point, we derive in Appendix C two formulas to express $f(t_i)$ the electronic current at timeslice t_i, either from the total current $I(t)$, which is a convolution of the electronic and the ionic currents, or from the derivative of the Flash signal $D(t)$:

$$\begin{cases} f(t_i) \propto I(t_i) - e^{-A\Delta t} I(t_{i-1}) \quad , \; i > 0 & (8.2) \\ f(t_i) \propto D(t_i) - D(t_{i-1}) - e^{-A\Delta t}\Big\{D(t_{i-1}) - D(t_{i-2})\Big\} \quad , \; i > 1 & (8.3) \end{cases}$$

The definition of parameter A is provided in Appendix C and it depends on physical quantities: the ion velocity, the Townsend coefficient, and the gap. We would like to express A experimentally, directly from the Flash signal, without computing it from the theoretical expression since some physical quantities are unknown, and since it would require converting the charge into ADC-channel through a calibration.

To do so, we evaluate $f(t_i)$ from Eq. (8.3) at two different timeslices, t_α and t_β. We can then extract the exponential term:

$$e^{-A\Delta t} = \frac{\frac{f(t_\beta)}{f(t_\alpha)}\Big(D(t_\alpha) - D(t_{\alpha-1})\Big) - D(t_\beta) + D(t_{\beta-1})}{\frac{f(t_\beta)}{f(t_\alpha)}\Big(D(t_{\alpha-1}) - D(t_{\alpha-2})\Big) - D(t_{\beta-1}) + D(t_{\beta-2})} \tag{8.4}$$

The next step is to determine the ratio $f(t_\beta)/f(t_\alpha)$ from the Flash signal. There are two typical positions in the Flash that are always identifiable in the data: (1) the first detected charges; (2) the maximum of the Flash derivative. While the first case is mainly correlated with the electronic current, the second one depends both on the electronic and the ionic contributions. At this point we will do an approximation, whose validity will indirectly be determined in the next section, to rely the ratio to these remarkable positions:

$$\frac{f(t_\beta)}{f(t_\alpha)} \simeq \frac{D(t_\beta)}{D(t_\alpha)} \tag{8.5}$$

Under this approximation, we can retrieve the electronic current (in arbitrary units) from any Flash signal, without introducing any parameter.

Some comments are required at this stage. First, the deconvolution formula Eq. (8.3) can be applied to any MIMAC measurements using any gas mixture, with no use of prior nor introduction of *ad hoc* parameters. Second, the formulas are derived by means of two approximations: the primary electron cloud is considered uniform at grid; (2) the parameter A is determined directly from the Flash measurements with the approximation Eq. (8.5). These assumptions are the price to pay for having analytical formulas not relying on any physical parameter. Third, the obtained electronic current is only proportional to the above expressions because, as explained in Appendix C, we have chosen to drop the normalization factors that could not be determined directly from the Flash. As emphasized in this paragraph, the philosophy that lies behind the deconvolution formulas is to have a robust method that can be applied to any measurement.

The formula in Eq. (8.3) can be applied to Flash measurements but this is not the case of Eq. (8.2) since it requires the total current $I(t)$, a quantity that is not measured by MIMAC. We anyway give its

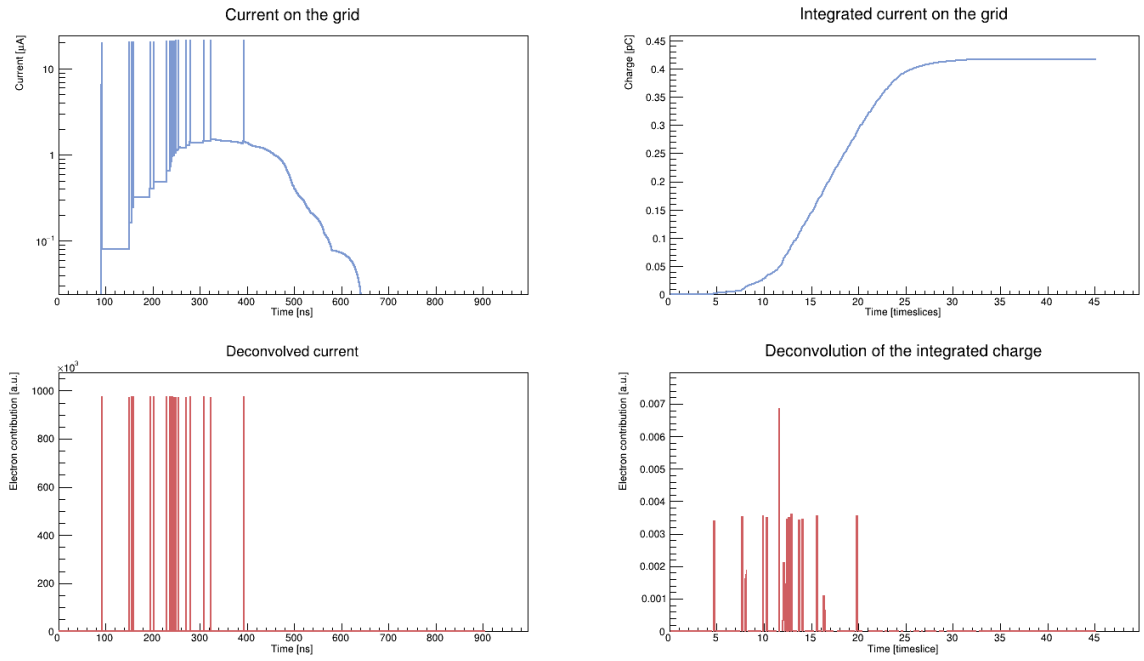

Figure 8.4: Example of the deconvolution formulas for an initial signal determined by the Dris and Alexopoulos model for 20 electrons that have drifted over 5 cm. The two top plots correspond to the initial current (left) and the Flash (right). The two bottom plots are obtained by applying the deconvolution formula, Eq. (8.2) (left) and Eq. (8.3) (right), on the signals shown in the top plots. In this example, we use a timeslice of 2 ns instead of the usual MIMAC 20 ns.

expression because it can be used on simulated data. We generate a uniform primary electrons cloud and we drift it over 5 cm according to `Magboltz` diffusion coefficients. The current induced on the grid and the corresponding Flash signal are determined thanks to the Dris and Alexopoulos model. We can then test the deconvolution formulas by applying them to the modelled signals. Figure 8.4 illustrates such deconvolution for 20 primary electrons. In the figure, the peaks in the top left panel are due to the electronic current, so the deconvolution should give access to the same time distribution. One can see in the bottom plots that it is indeed the case. This is a first validation of the deconvolution formulas, while we will later provide more robust validations. However, for this figure we discretize the Flash with a timeslice of 2 ns. By simulations, we observed that up to a timeslice of 5 ns the deconvolution of the Flash signal gives almost exactly the time distribution of the electronic current. For larger timeslices, this is not the case because the time resolution of the Flash becomes too coarse compared to the mean time separation between electrons.

This sampling issue is the main limitation of the deconvolution. Since the deconvolution propagates recursively from the values at the two previous timeslices, a sampling time larger than 5 ns introduces an undershoot in the reconstructed electronic current. An example of this bias is presented in the left panel of Figure 8.5. Since MIMAC samples at 20 ns, we had to find a way to cope with this issue. We have developed and tested several empirical approaches, for instance based on the Flash derivative. The one that gives the best performance consists in adding a linear offset (that increases linearly at each timeslice) such that the minimum of the electronic current is equal to zero after the correction.

We here write the total procedure to apply to the data in order to deconvolve the ionic signal:

1. Apply a ballistic correction, as described in Section 5.1, in order to correct for the self-discharge of the charge-sensitive preamplifier

2. Apply a smoothing of the Flash in order to reduce noise propagation in our recursive deconvolution. We usually operate with a forward-backward moving average with a window of 4 timeslices.

3. Determine t_0 the timeslice of arrival of the first primary electron. It can be determined from the Flash derivative.

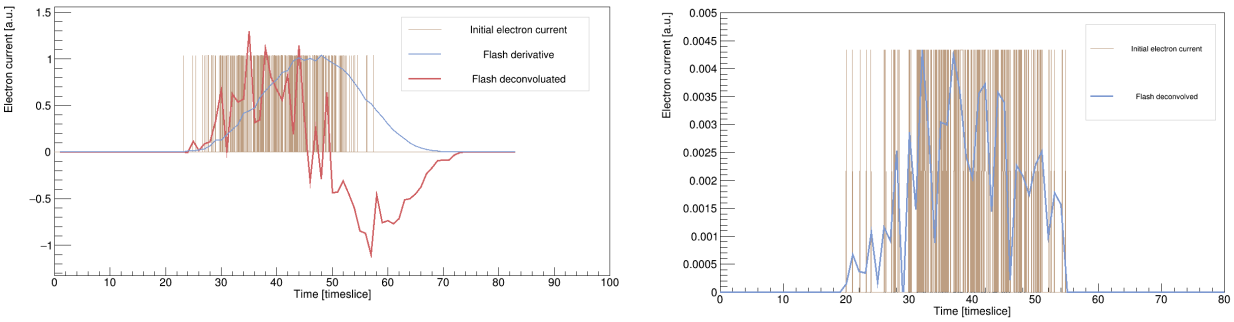

Figure 8.5: Two examples of the deconvolution of the ionic signal from simulated Flash signals corresponding to a 10 keV proton after 5 cm drift in the *High-gain gas*. In both cases, the brown peaks correspond to the initial electron current used to generate the Flash signal to be deconvolved. Left: direct application of Eq. (8.3). Right: deconvolution after applying the empirical correction.

4. Determine $A\Delta t$ from Eq. (8.5) in comparing the Flash signal at t_0 and at $t_{\max}$, the timeslice of the maximal Flash signal.

5. Apply the deconvolution formula Eq. (8.3).

6. Add a linear offset to the obtained electronic current in order to have the minimum of the obtained signal at zero.

7. Only keep the positive part of the obtained signal.

So far we have highlighted the approximations and the empirical correction used to obtain the electronic current from the Flash. Our method suffers from multiple uncertainties. However, we will see below that it is anyway sufficient and it provides valuable information. An example of the obtained electronic current on simulated data, after applying the entire deconvolution procedure, is shown in the right panel of Figure 8.5. One can see that, even with a 20 ns sampling time, the electronic current obtained from the Flash signal (in blue) has a similar distribution than the initial electronic signal used to construct the Flash (brown). Finally, we emphasize one more time the fact that this deconvolution can be applied to all measurements with no use of any parameter.

Figure 8.6 presents an example of the deconvolution procedure applied on 10 keV proton sent by Comimac in the *High-gain gas*. The electronic current is represented in brown and one can see, in the derivative plot, that it stops about 10 timeslices before the measured signal, the difference being attributed to the ionic contribution: when no longer primary electron enters the gap the electronic current stops whereas the ions keep inducing a signal on the Flash and on the anode. The top right plot compares the measured Flash, after correction of the ballistic deficit, to a charge profile reconstructed from the electronic current distribution based on the Dris and Alexopoulos model. The observed agreement between the two signals gives a qualitative validation of the deconvolution while we will now move to quantitative validations.

8.2.2 Evaluation of the deconvolution efficiency

We evaluate by several means the efficiency of the deconvolution formula. The first one is by simulations, as before: (1) generation of a primary electrons cloud, (2) modelling of the corresponding Flash signal, (3) application of the deconvolution procedure, (4) comparison to the initial primary electrons cloud. While the time of arrival (ToA) of the first primary electron is easily detectable on the Flash, the ToA of the last primary electron can only be accessed by deconvolution. We generate n physical tracks whose lengths, angles, and numbers of primary electrons are chosen randomly. For each track we apply the deconvolution on the corresponding simulated Flash signal, we determine the last time of the electron current and we compare it to the known ToA of the last primary electron. The results are shown in the left panel of Figure 8.7. On average, the deconvolution under-estimates the ToA of the last primary electron by less than one timeslice. The deconvolution procedure then introduces a bias

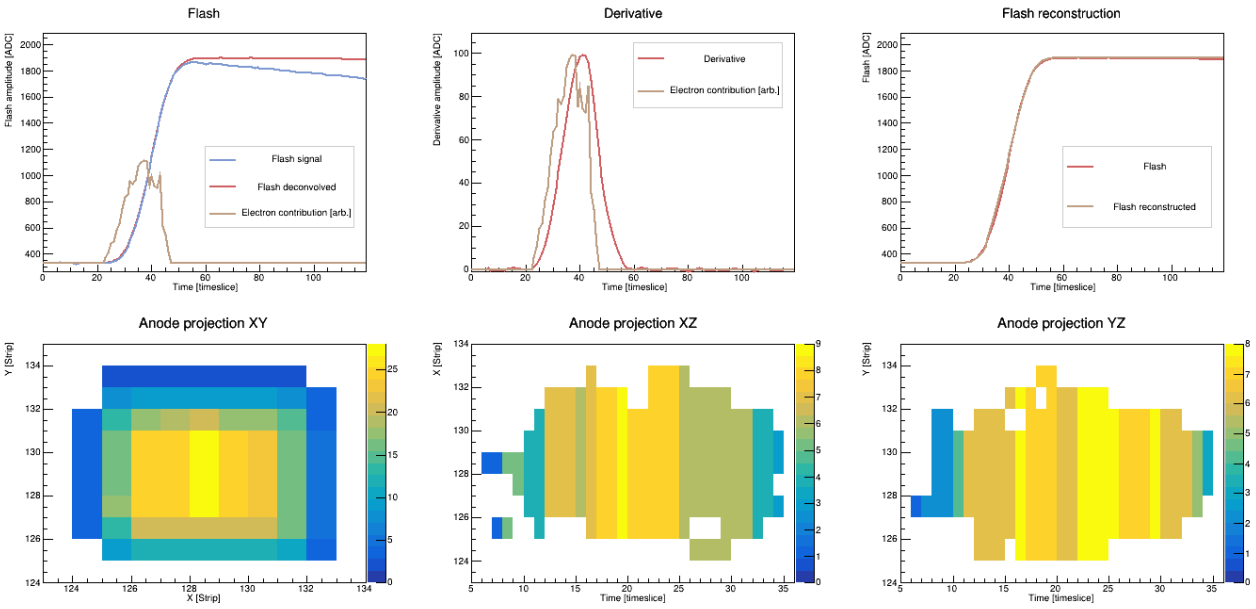

Figure 8.6: Example of the deconvolution on a 10 keV proton sent by Comimac in the *High-gain gas* after 5 cm drift. In the top plots, the blue signal corresponds to the measurement; the red ones are obtained after smoothing and correction of the ballistic deficit; and the electronic current given by the deconvolution is shown in brown and it has been scaled by an arbitrary factor chosen for visual convenience. The top right plot shows the corrected Flash, in red, compared to the Flash that can be reconstructed from the electronic current by applying the model of Dris and Alexopoulos. The three bottom plots show the corresponding measurements on the pixelated anode.

on this observable. However, this bias remains small ($\sim 3\%$ of the total duration) according to the fact the simulation takes into account tracks of multiple lengths, angles, and primary electrons densities.

A second method to evaluate the efficiency of the deconvolution has already been presented in Chapter 6 when discussing the gain curve. Remind that we performed experiments with Comimac where we sent a particle of known kinetic energy (5 keV electron or 10 keV proton) and we varied the gain of the detector. The measured track lengths increased with the gain whereas the duration of the deconvolved signal remained constant, as one can see in Figure 6.6. This result is an important validation of the deconvolution: since we claim that the deconvolution, by extracting the electronic current from the Flash signal, gives access to the time distribution of the primary electrons cloud, its duration should not depend on the gain of the detector, on the contrary of the measured track length that is affected by the ionic contribution.

A third approach to check that the deconvolution is efficiently working concerns the integral of the electronic current, resulting from the deconvolution of the ionic signal. This integral should be proportional to the number of primary electrons, thus it should be linear with the kinetic energy. To perform such analysis, parameter A must be fixed for an entire run. We thus first process the data where A is computed event-by-event, then we determine its mean value, and we re-process the data by fixing A to its mean value. An electron calibration performed with Comimac using the *Mimac gas* at 50 mbar is presented in the right panel of Figure 8.7. As expected, the integral of the electronic current obtained by deconvolution follows the same tendency as the ionization energy and consequently demonstrates that the deconvolution does not affect the number of primary electrons. However we observe the presence of an offset: null kinetic energy will still produce a non-zero electronic current. This offset is due to the approximations performed in the derivation of the deconvolution formula and also in the determination of the parameter A.

In some gas mixtures, the kinematics of the ionic signal sufficiently dominates over the one of the electronic signal so that the amplitude of the Flash signal is no longer proportional to the ionization energy. In other words, in some gas mixtures the MIMAC definition of the measured energy is not well-defined. This is for instance the case in 100 mbar of methane with a drift electric field of 100 V/cm and 19.5 kV/cm amplification electric field in a 256 μm Micromegas. A typical example of the Flash signal

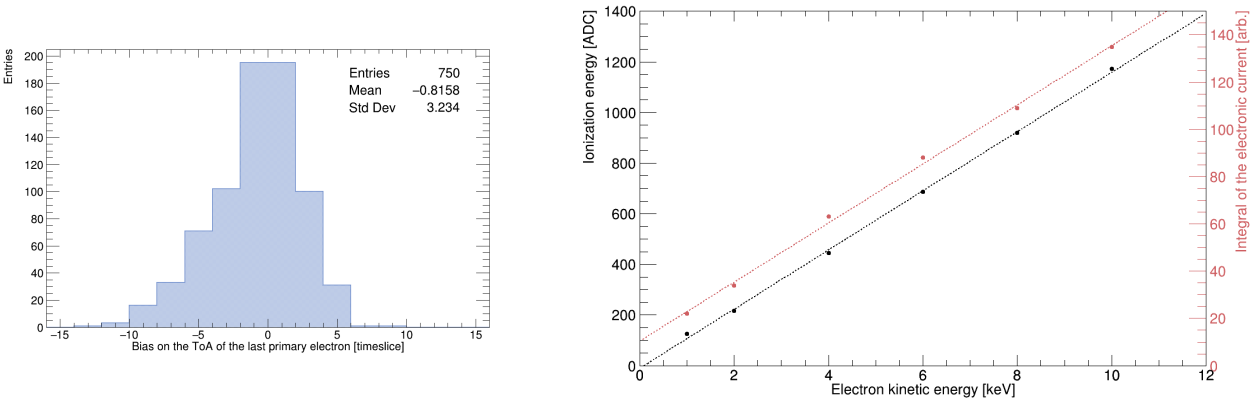

Figure 8.7: Evaluation of the efficiency of the deconvolution.
Left: bias on the time of arrival of the last primary electron determined by the deconvolution procedure, $t_{\text{deconv.}} - t_{\text{prim.}}$, for 750 simulated tracks with lengths, angles, and numbers of primary electrons chosen randomly. Right: electron calibration in the *Mimac gas* at 50 mbar with a gain around 2×10^4. The kinetic energy of the electrons is given by Comimac, the ionization energy (black dots) is derived from the amplitude of the Flash signal, and the red data points represent the integral of the electronic current obtained by deconvolution.

and its derivative is presented in the top panel of Figure 8.8 for a 15 keV electron sent by Comimac. One can see that the derivative is significantly asymmetric. The electron calibration associated with this experiment is shown in the bottom panel of Figure 8.8. The usual approach considering that the ionization energy is proportional to the Flash amplitude is shown in black. One can see that it gives a non-linear calibration. On the contrary, the calibration obtained by the integral of the deconvolved Flash, shown in red, remains linear. In this case, where the ionic contribution dominates the Flash signal, we can see that our standard definition of the ionization energy fails whereas the integral of the electronic current remains proportional to the incident kinetic energy. We draw an important conclusion from this analysis: the influence of the ions in the gap can alter the energy measurements if not correctly taken into account. However, we moderate this comment by reminding that in the large majority of the gas mixtures that we have studied, we obtained a linear calibration by using the Flash amplitude as a definition of the ionization energy. In this thesis, the only measurements possibly affected by this behavior are the ones obtained in methane in Chapter 7.

To sum up, we have validated that the deconvolution of the ionic contribution to the Flash signal determines the ToA of the last primary electron with a bias lower than one timeslice, it enables gain-independent track length measurements, and its integral is proportional to the ionization energy deposited by a particle. In some particular gas mixtures where the kinematics of the ionic signal significantly dominates over the electronic one, the deconvolution of the ionic signal is required to get the ionization energy released by a particle.

8.2.3 Head-tail recognition

In addition to the measurements of the direction of a nuclear recoil, directional detectors aim to distinguish between the *head* and the *tail* of a track (we define the tail as the closest point to the initial collision). We have discussed in Section 2.3 the crucial role played by head-tail recognition in the discrimination of the background [163,166] and it reduces by about one order of magnitude the number of events required for directional detection [385]. The usual approach for head-tail recognition relies on the detection of an asymmetry in the charge distribution of the measured signal, the asymmetry being correlated to the stopping power of the nuclear recoil as a function of its kinetic energy. We have seen in Section 6.1 that the ionic signal induces a similar asymmetry at high gain in a large gap of 512 μm. For this reason, it is mandatory to separate the asymmetry due to the ionic contribution, to the asymmetry due to the stopping power.

We have experimentally validated that the deconvolution of the Flash signal gives access to the time distribution of the primary electrons cloud at the Micromegas grid, its integral being linearly

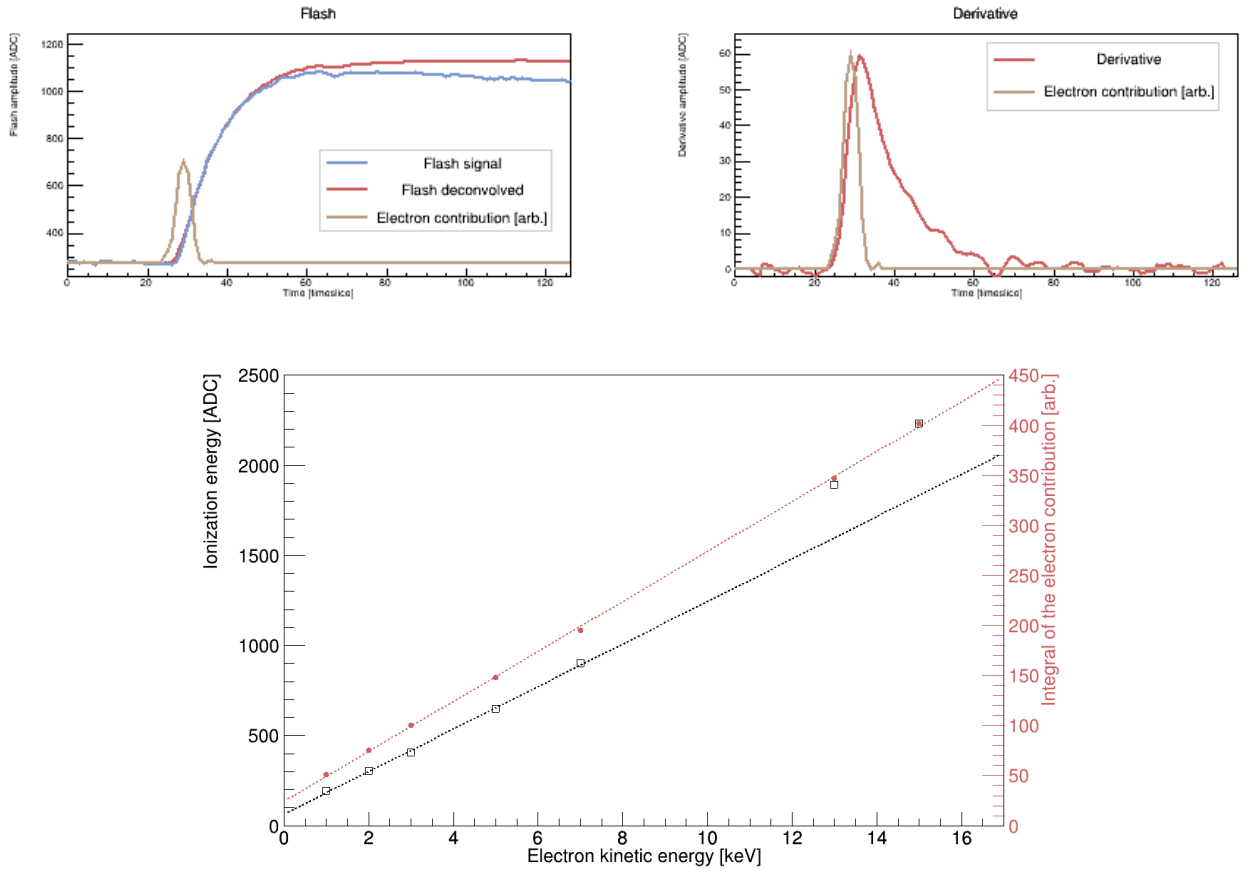

Figure 8.8: Comimac measurements in 100 mbar of methane in a 256 μm Micromegas.
Top: typical signal for a 15 keV electron. The color legend is the same as in Figure 8.6.
Bottom: electron calibration. The black hollow squares are obtained by defining the ionization energy as the amplitude of the Flash signal. The red dots are obtained by the integral of the deconvolved Flash signal. Two linear fit functions are represented in order to highlight the deviation to linearity in the case of the black signal.

correlated with the ionization energy. This approach enables us to better describe the fine structure of the primary electrons cloud since the kinematics of the electronic current is hundreds times faster than the one of the ionic current. For the kinetic energies and the gas conditions considered in this work, the stopping power $(-dE/dx)$ of a proton decreases when its kinetic energy decreases, *c.f.* Chapter 4. In other words, the Bragg peak is located at the beginning of the track and more charges are deposited close to the tail. This signature based on the stopping power can be used to distinguish between the head and the tail of the track.

In the left panel of Figure 8.9 we present a typical example of the measurements of a 13 keV proton sent by Comimac in the *High-gain gas* at 30 mbar. The brown curve is the electronic current obtained by deconvolution of the Flash signal. We have normalized it to appear as high as the Flash. One can see an asymmetry in the time distribution of the electronic current: most of the primary electrons arrive in the second half of the signal. In a Comimac experiment the ions are sent at the cathode, so the last timeslices correspond to the first interactions of the track. The asymmetry presented in the left panel of the figure follows the expected tendency from the stopping power of the protons.

It is possible to quantify this asymmetry by measuring the integral of the electronic current in the first and second half of the signal, called I_1 and I_2 respectively in the figure. The ratio $R = I_2/(I_1+I_2)$ describes the proportion of the electronic current located in the second half of the signal. This ratio determines if the track is oriented along $+\hat{\mathbf{z}}$ or $-\hat{\mathbf{z}}$. When $R > 0.5$, the tail is located at the end of the signal so the track is oriented towards the grid; and towards the cathode for $R < 0.5$. In the example of the left panel of Figure 8.9 we obtain $R = 0.61$. The right panel of the figure shows the distribution of R over an entire run. Its mean value at $R = 0.598$ indicates that the tracks are mainly oriented towards the grid, as expected from the experiment geometry. Note that in these measurements, the

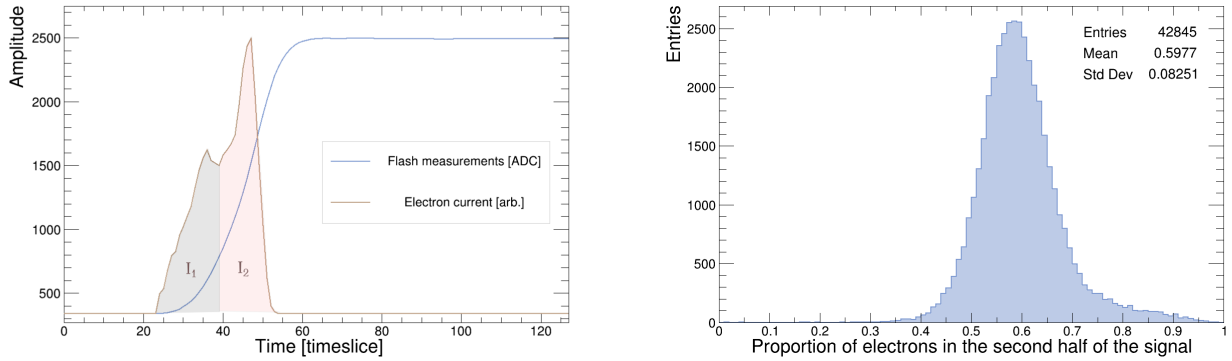

Figure 8.9: The asymmetry of the time distribution of the electronic current measured for 13 keV protons sent by Comimac in the *High-gain gas* at 30 mbar.
Left: a typical example of the Flash signal and the electronic current obtained by deconvolution. The filled areas correspond to the integrals, I_1 and I_2, of the electron current in the first and the second half of the signal, respectively.
Right: the histogram, for the entire run, of the proportion of electronic current located in the second half of the signal. The plotted proportion is defined as $I_2/(I_1 + I_2)$. In this situation, since the ions are sent at the cathode, the last timeslices correspond to the first interactions of the track (*i.e.* to the tail).

proton ionization energy is well defined with an energy resolution of 17% (the FWHM divided by the mean value).

We can conclude that the deconvolution of the ionic signal leads to head-tail recognition, event-by-event, since it reveals the asymmetry in the time distribution of the primary electrons cloud. However, in order to quantify the efficiency of head-tail recognition we aim to perform a new experiment at the end of 2022: the detector will be placed in a mono-energetic neutron field of 27 keV for two runs, one at an angle of 0° with the incident neutron direction, the other at 180°. This experiment would insure the production of recoils at almost any angles in the detector and multiple energies while knowing the sense of the recoil (along $\hat{\mathbf{z}}$ in the 0° configuration and along $-\hat{\mathbf{z}}$ in the 180° configuration).

8.3 Directionality at 27 keV and at 8 keV from the Flash

We illustrate in this section how the deconvolution of the ionic signal on the Flash signal can lead to additional observables for directionality. This work is exploratory and aims to open windows for improving usual methods, based on 3D track reconstruction, involved in directional detection. The directional performance of the MIMAC detector can be evaluated experimentally in a mono-energetic neutron field.

8.3.1 Experimental setup

We have performed an experiment on the AMANDE facility, described in Section 5.5, to produce mono-energetic neutron field with kinetic energy of 8.12 ± 0.01 keV or 27.24 ± 0.05 keV from the nuclear reaction $^{45}\mathrm{Sc}\,(p, n)$. The energy of the proton is adjusted between 2.91 MeV and 2.93 MeV to activate the chosen resonance for neutron production in the target. A MIMAC chamber specially designed for neutron spectroscopy, MIMAC-FastN [321], is placed in front of the ^{45}Sc target, at a distance of 33 cm, such that the proton beam is parallel to the Z-axis of the detector. A picture of the experimental setup is shown in Figure 5.18. The chamber is filled with the *High-gain gas* at 30 mbar stored in a buffer volume that has previously been used to perform the energy calibration of the detector with Comimac by sending electrons of multiple kinetic energies between 3 keV and 15 keV. We will here only consider proton recoils, since in the *High-gain gas* they represent 87% of the total nuclear recoils, according to stoichiometry and cross-sections from the `ENDF` database [386]. The uncertainty introduced by considering only proton recoils will be discussed in the next section. We here remind that the kinetic energy of a proton recoil is related to the kinetic energy of the incident neutron via

the scattering angle, *c.f.* Eq. (8.1).

The Ionization Quenching Factor (IQF) of protons in our gas mixture must be determined in order to convert the measured ionization energy into the kinetic energy, E_p. As stated in Section 4.2, large discrepancies between IQF measurements and simulations are observed below 50 keV in low-pressure gas mixtures. For this reason, we have performed a measurement of the proton IQF in our gas mixture, following the procedure described in Chapter 7. The direct comparison of the ionization energy of protons and electrons, of the same kinetic energy sent by Comimac, gives access to the IQF for the protons. Following the parametrization of [359], we obtain $\text{IQF}(E_p) = E_p^\alpha/(\beta + E_p^\alpha)$ with $\alpha = 0.24$ and $\beta = 1.20$. Our measurements follow similar tendency as `SRIM`'s IQF but shifted to lower IQF by about 37% at 10 keV.

High-energetic gamma-rays ($E_\gamma >$ MeV) are also produced during the nuclear reaction on the ^{45}Sc target with a fluence about 20 times larger than the neutron's one [336]. The electron-recoil discrimination represents then a central element of our data analysis in order to extract the proton recoils from the γ-induced electron background. We first apply a few *minimal cuts*, as detailed in Section 5.3, that suppress almost 98% of the events that are easily identified as non-recoil events. After this step, the strategies for electron-recoil discrimination differ between the two datasets presented below: the one at 27 keV and the other at 8 keV.

The discrimination procedure at 27 keV has been detailed in Section 5.3. It uses Boosted Decision Trees (BDT) that are trained on two samples, a "background only" sample and a "background + signal" sample, to identify background events from a set of discriminating observables. We remind that we obtain a background rejection power, that is the number of background events rejected for a single background event passing the cuts, of 8×10^4. The acceptance is estimated at around 50%, so half of the proton recoils are kept. For this dataset we keep 2300 events, identified as neutron-induced recoils, distributed in an ionization energy range of [2, 14 keV].

For the dataset with neutrons of 8 keV, we measure proton recoils down to 1 keV. In these conditions the BDT is not uniform: it accepts more recoils at large energy than at low energy. This non-uniformity would introduce a bias on the angle reconstruction so we instead decide to implement standard discrimination based on track observables, as in [321]. As an important drawback, this approach rejects fewer background events than the BDT but it accepts almost all recoil events. We estimate that 30% of the kept events are due to the background by comparing the cut efficiencies at 8 keV and 27 keV as well as the neutron production cross-sections [337] (10% larger neutron production at 8 keV). For this dataset we keep 5400 events distributed in an ionization energy range of [1, 8 keV]

8.3.2 Directionality from the deconvolution of the ionic signal

We here describe a novel approach for accessing directionality from the deconvolution of the ionic contribution to the Flash signal. The neutron field produced by the AMANDE facility covers a detection solid angle that can be determined for each event from the pixelated anode, with a maximal deviation of the neutron incident direction to the Z-axis that lies below 6° (for a distance of 33 cm between the target and the detector). In this situation, the scattering angle is roughly equivalent to the polar angle. Since we ignore the absolute Z-coordinate of the interaction, we place it (in our analysis) at the center of the detector, leading to a maximal error of 1.7° in the worst-case scenario.

There is a direct correlation between the polar angle and the detector sensitivity to the ionic signal. To describe this correlation, we proceed in two steps. First, we remind that the larger the number of charges per timeslice at the grid, the greater the ionic current, so the longer the ionic signal overpasses the detection threshold. We note `IonDuration` the duration between the time of arrival of the last primary electron and the time for which the Flash stops to record a signal. For instance in Figure 8.1, `IonDuration` is equal to 0 for the brown curve, and $\sim$ 200 ns for the blue curve. The second step consists in determining the number of charges per timeslice at the grid, a quantity that we hereafter call the *longitudinal charge density*. Three main processes influence this quantity, all of them being related to the polar angle: (1) the energy transferred to the proton recoil by the neutron; (2) the track length projected along the Z-axis; (3) the diffusion of the charges in their drift towards the grid, whose deviation to the mean value is mainly observed, statistically, for a small number of charges, so for a large polar angle. One can show that the longitudinal charge density, and consequently `IonDuration`,

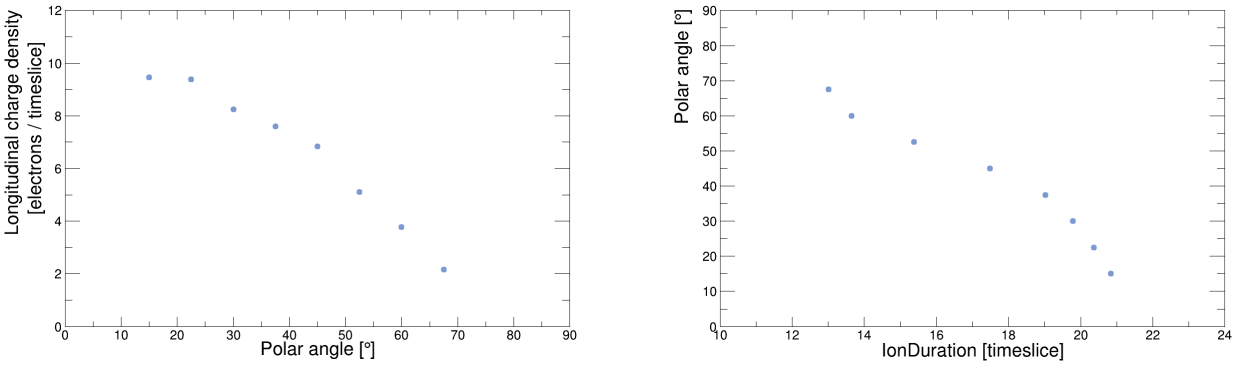

Figure 8.10: Monte-Carlo simulations showing the influence of the polar angle on the longitudinal charge density and on `IonDuration` after 12.5 cm of drift. The simulations model 2×10^4 proton recoils induced by 27 keV neutrons.
Left: the correlation between the longitudinal charge density and the polar angle.
Right: the correlation between the polar angle and `IonDuration`.

decreases when the polar angle increases. In a first approximation, `IonDuration` and the polar angle are correlated by an inverse cosine function.

To confirm these tendencies, we have implemented a Monte-Carlo simulation that generates n initial primary electrons clouds placed at the center of the detector ($z = 12.5\,\text{cm}$) and drifts them towards the grid. In this simulation, the scattering angle θ is fixed and it enables determining the proton kinetic energy, E_p, by setting $E_n = 27.24\,\text{keV}$; E_p is then converted into ionization energy using our measured IQF; the primary electrons clouds are obtained from `SRIM`; and the diffusion coefficients and drift velocity are retrieved from `Magboltz`. In other words, we model n proton recoils induced by elastic collisions with 27 keV neutrons in the detector. The correlation between the longitudinal charge density and the polar angle is presented in the left panel of Figure 8.10. The next step uses the Dris and Alexopoulos model to determine the Flash signals induced by the simulated clouds. We finally apply our deconvolution and we consequently determine `IonDuration`. The results are presented in the right panel of Figure 8.10. As expected, the simulations show a correlation between `IonDuration` and the polar angle that can be described in first approximation by an inverse cosine function. The simplicity of this function allows us to easily adapt its parameters to each experimental working conditions.

The measurement of `IonDuration`, obtained from the deconvolution of the Flash signal, provides an indirect determination of the scattering angle for a neutron field aligned with the Z-axis of the detector. This procedure only relies on the Flash signal which has a low detection threshold (lower than the anode's one) and is consequently sensitive to low-energy recoils. We also emphasize that this method gets more precise when the gain increases with direct advantages for searches dedicated to the low-energy region. However, it relies on several conditions:

- the neutron direction must be aligned with the Z-axis of the detector.
- one must consider that only one type of recoils is produced (in this section we neglect carbon recoils).
- large enough statistics are required ($\gtrsim 1000$ events) to determine the parameters of the inverse cosine function.

8.3.3 Mono-energetic neutron spectra reconstruction

We apply the procedure described above to determine the scattering angle from the Flash signal in order to reconstruct the kinetic energy of the incident neutron with Eq. (8.1). The reconstructed spectrum at 27 keV, presented in Figure 8.11, shows a Gaussian-like tendency with a resolution of 56% (FWHM over mean value) and it peaks at 26.3 keV, so we under-estimate the energy by 4%. The energy spectrum reconstruction from the measurement of the scattering angle embeds all experimental

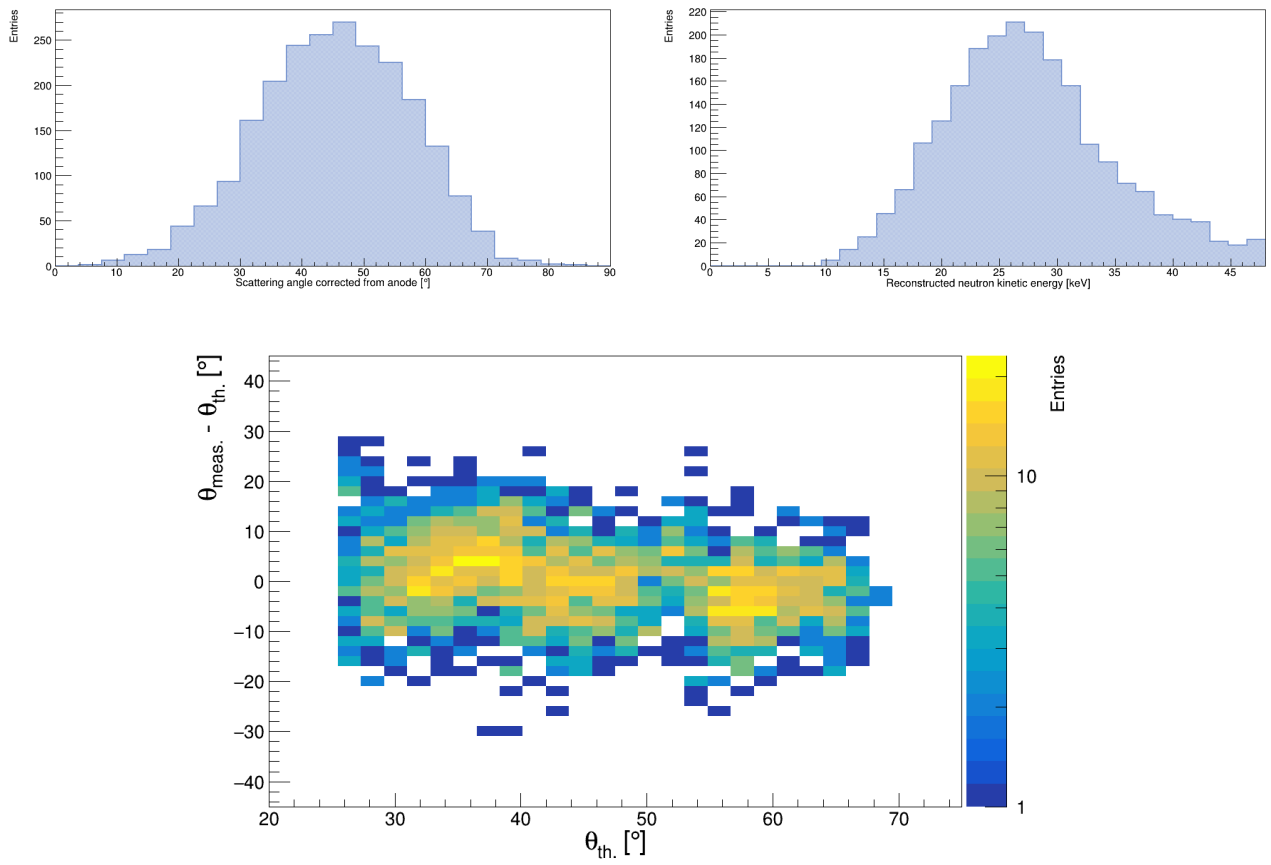

Figure 8.11: Proton recoils measurements in a mono-energetic neutron field at 27 keV produced by AMANDE. Top: reconstruction of the neutron scattering angular distribution (left) and the energy spectrum (right). Bottom: angular resolution of the reconstruction of the neutron spectrum.

uncertainties introduced by the directional method (by deconvolution of the ionic signal), but also by the IQF, the energy calibration, and the electron-recoil discrimination. Note also that we only consider proton recoils, for simplicity, neglecting then the proportion of carbon recoils.

The performance of the angle reconstruction is presented in the bottom panel of Figure 8.11 where $\theta_{meas.}$ is the reconstructed angle and $\theta_{th.}$ is the theoretical angle determined from Eq. (8.1) by setting $E_n = 27.24\,\text{keV}$. No significant bias is observed on the mean value of $\theta_{meas.} - \theta_{th.}$ and the standard deviation remains below 12° in the entire range. This standard deviation corresponds to the angular resolution. Two competing phenomena explain the uniform behaviour of the angular resolution: on the one hand, a low scattering angle results in a large number of charges which improves the track definition. On the other hand, the number of charges per timeslice increases for large scattering angles, leading to a better sensitivity to the ionic signal (*c.f.* Figure 8.10). We mention that the detector was saturating for kinetic energies above 22 keV, according to the measured IQF, explaining why no event is detected for theoretical angles below 26° in Figure 8.11. Such saturation does not limit our analysis since proton recoils above 22 keV are statistically rare.

The analysis at 8 keV is presented in Figure 8.12. We reconstruct a neutron spectrum peaking at 7.4 keV, *i.e.* 9% less than expected, the difference being likely explained by the presence of background events at low energy where the electron-recoil discrimination efficiency decreases. This phenomenon is also observed in the bottom panel of the figure where the low scattering angle region (below 15°) is almost exclusively populated by background events. We nevertheless measure an angular resolution better than 15° in the entire angular range.

Several comments are required at this stage. First, the reconstructions of the neutron energy spectra suffer from experimental uncertainties but they nevertheless demonstrate the directional sensitivity of the MIMAC detector to proton recoils with ionization energy in the keV-range. To the author's knowledge, this work presents the first reconstruction of a neutron spectrum below 10 keV in a TPC,

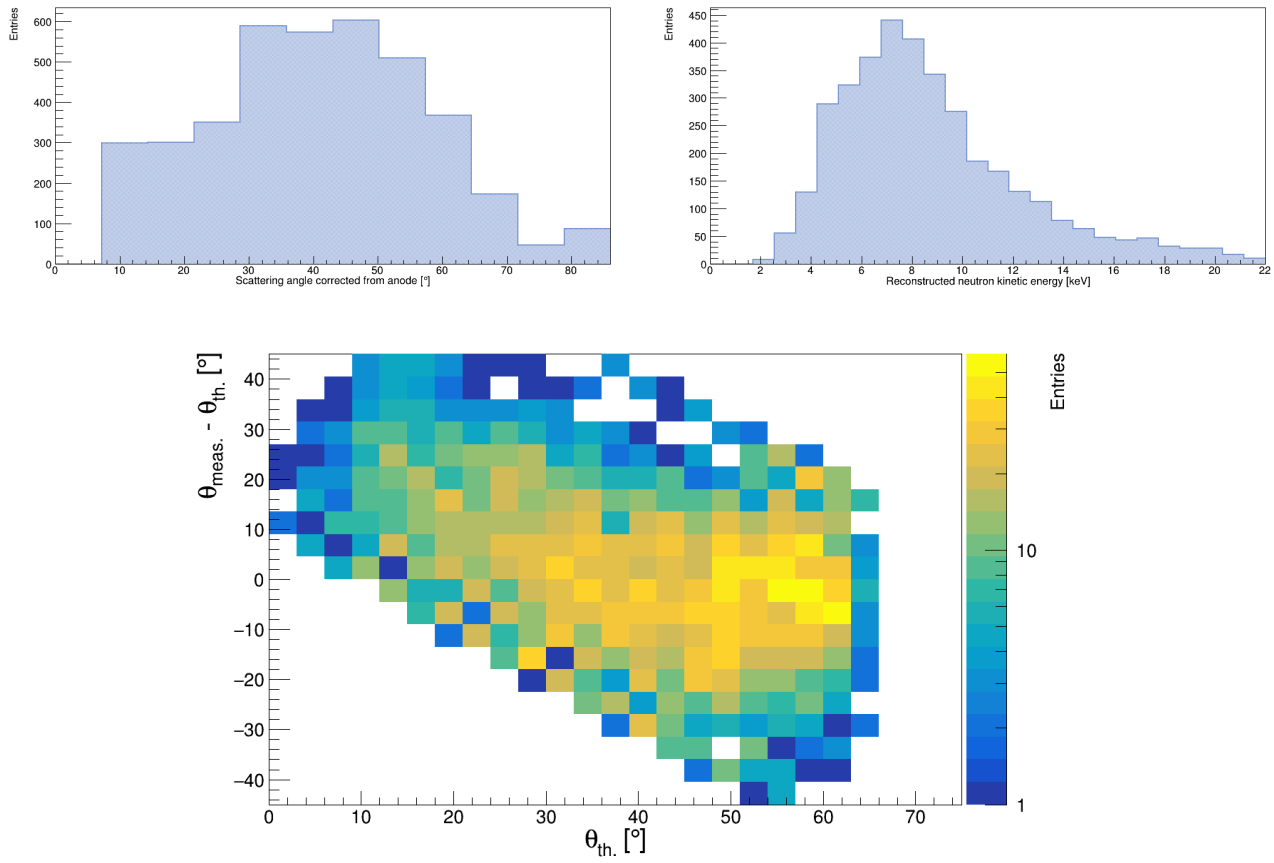

Figure 8.12: Proton recoils measurements in a mono-energetic neutron field at 8 keV produced by AMANDE. Top: reconstruction of the neutron scattering angular distribution (left) and the energy spectrum (right). Bottom: angular resolution of the reconstruction of the neutron spectrum.

so of an epithermal neutron field.

Second, the 15° angular resolution measured for proton recoils in the keV-range is definitely good enough for a directional detector. To the author's knowledge it is the best angular resolution obtained with a directional detector. However, to moderate the statement, such a result is obtained on proton recoils which are the easiest for measuring directionality since proton is the target with the longest tracks. We know from the WIMP phenomenology, as detailed in Chapter 2, that a WIMP would transfer at maximum a few keV to a proton recoil. In this sense, an additional step is required to fully demonstrate that directional detectors are able to search for light WIMPS: either one must perform similar measurements for lower energy neutron-field, or one must reproduce it by using fluorine as a target.

Finally, the main comment concerns the strategy of directional detection. The standard MIMAC method relies on the pixelated anode to reconstruct the direction of the nuclear recoil. This strategy has enabled for instance to reconstruct a neutron spectrum at 27 keV when operating at low gain with a gap of 256 μm [336]. In this chapter, we highlight how the situation changes at high gain. We have proposed an approach for directionality from the deconvolution of the ionic contribution to the Flash signal. We focused on the Flash signal for its simplicity to demonstrate the importance of the ionic contribution and to develop deconvolution tools. The next step consists in applying a similar approach to the pixelated anode measurements.

8.4 Towards directionality from the anode at high gain

This section presents preliminary results and further studies are still required to validate them. We have anyway decided to include them since they show possibilities for improving directional performances

thanks to the anode. This section can be considered an introduction to the future work of the MIMAC team and it draws the contours of the angle reconstruction on the anode when operating at high gain and large gap.

8.4.1 Angle reconstruction on the anode

We have discussed in the preamble how the ionic signal distorts the track reconstruction, hence distorting the measured angle. In the previous section, we have presented a method to extract the electronic signal from the Flash measurements by the deconvolution of the ionic contribution. At first glance, one could think a similar approach could also be applied to the anode signal. However the anode signal has some specificities compared to the Flash signal:

- The strips give binary information: activated or not. Moreover, we do not have access to the current intensity. This is the main limitation that prevents us from deconvolving the ionic contribution on the anode.
- The strip weighting fields are non-linear both on the transverse (X or Y) and the longitudinal (Z) components, *c.f.* Section 4.3. Consequently, the modelling of the signal on the anode is complex and does not enable an analytical deconvolution of the ionic contribution.
- The strips have a threshold, each strip having its own threshold auto-calibrated depending on the intrinsic noise. Unlike the Flash that collects all charges, the strips are activated only if their thresholds are overpassed, so for a large enough induced current during a timeslice. It means that a small current, for instance the one induced by the first avalanches when only a small number of ions are in the gap, will not necessarily be sufficient to activate the strips.

These specificities of the anode signal make difficult the deconvolution of the ionic contribution on the anode. However, since the anode and the Flash are synchronized, one could use the information provided by the Flash to better interpret the anode signal. For instance, one can weigh the anode signal according to the electron current obtained by the deconvolution formula. We have extensively investigated such approaches, trying to reduce the ionic influence on the anode signal, and we conclude, for the moment, that such approaches result in a reduction of the available information and fail in reconstructing a physical angle.

We have however obtained interesting results by considering the situation from another perspective: instead of correcting the signal from the ionic contribution, we rather use the additional information it provides in order to improve our description of the angle. When the number of ions accumulated in the gap is large enough, the electronic signal induced by an avalanche overpasses the strip threshold and consequently activates a strip. In other words, the more ions in the gap, the more sensitive the anode.

Several effects have opposed contributions in the signal formation on the anode. First, due to the ionization process and diffusion, some primary charges will not be able to activate the strips. This is the case of the extreme charges of the primary electrons cloud. On the contrary, the presence of the ions close to a strip enhances the probability of activating it, so the anode gets more sensitive to the last primary electrons to reach the grid. The track angle with respect to the Z-axis plays a role in the enhancement process: the smaller the polar angle, the more primary charges arrive at the same position in the (X-Y) plane, so the more sensitive to the primary electrons is the anode thanks to the accumulated ions. Figure 8.13 illustrates these explanations. We have represented in 2D the signal induced on the anode for two different angles. The blue area corresponds to the detectable region when the total current (electronic and ionic) exceeds the strip thresholds. The sensitivity of the anode depends on the current intensity in the gap, so on the density of the accumulated ions close to the strips that provides a baseline for the electronic signal produced during an avalanche.

In first approximation, we neglect the asymmetry of the diffusion, so we can express the polar angle in the (X-Z) plane as:

$$\tan\theta_X \simeq \frac{\Delta X^g}{\Delta Z^g} \tag{8.6}$$

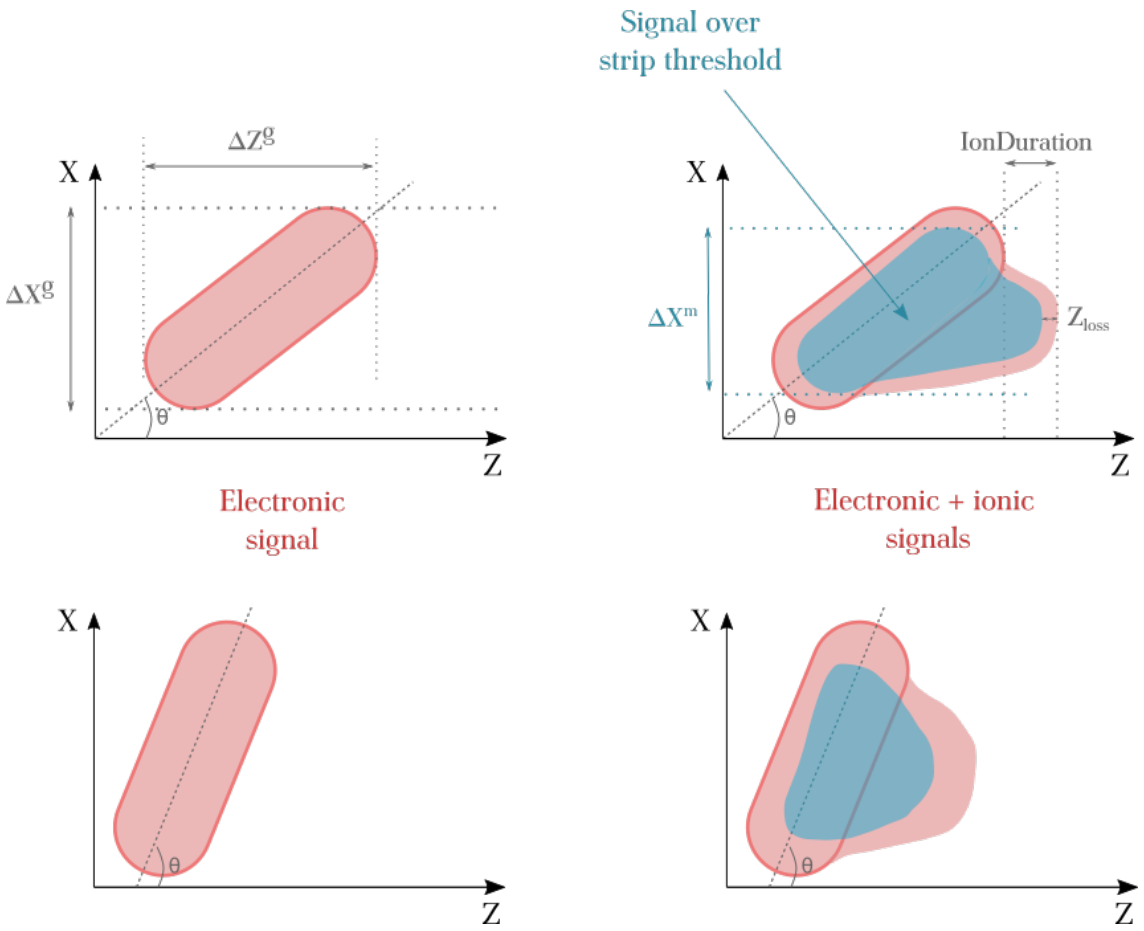

Figure 8.13: Schematics of the signal induced on the anode strips. The electronic signal is shown in the left panel whereas the right one also includes the ionic contribution. The blue area corresponds to the detectable signal on the anode, *i.e.* when the current exceeds the strip thresholds. We have illustrated the case of a medium angle (top) and a large angle (bottom).

where ΔX and ΔZ are the width and the depth of the primary electrons cloud, respectively, and the superscript g indicates that they are evaluated at the grid. These quantities are represented in Figure 8.13. The quantity ΔZ^g can be determined thanks to the deconvolution of the ionic contribution on the Flash. However, the quantity ΔX^g can only be accessed on the anode. We know that the anode signal is altered both by the ions accumulated in the gap and by the anode sensitivity, *i.e.* by the strip thresholds. The measured width on the anode will then be underestimated: $\Delta X^m < \Delta X^g$. However, the smaller the polar angle, the more ions accumulated close to the strips, so the smaller the loss in X, estimated as $\Delta X^g - \Delta X^m$.

We have defined an empirical factor for correcting the loss in X:

$$\tan\theta_X \simeq \frac{\Delta X^m}{\Delta Z^g}\,\frac{2\,Z_{\text{loss}}}{\text{IonDuration}} \tag{8.7}$$

where Z_{loss} is determined by comparing the Flash and the strip signal and where `IonDuration` is the observable defined previously corresponding to the duration of the Flash signal after the arrival of the last primary electron. This correction factor has been determined from several sets of data and it estimates the proportion of loss in X by assuming that the losses are similar along the X and the Z directions. It is then an empirical factor that relies conceptually on a hypothesis. The validity of this hypothesis, as well as the efficiency of the empirical factor, must be validated both from a dedicated experiment and from simulations. At the time of writing, this validation was not performed yet so the following results are preliminary and must be considered carefully.

The projected angle θ_X can be evaluated from Eq. (8.7), and similarly for θ_Y by replacing ΔX^m with ΔY^m, while the total polar angle is given by $\tan^2\theta = \tan^2\theta_X + \tan^2\theta_Y$. The equation relies on several approximations: (1) the asymmetry in the diffusion is neglected (we consider isotropic

diffusion); (2) we consider that the strip thresholds are identical; (3) we assume the proportion of signal loss due to the anode sensitivity is similar along X and Z.

While this approach relies on an empirical correction and several approximations, we will see that it gives interesting and consistent results when applied to the data. The philosophy of this approach is similar to the one for directionality on the Flash: we use the additional information provided by the ionic contribution to better define the track angle. In the rest of the chapter, this reconstruction of the angle will be referred to "the anode method".

8.4.2 Application to neutron data

We are ready to apply our method for reconstructing the scattering angle on the AMANDE 27 keV data. We reconstruct the polar angle from Eq. (8.7) and we determine the scattering angle, as explained previously, by considering the neutron direction. We obtain the angular distribution presented in Figure 8.14. While the distribution is centered on 45°, as expected, one can see a sub-structure around 20°. Such events can be identified as dense and short recoil events according to their Flash profile and their anode signal. They could possibly be carbon or fluorine recoils. Note also that the sub-structure contains about 10% of the events, which roughly is the expected proportion of non-proton recoils. We will first start by understanding the origin of the sub-structure before studying the differences with the angular distribution obtained by the Flash method.

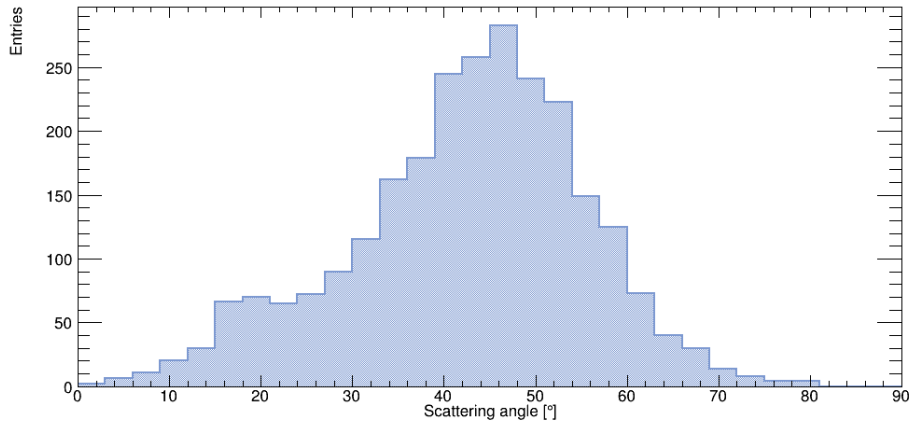

Figure 8.14: Reconstruction of the scattering angle from the anode for the AMANDE data at 27 keV.

`GEANT4` [387] simulations tell us that the angular distribution for carbon recoils, after an elastic scattering of a neutron of 27 keV, follows a similar tendency as the one for proton recoils: it is centered on 45° with a standard deviation around 20°. If we are measuring carbon recoils, then their angular distribution should approximately match the one of proton recoils. However, it depends on the kinematics described by Eq. (8.1): the energy transferred to a carbon recoil is smaller than the one to a proton recoil.

During the experiment, the detection threshold was approximately 2 keV in ionization energy. When the ionization energy was larger than 14 keV, the Flash was saturating so we rejected the events. The energy range of the experiment will then set constraints on the scattering angle for each species. To determine these constraints, one needs the IQF of each species. We already have discussed the IQF of proton in the *High-gain gas*, however we have not measured the IQF for carbon nor for fluorine. We then decide to perform a `SRIM` simulation of their IQF and we normalize it according to the 37% difference we have measured for proton IQF at 10 keV. We then define:

$$\mathrm{IQF(E)} = \mathrm{N\,E}^{\alpha}/(\beta + \mathrm{E}^{\alpha}) \tag{8.8}$$

where $N = 0.63$ is the normalization factor scaling the IQF measurements and where $\alpha = 0.41$ and $\beta = 2.43$ for carbon IQF whereas for fluorine we get $\alpha = 0.35$ and $\beta = 3.00$.

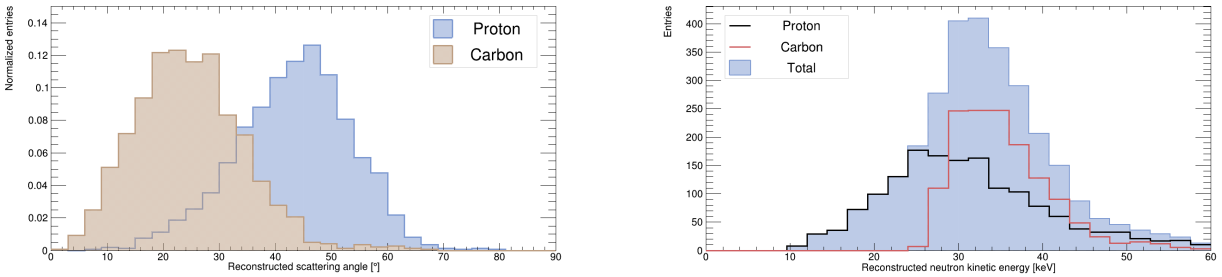

Figure 8.15: Angular distribution (left) and neutron energy spectrum (right) reconstructed from proton and carbon recoils for the AMANDE 27 keV experiment by using the method on the anode. The IQF of proton has been measured whereas the IQF of carbon is scaled from `SRIM` thanks to a normalization factor determined from the difference between simulated and measured IQFs for proton.

According to the IQF, the maximum ionization energy transfer to fluorine recoils, the so-called *endpoint*, is about 1.2 keV. Since this value is lower than our detection threshold, fluorine recoils are not detectable in this experiment. For carbon recoils, if the scattering angle is larger than 20°, the carbon recoil energy will be below the detection threshold. Finally, the detection threshold and the saturation of the Flash signal constrain the scattering angle for protons to remain in the range [25°, 65°]. Due to the energy range of the experiment, we know that for a scattering angle below 25° one can only detect carbon recoils whereas one detects proton recoils for larger angles. These limits are affected by the energy resolution of the detector as well as the uncertainties on the IQF and on the angle reconstruction. At this stage we can claim that the sub-structure observed around 20° in the angular distribution is made of carbon recoils. In other words, although `GEANT4` predicts similar angular distributions for carbon and proton recoils, they are detected differently during the experiment due to the energy range of the detector and to kinematics.

The measured carbon recoils are denser and shorter than proton recoils. It is then possible to establish observables for identifying them. For this reason, we decide to perform the electron-recoil discrimination in two steps: first, on an energy range up to the carbon endpoint for which we identify carbon recoils thanks to a BDT; second, we take off the identified carbon recoils from the data and we re-perform a BDT on the entire energy range to identify the proton recoils. Although there is more proton than carbon recoils, carbon recoils are easier to discriminate from the background. After the 2-step BDT, we keep 1610 proton recoils and 1406 carbon recoils.

The reconstructions of the angular distributions and the neutron spectra for proton and carbon recoils are presented in Figure 8.15. The angular distribution for carbon recoils is centered on 20°, as expected, but is pretty symmetric whereas it should follow a truncated distribution above $\sim$ 20°. This difference comes from several uncertainties and statistical effects in the energy resolution and in the angle reconstruction. On the other hand, the proton angular distribution follows the expected tendency. The right panel of Figure 8.15 shows the reconstructed neutron spectrum for both recoils. In both cases one can see a peak, centered on $\sim$ 27 keV for proton recoils and $\sim$ 33 keV for carbon recoils. This shift is likely due to the IQF that we extrapolate from `SRIM`. For instance, by setting the normalization factor to 0.75 instead of 0.63 we reconstruct a total neutron spectrum (from carbon and proton recoils) with a Gaussian peak on 27.6 keV having a sigma of 4.0 keV. A measurement of the carbon IQF in the *High-gain gas* is required to push further this analysis.

Finally, similarly to the results of the previous section, one can study the deviation between the measured angle and the angle expected to reconstruct the mono-energetic neutron spectrum at 27.24 keV according to the measured energy and the IQF. The deviations for proton and carbon recoils are presented in Figure 8.16. In both cases one can see an offset in the distribution: we reconstruct an angle larger than the expected one. This difference could be explained by several systematic effects:

- From the IQF, in particular for carbon since it has not been measured.
- From the electron drift velocity. We use the value predicted by `Magboltz` although we have discussed in Section 5.4 that the experimental drift velocity can differ from simulations due to

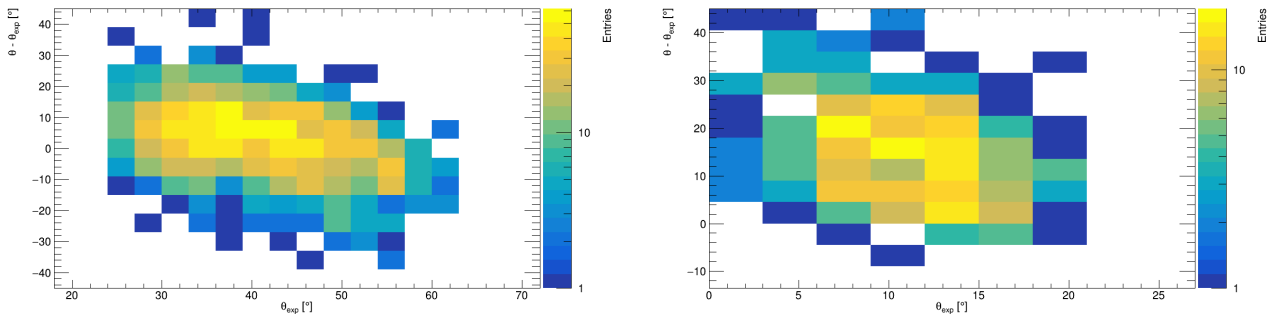

Figure 8.16: Comparison of the measured scattering angle to the angle expected for reconstructing a mono-energetic neutron spectrum at 27.24 keV according to the measured energy and the IQF. Proton recoils are presented on the left panel, carbon recoils are on the right.

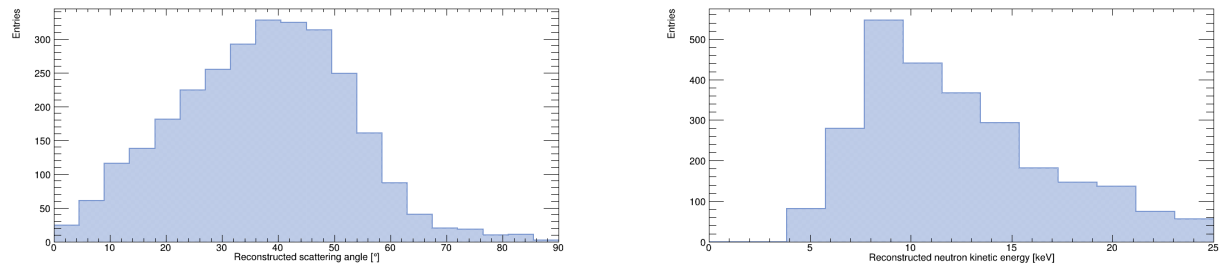

Figure 8.17: Angular distribution (left) and neutron energy spectrum (right) reconstructed from proton recoils for the AMANDE 8 keV experiment by using the method on the anode.

gas impurities.

- From the reconstruction of the angle on the anode since it relies on an empirical correction factor whose validity and efficiency have not been determined yet. Besides the empirical factor, the angle reconstruction formula, Eq. (8.7), embeds terms both from the anode measurements and from the deconvolution of the ionic contribution on the Flash. It then increases the sources of uncertainties.

The comparison from the expected angle shown in Figure 8.16 remains quite constant over the angular range considered. This behavior tells us that, except for the offset that can possibly be due to the IQF, the method for reconstructing the scattering angle seems not introducing any significant bias as a function of the scattering angle. This is a central element for directional performances. Let us also remark, as previously, that in such figures the standard deviation for a given angle corresponds to the angular resolution. The angular resolution remains constant in the entire angular range considered and it is 10° both for proton and carbon recoils.

Let us apply the same procedure to the AMANDE 8 keV data. During this experiment the detection threshold was around 1 keV, which is above the endpoint of both carbon and fluorine recoils. In other words, we can only detect proton recoils. We remind that for these energies the BDT introduced a bias in energy so we have implemented electron-recoil discrimination based on successive cuts. We estimate that about 30% of the kept events are due to background. The measured angular distribution and the reconstructed neutron spectrum are presented in Figure 8.17. We obtain similar results than previously: the angular distribution has an asymmetry, possibly due to background events, which results in a tail at high energy in the reconstructed neutron spectrum. We are anyway able to reconstruct a spectrum, indicating that we access directionality on proton recoils with kinetic energies below 8 keV. Note also that this energy range is significantly affected by quenching effects, so the spectrum suffers from the uncertainties on the measured IQF.

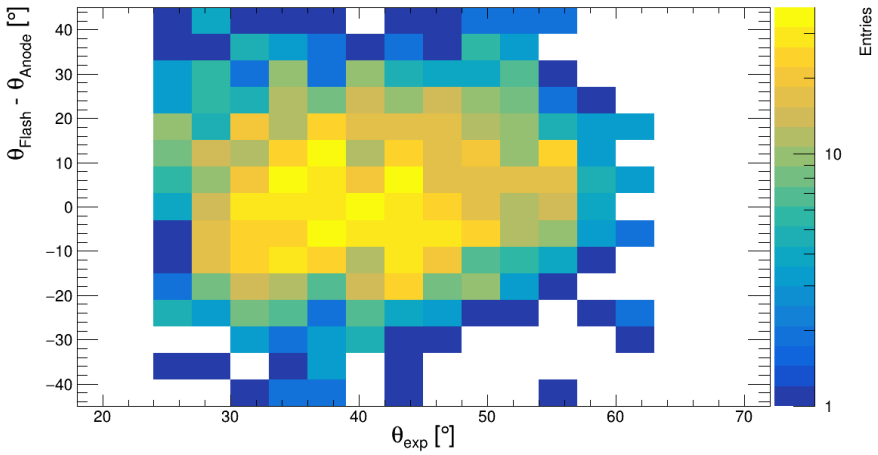

Figure 8.18: Comparison of the Flash and the anode methods for reconstructing the scattering angle in the AMANDE 27 keV data. The presented dataset has been obtained by the two-step BDT to select proton recoils.

8.4.3 Comparison to the Flash method and prospects

In this chapter, we have introduced two methods for accessing directionality at high-gain and a large gap of 512 μm: the deconvolution of the ionic contribution on the Flash and the anode method. Both take advantage of the ions accumulated in the gap. We are now ready to compare them. The first question to answer is the following: why do we not observe the carbon population when reconstructing the scattering angle from the Flash method? We remind that the reconstruction method from the Flash is based on the correlation between the duration of the ionic signal, once the last primary electron has been collected, and the polar angle. The conversion function has been determined by simulations and it follows an inverse cosine tendency: the larger the duration of the ionic signal, the smaller the polar angle. This correlation depends, among others, on the track length and on Eq. (8.1) that links the recoil energy to the scattering angle. This relation, and moreover the method used to determine its parameters, presupposes the presence of a single recoil species. For a given ionization energy, the density of the primary charges per timeslice (which is the central element of the Flash method) is comparable for a carbon recoil emitted at a small angle and for a proton recoil emitted at a large angle. In other words, the difference in track lengths is compensated by the polar angle. Carbon recoils with angles $< 20°$ are identified, by the Flash method, as proton recoils with angles $> 60°$. We anyway remind that the proportion of carbon recoils is about 10% according to the anode method, as one can see in Figure 8.14. For this reason, the Flash method is still able to reconstruct a neutron spectrum since most of the considered events are correctly identified as proton recoils.

Figure 8.18 presents the difference between the Flash and the anode methods for reconstructing the scattering angle for proton recoils in the AMANDE 27 keV data. The difference is shown as a function of the expected angle required to reconstruct the mono-energetic spectrum, as in previous figures. One can see that the two methods agree in the entire angular range since the difference is centered on 0°. This can be seen as an indirect validation of the empirical method on the anode. A large dispersion can still be observed, which indicates that at least one of the two methods sometimes fails in reconstructing the angle. Since the Flash and the anode methods rely on different hypotheses and working principles, one can use the redundancy between them to improve the directional performance. For instance, one can keep events for which the two methods agree within 10°, reducing possible fails in the angle reconstruction.

We remind that the presented results correspond still to a preliminary work. A few comments are required at this stage:

- The method of angle reconstruction from the anode is based on an empirical factor whose validity must be tested both experimentally and by simulations. Instead of correcting the ionic contribution on the anode strips, this method takes benefits from the additional information provided by the ions accumulated in the gap. If the preliminary results presented in this section are validated,

it would mean that directional performances can be enhanced by operating at high-gain and large gap.

- This new method has revealed the presence of carbon recoils and seems to be able to reconstruct the direction of carbon recoils below 2.5 keV_{ee}, which is the endpoint of carbons in the AMANDE 27 keV experiment. This is a promising preliminary result for the community of directional detectors.

- The reconstruction of the scattering angle is sensitive to the electron drift velocity. The reconstruction of the neutron spectrum is also sensitive to the IQF. These two physical quantities must be measured in our gas mixtures.

- We have two independent methods for reconstructing the angle, one from the Flash and another from the anode, that agree on average, over the entire tested angular range. The redundancy and the complementarity between the two approaches can improve the angular resolution.

This section has introduced a promising preliminary method for exploiting the ionic contribution on the anode in order to reconstruct the direction of a nuclear recoil, either being a proton or a carbon recoil. The next steps can be divided into three types. First, the test of the empirical factor introduced in the anode method. One must test the validity of such correction and its accuracy. This can be done by simulations thanks to `SimuMimac` and it must also be checked on experimental data, in particular by using Comimac and mono-energetic neutron fields. The second point consists in measuring the carbon IQF and the drift velocity in our gas mixture. The third step will be to investigate the complementarity between the Flash and the anode methods and to improve the MIMAC angular resolution by combining the methods. Finally, if we validate the anode method and the preliminary results presented in this section, then a new experiment on AMANDE would be required to: (1) detect fluorine recoils by reducing the detection threshold; (2) rotate the detector by 180° to measure the head-tail recognition efficiency; (3) vary the gain of the detector to optimize the ionic contribution to the signal.

Summary

Directionality is so far the only known strategy to overpass the neutrino floor and to identify a WIMP signal without ambiguity. For a WIMP mass below 100 GeV, directional gaseous TPCs must search recoils in the keV-range, resulting in track lengths of the order of millimeter. Measuring the direction of such recoils requires, for a Micromegas detector, to operate at high-gain and large gap in order to be sensitive to all primary charges. However, in such conditions, the detector gets more sensitive to the ions accumulated in the gap after the avalanches, resulting in distortions of the measured 3D tracks. In particular, the sensitivity to the ionic contribution on the anode leads to an under-estimation of the reconstruction polar angle of the track. In this chapter, we evaluate for the first time the directional performance of the MIMAC detector in the keV-range by using mono-energetic neutron fields produced by the AMANDE facility. Neutrons will make similar interactions than WIMPs, and they produce nuclear recoils whose energy is related to the scattering angle. Measuring the scattering angle and the energy of the recoil enables reconstructing the neutron kinetic energy, and then one can determine the angular resolution of the detector.

The Flash signal is made of an electronic contribution, having abrupt and fast kinematics, and of an ionic contribution that holds for about 300 ns after each avalanche and corresponds to the baseline of the signal. The time distribution of the primary electrons cloud is embedded into the electronic signal, so we have developed an analytical formula to deconvolve the ionic contribution on the Flash in order to extract the electronic signal. This deconvolution formula is derived thanks to several approximations and it can be applied to any measurements, without any parameter, since it only depends on the time development of the Flash profile. However, while we have validated that the deconvolution is very efficient for a sampling time lower than 5 ns, it suffers from some uncertainties at the MIMAC sampling time of 20 ns. We have estimated the efficiency of the deconvolution and we obtained a good performance: it is gain-independent, it biases the time of arrival of the last primary electron by less than one timeslice, and the integral of the obtained signal is proportional to the ionization energy.

The deconvolution of the ionic contribution to the Flash signal informs us about the time distribution of the primary electrons cloud. It precisely describes the asymmetry of the charge deposition as a function of time, which is related to the stopping power. This asymmetry could be used to distinguish between the head and the tail of the recoil, so to determine the sense the recoil which is a critical parameter for directionality. The deconvolution of the Flash also offers a promising approach for measuring the polar angle of a nuclear recoil produced by an elastic collision with a neutron. We have shown that the duration of the measured ionic signal after the arrival of the last primary electron is directly correlated with the polar angle (when the neutron is aligned with the Z-axis of the detector). The sensitivity to the ionic signal, compared to the electronic one, depends on the longitudinal charge density that governs the number of accumulated ions in the gap. By exploiting this information, we have been able to determine the angular distribution and the energy spectra of mono-energetic neutron fields at 27 keV and 8 keV. In both cases we obtained a better than 15° angular resolution for proton recoils in the keV-range.

The determination of the polar angle from the pixelated anode gets difficult at high-gain and large gap since the 3D tracks are distorted by the ionic signal. In this chapter, we have presented preliminary results for accessing the polar angle based on the pixelated anode. We have developed an empirical method that still requires additional tests and validations. This method takes advantage of the ionic signal since, due to the accumulation of ions in the gap, it increases the sensitivity of the anode. When applying this approach to the AMANDE 27 keV data we observe a sub-structure in the angular distribution of the recoils being composed of about 10% of the events. We have shown that this sub-structure is explained by carbon recoils. We have used BDTs to separate the carbon from the proton recoils, and we have been able to reconstruct a neutron spectrum from both species. We anyway observe an offset for the carbon-reconstructed spectrum probably due to the IQF that we used since we had to scale a `SRIM` simulation because we have not measured yet the carbon IQF in our gas mixture. The angular resolution is about 10° both for proton and carbon recoils.

The method for reconstructing the angle based on the anode information is preliminary and must be checked on additional data and by simulations. However, it is promising since it does not show any bias when compared to the Flash method. If we validate such preliminary results, we would have two independent and complementary methods for measuring the direction of a nuclear recoil, one from the Flash and the other from the anode. The redundancy of the two approaches could improve the MIMAC angular resolution in the keV-range. In both cases, the method exploits the information provided by the ions accumulated in the gap. In other words, once controlled, the ionic contribution to the signal could open new possibilities for directionality by offering additional degrees of freedom and by improving the anode sensitivity. The good angular resolution measured for keV recoils, the head-tail recognition, and the preliminary results from the anode, are a set of promising approaches for opening a new era for directionality in the keV-range.

Chapter 9

Searches for solar Kaluza-Klein axions

I called this particle the axion, after the laundry detergent, because that was a nice catchy name that sounded like a particle and because this particular particle solved a problem involving axial currents.

Frank Wilczek – 1991 [388]

The phenomenology of the axion propagating in large extra dimensions drastically differs from the four-dimensional case. We have seen in Chapter 3 that the bulk axion is observed from our brane as an "infinite" superposition of KK axions, thus significantly increasing the abundance of the axions as well as their masses, and decreasing their lifetime. The Sun, due to its proximity to the Earth, could be an interesting source and we have previously shown that it would produce KK axions with masses in the range $\mathcal{O}(1-20)$ keV. Part of them would be sufficiently non-relativistic to get trapped into the solar gravitational field, thus orbiting the Sun and accumulating over cosmic times.

In 2003, the model of Di Lella and Zioutas [211] pioneered the phenomenology of trapped KK axions. This work, while paving the way for many promising studies, was mainly qualitative and contained only a few mathematical details. We have then entirely revised the solar KK axions model with Mar Bastero-Gil in [218] and our results are presented throughout this thesis. Starting from the basis set twenty years ago, we have derived analytically the relevant expressions for the KK axions phenomenology. In Section 9.1, we start by updating the astrophysical constraints that apply to the model: we revise the calculations and we compare the model predictions to recent data. We will see that stringent limits constrain the solar KK axions model with major consequences for the detection of such particles.

Supposing the presence of massive pseudoscalars orbiting the Sun offers new mechanisms for explaining puzzling observations in the solar system. We will see in Section 9.2 that the decay of the trapped KK axions into photons could solve the coronal heating problem [211] and could explain the non-thermal distribution of the solar X-rays measurements [212, 218]. It then provides additional motivation for searching for KK axions. We will see that most of the experiments dedicated to axion detection could update their analyzes to incorporate the searches for KK axions and exclusion limits on the bulk axion have already been obtained from helioscopes [389, 390] and from nuclear transition experiments [391]. Some experiments are able to efficiently probe the extra dimensions and to measure the compactification radius if an axion signal were to be detected. The KK axions are mainly searched via their decay into photons, a channel that is considered as inaccessible for standard axions. We will revise the $a \to \gamma\gamma$ event rate in the light of the updated solar KK axions model. In Section 9.3, we will see that MIMAC is an appropriate detector for searching for KK axions via the decay into photons. We will briefly explore the discovery potential of the detector.

The main conclusions of our revision of the solar KK axions model significantly moderate the possible detection of KK axions via the decay channel in the near future. We are currently working on an extension of the model to non-hadronic axions, that is by considering a coupling to fermions at tree-level, providing additional mechanisms that could possibly relax the main constraint, then increasing the $a \to \gamma\gamma$ event rate in the detector. The main idea behind this extension is that the trapped KK axions are frequently crossing the Sun in their orbits, with a non-negligible probability of being re-absorbed by the Sun, in particular for the large masses. We will discuss such a hypothesis in Section 9.4 as an outlook on a possible detection of KK axions in a TPC, although our preliminary work seems to indicate that the re-absorption mechanism would not be sufficient to relax the main constraint.

9.1 Constraining the solar KK axions model

The existence of extra dimensions and KK axions would alter some astrophysical and cosmological considerations. To be viable, the solar KK axions model must be compatible with experimental constraints. In this section, we review the constraints applying to the model in order to determine the parameter space in which KK axions should be searched for.

9.1.1 Solar luminosity

The first constraint that we will consider is the one that puts the most stringent limits on the solar KK axion model. Paradoxically, it is also the constraint that brings one of the most interesting motivations for KK axions, as we will see. As explained in Chapter 3, part of the KK axions gets trapped in the solar gravitational field and accumulates. A KK axion eventually decays into two photons and contributes to the solar luminosity. This solar luminosity due to trapped KK axions should not exceed the observed solar luminosity, a requirement that sets constraints on the parameters of the model.

The maximal value for the axion-photon coupling obtained by DiLella and Zioutas using ASCA/SIS X-ray data [211] has been reduced by more than one order of magnitude a few years later using measurements of the quiet Sun from RHESSI [392, 393]. While the solar axion luminosity is stable during short time periods, the standard solar luminosity depends on the Sun's activity. For this reason, we must compare our predictions to measurements of the quiet Sun when the solar X-ray emissions are not related to flares, sunspots, or active regions. In this work, we refer to solar X-rays measurements in the range $(1-6)\,\mathrm{keV}$ from the SphinX spectrophotometer [394, 395] during a period of deep solar minimum in 2009 known for its extremely low solar activity.

The SphinX spectrometer is orbiting the Earth and it has a conical field of view (FoV) of 2°. We want to determine the flux of photons coming from KK axion decays that enter the FoV of SphinX. Considering for simplicity that the detector covers a cone of aperture α_0, we should integrate the number density of trapped KK axions over the solid angle of the detector, $d\Omega_D$, and over a radial distance D from the detector (*i.e.*, the Earth). Here we follow the approach in references [396–399]. In these references, the flux of photons due to decaying dark matter (number of photons per unit time

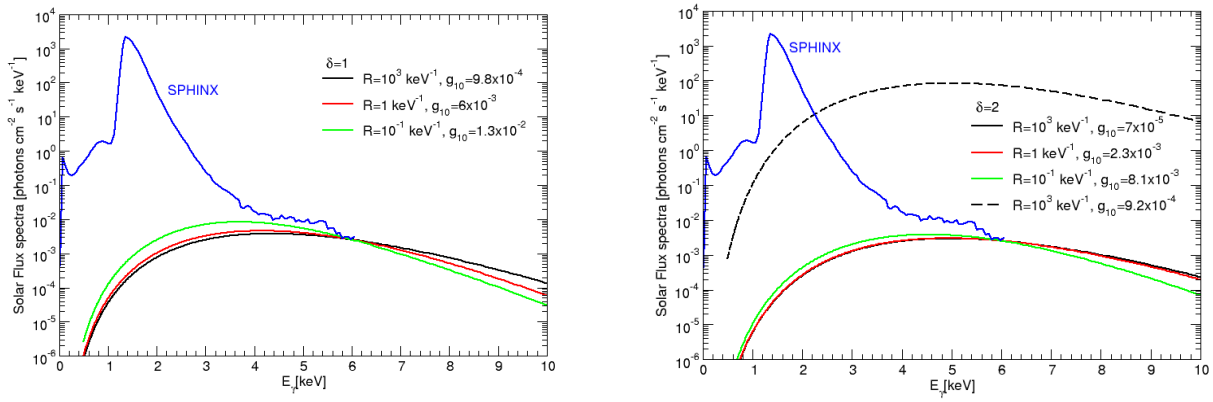

Figure 9.1: The spectral photon flux from trapped KK axions as observed from Earth and the flux measured by SphinX. The left panel shows the case $\delta = 1$ whereas $\delta = 2$ is presented on the right one. Model parameters are indicated in the plots and they have been adjusted to remain below the SphinX measurements. The black dashed line on the bottom panel represents the photon flux obtained using the parameters from [211].

and unit surface) is given by:

$$F_{DM} = \Gamma_{DM} \frac{E_\gamma}{m_{DM}} \int_{FoV} \frac{\rho_{DM}(r)}{4\pi |\mathbf{r_D} + \mathbf{r}|^2} d^3\mathbf{r} \tag{9.1}$$

where Γ_{DM} is the decay rate into photons, r_D is the distance between the Sun and the Earth, and ρ_{DM} is the local DM density. The integral is done within the FoV of the detector. For example, for a small FoV, and DM decaying into two photons with $E_\gamma = m_{DM}/2$, one has:

$$F_{DM}[\alpha] \simeq \Gamma_{DM} \frac{\Omega_{fov}}{8\pi} \int \rho_{DM}(r) dz \tag{9.2}$$

where the integral is the column integral along the line of sight z, $r = r_D^2 + z^2 - 2 r_D z \cos\alpha$, and α is the angle between D and r_D centered on the Earth.

The detail of the derivation of the physical quantities is provided in [218]. We here only quote the main results. The number of trapped KK axions in the detector FoV is given by:

$$\begin{aligned} N_a^{T,\,FoV}(m) &= \int_{FoV} d\mathbf{r}^3 \frac{r^2}{4\pi D^2} n_a^T(r, m) \\ &\simeq \frac{R_\odot n_a^T(R_\odot, m)}{2\bar{r}_D^3} \left(2\bar{r}_D - \frac{2}{3\bar{r}_D} - \frac{1}{2}(1 - \frac{\alpha_0 - \pi}{\tan\alpha_0}) \right) \end{aligned} \tag{9.3}$$

and the flux of photons due to the decay of trapped KK axions and that enter the FoV of the detector by:

$$\frac{dF}{dE_\gamma} = 2\frac{dF}{dm} = 2\frac{2\pi^{\delta/2}}{\Gamma[\delta/2]} (Rm)^\delta m^{-1} \Gamma_{a\gamma\gamma} N_a^{T,\,FoV}(m) \tag{9.4}$$

The spectral photon flux in a SphinX-like detector from the decay of trapped KK axions is presented in Figure 9.1, for $\delta = 1$, 2 and different values of the extra dimension radius[1]. Remaining below the SphinX measurements implies stringent limits on the maximal value of the axion-photon coupling. The set of parameters proposed by DiLella and Zioutas [211] is now ruled out.

Measurements of the X-ray spectrum of the quiet Sun in Figure 9.1 does not follow an isothermal distribution as expected from the element abundances. Significant deviations from the theoretical spectrum obtained with the CHIANTI database are observed for energies above 2.5 keV [395]. Similar

[1]Notice that strictly speaking the curves for $R = 10^{-1}$ keV^{-1} should start at $E = 5$ keV, given that the lightest state in the KK tower would have a mass $m_1 = 10$ keV, but we include the full curves for comparison.

deviations are observed by RHESSI [393]. This could indicate the presence of non-thermal components (for instance via particle acceleration in solar microflares as measured by NuSTAR [400]), but it could also be explained by trapped KK axions as initially proposed by Zioutas *et al.* [212]. In Figure 9.1, one can see that the predictions of the photon flux from KK axions decay follow similar tendencies as the spectrum measured by SphinX, in particular for the case $\delta = 1$. Measurements of the solar X-rays spectrum do not only constrain the KK axions model, but they also contribute to motivating it as a promising explanation for the non-thermal behavior of the solar X-rays emission.

9.1.2 Solar energy loss

KK axions production in the solar core would result in energy loss and would consequently modify the helioseismological sound-speed profiles and the fluxes of neutrinos emitted by the Sun. Helioseismology has implied that the solar axion production would be indistinguishable from standard solar models as long as $L_a^D < 0.2\, L_\odot$ [401], a value that has been used to establish the solar KK axion model [211,254]. Solar neutrino fluxes have restrained to $L_a^D < 0.1\, L_\odot$ [402] and a study combining helioseismology and neutrino emissions has set the limit $L_a^D < 0.03\, L_\odot$ [403]. The solar axion luminosity referred to here is the direct luminosity from axions produced inside the Sun, which we distinguish from the trapped axion luminosity thanks to the superscript D (L_a^D).

The direct solar KK axion luminosity has been derived in [254],

$$L_a^D = A\, L_\odot\, g_{10}^2 \left(\frac{R}{\mathrm{keV}^{-1}}\right)^\delta \tag{9.5}$$

with $A = 0.018$ for $\delta = 1$, $A = 0.19$ for $\delta = 2$, and $A = 2.1$ for $\delta = 3$. We remind that $g_{10} = g_{a\gamma\gamma} \times 10^{10}\,\mathrm{GeV}$. Using the limit $L_a^D < 0.03\, L_\odot$ we obtain the constraint from solar energy loss:

$$g_{10} \left(\frac{R}{\mathrm{keV}^{-1}}\right)^{\delta/2} < \begin{cases} 1.3 & \text{for } \delta = 1 \\ 0.40 & \text{for } \delta = 2 \\ 0.12 & \text{for } \delta = 3 \end{cases} \tag{9.6}$$

9.1.3 Extragalactic background light

The last constraint we will revise relies on the Extragalactic Background Light (EBL). We have already discussed this constraint for ALPs in Section 3.1. We remind the reader that the photon flux due to late decaying ALPs (or KK axions) should not exceed the measured flux from outside the galaxy, that is the EBL. We extend our previous calculations to the case of the KK axions. However, this time we only consider possible photon absorption by the atoms of the intergalactic medium via photoionization since we have shown in Section 3.1 that the Compton scattering has a negligible influence on the energy range considered.

We need to compare the EBL measurements with the intensity of the photons flux from the KK axions decay denoted by I_E, multiplied by the energy to recover usual units. It is given by:

$$EI_E = \int_{2E_0}^{\infty} dm \frac{2\pi^{\delta/2}}{\Gamma[\delta/2]} R^\delta m^{(\delta-1)} \frac{3E_0 \rho(z_0, m)}{4\pi m} x e^{-x} e^{-\kappa_P(E_0)} \tag{9.7}$$

where the subindex "0" denotes values today, $x = \Gamma_{a\gamma\gamma} t_0 (2E_0/m)^{3/2}$, $\rho(z_0, m)$ is the energy density today, and $\kappa_P(E_0)$ is the absorption factor due to photoionization process that is parametrized by the function of Eq. (3.19).

The main difference with standard ALPs lies in the superposition of states in the KK tower. To determine the EBL contribution due to KK axions, one must consider how the energy is distributed among the KK modes, which is given by the spectral function $\rho(z_0, m)$. This distribution depends on the production mechanism but also on mode-mixing: when the system starts oscillating, the energy gets redistributed among the whole KK tower. The system starts oscillating during the phase transition

at which the axion gets a mass and, following the approach of [404], one can parametrize the time dependent mass like:

$$m(t) = \frac{m}{2}\left(1 + \mathrm{erf}\left(\frac{1}{\sqrt{2\delta_G}}\ln\frac{t}{t_G}\right)\right) \tag{9.8}$$

where m is the late time axion mass, $m(t_G) = m/2$, and δ_G controls how fast the transition takes place. In general, increasing δ_G suppresses the energy density in the KK tower; while increasing mt_G leads to the opposite effect, the energy density tends to be more democratically distributed. The authors of [404] define the parameter:

$$\eta_{KK} = 1 - \mathrm{max}_\lambda \frac{\rho_\lambda}{\rho} \tag{9.9}$$

where the subindex λ refers to the mass eigenstate, and ρ is the total energy density. Small values of η_{KK} indicate that most of the energy density is stored practically in one mode.

The next step is to determine the mass distribution function $\rho(z_0, m)$. The derivation of this function should follow from integrating the EoM of the coupled systems, but such a detailed study is beyond the scope of this work. Instead, we proceed by making a plausible ansatz for this function by considering a Gaussian of width Δ_K:

$$\rho(z_0, m) = \bar{\rho}_{KK} f_G(\bar{m}, \Delta_K) \tag{9.10}$$

$$f_G(\bar{m}, \Delta_K) = \frac{2}{\sqrt{\pi\Delta_K}} exp(-(\bar{m})^2/\Delta_K) \tag{9.11}$$

where $\bar{m} = m/m_1$, $m_1 = 1/R$, and $\bar{\rho}_{KK}$ is a parameter with units of energy density. We choose to normalize the function $f_G(\bar{m}, \Delta_K)$ to have unit area, such that:

$$\rho_{KK} \;=\; \bar{\rho}_{KK}\frac{2\pi^{\delta/2}}{\Gamma[\delta/2]}\int_1^\infty d\bar{m}\bar{m}^{(\delta-1)} f_G(\bar{m}, \Delta_K) \;\equiv\; \bar{\rho}_{KK} I_\delta^\infty \tag{9.12}$$

We still need to relate the value of $\bar{\rho}_{KK}$ with the DM energy density today. Note that within the KK tower most of the modes will have lifetimes smaller than the age of the universe and will not contribute to the present DM energy density. The heaviest stable mode is given by:

$$m_{DM} = \left(\frac{1.327\times10^{-4}}{g_{a\gamma\gamma}^2 \tau_u}\right)^{1/3} = \left(1.46\times10^{-2}\ \mathrm{keV}\right) \mathrm{g}_{10}^{-2/3} \tag{9.13}$$

and the fraction of KK modes that contribute to the DM energy density is:

$$\rho_{KK}^{DM} \;=\; \bar{\rho}_{KK}\frac{2\pi^{\delta/2}}{\Gamma[\delta/2]}\int_1^{\bar{m}_{DM}} d\bar{m}\bar{m}^{(\delta-1)} f_G(\bar{m}, \Delta_K) \;\equiv\; \bar{\rho}_{KK} I_\delta^{\bar{m}_{DM}} \tag{9.14}$$

Finally, using the present value of the DM energy density, we obtain:

$$\begin{aligned} EI_E = &\left(1.28916\times10^9 \mathrm{nW\ m^{-2}\ sr^{-1}}\right) \\ &\times \frac{2\pi^{\delta/2}}{\Gamma[\delta/2]}\, g_{10}^2\, \frac{\eta_{KK}}{(1-\eta_{KK})I_\delta^\infty + \eta_{KK} I_\delta^{\bar{m}_{DM}}} \left(\frac{E_0}{m_1}\right)^{5/2} \left(\frac{m_1}{\mathrm{keV}}\right)^3 F_{A\delta}\left\{\frac{E_0}{m_1}, g_{10}, m_1\right\} \end{aligned}$$

$$F_{A\delta}\left\{\frac{E_0}{m_1}, g_{10}, m_1\right\} = \int_{\bar{m}_{min}}^\infty d\bar{m} f_G(\bar{m}, \Delta_K)\bar{m}^{(\delta-1/2)} e^{-C_x\bar{m}^{3/2}}\, e^{-\kappa_P(E_0)} \tag{9.15}$$

$$C_x \equiv 92 \times g_{10}^2 \left(\frac{E_0}{m_1}\right)^{3/2} \left(\frac{m_1}{\mathrm{keV}}\right)^3 \tag{9.16}$$

Each KK mode cannot contribute to the spectrum with energies E_0 larger than half their mass, and therefore $\bar{m}_{min} = 2E_0/m_1$ when $2E_0 \geq m_1$ and one otherwise.

We are now ready to compare the expected light from KK axions decay to the EBL measurements. We approximately parametrize the upper limit of EBL published in [405] and [232] by the formula:

$$EI_E^{max} \simeq 0.20412 \times \lambda[\mathring{A}]^{0.47317}\, \mathrm{nW\ m^{-2}\ str^{-1}} \tag{9.17}$$

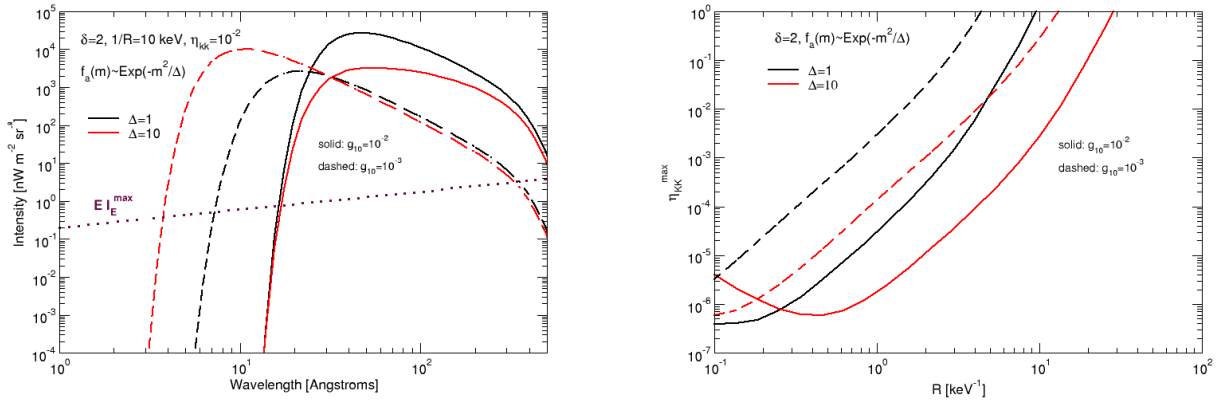

Figure 9.2: Left: spectral intensity function from the decay of the KK tower for a set of parameters indicated in the plot. Solid lines correspond to $g_{a\gamma\gamma} = 10^{-12}\,\mathrm{GeV}^{-1}$ and dashed lines are obtained for $g_{a\gamma\gamma} = 10^{-13}\,\mathrm{GeV}^{-1}$. The purple dotted line $EI_E^{\max}$ corresponds to the experimental limit given by Eq. (9.17).
Right: the maximum allowed value of η_{KK} in order to have $EI_E \leq EI_E^{max}$.

$(\delta\,,\,n)$	R [keV^{-1}]	g_{10}	η_{KK}	Δ_K	M_* [TeV]	f_{PQ} [GeV]	$\bar{f}_{PQ}$ [GeV]
$(1\,,\,2)$	5×10^{-1}	7.3×10^{-3}	8×10^{-6}	1	2.0×10^{3}	1.6×10^{9}	6.4×10^{2}
$(1\,,\,2)$	10^{3}	9.8×10^{-4}	–	–	4.4×10^{1}	1.2×10^{10}	7.1×10^{2}
$(2\,,\,2)$	5×10^{-1}	3.2×10^{-3}	3×10^{-5}	1	2.0×10^{3}	3.6×10^{9}	5.9×10^{-4}
$(2\,,\,3)$	5×10^{-1}	3.2×10^{-3}	3×10^{-5}	1	5.4	3.6×10^{9}	2.1×10^{-1}
$(3\,,\,3)$	5×10^{-1}	1.7×10^{-3}	10^{-4}	1	5.4	6.8×10^{9}	3.1×10^{-6}

Table 9.1: Possible sets of parameters allowed experimentally and the corresponding quantities defined in Section 3.2.

In Figure 9.2 are presented the EBL predictions from our model for several sets of parameters (left panel) and $\delta = 2$ as an example. On the right panel we have plotted the maximum allowed value for η_{KK} to guarantee that the contribution remains below the observational constraint as a function of the compactification radius R. In general, the smaller the width of the Gaussian, the easier to fulfil the EBL constraint since the energy density left in the tower diminishes. However, this trend is reversed when increasing $g_{a\gamma\gamma}$ (and therefore their decay rate into photons) and $R \lesssim 1\,\mathrm{keV}^{-1}$, as shown on the right panel in Figure 9.2. Nevertheless, while the EBL puts stringent limits in the case of standard ALPs in the energy range considered [85], KK axions can easily escape this constraint, depending on how the energy is distributed among the KK tower.

The revision and the update of the constraints that apply to the solar KK axion model, as detailed in this section, bring us to the determination of possible sets of parameters. Some of them are proposed in Table 9.1. For instance, we see that the case $\delta = 1$, $R = 10^3\,\mathrm{keV}$, and $g_{10} = 9.8\times10^{-4}$ fulfils the constraints and allows to have the fundamental gravitational scale, M_*, as well as the overall scale of the PQ symmetry breaking, $\bar{f}_{PQ}$, near the electroweak scale.

9.2 KK axion detection

9.2.1 Hints from astrophysics

In the previous section, we have derived the constraints that apply to the solar KK axion model. Besides the constraints, we would appreciate some hints to motivate a particular coupling to be searched for. The possible existence of trapped KK axions around the Sun could shine a light on astrophysical puzzling observations. The pioneering paper [211] proposed the decay of trapped KK axions as the

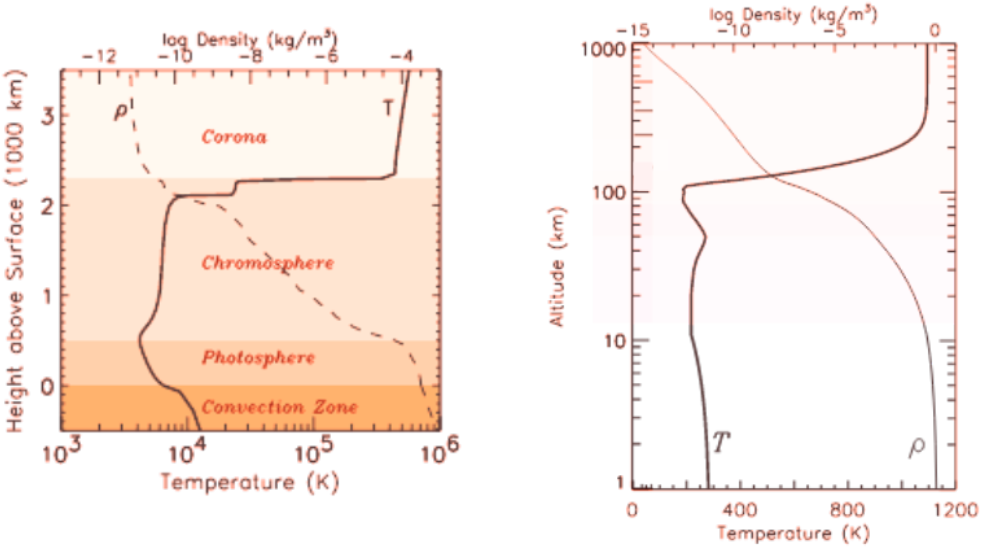

Figure 9.3: The mean temperature T and density ρ profiles as a function of the altitude for the Sun (left) and for the Earth (right). Figure adapted from [211].

explanation for a remarkably large number of astrophysical problems. The article is mainly qualitative and exploratory, requiring finer analyses such as the analytical derivation of the number density of trapped KK axions as presented in this thesis.

The decay of trapped KK axion into photons was proposed in [211] as an explanation for the solar corona problem. Stated simply, this long-standing problem is the question of why the solar corona is about 300 times hotter than the solar surface underneath? The corona could not be in equilibrium with the surface because it would violate the laws of thermodynamics. The high temperature of the corona must then be maintained by processes dissipating some energy non-thermally in the upper atmosphere.

The KK axion solution to the solar corona problem comes from an analogy with the heating of the Earth's atmosphere. The abrupt temperature changes in the solar corona show similar tendencies to the temperature fast increases in the Earth's atmosphere under X-ray irradiation from the Sun [406]. The similarities for the temperature and the density profiles are shown in Figure 9.3. If KK axions are produced in the Sun, part of them would be trapped around it and would eventually decay into photons, leading to an external X-ray source for the Sun. The emitted photons with energy of a few keV would be absorbed by the solar corona, increasing its temperature. Photons with higher energies would travel a longer path before being absorbed and could be related to the slow increase in the temperature of the chromosphere. The authors of [211] have concluded that the solar corona problem could be solved by KK axions of masses around 400 eV and in the keV-range. While further work is required to reinforce this hypothesis, it remains a plausible solution and it is consistent with simulations of stellar atmosphere irradiation from a hotter X-ray source [407].

Trapped KK axions were also proposed in [211] as the explanation for the observed X-ray spectrum coming from the dark side of the Moon, which is two orders of magnitude lower than the irradiation from the bright side. However, later measurements recorded by CHANDRA [408] seem to rule out this hypothesis due to the time-variation of the X-ray intensity and rather support the explanation of the geocoronal solar-wind charge transfer.

The most motivating astrophysical hint for trapped KK axions is probably the solar luminosity measurement. As discussed in the previous section, the measured X-ray spectrum of the Sun shows a non-thermal component above 2.5 keV. As presented in Figure 9.1, this non-thermal component is well reproduced by the expected luminosity from the decay of trapped KK axions. It is too soon to determine the best set of parameters to match the SphinX data since, as we will see in Section 9.4, we are still developing the solar KK axion model. However, we can already say that besides constraining the model, the measurement of the solar luminosity is likely the strongest argument for KK axions.

9.2.2 Strategies of detection

While extensive searches for axion and ALP are performed, only a few experiments have set constraints on the KK axions. However, revisiting the analyses and adapting the designs of the ALP experiments to the framework of extra dimensions could open new detection channels. Let us briefly describe the main strategies of detection for the solar KK axions. We here discuss the detection of hadronic axions, which do not couple to fermions at tree-level, since it is the most general model that we have considered in this work.

LSW and helioscope

The majority of the experiments searching for standard axion makes use of a magnetic field to exploit the Primakoff effect for converting an axion into a detectable photon [219]. In a gas, the probability that an axion has been converted into a photon after a path L in a homogeneous magnetic field B is given by [389]:

$$P(a \to \gamma) = \left(\frac{g_{a\gamma\gamma}B}{2}\right)^2 \frac{1}{q^2 + \Gamma^2/4}\left\{1 + e^{-\Gamma L} - 2e^{-\Gamma L/2}\cos\left(qL\right)\right\} \tag{9.18}$$

where $q = \left|(m_\gamma^2 - m^2)/2E\right|$ is the momentum transfer, m_γ is the effective photon mass (*c.f.* Section 3.3), and Γ is the inverse absorption length. Note that in vacuum $m_\gamma = \Gamma = 0$.

This conversion probability can be used to search for axions in laboratory experiments. For instance, the *light shining through walls* (LSW) experiments send a laser to an opaque wall and aim for the process $\gamma \to a \to \gamma$, enhanced by a strong magnetic field, to convert a photon into an axion in order to cross the wall before being converted back into a photon. A similar concept, also relying on the Primakoff conversion, is the backbone for the axion helioscopes. Helioscopes are searching for solar axions by pointing a detector with a homogeneous magnetic field towards the Sun, expecting to detect a photon on the opposite side, arising from the conversion of a solar axion inside the detector. The helioscope community has now joined their efforts into the IAXO collaboration [409] to build a next-generation helioscope aiming for a sensitivity in $g_{a\gamma\gamma}$ down to a few 10^{-12} GeV^{-1}.

In the case of solar KK axions, the mass is of the order of the keV. We then see that the probability $P(a \to \gamma)$ gets suppressed in this range. Depending on the compactification radius, helioscopes can still search for the lightest modes of the KK tower, as it has been done with the CAST helioscope [390]. Let us remark from Eq. (9.18) that the probability has a resonance for the coherence condition $m \simeq m_\gamma$. The helioscopes can operate in a scanning mode where the pressure is varied to modify m_γ and hence the coherence condition. For a four-dimensional axion, the coherence condition is fulfilled for a single axion mass. However, the situation changes for KK axions since the condition is fulfilled for each individual KK mode. Thus, the detection of a helioscope signal at two different pressures would demonstrate not only the existence of the axion, but the existence of extra dimensions. This signature, proposed by CAST members [389, 390], can serve as a probe for extra dimensions. Similar reasoning applies to LSW experiments.

Haloscope

In case the axions constitute the entire dark matter, the local axion density and its velocity distribution can be inferred from the DM halo models introduced in Section 2.1. Haloscopes aim to detect these galactic axions by conversion of an axion into a photon in a resonant cavity immersed in a magnetic field. When the resonant frequency of the cavity matches the axion frequency, near the axion mass, the axion-photon conversion is enhanced and a weak but detectable signal ($\sim 10^{-23}$ W) can be extracted. Haloscopes are mainly designed to search for light axions (< 100 μeV) since for higher frequencies the cavity volume must be decreased, reducing the expected power. Note also that haloscopes are based on the assumption that the galactic axion field is constant within the detector [219], which is a relevant assumption for QCD axion but fails for heavy axions when the De Broglie wavelength is smaller than the size of the experiment ($\lambda_c < 1$ cm for $m > 0.2$ eV). Haloscopes are restrained to search for light axions which could be the case of the relic KK axions depending on the production mechanisms in the

Early Universe. Further investigations are required to determine the haloscope discovery potential for KK axions.

The haloscope, similarly to the helioscope, could be used as a probe for extra dimensions since it is sensitive to a narrow mass window that is tuned by varying the cavity frequency. The measurement of a signal at two different frequencies would be the signature of KK axions, the frequency difference being the inverse of the compactification radius.

Nuclear transitions

Another strategy of detection of standard axions makes use of the nuclear transition of ^{57}Fe and ^{7}Li. These two stable nuclei are produced in the solar interior and they could emit an axion during a transition from the first excited state to the ground state. The energy of such axions is well determined from nuclear physics: 14.4 keV and 478 keV for ^{57}Fe and ^{7}Li, respectively. These mono-energetic axions could be resonantly absorbed by the nuclei of a detector on Earth, resulting in the emission of photons of corresponding energy that could be detected. The rate of the resonant absorption is directly related to the solar axion flux and to the axion properties.

This strategy of detection has been extended to the case of solar KK axions in [391] by adapting the excitation rate and integrating out the KK tower. One of the advantages of this method is that it only consists of a second analysis of the data collected by detectors searching for standard axion. In other words, the design of the experiment does not need to be updated to search for KK axions.

Indirect searches

The search for KK axions can also be performed via indirect processes. In the previous section, we have shown examples of how the phenomenology of the Sun or the Extragalactic Background Light could be affected by the possible existence of KK axions. A burst of axions is expected in supernovae leading to a photon flux after axion decay or after axion-photon conversion. Oscillations between axions and photons are also expected, which would modify the photon fluxes from distant sources. Revisiting X-rays and γ-rays measurements in the framework of KK axions instead of standard ALPs could lead to interesting results. We have shown that the trapped KK axions density evolves as $1/r^4$, with r the distance to the Sun. Measurements of the solar photon flux at multiple distances to the Sun could reveal this $1/r^4$ behavior. For instance, the STIX telescope [410] placed on Solar Orbiter will soon measure hard X-rays at distances to the Sun down to $0.22\,A.U.$.

Axion decay

The above strategies of detection are, for most of them, relying on an extension of the searches for standard axion to extra dimensions. However, as already discussed, on the contrary of the QCD axion, KK axions could also be detected by the decay channel $a \to \gamma\gamma$. The signature of the decay of a KK axion is the emission of two photons back-to-back, each of them carrying the same energy $E_\gamma = m/2$ since the gravitationally trapped axions are non-relativistic. This channel is available given the larger masses of the KK axions compared to the standard axion.

In a Time Projection Chamber (TPC) the $a \to \gamma\gamma$ signature is almost unique, so it would lead to a very efficient background discrimination. The axion decay rate does not depend on the type of detector but only on its active volume. Low-pressure gaseous TPCs, such as MIMAC, are then appropriate for searching for KK axions with the axion decay since they can reach a large detection volume and that they are suitable to detect keV photons. Searching for KK axions via the detection of the photons emitted by the decay has been proposed in [213–215, 254] and was used to set exclusion limits on solar KK axions [216, 217]. The authors of [216] make use of the annual modulation of the signal expected from the $1/r^4$ behavior of the axion density to derive the exclusion limits.

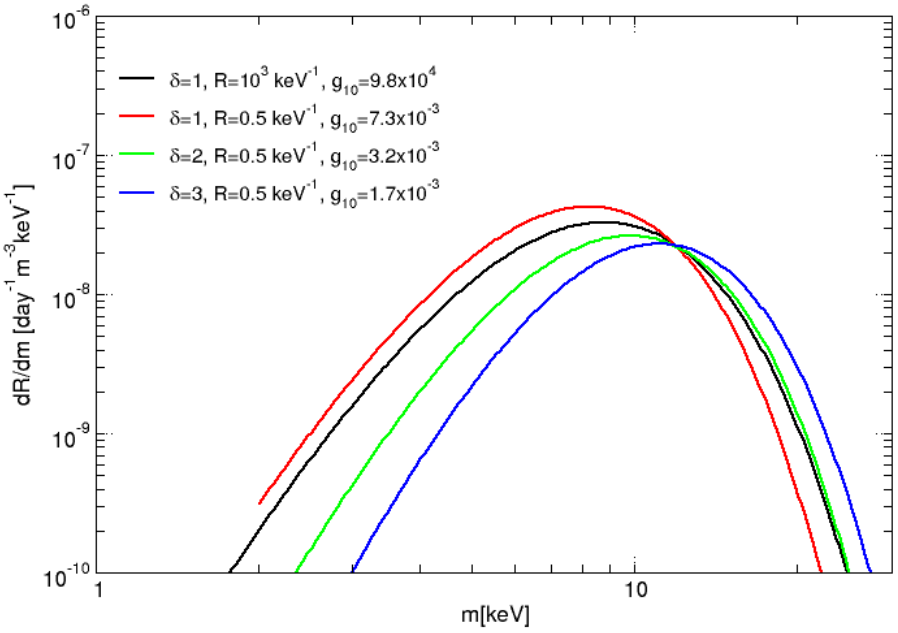

Figure 9.4: Differential decay rate of trapped KK axions into photons in a detector on Earth, as a function of their masses, for the experimentally allowed sets of parameters indicated in the plot.

9.2.3 The $a \to \gamma\gamma$ event rate

The differential decay rate of trapped KK axions into photons is given by:

$$\frac{dR}{dm}(r) \;=\; \Gamma_{a\gamma\gamma}\,\frac{dn_{KK}^{(T)}}{dm}(r) \;=\; \left(6.51\times 10^{-12}\,\mathrm{day}^{-1}\right) g_{10}^2 \left(\frac{m}{\mathrm{keV}}\right)^3 \frac{dn_{KK}^{(T)}}{dm}(r) \tag{9.19}$$

where $n_{KK}^{(T)}(r)$ is the trapped KK axion density evaluated at a distance r to the Sun whose formula is given in Eq. (3.61). The decay rate is represented in Figure 9.4 for several sets of parameters that fulfil all the constraints described previously. We see that the KK axion mass ranges from roughly $(1-30)\,\mathrm{keV}$ with an expected peak at $m = 2E_\gamma \simeq O(10)$ for each set of parameters. The number of extra dimensions slightly shifts the position of the peak.

Several comments are required at this stage. First, the event rate can be determined by integrating the event rate Eq. (9.19) over the mass. For the set of parameters in Figure 9.4, the event rate in a detector on Earth gives $R \simeq 3\times 10^{-7}\,\mathrm{day}^{-1}\cdot\mathrm{m}^{-3}$. This is a major conclusion from our analysis. This value must be compared to $R \simeq 0.21\,\mathrm{day}^{-1}\cdot\mathrm{m}^{-3}$ that was obtained from the DiLella and Zioutas model [214]. The difference comes from two reasons: the revision of the number density since we obtain a density about 50 times lower than in [211], and the updated constraints from more recent solar measurements.

A second comment concerns the axion production channels. So far we have restricted our study to hadronic axion models, even though considering a non-zero axion-electron coupling, g_{ae}, offers additional mechanisms to produce KK axions in the Sun at a lower mass. The solar photon flux due to the electron-axion coupling will be proportional to $g_{a\gamma\gamma}^2 g_{ae}^2$, while that due to coalescence is proportional to $g_{a\gamma\gamma}^4$. And the same coupling dependence holds for the detection rate. So let us call F_{SphinX} the measured solar photon flux, and $F^\gamma = g_{a\gamma\gamma}^4 \bar{F}^\gamma$ and $F^e = g_{a\gamma\gamma}^2 g_{ae}^2 \bar{F}^e$ the flux due to coalescence and axion-electron production respectively, such that:

$$g_{a\gamma\gamma}^2 (g_{a\gamma\gamma}^2 \bar{F}^\gamma + g_{ae}^2 \bar{F}^e) \leq F_{\mathrm{SphinX}} \tag{9.20}$$

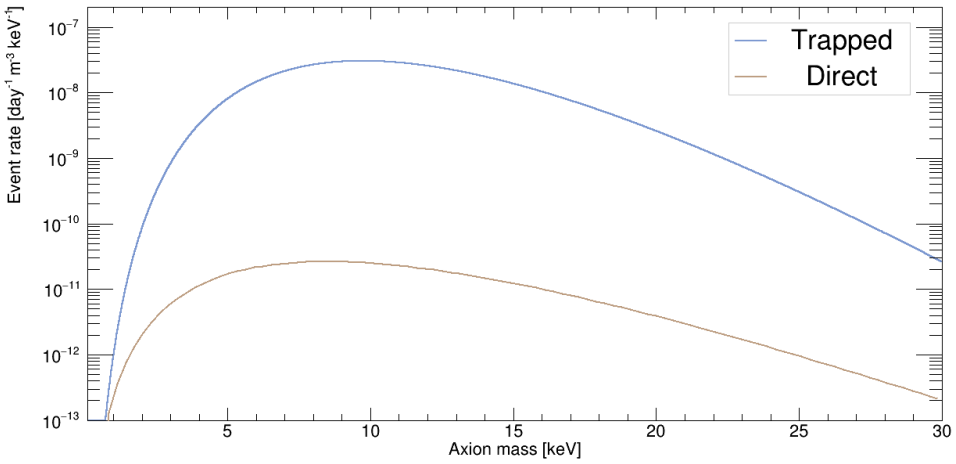

Figure 9.5: The event rate in an Earth-based detector for trapped KK axions compared to the one for the direct emission from the Sun. The curves are obtained for $\delta = 1$, $R = 10^3$ keV^{-1}, and $g_{10} = 9.8 \times 10^{-4}$.

Similarly denoting by $R_{\gamma,\,e}$ the event rate from axion-photon or axion-electron coupling respectively, and using the "bar" notation to normalize quantities from values at unit coupling, one can then show that:

$$R = g_{a\gamma\gamma}^2(g_{a\gamma\gamma}^2\bar{R}_\gamma + g_{ae}^2\bar{R}_e) = g_{a\gamma\gamma}^4\bar{R}_\gamma + (\frac{F_{\text{SphinX}}}{\bar{F}^e} - g_{a\gamma\gamma}^4\frac{\bar{F}^\gamma}{\bar{F}^e})\bar{R}_e \tag{9.21}$$

Eq. (9.21) tells us that considering the axion-electron coupling to produce KK axions via other processes in the Sun would only have a minor influence on the constraint on $g_{a\gamma\gamma}$ imposed by measurements of the solar X-rays spectrum. In other words, any detector searching for KK axions via the coupling to photons will be limited by the constraint on $g_{a\gamma\gamma}$ from solar luminosity regardless of the production mechanisms.

Finally, let us compare the trapped event rate with the event rate for the direct flux of KK axions that are emitted continuously by the Sun. This flux is significantly dominated by the Primakoff production [254]. Figure 9.5 presents a typical comparison of the two event rates in an Earth-based detector and one can see that considering the trapped KK axions increases the event rate by about 3 orders of magnitude. The difference obtained by Di Lella and Zioutas [211] was even larger due to the $\mathcal{O}(50)$ factor difference that we obtain in our derivation of the number density, *c.f.* Section 3.4.

The updated event rate for the decay of trapped KK axions, being 6 orders of magnitude lower than the one determined from the previous model [211], seems to close the window for KK axion detection via the decay channel. However, let us anticipate over Section 9.4 by saying that part of the trapped KK axions could be re-absorbed by the Sun since their orbit often crosses the Sun. In Section 9.4 we discuss such a possibility although we do not have concluding results at the moment.

9.3 KK axion searches with MIMAC

9.3.1 Proof of concept

A non-relativistic axion decay results in the emission of two identical photons, back-to-back, both carrying an energy $E_\gamma = m/2$ in the keV-range. In a MIMAC chamber, the two photons will travel some distance before interacting via the photoelectric effect on an electron of a molecule of the gas. As discussed in Section 5.1, after the absorption of the photon, the gas molecule emits a photoelectron of a well-defined energy that will ionize the gas. This photoelectron is accompanied by the emission of Auger electrons (or more rarely by photons that are absorbed in a short range) which cannot be spatially resolved by the detector compared to the photoelectron. The total energy of the photoelectron plus the Auger electrons is equal to E_γ. In other words, the axion-induced photons will be absorbed by the gas molecule and will result in a primary electrons cloud whose number of electrons is directly

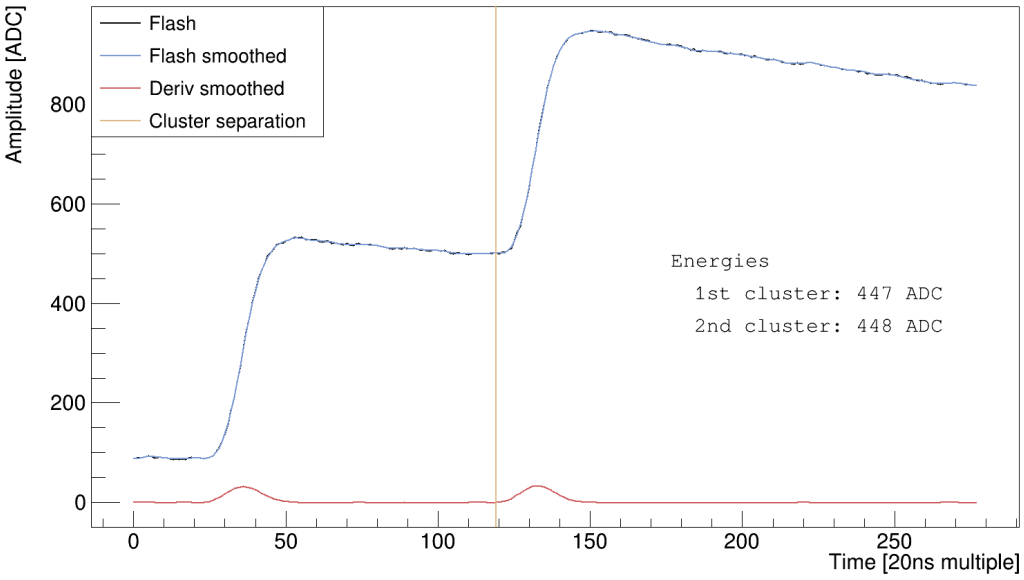

Figure 9.6: Comimac experiment reproducing the expected signal of a $a \to \gamma\gamma$. 4 keV electrons are sent in a MIMAC chamber at a high rate in order to produce some pile-up to detect two electrons of the same energy in the same time window.

proportional to the energy of the photon.

The emission of the electron during the photoelectric effect is almost isotropic so the directional information (the back-to-back photons) is lost at this point. However, the 3D track reconstruction offered by MIMAC can anyway be used to spatially resolve the two photons to better discriminate the background.

In a MIMAC detector, the signature of the $a \to \gamma\gamma$ event will then be two electrons of the same energy separated by a given distance L that depends on the mean free path of the photons in the gas, so that can be optimized by varying the gas mixture and the pressure. On the Flash, we expect to observe two bumps of the same amplitude, *i.e.* of the same energy, in a single time window. On the anode, we expect two spatially separated clusters of pixels that can be associated with an electron track, *c.f.* Section 5.3. Such a signature is almost unique so it cannot easily be mimicked by the background.

We have used Comimac to demonstrate the ability of MIMAC for detecting such a signal. In this experiment, we have sent electrons between 1 keV and 4.5 keV in the *Mimac gas* at 50 mbar and we have set the `PostMax` value to 256 timeslices to benefit from a large time window. We have boosted the Comimac beam to operate at a high event rate in order to produce some pile-up, which is the measurement of two independent events in the same time window. We then expect to measure events with two electrons of the same energy. We have developed an algorithm to detect multi-cluster events, from the smoothed derivative of the Flash signal, to identify a pile-up. In Figure 9.6 we show an example of such a pile-up for 4 keV electrons sent by Comimac. One can see that the two bumps on the Flash are easily identified and their amplitude difference is only 1 ADC.

This experiment with Comimac acts as a proof of concept for demonstrating the ability to detect an axion decay on the Flash signal. Since we Comimac all particles are sent at the same position in the detector, we cannot exploit the anode to separate the two clusters.

9.3.2 Detection efficiency

Due to the energy resolution of the detector, that is a Gaussian with a width $\sigma(E)$ following a $1/\sqrt{E}$ tendency, the measured energy difference $E_1 - E_2$ between the two photons will be distributed into a Gaussian with null-mean and a variance given by $2\sigma^2(m/2) = \sigma^2(m)$. We can then define an energy cut that will depend on $\sigma(m)$, for instance $|E_1 - E_2| < 2.35\,\sigma(m)$ accepts 90% of the events. The spatial distance s between the two interactions, for a photon mean free path $\lambda(m/2)$, is distributed

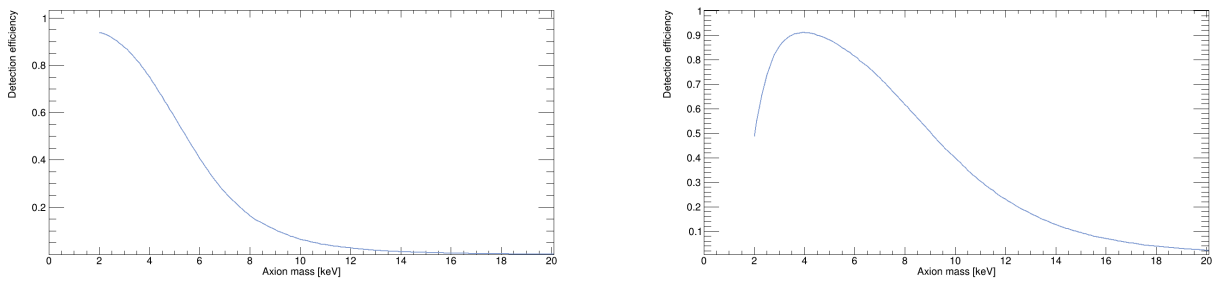

Figure 9.7: Monte-Carlo simulation of the $a \to \gamma\gamma$ detection efficiency in a 1 m^3 MIMAC detector as a function of the axion mass. Left: the *Mimac gas* at 50 mbar. Right: 95% C_3F_8 + 5% i-C_4H_{10} at 100 mbar.

as [214]:

$$P(s,m) = \frac{s}{\lambda^2(m/2)} \exp\left\{-\frac{s}{\lambda(m/2)}\right\} \tag{9.22}$$

allowing to define a range in s for accepting the event: a loo large s distance is unlikely to be attributed to an axion decay; a too short s will not be spatially resolved by the detector. A maximal value of $s \simeq 4\,\lambda(m)$ accepts 90% of the events. The minimal value depends on the gas properties and, for the rest of the analysis, we have worked with the conservative value of $s = 2$ mm to account for diffusion. In our low-pressure gas mixtures, the photon mean free path is usually large enough so that the minimal value of s is not a sensitive parameter. On the contrary, the maximal value is more critical and is mainly limited by the detector geometry.

We have performed a Monte-Carlo (MC) simulation to determine the detection efficiency of the MIMAC detector. For a given gas mixture, the photon mean free path $\lambda(E)$ is provided by the relation $\lambda(E) = \left(\frac{\mu(E)}{\rho}\,\rho\right)^{-1}$ where ρ is the gas density and $\mu(E)/\rho$ is the mass attenuation coefficient that we get from the `XCOM` database [411]. We use the geometry of the 1 m^3 future MIMAC detector. An axion decay is placed at a random position in the detector and the direction of the photon emission is drawn from an isotropic distribution, imposing the condition that the two photons are emitted back-to-back. For each photon, the path travelled before performing a photoelectric effect is drawn from an exponential distribution with $\lambda(E)$ as a mean value. An event is considered as detected if the two photons are absorbed before escaping the volume and if the distance between the two photoelectrons is larger than $s_{\min} = 2$ mm. In order to properly detect the bumps on the Flash, we also ask for a time difference larger than 5 timeslices. To convert the timeslices into a distance, we use the drift velocity simulated by `Magboltz` for a drift electric field of 150 V/cm. The MC then provides the probability of detecting an $a \to \gamma\gamma$ event as a function of the gas mixture, the pressure, and the axion mass.

The simulated detection efficiency of the MIMAC 1 m^3 detector is presented in Figure 9.7 for two experimental conditions. We see that the detection efficiency presents a maximum: for large axion mass, the photon mean free path is too large to be contained inside the detection volume; for low axion mass, it is too small to resolve individually the clusters. The pressure is a key parameter in the simulation: the efficiency peak is shifted to larger masses for a larger pressure. The total detection efficiency is determined by weighting the different event rate in a detector by the detection efficiency for each mass. For this reason, the total efficiency is optimized when the efficiency peak matches the peak in the event rate, which is around $(8 - 10)$ keV. In the figure, we see that our usual working condition for WIMP searches, that is the *Mimac gas* at 50 mbar, is not adapted to search for trapped KK axions since the efficiency peaks for low masses of 2 keV. On the right panel of the figure, the gas mixture 95% C_3F_8 + 5% i-C_4H_{10} at 100 mbar gets more appropriate and it has a larger number of fluorine targets and, when operated at low pressure, could be suitable for directional detection of WIMP.

The optimization of the detection efficiency can be performed by varying the gas mixture, the detector geometry, and the operating pressure. A mixture of 95% Ar + 5% i-C_4H_{10} at 300 mbar results in a total detection efficiency of 70% and gives well-resolved signals when operating with a 256 μm Micromegas. However, this mixture does not allow a directional search for WIMPs. A compromise must then be found between optimizing the searches for KK axions and the directional searches for WIMPs.

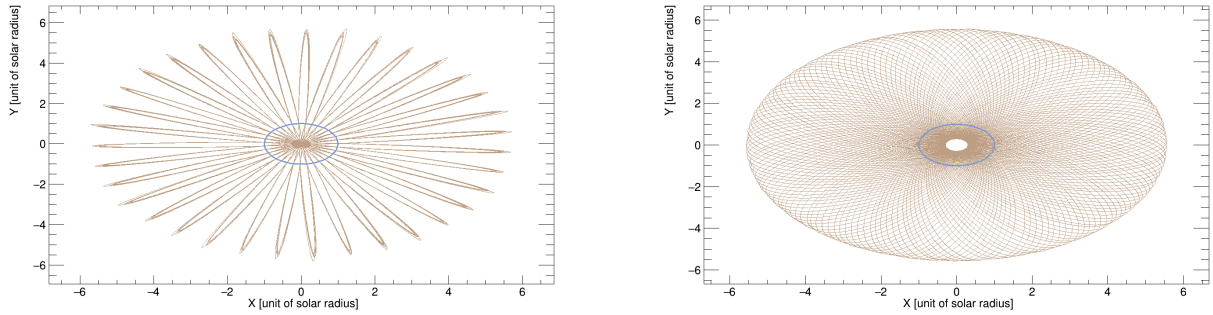

Figure 9.8: Trajectories of trapped KK axions produced at $\bar{r}_0 = 0.3$ and tracked for a year. The blue ellipse represents the Sun's surface. Left: almost radial trajectory (for visual purposes we have emitted the axion at an angle $\theta = 0.03\pi$ instead of $\theta = 0$). Right: axion emitted at an angle $\theta = \pi/2$.

The $a \to \gamma\gamma$ event rate could be shifted to lower axion masses by re-absorption effects discussed in the following section, so additional work is still required before determining the best-compromise operating conditions.

Finally, to determine the discovery potential of the MIMAC detector, we would have to study the background of the experiment. We have not yet performed this study. The gamma background takes its origin from the decay chains of uranium and thorium, and from the decay of ^{40}K, due to contamination of the detector materials or the rock of the laboratory walls. These gammas can interact either by Compton scattering or photoelectric effect. An axion-like event may be produced either by a random coincidence of two background photons, or by a double scattering of a single background photon. The axion-like background in a TPC located in the Boulby mine has been simulated in [214] and they show that, when the detector is shielded, the double-scatter background significantly dominates over the random coincidences. Another source of background is the β-decay of some detector components, for instance the decay of ^{210}Pb into ^{210}Bi, although they originate from the surface of the detector so the localization of the event with MIMAC provides a veto for them.

9.4 Axion re-absorption in the Sun as an opportunity?

We present here an ongoing work that we have not yet concluded. From the equations of motion (EoM) of a massive particle around the Sun, Eq. (3.56), we can track the axion during its orbit. The trajectory of the trapped axion often crosses the Sun. The angular momentum of the axion at production will influence the minimal radius $\bar{r}_{\rm min}$ that reaches the axion inside the Sun: for radial trajectories $\bar{r}_{\rm min} = 0$, whereas for non-zero angular momentum $\bar{r}_{\rm min} > 0$, defining a zone in the solar interior in which the axion never goes. This behavior is represented in Figure 9.8 where the trajectories of KK axions are shown, computed over a year, for two different angular momenta.

Trapped KK axions are then crossing the Sun during their orbits. The depth at which they enter the Sun depends on their initial angular momentum given at production. The time spent inside the Sun is mainly dependent on the initial velocity. In the two examples of Figure 9.8, the axions have spent about 5% of their time inside the Sun. The frequency at which an axion crosses the Sun decreases when the maximum radius of the trajectory increases, so for large orbits. For instance, an axion reaching the Earth crosses the Sun about 200 times less often than the axions of Figure 9.8. For this reason, the KK axions contributing to the solar luminosity detected by SphinX, which are the ones with $\bar{r}_{\rm max} \lesssim 7$, are significantly more likely to be re-absorbed by the Sun than the KK axions detectable in an Earth-based detector. So far, we have neglected possible re-absorption effects. We now aim to study them for completeness, but also because they could relax the solar luminosity constraint without reducing the $a \to \gamma\gamma$ event rate in a detector.

For hadronic KK axions, the only mechanism that could participate to re-absorption in the Sun is the inverse Primakoff scattering $a + Ze \to \gamma + Ze$ since it is the only one that depends on the solar environment. A back-on-the-envelope calculation from the Primakoff transition rate Eq. (3.36) tells us that the probability of converting a trapped KK axion into a photon via the Primakoff effect is greatly

negligible, because the mechanism is suppressed for the low-momenta of the trapped KK axions.

The situation can however differ in case the KK axions couple to fermions at tree-level, that is in allowing the dimensionless axion-electron coupling g_{ae} to take non-zero values. The electron number density in the Sun varies between $n_e = 1.2 \times 10^{13}$ cm^{-3} at the surface to $n_e = 6.1 \times 10^{25}$ cm^{-3} at the center [257], so possible re-absorption mechanisms will significantly depend on the trajectory of the KK axions inside the Sun. The time evolution of the number density of trapped KK axions will then be balanced by several effects:

- The production inside the Sun which now also gets contributions from the axion-electron processes. The procedure described in Section 3.4 must be applied to determine, for each process, the proportion of KK axions that is trapped into the solar gravitational field to derive the total number density.
- The decay into photons.
- The re-absorption in the Sun via axion-electron effects depending on the frequency and the radius at which the KK axions cross the Sun, as well on their momentum.

The axion production in the Sun via the axion-electron coupling has been studied in [412] in which the author details five additional production mechanisms compared to the hadronic case, mainly contributing in producing axions with energies slightly lower than when produced by the coalescence process. In our situation, the study must be extended to the case of KK axions whose masses cannot be neglected in the calculations.

The next steps consist of (1) including these additional processes in the KK axion production inside the Sun; (2) determining the proportion of KK axions that is trapped into the solar gravitational field; (3) evaluating their probability of being re-absorbed by the Sun in their orbits before the present time; (4) computing the photon flux detectable in the SphinX field of view due to the decay of these trapped KK axions for evaluating the excluded parameter space; and (5) determining the corresponding decay event rate in an Earth-based detector.

At the time of writing, we are addressing the situation from two approaches, a Monte Carlo simulation and an analytical calculation, and the preliminary results are so far not optimistic. They seem to indicate that, when the KK axions are produced by coalescence, a coupling to electrons of order $g_{ae} \sim 10^{-12}$ would give enough re-absorption to fulfil the SphinX constraint while having a detectable decay event rate on Earth. However, with such a large coupling to electrons, the axion-electron production could get dominant, so one should increase the coupling to photons to fulfil the SphinX constraint, leading to a too large coalescence production. This balance between production, decay, and re-absorption, which is correlated both to g_{ae} and $g_{a\gamma\gamma}$, seems to limit too much the possibilities for relaxing the solar luminosity constraint.

However, we point out that the analyses are not completed yet and that additional work is required before concluding. At the time of writing, the re-absorption mechanism remains a possibility for relaxing the constraints applying to the solar KK axions model. In any case, including the re-absorption mechanism is required for completeness of the model and one can use the measured solar luminosity flux to set exclusion limits on the product $g_{ae}g_{a\gamma\gamma}$, both for KK axions and for standard ALPs.

Summary

We review the three main constraints applying to the solar KK axion model. The decay of trapped KK axions into photons would contribute to the observed solar luminosity and must then be compatible with solar observations. Measurements of the solar X-rays flux during a deep solar minimum have been performed by the SphinX detector and they set stringent limits to the model. While the solar luminosity is the dominant constraint to the solar KK axions model, it also offers an additional motivation to it. The measured X-ray spectrum does not follow an isothermal behavior, as one would expect according to solar models. We show that this non-thermal behavior could be explained by the presence of the trapped KK axions that decay into photons. Besides this motivation, the KK axions have also been proposed as an explanation of the solar corona problem since they would act as an external X-rays

source heating the corona. Another constraint on the solar KK axions model is derived by requiring that the axion production in the Sun would not result in a too large energy loss that would be incompatible with the measured neutrino flux and helioseismology. Finally, we also revise the EBL constraint that significantly limits the four-dimensional keV-axion. We show that the energy distribution inside the KK tower allows escaping the EBL constraint in the frame of large extra dimensions. We then provide some sets of allowed parameters for the solar KK axion model.

The detection of KK axions can be performed from multiple channels. Most of the experiments dedicated to standard axions detection could extend their analyses or designs to search for higher-dimensional axions. Experimental exclusion limits on KK axions have been obtained from helioscopes, nuclear transition experiments, and experiments searching for axion decay. The TPCs exploit the decay channel $a \rightarrow \gamma\gamma$ that becomes accessible since the solar KK axions have masses in the keV-range. The revision of the KK axions model presented in this thesis have led to an $a \rightarrow \gamma\gamma$ event rate 6 orders of magnitude lower than the one predicted in the pioneering paper and commonly used in the literature. This drastic difference mainly comes from the update of the solar luminosity constraint. However, we are currently working on an extension of the model to non-hadronic KK axions that could possibly relax the constraint. In this situation, the trapped KK axions could be re-absorbed when crossing the Sun due to axion-electron interactions. Our preliminary work indicates that an efficient re-absorption mechanism would be counter-balanced by a too large KK axion production but additional studies are still required before drawing any conclusion.

The MIMAC detector is appropriate to detect a KK axion decay that would emit two photons of the same energy back-to-back. These photons would produce photoelectric effects in the detector, resulting in an almost unique signature: two bumps of the same amplitude in the Flash, and two separated clusters on the anode signal. We have used Comimac to demonstrate that MIMAC could efficiently detect such a signal. In this experiment, we have sent electrons of 4 keV at a large rate to produce some pile-up, and we have developed an algorithm to detect multi-cluster signals. The detection of the two photons mainly depends on their mean free path, so on the gas mixture and the density. We have developed a Monte Carlo simulation to evaluate the MIMAC detection efficiency for multiple working conditions. When the photon energy is too large, the photons escape the detection volume before being absorbed whereas when it is too low, the two photoelectrons are not resolved spatially. By adjusting the gas mixture and the pressure, one can optimize the detection efficiency, depending on the expected axion mass. While the *Mimac gas* is not adapted to search for KK axions, we show that a mixture of 95% C_3F_8 + 5% i-C_4H_{10} at 100 mbar reaches 90% efficiency of detection for an axion mass of 4 keV in a 1 m^3 active volume. If the re-absorption mechanism sufficiently relaxes the solar luminosity constraint to give detectable event rates, then we would be able to find an appropriate gas mixture to simultaneously search for KK axions and WIMPs with the MIMAC detector.

Conclusion and outlook

While some fields of particle physics are facing limits at high energy, we have been motivated, during this thesis, by extending to low energy the scope of possibilities for dark matter (DM) searches with the MIMAC detector. The detection of the DM, which composes 84% of the mass of the universe, represents a burning issue. We tried to contribute, at our level, by improving the experimental performances of directional detection, which is the only strategy of detection able to identify unambiguously a WIMP. In parallel, motivated by the new window opened at high gain for detecting keV electrons, we have revised a model of the axion propagating in extra dimensions. The higher-dimensional axion is a suitable dark matter candidate able to solve some puzzling solar observations and some problems of the Standard Model (SM) of particle physics. The work presented in this thesis is articulated around three main axes.

The first axis concerns the study of phenomena involved in low energy detection with a gaseous TPC, and more specifically with MIMAC. Observing low energy events, which deposit ionization energies in the keV-range, requires being sensitive to any primary charge, so to operate at high gain ($> 10^4$). In these conditions, we measured track lengths a few times longer than the ones predicted by simulations, the measurements showing a dependency on the detector gain. These measurements indicated the existence of distortion in the track reconstruction, which is an important issue for a directional detector, and the central work of this thesis has been the understanding of this phenomenon. The signal induced on the electrodes of a gaseous detector is a combination of two contributions: a fast and intense current due to the moving electrons and a slower current due to the moving ions. The ions require about 300 ns to be collected on the Micromegas grid and they consequently accumulate in the gap while primary electrons keep producing avalanches. At high gain, the number of accumulated ions becomes sufficiently large so the detector gets sensitive to the ionic signal, even when no longer primary electrons are initiating avalanches. We have demonstrated, both from experiments and simulations, that this interplay between the ionic and the electronic signal was the origin of the puzzling measurements described previously. We have developed `SimuMimac`, a simulation tool that, for a given incoming particle, determines the MIMAC observables at high gain. `SimuMimac` agrees with measurements, providing a valuable tool for determining physical quantities and for estimating the influence on measurements for processes involved in particle detection such as ionization, diffusion, avalanche, and signal formation. We have also shown that up to a gain 10^5, the local distortions of the electromagnetic field by the accumulated ions, *i.e.* an event-based space-charge effect, do not result in measurable effects.

Direct DM experiments measure the energy of a WIMP-induced nuclear recoil in the detection volume. The nuclear recoil releases only part of its energy as ionization. This deposited energy in ionization is lower than the one deposited by an electron of the same kinetic energy; we then say that the ion is "quenched". The Ionization Quenching Factor (IQF) converts the measured ionization into kinetic energy when considering the electron as the energy reference. The IQF is then a crucial quantity for all direct experiments exploiting the ionization channel. In the direct DM community, the IQF is sometimes estimated from the Lindhard model or the `SRIM` simulation tool, although significant deviations between measurements and simulations have often been pointed out in gases, noble liquids, or crystals. While the IQF is close to unity above intermediate energies, for instance $\gtrsim$ 100 keV for protons depending on the medium, it decreases non-linearly at low energies. The NEWS-G collaboration aims for low-mass WIMP detection (down to 50 $\mathrm{keV_{nr}}$ leading to sub-keV ionization energies) with a gaseous SPC. We have carefully handled the IQF measurements of protons in 100 mbar of methane by means of the Comimac facility coupled with a SPC with a NEWS-G sensor, in order to directly compare the ionization released by an ion to the one released by an electron. The measured IQF is lower than the `SRIM` quenching factor, the difference reaching 33% at 2 keV. This experiment is one more indication that the IQF must be measured for each experimental condition instead of being simulated.

The second axis of this work addresses the directional performance of the MIMAC detector. Directionality consists in measuring simultaneously the energy and the direction of a WIMP-induced nuclear recoil. The statistical correlation between the recoil directions and the expected incoming direction of

WIMPs, related to our motion in the galactic DM halo, would lead to the unambiguous identification of WIMP, even beyond the neutrino floor. As explained previously, the ionic signal distorts the measured tracks at high gain. While at first glance it appears as an issue, we have demonstrated that it also provides additional directional information. We have developed an analytical formula for extracting the electronic current from the Flash signal measured on the Micromegas grid. This deconvolution of the ionic signal can be applied to any measurements, with no need of prior nor *ad hoc* parameters. It provides the time distribution of the primary electrons cloud at the grid level, so before the avalanche. The bias on the time of arrival of the last primary electrons is lower than 20 ns. As expected, the integral of this distribution is proportional to the ionization energy. By revealing the fine structure of the primary electrons cloud, this procedure highlights the charge asymmetry of the ionization process and then enables head-tail recognition, *i.e.* the determination of the sense of the nuclear recoil.

The performance of a directional detector can be evaluated experimentally in a mono-energetic neutron field. Neutrons produce nuclear recoils in a wide angular distribution and the joined measurements of the energy and the direction of the recoils are required to reconstruct the neutron energy spectrum. We have developed a method for reconstructing the polar angle of a neutron-induced nuclear recoil based on the interplay between the ionic and the electronic signal. This method only relies on the Flash signal, so it does not exploit the information of the MIMAC pixelated anode. We have been able to reconstruct the energy spectrum of mono-energetic neutron fields at 27 keV and 8 keV from proton recoils with an angular resolution better than 15° over the entire angular range. To the best of our knowledge, this is the first directional measurement in the keV-range, down to an ionization energy of 1 keV. In this thesis, we have also presented ongoing work for accessing directionality at high gain from the pixelated anode signal in the light of the track distortions due to the ionic signal. While the results are still preliminary, we have been able to reconstruct the 27 keV and 8 keV neutron spectra from proton recoils and, for the run at 27 keV, we also reconstruct the spectrum from carbon recoils having ionization energies lower than 2.5 keV. If we confirm this analysis, we would have two methods, one on the grid and the other on the pixelated anode, for accessing the polar angle of the track in the keV-range. We have enough elements to say that, when correctly handled, the numerous ions accumulated in the gap at high gain improve the MIMAC directional performance by increasing the anode sensitivity and by inducing a measurable ionic signal on the Micromegas grid which can be separated from the electronic signal.

The third axis of this thesis is dedicated to solar axions searches in the frame of large extra dimensions. The axion is a hypothetical pseudoscalar particle arising from the breaking of a $U(1)$ symmetry introduced to solve the strong CP problem and it is also an appropriate DM candidate. The axion, as a singlet under the SM gauge group, could propagate into extra spatial dimensions. In such a case, it would be seen from our 4D brane as an "infinite" superposition of massive states called Kaluza-Klein (KK) axions. Extra spatial dimensions, that would be curled up with a compactification radius R, are theoretically motivated and experimentally allowed as long as $R \lesssim 1$ μm. KK axions would be produced in the Sun, most of them having a mass in the range [1, 20 keV]. The phenomenology of solar KK axions drastically differs from the case of the standard axion due to their large mode multiplicity, their masses in the keV-range, and their lifetimes that can be comparable to the age of the universe. In particular, part of the KK axions would be trapped into the solar gravitational field and they would accumulate over cosmic times. Such a model has been introduced twenty years ago in a pioneering paper, proposing notably to solve the solar corona problem, and opening the window for KK axions searches via the decay into two identical photons $a \to \gamma\gamma$. We have entirely revised the model in collaboration with Mar Bastero-Gil. First, we have updated the production event rates for the three main mechanisms in the Sun for hadronic axions. Second, we have derived analytically the number density of trapped KK axions around the Sun, providing for the first time an expression for this key quantity for phenomenology. Third, we have revised the astrophysical constraints applying to the model and we have compared them to recent data.

Besides providing analytical expressions for all phenomenologically interesting quantities, this work has led to important conclusions concerning KK axions detection via the decay channel. We have reduced by six orders of magnitude the expected $a \to \gamma\gamma$ event rate in a TPC. This result mainly arises from the solar luminosity constraint: the KK axions trapped around the Sun would contribute to the

solar luminosity by their decay into photons, and this additional luminosity should remain consistent with solar X-ray measurements. On the one hand, our work offers additional motivation for the solar KK axions model by possibly explaining the non-thermal behavior of the solar X-ray spectrum. On the other hand, the detection of KK axions via their decay into photons seems technologically inaccessible, leading to negative consequences for the experiments relying on the previous model. This conclusion also impacts MIMAC since we had shown that our detector could efficiently search for the KK axion decay. In parallel, we have revised the main constraint applying to Axion-Like Particles (ALP) in the keV-range, from the measurements of the extragalactic background light, and we conclude that the parameter space that could be probed by MIMAC is excluded by astrophysical considerations, although relying on assumptions, in case the axion (or any ALP) does not propagate into extra dimensions. While other detection channels are still accessible, we are currently working on an extension of the model to non-hadronic KK axions that have a probability of being re-absorbed by the Sun during their orbits, possibly relaxing the solar luminosity constraint.

The present assessment would not be complete without addressing a feeling that creeps in between each line of this manuscript although rarely expressed openly. This feeling is a mixture of doubt, hesitation, and fragility that regularly makes us retrace our steps, challenge what we thought was right, and revisit our analyses. It is destabilizing to doubt the value of the work we have done, just as it seems presumptuous to doubt the work of others. Yet the main results of this thesis are most probably arising from the intensity of such a feeling. A hesitation that is sufficient to continuously look for flaws in the reasoning, but which must be counterbalanced by the enthusiasm and positivity that is the hallmark of our team.

The work presented in this thesis has somehow introduced new concepts and has widened the scope of possibilities for the MIMAC detector. The extension of the detection strategy to the search for axion has been initiated with this thesis. The development of `SimuMimac` and the description of the detector behavior at high gain and large gap have opened a new era for directional detection and axion searches with MIMAC. We aim to confirm and extend the preliminary work initiated for directionality on the anode at high gain. A joined analysis based on the two directional methods developed in this thesis should improve the directional performance of MIMAC. We also plan a new experiment in a mono-energetic neutron field in which we will vary the orientation of the detector in order to measure the head-tail recognition efficiency in the keV-range. The most limiting parameter for directional detection is the energy threshold. While we have reached a threshold down to 1 $\mathrm{keV_{ee}}$ for reconstructing the neutron 8 keV spectrum, the current status of the *low-noise* prototype should enable sub-keV directional detection in the upcoming year. We aim to determine at the same time the directional performance of the three targets of our gas mixtures: hydrogen, carbon, and fluorine. The preliminary results obtained on the anode indicate that we already access directionality both on proton and carbon recoils in the keV-range.

In parallel, we are pushing further the solar KK axions model by extending it to non-hadronic models in which the axion couples to fermions at tree-level. The re-absorption mechanism could possibly relax the solar luminosity constraints and re-open the window for $a \to \gamma\gamma$ detection. In case the event rate remains too low for detection with a TPC, our model could still be explored by other detection techniques such as haloscopes and helioscopes. One can easily convert our work on trapped axions into exclusions limits, by comparing the model predictions to SphinX measurements, in order to set constraints in the parameter space $(g_{a\gamma\gamma} - m_a)$ both for KK axions and for four-dimensional axions.

On the way, we often stepped out of the main path to explore other directions. While we have not yet obtained conclusive results for some of them, let us briefly introduce part of the ongoing work that we judge promising. Thanks to the technology of the *low-noise* detector, we have measured 3D tracks of Comimac electrons down to 150 eV. A preliminary analysis indicates that the detector gets sensitive to the statistical fluctuation of the number of primary electrons, which is expected at low energy, with separable populations on the track observables. We are pushing further this analysis to experimentally describe the low-energy ionization process in gases. The sub-keV 3D track reconstruction is also a valuable tool for investigating the low-energy background, in particular when coupled with a validated simulation tool such as `SimuMimac`. The background complexity is not well understood and it limits

electron-recoil discrimination. As a priority, we are currently working on an extension of our work on the IQF and we aim to submit a paper clarifying the main concepts and experimental prospects by the end of the year.

The 35×35 cm^2 MIMAC prototype and the corresponding electronic card are being tested at the time of writing. This chamber exploits the *low-noise* technology and has 1792 strips. Once assembled into a bi-chamber volume, it constitutes an elementary brick of 60 L that will be duplicated to build the 1 m^3 MIMAC detector. Since the drift length remains 25 cm, as for the directional measurements presented in Chapter 8, we expect all the tools developed in this thesis to be adapted to this new prototype. We would appreciate to share our tools with other experiments, for instance by performing IQF measurements with Comimac in gas mixtures used by other collaborations or by discussing simulations and providing the code of `SimuMimac`. The larger detection volume that will be achieved in the near future will increase the sensitivity to the axion decay, MIMAC will thus be able to simultaneously search for WIMPs and KK axions. The work presented in this thesis has demonstrated, for the first time, the ability to directionally search for WIMP in the keV-range, probing WIMP masses down to $\sim$ GeV, and the MIMAC technology will soon be scaled to physically promising detection volumes. We are thus currently entering a new era for directional detection.

A Plasmon decay rate

To compute the rate of KK axion production from the plasmon decay $\gamma_T \to a + \gamma_L$ we need the thermal decay rate:

$$\Gamma_{\gamma_T \to a\gamma_L}(T) = \frac{1}{2E}\int \frac{d^3k_T}{(2\pi)^3 2\omega_T}\frac{d^3k_L}{(2\pi)^3 2\omega_L}(2\pi)^4\delta^4(k_T - k_L - p)\left|M_{\gamma_T\to a\gamma_L}\right|^2(1+f^{eq}(\omega_T)) \tag{A.23}$$

where [258]:

$$\left|M_{\gamma_T\to a\gamma_L}\right|^2 = g_{a\gamma\gamma}^2\frac{\left|(\mathbf{e}_T\times\mathbf{k}_T)\cdot\mathbf{k}_L\right|^2}{k_L^2}\frac{\omega_P^2}{k_L^2+\omega_P^2}\omega_L^2 = g_{a\gamma\gamma}^2\frac{|\mathbf{k}_T\times\mathbf{k}_L|^2}{2k_L^2}\frac{\omega_P^2}{k_L^2+\omega_P^2}\omega_L^2 \tag{A.24}$$

and $\delta^4(k_T - k_L - p) = \delta^3(\mathbf{k}_T - \mathbf{k}_L - \mathbf{p})\delta(\omega_T - \omega_L - E)$ enforces energy and momentum conservations:

$$E = \omega_T - \omega_L \tag{A.25}$$
$$\mathbf{p} = \mathbf{k}_T - \mathbf{k}_L \tag{A.26}$$
$$k_L^2 = k_T^2 + p^2 - 2k_T p\cos\theta_T \tag{A.27}$$

Neglecting the thermal correction for the time being (*i.e.*, taking $f^{eq}(\omega_T) \ll 1$), we have:

$$\begin{aligned}
2E\Gamma_{\gamma_T\to a\gamma_L}(T) &= \frac{1}{2\pi^2}\cdot\frac{1}{4\omega_L\omega_T}\int d^3k_T\delta(\omega_T-\omega_L-E)\left|M_{\gamma_T\to a\gamma_L}\right|^2 \\
&= \frac{g_{a\gamma\gamma}^2}{2\pi^2}\cdot\frac{\omega_L^2}{4\omega_L\omega_T}\int d\Omega_T\frac{k_T^2}{|dW/dk_T|}\cdot\frac{\omega_P^2}{k_L^2+\omega_P^2}\cdot\frac{k_T^2p^2(1-\cos^2\theta_T)}{k_L^2} \\
&= \frac{g_{a\gamma\gamma}^2}{32\pi}\cdot\frac{\omega_L^2\omega_P^2k_T^2}{\omega_T p}\int d\cos\theta_T\frac{1-\cos\theta_T^2}{(A-\cos\theta_T)(B-\cos\theta_T)(C-\cos\theta_T)}
\end{aligned} \tag{A.28}$$

where in the second line we have:

$$W = \omega_T - \omega_L - E \tag{A.29}$$
$$\frac{dW}{dk_T} = \frac{k_T}{\omega_T} - \frac{k_L}{\omega_L}\frac{dk_L}{dk_T} = \frac{p}{\omega_L}\left(\frac{E}{\omega_T}\cdot\frac{k_T}{p} - \cos\theta_T\right) \tag{A.30}$$

and in the last line in Eq.(A.28) we have defined:

$$A = \frac{E}{\omega_T}\cdot\frac{k_T}{p} \tag{A.31}$$
$$B = \frac{1}{2}\left(\frac{k_T}{p}+\frac{p}{k_T}\right) \tag{A.32}$$
$$C = B + \frac{\omega_P^2}{2k_Tp} \tag{A.33}$$

For slow-moving axions, in the limit $p/k_T \ll 1$ we have:

$$2E\Gamma_{\gamma_T\to a\gamma_L} \simeq \frac{g_{a\gamma\gamma}^2}{16\pi}\frac{\omega_P^2\omega_L^2p^2}{k_TE}\cdot\frac{k_T^2}{k_T^2+\omega_P^2}\int\int d\cos\theta_T(1-\cos\theta_T^2) \simeq \frac{g_{a\gamma\gamma}^2}{12\pi}\frac{\omega_P^2\omega_L^2p^2}{k_TE}\cdot\frac{k_T^2}{k_T^2+\omega_P^2} \tag{A.34}$$

and therefore in this limit:

$$\frac{dN_a}{dE} \simeq \frac{f_a^{eq}(E)}{2\pi^2}\frac{g_{a\gamma\gamma}^2}{24\pi}\frac{\omega_P^4k_T}{k_T^2+\omega_P^2}\cdot\frac{p^3}{E} \tag{A.35}$$

where we have replaced $\omega_L^2 \simeq \omega_P^2$.

B Main code of SimuMimac

We report below one example of the main program of SimuMimac. The beginning of the code set the parameters of the setup, for instance in this case we operate in the High-gain gas. In the second part of the code one must define the primary electrons cloud. In this example, a SRIM simulation is run inside the code to generate a cloud for 10 keV protons. Finally, the simulation starts with the command PerformCompleteSimulation.

```
#include "SimulationSetup.hh"
#include "Fundamentals.hh"
#include "TransportParticle.hh"
#include "GeneratePrimaryCloud.hh"
#include "SignalFormation.hh"

using namespace SimuMimac;
using namespace std;

int main(int argc, char** argv){

    ///Generate the setup class
    SimulationSetup *simu = new SimulationSetup();

//=================================//
//       OPTIONS
//=================================//

    simu->EnableVerbose();//Print more outputs in the terminal when running the code
    simu->DisableStoreTrajectories();//When enabled the positions of the particles are stored at each timestep so one can plot the trajectories afterwards
    simu->EnableSignalAnode();//When enabled the signal is computed both on the grid and on the anode.
        //Computing the signal on the anode slows down the simulation by about a factor 10
    simu->DisableDriftOnly();//When enabled, the code drifts the electrons but it does not perform the avalanche, does not drift ions and does not compute the signal.
        //The properties of the electrons once they arrive at the grid is stored in "output/electronsAtGrid.dat".

//=================================//
//       PARAMETERS
//=================================//

    ///Geometry
    simu->SetWidth(10.8);//in cm (X axis)
    simu->SetDepth(5.0);//in cm (Y axis <=> along electric field)
    simu->SetHeight(1.0);//in cm (Z axis ; not used since we work in 2D but sometimes needed for Garfield's functions)
    simu->SetGap(0.0512);//in cm
    simu->SetWireDiameter(0.0018);//in cm ; diameter of the wires of the grid
    simu->SetWirePitch(0.0045 + simu->GetWireDiameter());//in cm ; distance between the centers of the wires
    simu->SetNstrips(256);
    simu->SetStripPitch(0.0424);//cm ; distance between the centers of 2 consecutive strips
    simu->SetInterStrip(0.01);//cm ; distance between 2 strips
    simu->SetSamplingTime(20.);//ns

    ///Voltages
    simu->SetVoltageGrid(-510);//in V ; voltage on the grid
    simu->SetVoltageCathode(simu->GetVoltageGrid() - 84.4*(simu->GetDepth() - simu->GetGap()));//in V ; voltage on the cathode
    simu->SetVoltageAnode(0.);//in V ; voltage on the anode

```

```
47      ///Physical parameters
48      simu->SetIonMass((12+2*19 +1) * SimuMimac::ATOMICMASS);//<=> number of nucleons *↩
            amu
49      simu->SetIonMobility(28.);//cm^2/V/s ; constant mobility approximation
50          //This is not the reduced mobility K0 but the physical one K = K0 * T/T0 * P0↩
                /P
51      simu->SetWorkFunction(25.);//in eV
52
53      ///Gas
54      simu->GetGas()->SetComposition("CHF3", 50., "iC4H10", 50.);//Gas idenfifier ; ↩
            fraction
55      simu->GetGas()->SetTemperature(293.15);//in K
56      simu->GetGas()->SetPressure(22.5);//in torr
57
58      ///Simulation parameters
59      simu->SetTimeStep(5e-10);//in seconds ; typically 5e-10; should not be larger ↩
            than 1e-9 nor lower than 1e-10
60          //Timestep to solve the Langevin equation for drifting ions
61
62      ///Signal region
63          //region in which we will drift ions and compute the signal induced on the ↩
                grid and the anode
64      simu->SetMinX(simu->GetWidth()/2. - 5*simu->GetGap());//in cm
65      simu->SetMaxX(simu->GetWidth()/2. + 5*simu->GetGap());//in cm
66      simu->SetMinY(0.);//in cm
67      simu->SetMaxY(1.1 * simu->GetGap());//in cm ;
68          //there is always some ion backflow. If MaxY is too large the computing time ↩
                can be large.
69
70  //======================================//
71  //        SIMULATION
72  //======================================//
73
74      ///Generate the geometry
75      simu->GenerateGeometry();//Mandatory
76
77      ///Write the setup in a log file
78      simu->SaveSetup();
79
80      ///Run a SRIM simu
81      double x0 = simu->GetWidth()/2.;
82      double y0 = simu->GetDepth();
83      double trackAngle = 0.;//deg ; If theta = 0 the track is perpendicular to the ↩
            anode ; theta°=90 => parallel
84      double ionKineticEnergy = 10.;//keV
85          //Run a SRIM simulation
86      simu->NewSRIMsimu(nCloud, x0, y0, ionKineticEnergy, trackAngle, "H");//SRIM must ↩
            be installed
87
88      ///Generate the primary cloud according to SRIM results
89      GeneratePrimaryCloud *primary = new GeneratePrimaryCloud(simu);
90      primary->PrimaryFromSRIMvector(0);
91
92      ///Run the simu
93      simu->PerformCompleteSimulation("output/signal.dat");
94
95      delete primary;
96      delete simu;
97
98      return 0;
99  }
```

C Deconvolution of the ionic signal

In this appendix we derive a formula to extract the electronic signal from the measured Flash signal. We have seen in Chapter 4 that the current induced on the Micromegas grid can be expressed from the Dris and Alexopoulos model [313]:

$$\begin{cases} f(t) &= \frac{qu_n}{d}\, e^{\alpha u_n t} &, \text{ for } 0 \leq t \leq d/u_n \\ g(t) &= \frac{qu_p}{d}\left(e^{\alpha d} - e^{\alpha u_p t}\right) &, \text{ for } 0 \leq t \leq d/u_p \end{cases} \tag{C.36}$$

where $f(t)$ is the electronic current induced on the grid, $g(t)$ is the ionic one, q is the elementary charge, u_n is the mean electron drift velocity in the gap, u_p is the mean ion drift velocity in the gap, d is the gap length, and α is the Townsend coefficient.

The measured Flash signal corresponds to the time integral of the charge induced on the grid. Before working on the Flash, we will first derive a formula to deconvolve the ionic current from the total current. While MIMAC does not measure the total current, this first step in the derivation is enlightening and it can be used on simulated data.

First step: the current

The total current is a convolution of both contributions $I(t) = \big(f \circledast g\big)(t)$. To extract the electronic current $f(t)$ from $I(t)$ we will make use of some properties of the Laplace transform:

$$\mathcal{L}\Big\{ f \circledast g \Big\} = \mathcal{L}\Big\{ f \Big\} \cdot \mathcal{L}\Big\{ g \Big\} \tag{C.37}$$

$$\mathcal{L}\Big\{ f'(t) \Big\}(s) = s\mathcal{L}\Big\{ f(t) \Big\}(s) - f(t)\Big|_{t=0} \tag{C.38}$$

According to Eq. (C.36), one has:

$$\begin{aligned} \mathcal{L}\Big\{ g(t) \Big\}(s) &= \frac{qu_p}{d} \int_0^\infty dt \left(e^{\alpha d} - e^{\alpha u_p t}\right) e^{-st} \\ &= \frac{qu_p}{d} \left(\frac{e^{\alpha d}}{s} - \frac{1}{s - \alpha u_p} \right) \\ &\simeq \frac{qu_p}{ds} \left(e^{\alpha d} - 1\right) \left(1 - \frac{\alpha u_p}{s\big(e^{\alpha d} - 1\big)} \right) \end{aligned}$$

where at the first line we imposed $s \gg \alpha u_p$ in order to Taylor expand the expression at the second line. The same condition can be used to derive the inverse expression:

$$\frac{1}{\mathcal{L}\Big\{ g(t) \Big\}(s)} \simeq \frac{d}{qu_p\big(e^{\alpha d} - 1\big)} \left(s + \frac{\alpha u_p}{e^{\alpha d} - 1} \right) = \frac{s + A}{B} \tag{C.39}$$

In the previous equation we have introduced the parameters A and B defined as:

$$\begin{cases} A \equiv \frac{\alpha u_p}{e^{\alpha d} - 1} \\ B \equiv \frac{qu_p\left(e^{\alpha d} - 1\right)}{d} \end{cases} \tag{C.40}$$

We are ready to extract the electronic contribution:

$$\begin{aligned} f(t) &= \mathcal{L}^{-1}\left\{ \frac{\mathcal{L}\{ f \circledast g \}}{\mathcal{L}\{ g \}} \right\} \\ &= \mathcal{L}^{-1}\left\{ \frac{d}{qu_p\big(e^{\alpha d} - 1\big)} \left(s + \frac{\alpha u_p}{e^{\alpha d} - 1} \right) \mathcal{L}\{ f \circledast g \} \right\} \\ &= \frac{d}{qu_p\big(e^{\alpha d} - 1\big)} \left(\big(f \circledast g\big)'(t) + \mathcal{L}^{-1}\big\{ \big(f \circledast g\big) \big\}\Big|_{t=0} + \frac{\alpha u_p}{e^{\alpha d} - 1} \big(f \circledast g\big)(t) \right) \end{aligned} \tag{C.41}$$

This result has been obtained thanks to the property Eq. (C.38). We now consider that at $t = 0$ the signal is zero, enabling to suppress the second term of Eq. (C.41). Finally, one can remark that Eq. (C.41) is a first order differential equation whose solution is:

$$\big(f \circledast g\big)(t) = e^{At} \int_0^t dx\, B e^{Ax} f(x) + e^{-At} \big(f \circledast g\big)\Big|_{t=0} \tag{C.42}$$

Up to now we have considered continuous signals. We will now discretize the signals with a constant time step Δt such that $t_i = i\Delta t$. The previous equation is discretized as:

$$\begin{aligned}
\big(f \circledast g\big)(t_i) &= e^{At_i} \sum_{j=0}^{i} \Delta t\, B e^{At_j} f(t_j) + e^{-At_i} \big(f \circledast g\big)\Big|_{t=0} \\
&= e^{At_i}\, B \left(\sum_{j=0}^{i-1} \Delta t\, e^{At_j} f(t_j) + \Delta t\, e^{At_i} f(t_i) \right) + e^{-At_i} \big(f \circledast g\big)\Big|_{t=0} \\
&= e^{-A\Delta t} \big(f \circledast g\big)(t_{i-1}) + B\Delta t f(t_i)
\end{aligned}$$

So we can obtain the electronic current:

$$\begin{cases} f(t_0) & = 0 \\ f(t_i) & = \frac{1}{B\Delta t} \Big(\big(f \circledast g\big)(t_i) - e^{-A\Delta t} \big(f \circledast g\big)(t_{i-1}) \Big) \quad , \; i \neq 0 \end{cases} \tag{C.43}$$

This expression can be applied on any current $I(t)$, no matter the arrival time of the first electron nor the time spacing between two electrons.

Deconvolution of the ionic contribution on the Flash

We now are ready to extend the previous calculations to the Flash signal. The goal is to obtain a formula enabling to extract the electronic current from the Flash signal. The measured Flash corresponds to the integral of the charge induced on the grid over a timeslice of duration Δt:

$$C(t) \;=\; C(t - \Delta t) + \int_{t-\Delta t}^{t} d\tau\, \rho(\tau) \big(f \circledast g\big)(\tau) \tag{C.44}$$

where $\rho(\tau)$ describes the charge density of the primary electrons cloud at grid, and where $f(\tau)$ and $g(\tau)$ are respectively the electronic and the ionic current given in Eq. (C.36). We note $D(t)$ the charge difference in between two timeslices. We will here proceed by making an ansatz on the distribution $\rho(\tau)$: we assume a constant charge distribution, *i.e.* $\rho(\tau) \simeq \rho = \frac{1}{N}$ where N is a normalisation factor. This ansatz is a strong approximation, but it will enable us to perform analytically the deconvolution of the signal. The validity of the deconvolution is experimentally tested in Chapter 8. With such ansatz, one has:

$$D(t) \;\equiv\; C(t) - C(t - \Delta t) \;\simeq\; \frac{1}{N} \int_{t-\Delta t}^{t} d\tau \big(f \circledast g\big)(\tau) \tag{C.45}$$

As previously, we make use of Laplace transform:

$$\mathcal{L}\{D\} = \frac{1}{Ns}\, \mathcal{L}\{f\} \cdot \mathcal{L}\{g\} \tag{C.46}$$

We can compute the Laplace transform of the ionic current:

$$\begin{aligned}
\mathcal{L}\Big\{g(t)\Big\}(s) &= \frac{qu_p}{d} \int_0^\infty dt \Big(e^{\alpha d} - e^{\alpha u_p t} \Big) e^{-st} \\
&= \frac{qu_p}{d} \left(\frac{e^{\alpha d}}{s} - \frac{1}{s - \alpha u_p} \right) \\
&\simeq \frac{qu_p}{ds} \Big(e^{\alpha d} - 1 \Big) \left(1 - \frac{\alpha u_p}{s\big(e^{\alpha d} - 1\big)} \right)
\end{aligned} \tag{C.47}$$

where we have imposed the condition $s \gg \alpha u_p$ to Taylor expand the expression. This same condition brings us to the determination of the inverse:

$$\frac{1}{\mathcal{L}\Big\{g(t)\Big\}(s)} \simeq \frac{d}{qu_p\big(e^{\alpha d}-1\big)}\left(s+\frac{\alpha u_p}{e^{\alpha d}-1}\right) = \frac{s+A}{B} \tag{C.48}$$

We have used the parameters A and B introduced in Eq. (C.40). We now have all elements to inverse Eq. (C.46) and to return in the real time domain:

$$\begin{aligned} f(t) &= \frac{N}{B}\,\mathcal{L}^{-1}\Big\{s(s+A)\,\mathcal{L}\big\{D(t)\big\}\Big\} \\ &= \frac{N}{B}\Big(D''(t)+A\,D'(t)\Big) \end{aligned} \tag{C.49}$$

where at the last line we used the fact that there is no charge at $t=0$. This is a differential equation of second order in $D(t)$, whose solution can be expressed as:

$$D(t) = \int_0^t dx\left(C_1 e^{-Ax} + e^{-Ax}\int_0^x dy\,\frac{B}{N}e^{Ay}f(y)\right) + C_2 \tag{C.50}$$

We can show that $C_1 = C_2 = 0$ since the Flash starts to record a signal before the arrival of the first primary electrons. Finally, we must apply a discretization since the Flash is a digital signal. Eq. (C.50) turns to:

$$\begin{aligned} D(t_i) &= \frac{B}{N}\sum_{j=0}^{i}\Delta t\,e^{-At_j}\sum_{k=0}^{j}\Delta t\,e^{At_k}\,f(t_k) \\ &= D(t_{i-1}) + \frac{B}{N}\,\Delta t\,e^{-At_i}\sum_{k=0}^{i}\Delta t\,e^{At_k}\,f(t_k) \end{aligned} \tag{C.51}$$

We are now ready to express the electronic current as a function of the Flash signal:

$$f(t_i) = \frac{N}{B\Delta t^2}\Big(D(t_i) - \big(1+e^{-A\Delta t}\big)D(t_{i-1}) + e^{-A\Delta t}\,D(t_{i-2})\Big) \tag{C.52}$$

This expression depends on physical quantities that cannot be easily determined experimentally. However, we are rather interested in the time distribution of the electronic current instead of its absolute value. For this reason, we can ignore the constant factor $\frac{N}{B\Delta t^2}$. The last step consists in determining A and is presented in Chapter 8.

Bibliography

[1] A.M. Clerke, *Problems in astrophysics*, A. &C. Black (1903).

[2] H.S. Kragh, *Conceptions of cosmos: From myths to the accelerating universe: A history of cosmology*, Oxford University Press (2006), DOI.

[3] F. Bessel, *XII. Extract from the Translation of a Letter from Professor Bessel, dated Konigsberg, 10th of August, 1844. On the Variations of the Proper Motions of Procyon and Sirius*, *Mon. Not. Roy. Astron. Soc.* **6** (1844) 136.

[4] G. Bertone and D. Hooper, *History of dark matter*, *Rev. Mod. Phys.* **90** (2018) 045002 [1605.04909].

[5] J.B. Holberg and F. Wesemael, *The discovery of the companion of sirius and its aftermath*, *J. Hist. Astron.* **38** (2007) 161.

[6] J. Laskar, *Des premiers travaux de le verrier à la découverte de neptune*, *C. R. Phys.* **18** (2017) 504.

[7] T. Close, *Lunatic on a Mountain: Fritz Zwicky and the Early History of Dark Matter*, Canadian theses, Thesis (M.Sc.)–Saint Mary's University (2001).

[8] Montgomery, Colin and others, *Michell, Laplace and the origin of the black hole concept*, *J. Astron. Hist. Herit.* **12** (2009) 90.

[9] W. Steinicke, *William Herschel's 'Hole in the Sky' and the discovery of dark nebulae*, *J. Astron. Hist. Herit.* **19** (2016) 305.

[10] C. Brock, *Public Experiments*, *Hist. Workshop* **58** (2004) 306.

[11] V. Trimble, *History of dark matter in galaxies*, in *Planets, Stars and Stellar Systems: Volume 5: Galactic Structure and Stellar Populations*, T.D. Oswalt and G. Gilmore, eds., (Dordrecht), pp. 1091–1118, Springer Netherlands (2013), DOI.

[12] J. Oort, *The force exerted by the stellar system in the direction perpendicular to the galactic plane and some related problems*, *Bull. Astron. Inst. Netherlands* **6** (1932) 249.

[13] J.H. Jeans, *The Motions of Stars in a Kapteyn-Universe*, *Mon. Not. Roy. Astron. Soc.* **82** (1922) 122.

[14] R.H. Sanders, *The Dark Matter Problem: A Historical Perspective*, Cambridge University Press (2010), DOI.

[15] S. Smith, *The mass of the Virgo cluster*, *Astrophys. J.* **83** (1936) 23.

[16] F. Zwicky, *On the Masses of Nebulae and of Clusters of Nebulae*, *Astrophys. J.* **86** (1937) 217.

[17] K. Freeman and G. McNamara, *In search of dark matter*, Springer Science & Business Media (2006).

[18] V. Rubin, *A brief history of dark matter*, in *The Dark Universe: Matter, Energy and Gravity*, M. Livio, ed., vol. 15, pp. 1–13, 2003, DOI.

[19] G. Bertone et al., *Particle dark matter: Evidence, candidates and constraints*, *Phys. Rept.* **405** (2005) 279 [hep-ph/0404175].

[20] A. Bosma, *The distribution and kinematics of neutral hydrogen in spiral galaxies of various morphological types*, Ph.D. thesis, Jan., 1978.

[21] M. Persic et al., *The Universal rotation curve of spiral galaxies: 1. The Dark matter connection*, *Mon. Not. Roy. Astron. Soc.* **281** (1996) 27 [astro-ph/9506004].

[22] L.E. Strigari, *Galactic Searches for Dark Matter*, *Phys. Rept.* **531** (2013) 1 [1211.7090].

[23] V.C. Rubin et al., *Rotation of the Andromeda Nebula from a Spectroscopic Survey of Emission Regions*, *Astrophys. J.* **159** (1970) 379.

[24] B. Paczynski, *Gravitational Microlensing by the Galactic Halo*, *Astrophys. J.* **304** (1986) 1.

[25] C. Wegg et al., *MOA-II Galactic microlensing constraints: the inner Milky Way has a low dark matter fraction and a near maximal disc*, *Mon. Not. Roy. Astron. Soc.* **463** (2016) 557.

[26] F. Iocco et al., *Dark Matter distribution in the Milky Way: microlensing and dynamical constraints*, *JCAP* (2011) 029 [1107.5810].

[27] P. Popowski et al., *Recent microlensing results from the MACHO project*, in *Gravitational Lensing: A Unique Tool for Cosmology*, 4, 2003 [astro-ph/0304464].

[28] EROS-2 collaboration, *Limits on the Macho Content of the Galactic Halo from the EROS-2 Survey of the Magellanic Clouds*, *Astron. Astrophys.* **469** (2007) 387 [astro-ph/0607207].

[29] D. Harvey et al., *The non-gravitational interactions of dark matter in colliding galaxy clusters*, *Science* **347** (2015) 1462 [1503.07675].

[30] D. Clowe et al., *A direct empirical proof of the existence of dark matter*, *Astrophys. J. Lett.* **648** (2006) L109 [astro-ph/0608407].

[31] M. Bradac et al., *Strong and weak lensing united. 3. Measuring the mass distribution of the merging galaxy cluster 1E0657-56*, *Astrophys. J.* **652** (2006) 937 [astro-ph/0608408].

[32] A. Mahdavi et al., *A Dark Core in Abell 520*, *Astrophys. J.* **668** (2007) 806 [0706.3048].

[33] D. Clowe et al., *On dark peaks and missing mass: A weak-lensing mass reconstruction of the merging cluster system a520,*, *Astrophys. J.* **758** (2012) 128.

[34] M.J. Jee et al., *Hubble Space Telescope/Advanced Camera for Surveys Confirmation of the Dark Substructure in A520*, *Astrophys. J.* **783** (2014) 78 [1401.3356].

[35] M. Bradac et al., *Revealing the properties of dark matter in the merging cluster MACSJ0025.4-1222*, *Astrophys. J.* **687** (2008) 959 [0806.2320].

[36] J. Merten et al., *Creation of cosmic structure in the complex galaxy cluster merger abell 2744*, *Mon. Not. Roy. Astron. Soc.* **417** (2011) 333–347.

[37] S.W. Randall et al., *Constraints on the Self-Interaction Cross-Section of Dark Matter from Numerical Simulations of the Merging Galaxy Cluster 1E 0657-56*, *Astrophys. J.* **679** (2008) 1173 [0704.0261].

[38] P.A. Zyla et al., *(Particle Data Group)*, *PTEP* **2020** (2020) 083C01.

[39] Planck collaboration, *Planck 2018 results. VI. Cosmological parameters*, *Astron. Astrophys.* **641** (2020) A6 [1807.06209].

[40] E. Di Valentino et al., *Beyond six parameters: extending ΛCDM*, *Phys. Rev. D* **92** (2015) 121302 [1507.06646].

[41] L. Perivolaropoulos and F. Skara, *Challenges for ΛCDM: An update*, 2105.05208.

[42] E.L. Wright, *Theoretical overview of cosmic microwave background anisotropy*, in *Carnegie Observatories Centennial Symposium. 2. Measuring and Modeling the Universe*, pp. 291–308, 5, 2003 [astro-ph/0305591].

[43] M. Roos, *Dark matter: The evidence from astronomy, astrophysics and cosmology*, 1001.0316.

[44] A.M. Green, *Dark Matter in Astrophysics/Cosmology*, in *Les Houches summer school on Dark Matter*, 9, 2021 [2109.05854].

[45] SDSS collaboration, *Detection of the Baryon Acoustic Peak in the Large-Scale Correlation Function of SDSS Luminous Red Galaxies*, *Astrophys. J.* **633** (2005) 560 [astro-ph/0501171].

[46] W.J. Percival et al., *Baryon acoustic oscillations in the sloan digital sky survey data release 7 galaxy sample*, *Mon. Not. Roy. Astron. Soc.* **401** (2010) 2148–2168.

[47] A. Coc and E. Vangioni, *Primordial nucleosynthesis*, *Int. J. Mod. Phys. E* **26** (2017) 1741002 [1707.01004].

[48] S.D.M. White et al., *Clustering in a neutrino-dominated universe*, *Astrophys. J* **274** (1983) L1.

[49] V. Springel et al., *Simulating the joint evolution of quasars, galaxies and their large-scale distribution*, *Nature* **435** (2005) 629 [astro-ph/0504097].

[50] T. Ishiyama et al., *The v2GC simulations: Quantifying the dark side of the universe in the Planck cosmology*, *Publ. Astron. Soc. Jpn* **67** (2015) .

[51] M. Sparre et al., *The star formation main sequence and stellar mass assembly of galaxies in the Illustris simulation*, *Mon. Not. Roy. Astron. Soc.* **447** (2015) 3548 [1409.0009].

[52] M. Vogelsberger et al., *Properties of galaxies reproduced by a hydrodynamic simulation*, *Nature* **509** (2014) 177 [1405.1418].

[53] M. Vogelsberger et al., *ETHOS – an effective theory of structure formation: dark matter physics as a possible explanation of the small-scale CDM problems*, *Mon. Not. Roy. Astron. Soc.* **460** (2016) 1399 [1512.05349].

[54] L. Bergström, *Nonbaryonic dark matter: Observational evidence and detection methods*, *Rept. Prog. Phys.* **63** (2000) 793 [hep-ph/0002126].

[55] J.L. Feng, *Dark Matter Candidates from Particle Physics and Methods of Detection*, *Ann. Rev. Astron. Astrophys.* **48** (2010) 495 [1003.0904].

[56] E.A. Baltz, *Dark matter candidates*, *eConf* **C040802** (2004) L002 [astro-ph/0412170].

[57] N. Bernal et al., *The Dawn of FIMP Dark Matter: A Review of Models and Constraints*, *Int. J. Mod. Phys. A* **32** (2017) 1730023 [1706.07442].

[58] L.J. Hall et al., *Freeze-In Production of FIMP Dark Matter*, *JHEP* **03** (2010) 080 [0911.1120].

[59] A. Boyarsky et al., *Sterile neutrino Dark Matter*, *Prog. Part. Nucl. Phys.* **104** (2019) 1 [1807.07938].

[60] M. Ibe et al., *Why three generations?*, *Phys. Lett. B* **758** (2016) 365 [1602.03003].

[61] M. Dutra, *Origins for dark matter particles : from the "WIMP miracle" to the "FIMP wonder"*, theses, Université Paris Saclay (COmUE), Feb., 2019.

[62] J.L. Feng, *Supersymmetry and cosmology*, *eConf* **C0307282** (2003) L11 [hep-ph/0405215].

[63] G. Steigman et al., *Precise Relic WIMP Abundance and its Impact on Searches for Dark Matter Annihilation*, *Phys. Rev. D* **86** (2012) 023506 [1204.3622].

[64] H. Baer et al., *Dark matter production in the early Universe: beyond the thermal WIMP paradigm*, *Phys. Rept.* **555** (2015) 1 [1407.0017].

[65] G.C. Branco et al., *Theory and phenomenology of two-Higgs-doublet models*, *Phys. Rept.* **516** (2012) 1 [1106.0034].

[66] A. Birkedal et al., *Little Higgs dark matter*, *Phys. Rev. D* **74** (2006) 035002 [hep-ph/0603077].

[67] I. Garcia Garcia et al., *Twin Higgs WIMP Dark Matter*, *Phys. Rev. D* **92** (2015) 055034 [1505.07109].

[68] H.-C. Cheng et al., *Kaluza-Klein dark matter*, *Phys. Rev. Lett.* **89** (2002) 211301 [hep-ph/0207125].

[69] P.J. Fox, *TASI Lectures on WIMPs and Supersymmetry*, *PoS* **TASI2018** (2019) 005.

[70] S.P. Martin, *A Supersymmetry primer*, *Adv. Ser. Direct. High Energy Phys.* **18** (1998) 1 [hep-ph/9709356].

[71] H. Baer et al., *Status of weak scale supersymmetry after LHC Run 2 and ton-scale noble liquid WIMP searches*, *Eur. Phys. J. ST* **229** (2020) 3085 [2002.03013].

[72] L. Roszkowski et al., *WIMP dark matter candidates and searches—current status and future prospects*, *Rept. Prog. Phys.* **81** (2018) 066201 [1707.06277].

[73] B.D. Wandelt et al., *Selfinteracting dark matter*, in *4th International Symposium on Sources and Detection of Dark Matter in the Universe (DM 2000)*, pp. 263–274, 6, 2000 [astro-ph/0006344].

[74] M. Boylan-Kolchin et al., *Too big to fail? the puzzling darkness of massive milky way subhaloes*, *Mon. Not. R. Astron. Soc.: Lett.* **415** (2011) L40–L44.

[75] N.E. Mavromatos et al., *Self-interacting dark matter*, in *14th Marcel Grossmann Meeting on Recent Developments in Theoretical and Experimental General Relativity, Astrophysics, and Relativistic Field Theories*, vol. 1, pp. 639–666, 2017, DOI.

[76] A. Robertson et al., *What does the Bullet Cluster tell us about self-interacting dark matter?*, *Mon. Not. Roy. Astron. Soc.* **465** (2017) 569 [1605.04307].

[77] J.S. Bullock and M. Boylan-Kolchin, *Small-Scale Challenges to the ΛCDM Paradigm*, *Ann. Rev. Astron. Astrophys.* **55** (2017) 343 [1707.04256].

[78] S. Tulin and H.-B. Yu, *Dark Matter Self-interactions and Small Scale Structure*, *Phys. Rept.* **730** (2018) 1 [1705.02358].

[79] Y. Hochberg et al., *Mechanism for Thermal Relic Dark Matter of Strongly Interacting Massive Particles*, *Phys. Rev. Lett.* **113** (2014) 171301 [1402.5143].

[80] P. Arias et al., *Wispy cold dark matter*, *JCAP* **2012** (2012) 013–013.

[81] P.W. Graham et al., *Experimental searches for the axion and axion-like particles*, *Annu. Rev. Nucl. Part. Sci.* **65** (2015) 485–514.

[82] N. Blinov et al., *Dark matter targets for axionlike particle searches*, *Phys. Rev. D* **100** (2019) .

[83] P. Di Vecchia et al., *Round Table on Axions and Axion-like Particles*, *PoS* (2019) 034 [1902.06567].

[84] G. Grilli di Cortona et al., *The QCD axion, precisely*, *JHEP* **01** (2016) 034 [1511.02867].

[85] D. Cadamuro and J. Redondo, *Cosmological bounds on pseudo nambu-goldstone bosons*, *JCAP* **2012** (2012) 032–032.

[86] D. Cadamuro et al., *Cosmological bounds on sub-mev mass axions*, *JCAP* **2011** (2011) 003–003.

[87] A. Ringwald, *Exploring the role of axions and other wisps in the dark universe*, *Phys. Dark Univ.* **1** (2012) 116.

[88] C. Thorpe-Morgan et al., *Theseus insights into axionlike particles, dark photon, and sterile neutrino dark matter*, *Phys. Rev. D* **102** (2020) .

[89] J. Jaeckel and M. Spannowsky, *Probing mev to 90 gev axion-like particles with lep and lhc*, *Phys. Lett. B* **753** (2016) 482–487.

[90] M.J. Dolan et al., *Revised constraints and belle ii sensitivity for visible and invisible axion-like particles*, *JHEP* **2017** (2017) .

[91] P.F. Depta et al., *Robust cosmological constraints on axion-like particles*, *JCAP* **2020** (2020) 009–009.

[92] U. Ellwanger and S. Moretti, *Possible Explanation of the Electron Positron Anomaly at 17 MeV in 8Be Transitions Through a Light Pseudoscalar*, *JHEP* **11** (2016) 039 [1609.01669].

[93] A.J. Krasznahorkay et al., *New evidence supporting the existence of the hypothetic X17 particle*, 1910.10459.

[94] F. Takahashi et al., *Xenon1t excess from anomaly-free axionlike dark matter and its implications for stellar cooling anomaly*, *Phys. Rev. Lett.* **125** (2020) 161801.

[95] P. Athron et al., *Global fits of axion-like particles to xenon1t and astrophysical data*, *JHEP* **2021** (2021) .

[96] D. Buttazzo et al., *Xenon1t excess from electron recoils of non-relativistic dark matter*, *Phys. Lett. B* **817** (2021) 136310.

[97] M. Milgrom, *MOND vs. dark matter in light of historical parallels*, *Stud. Hist. Phil. Sci. B* **71** (2020) 170 [1910.04368].

[98] M. Milgrom, *MOND theory*, *Can. J. Phys.* **93** (2015) 107 [1404.7661].

[99] B. Famaey and S. McGaugh, *Modified Newtonian Dynamics (MOND): Observational Phenomenology and Relativistic Extensions*, *Living Rev. Rel.* **15** (2012) 10 [1112.3960].

[100] M. Milgrom, *A modification of the Newtonian dynamics - Implications for galaxies.*, *Astrophys. J* **270** (1983) 371.

[101] F. Lelli et al., *The small scatter of the baryonic Tully-Fisher relation*, *Astrophys. J* **816** (2015) 14.

[102] S.S. McGaugh et al., *The Baryonic Tully-Fisher relation*, *Astrophys. J. Lett.* **533** (2000) L99 [astro-ph/0003001].

[103] A.A. Ponomareva et al., *From light to baryonic mass: the effect of the stellar mass-to-light ratio on the Baryonic Tully–Fisher relation*, *Mon. Not. Roy. Astron. Soc.* **474** (2017) 4366.

[104] S.S. McGaugh et al., *Radial Acceleration Relation in Rotationally Supported Galaxies*, *Phys. Rev. Lett.* **117** (2016) 201101 [1609.05917].

[105] M.H. Chan and A. Del Popolo, *The radial acceleration relation in galaxy clusters*, *Mon. Not. Roy. Astron. Soc.* **492** (2020) 5865 [2001.06141].

[106] S. Dodelson, *The Real Problem with MOND*, *Int. J. Mod. Phys. D* **20** (2011) 2749 [1112.1320].

[107] C. Skordis and T. Zlosnik, *New Relativistic Theory for Modified Newtonian Dynamics*, *Phys. Rev. Lett.* **127** (2021) 161302 [2007.00082].

[108] G.W. Angus, *Is an 11 eV sterile neutrino consistent with clusters, the cosmic microwave background and modified Newtonian dynamics?*, *Mon. Not. Roy. Astron. Soc.* **394** (2009) 527.

[109] S.S. McGaugh, *Distinguishing between CDM and MOND: Predictions for the microwave background*, *Astrophys. J. Lett.* **523** (1999) L99 [astro-ph/9907409].

[110] S.S. McGaugh, *A tale of two paradigms: the mutual incommensurability of ΛCDM and MOND*, *Can. J. Phys.* **93** (2015) 250 [1404.7525].

[111] G.W. Angus et al., *Can MOND take a bullet? Analytical comparisons of three versions of MOND beyond spherical symmetry*, *Mon. Not. Roy. Astron. Soc.* **371** (2006) 138 [astro-ph/0606216].

[112] X. Li et al., *Finslerian MOND vs. observations of Bullet Cluster 1E0657-558*, *Mon. Not. Roy. Astron. Soc.* **428** (2013) 2939 [1209.3086].

[113] D. Scott et al., *Cosmological difficulties with modified Newtonian dynamics (or, La Fin du MOND?)*, astro-ph/0104435.

[114] M. Kaplinghat and M.S. Turner, *How Cold Dark Matter Theory Explains Milgrom's Law*, *Astrophys. J. Lett.* **569** (2002) L19 [astro-ph/0107284].

[115] C.M. Ho et al., *Quantum Gravity and Dark Matter*, *Gen. Rel. Grav.* **43** (2011) 2567 [1105.2916].

[116] A. Lightman, *Oral History Interviews : Vera Rubin*, *American Institute of Physics* (1989) [https://www.aip.org/history-programs/niels-bohr-library/oral-histories/33963].

[117] F. Vargas, *Dans les bois éternels*, J'ai lu, translated by Sîan Reynolds (2009).

[118] J. Conrad, *Indirect Detection of WIMP Dark Matter: a compact review*, in *Interplay between Particle and Astroparticle physics*, 11, 2014 [1411.1925].

[119] O. Buchmueller et al., *Search for dark matter at colliders*, *Nature Phys.* **13** (2017) 217 [1912.12739].

[120] R. Catena, *Dark matter directional detection in non-relativistic effective theories*, *JCAP* **07** (2015) 026 [1505.06441].

[121] B.J. Kavanagh, *New directional signatures from the nonrelativistic effective field theory of dark matter*, *Phys. Rev. D* **92** (2015) 023513 [1505.07406].

[122] D.N. Spergel, *Motion of the earth and the detection of weakly interacting massive particles*, *Phys. Rev. D* **37** (1988) 1353.

[123] S.T. James Binney, *Galactic Dynamics*, Princeton Series in Astrophysics, Princeton University Press, 2nd ed. (2008).

[124] A.M. Green, *Effect of halo modeling on WIMP exclusion limits*, *Phys. Rev. D* **66** (2002) 083003 [astro-ph/0207366].

[125] F. Mayet et al., *A review of the discovery reach of directional Dark Matter detection*, *Phys. Rept.* **627** (2016) 1.

[126] J. Billard, *Détection directionnelle de matière sombre avec MIMAC*, thesis, Grenoble, 2012.

[127] L. Necib et al., *Inferred Evidence for Dark Matter Kinematic Substructure with SDSS-Gaia*, *Astrophys. J.* **874** (2019) 3.

[128] Y. Tao, *Directional Detection Of Galactic Dark Matter With A MIMAC Detector*, Ph.D. thesis, 2020.

[129] G. Jungman et al., *Supersymmetric dark matter*, *Phys. Rept.* **267** (1996) 195 [hep-ph/9506380].

[130] D.G. Cerdeno and A.M. Green, *Direct detection of WIMPs*, 1002.1912.

[131] Q. Riffard, *Détection directionnelle de matière sombre non-baryonique avec MIMAC*, Ph.D. thesis, 2015.

[132] J. Engel, *Nuclear form-factors for the scattering of weakly interacting massive particles*, *Phys. Lett. B* **264** (1991) 114.

[133] G. Belanger et al., *Dark matter direct detection rate in a generic model with micrOMEGAs 2.2*, *Comput. Phys. Commun.* **180** (2009) 747 [0803.2360].

[134] P. Gondolo, *Recoil momentum spectrum in directional dark matter detectors*, *Phys. Rev. D* **66** (2002) 103513.

[135] J. Billard et al., *Direct detection of dark matter—APPEC committee report**, *Rept. Prog. Phys.* **85** (2022) 056201 [2104.07634].

[136] K. Freese et al., *Colloquium: Annual modulation of dark matter*, *Rev. Mod. Phys.* **85** (2013) 1561 [1209.3339].

[137] M. Schumann, *Direct Detection of WIMP Dark Matter: Concepts and Status*, *J. Phys. G* **46** (2019) 103003 [1903.03026].

[138] R. Bernabei et al., *First model independent results from DAMA/LIBRA-phase2*, *Nucl. Phys. Atom. Energy* **19** (2018) 307 [1805.10486].

[139] C.E. Aalseth et al., *Search for an Annual Modulation in a P-type Point Contact Germanium Dark Matter Detector*, *Phys. Rev. Lett.* **107** (2011) 141301 [1106.0650].

[140] G. Angloher et al., *Results from 730 kg days of the CRESST-II dark matter search*, *EPJC* **72** (2012) .

[141] D. Buttazzo et al., *Annual modulations from secular variations: relaxing DAMA?*, *JHEP* **04** (2020) 137 [2002.00459].

[142] J.H. Davis et al., *Quantifying the evidence for Dark Matter in CoGeNT data*, *JCAP* **08** (2014) 014 [1405.0495].

[143] COSINE-100 collaboration, *Strong constraints from COSINE-100 on the DAMA dark matter results using the same sodium iodide target*, *Sci. Adv.* **7** (2021) abk2699 [2104.03537].

[144] R. Essig et al., *Direct Detection of Sub-GeV Dark Matter*, *Phys. Rev. D* **85** (2012) 076007 [1108.5383].

[145] R. Essig et al., *Direct Detection of sub-GeV Dark Matter with Semiconductor Targets*, *JHEP* **05** (2016) 046 [1509.01598].

[146] K.D. Nakamura et al., *Detection capability of the Migdal effect for argon and xenon nuclei with position-sensitive gaseous detectors*, *PTEP* **2021** (2021) 013C01 [2009.05939].

[147] M. Ibe et al., *Migdal Effect in Dark Matter Direct Detection Experiments*, *JHEP* **03** (2018) 194 [1707.07258].

[148] M.S. Rapaport et al., *K-shell electron shake-off accompanying alpha decay*, *Phys. Rev. C* **11** (1975) 1740.

[149] M.S. Rapaport et al., *L- and M-shell electron shake-off accompanying alpha decay*, *Phys. Rev. C* **11** (1975) 1746.

[150] C. Couratin et al., *First measurement of pure electron shakeoff in the beta decay of trapped 6he+ ions*, *Phys. Rev. Let.* **108** (2012) .

[151] X. Fabian et al., *Electron shakeoff following the β^+ decay of $^{19}Ne^+$ and $^{35}Ar^+$ trapped ions*, *Phys. Rev. A* **97** (2018) 023402 [1802.01298].

[152] M.J. Dolan et al., *Directly detecting sub-gev dark matter with electrons from nuclear scattering*, *Phys. Rev. Lett.* **121** (2018) 101801.

[153] J. Monroe and P. Fisher, *Neutrino Backgrounds to Dark Matter Searches*, *Phys. Rev. D* **76** (2007) 033007 [0706.3019].

[154] J. Billard et al., *Implication of neutrino backgrounds on the reach of next generation dark matter direct detection experiments*, *Phys. Rev. D* **89** (2014) 023524 [1307.5458].

[155] F. Ruppin et al., *Complementarity of dark matter detectors in light of the neutrino background*, *Phys. Rev. D* **90** (2014) 083510 [1408.3581].

[156] C.A.J. O'Hare, *New Definition of the Neutrino Floor for Direct Dark Matter Searches*, *Phys. Rev. Lett.* **127** (2021) 251802 [2109.03116].

[157] J.H. Davis, *Dark Matter vs. Neutrinos: The effect of astrophysical uncertainties and timing information on the neutrino floor*, *JCAP* **03** (2015) 012 [1412.1475].

[158] S. Sassi et al., *Solar neutrinos and dark matter detection with diurnal modulation*, *Phys. Rev. D* **104** (2021) [2103.08511].

[159] XENON collaboration, *Excess electronic recoil events in XENON1T*, *Phys. Rev. D* **102** (2020) 072004 [2006.09721].

[160] J. Billard et al., *Directional detection as a strategy to discover galactic dark matter*, *Phys. Let. B* **691** (2010) 156.

[161] N. Bozorgnia et al., *Ring-like features in directional dark matter detection*, *JCAP* **06** (2012) 037 [1111.6361].

[162] N. Bozorgnia et al., *Aberration features in directional dark matter detection*, *JCAP* **08** (2012) 011 [1205.2333].

[163] C.A.J. O'Hare et al., *Readout strategies for directional dark matter detection beyond the neutrino background*, *Phys. Rev. D* **92** (2015) 063518 [1505.08061].

[164] B. Morgan et al., *Directional statistics for WIMP direct detection*, *Phys. Rev. D* **71** (2005) 103507 [astro-ph/0408047].

[165] A.M. Green and B. Morgan, *The median recoil direction as a WIMP directional detection signal*, *Phys. Rev. D* **81** (2010) 061301 [1002.2717].

[166] J. Billard et al., *Assessing the discovery potential of directional detection of Dark Matter*, *Phys. Rev. D* **85** (2012) 035006 [1110.6079].

[167] J. Billard et al., *Markov chain monte carlo analysis to constrain dark matter properties with directional detection*, *Phys. Rev. D* **83** (2011) .

[168] J. Billard et al., *Directional detection of dark matter with MIMAC: WIMP identification and track reconstruction*, *Jour. of Phys.: Conf. Series* **309** (2011) 012015.

[169] J.B.R. Battat et al., *Readout technologies for directional WIMP Dark Matter detection*, *Phys. Rept.* **662** (2016) 1 [1610.02396].

[170] N.S. Phan et al., *The novel properties of SF_6 for directional dark matter experiments*, *JINST* **12** (2017) P02012 [1609.05249].

[171] D.P. Snowden-Ifft, *Discovery of Multiple, Ionization-Created Anions in Gas Mixtures Containing CS2 and O2*, 1308.0354.

[172] DRIFT collaboration, *First background-free limit from a directional dark matter experiment: results from a fully fiducialised DRIFT detector*, *Phys. Dark Univ.* **9-10** (2015) 1 [1410.7821].

[173] Y. Tao, C. Beaufort et al., *Track length measurement of $^{19}F^{+}$ ions with the MIMAC directional Dark Matter detector prototype*, *Nucl. Instrum. Meth. A* **985** (2021) 164569 [1903.02159].

[174] Y. Tao, C. Beaufort et al., *Dark Matter Directionality Detection performance of the Micromegas-based μTPC-MIMAC detector*, *Nucl. Instrum. Meth. A* **1021** (2022) 165412 [2003.11812].

[175] J. Battat et al., *Improved sensitivity of the DRIFT-IId directional dark matter experiment using machine learning*, *JCAP* **2021** (2021) 014.

[176] J.B.R. Battat et al., *First measurement of nuclear recoil head-tail sense in a fiducialised WIMP dark matter detector*, *JINST* **11** (2016) P10019 [1606.05364].

[177] Q. Riffard et al., *MIMAC low energy electron-recoil discrimination measured with fast neutrons*, *JINST* **11** (2016) P08011 [1602.01738].

[178] Q. Riffard et al., *First detection of radon progeny recoil tracks by MIMAC*, *JINST* **12** (2017) P06021 [1504.05865].

[179] C. Beaufort et al., *Directionality and head-tail recognition in the keV-range with the MIMAC detector by deconvolution of the ionic signal*, 2112.12469.

[180] T. Ikeda et al., *Direction-sensitive dark matter search with the low-background gaseous detector NEWAGE-0.3b"*, *PTEP* **2021** (2021) 063F01 [2101.09921].

[181] T. Hashimoto et al., *Development of a low-alpha-emitting μ-pic for newage direction-sensitive dark-matter search*, *AIP Conf. Proc.* **1921** (2018) 070001.

[182] K. Nakamura et al., *Direction-sensitive dark matter search with gaseous tracking detector NEWAGE-0.3b'*, *PTEP* **2015** (2015) .

[183] K. Miuchi et al., *Direction-sensitive dark matter search results in a surface laboratory*, *Phys. Lett. B* **654** (2007) 58.

[184] T. Ikeda et al., *Development of a negative ion micro TPC detector with SF_6 gas for the directional dark matter search*, *JINST* **15** (2020) P07015 [2004.09706].

[185] M. Leyton, *Directional dark matter detection with the dmtpc m 3 experiment*, *Jour. of Phys.: Conf. Series* **718** (2016) 042035.

[186] C. Deaconu et al., *Measurement of the directional sensitivity of Dark Matter Time Projection Chamber detectors*, *Phys. Rev. D* **95** (2017) 122002 [1705.05965].

[187] J.B.R. Battat et al., *The Dark Matter Time Projection Chamber 4Shooter directional dark matter detector: Calibration in a surface laboratory*, *Nucl. Instrum. Meth. A* **755** (2014) 6.

[188] S. Ahlen et al., *First Dark Matter Search Results from a Surface Run of the 10-L DMTPC Directional Dark Matter Detector*, *Phys. Lett. B* **695** (2011) 124 [1006.2928].

[189] F.D. Amaro et al., *The CYGNO Experiment*, *Instruments* **6** (2022) 6 [2202.05480].

[190] E. Baracchini et al., *CYGNO: a gaseous TPC with optical readout for dark matter directional search*, *JINST* **15** (2020) C07036 [2007.12627].

[191] I.A. Costa et al., *Performance of Optically Readout GEM-based TPC with a 55Fe source*, 1905.04066.

[192] S. Gorbunov and N. Konovalova, *New experiment newsdm for direct searches for heavy dark matter particles*, *Phys. At. Nucl.* **83** (2020) 83.

[193] N. Polukhina and N. Starkov, *New experiment for wimp direct search (newsdm)*, *EPJ Web Conf.* **191** (2018) 02023.

[194] A. Golovatiuk, *Directional dark matter search with the NEWSdm experiment*, *J. Phys. Conf. Ser.* **2156** (2021) 012044.

[195] G. De Lellis, *Directional dark matter search with the newsdm experiment*, *EPJ Web Conf.* **209** (2019) 01019.

[196] C. Couturier et al., *Dark Matter directional detection: comparison of the track direction determination*, *JCAP* **01** (2017) 027 [1607.08157].

[197] M. Cadeddu et al., *Directional dark matter detection sensitivity of a two-phase liquid argon detector*, *JCAP* **01** (2019) 014 [1704.03741].

[198] R. Ebadi et al., *Directional Detection of Dark Matter Using Solid-State Quantum Sensing*, in *2022 Snowmass Summer Study*, 3, 2022 [2203.06037].

[199] T. Naka and K. Miuchi, *CYGNUS 2013: 4th workshop on directional detection of dark matter*, *J. Phys. Conf. Ser.* **469** (2013) 011001.

[200] S.E. Vahsen et al., *CYGNUS: Feasibility of a nuclear recoil observatory with directional sensitivity to dark matter and neutrinos*, 2008.12587.

[201] C.A.J. O'Hare et al., *Recoil imaging for dark matter, neutrinos, and physics beyond the Standard Model*, in *2022 Snowmass Summer Study*, 3, 2022 [2203.05914].

[202] "Researchers grapple with XENON1T excess." https://cerncourier.com/a/researchers-grapple-with-xenon1t-excess/, Accessed: 2022-04-19.

[203] R.D. Peccei and H.R. Quinn, *CP Conservation in the Presence of Pseudoparticles*, *Phys. Rev. Lett.* **38** (1977) 1440.

[204] S. Weinberg, *A new light boson?*, *Phys. Rev. Lett.* **40** (1978) 223.

[205] F. Wilczek, *Problem of strong p and t invariance in the presence of instantons*, *Phys. Rev. Lett.* **40** (1978) 279.

[206] J. Preskill et al., *Cosmology of the Invisible Axion*, *Phys. Lett. B* **120** (1983) 127.

[207] L.F. Abbott and P. Sikivie, *A Cosmological Bound on the Invisible Axion*, *Phys. Lett. B* **120** (1983) 133.

[208] M. Dine and W. Fischler, *The Not So Harmless Axion*, *Phys. Lett. B* **120** (1983) 137.

[209] N. Arkani-Hamed et al., *The Hierarchy problem and new dimensions at a millimeter*, *Phys. Lett. B* **429** (1998) 263 [hep-ph/9803315].

[210] N. Arkani-Hamed et al., *Phenomenology, astrophysics and cosmology of theories with submillimeter dimensions and TeV scale quantum gravity*, *Phys. Rev. D* **59** (1999) 086004 [hep-ph/9807344].

[211] L. DiLella and K. Zioutas, *Observational evidence for gravitationally trapped massive axion(-like) particles*, *Astropart. Phys.* **19** (2003) 145 [astro-ph/0207073].

[212] K. Zioutas et al., *Quiet sun x-rays as signature for new particles*, *Astrophys. J.* **607** (2004) 575 [astro-ph/0403176].

[213] D. Naples et al., *Search for axion-like particles from the sun in an underground negative-ion TPC*, *Nucl. Phys. B Proc. Suppl.* **134** (2004) 130.

[214] B. Morgan et al., *Searches for solar Kaluza–Klein axions with gas TPCs*, *Astropart. Phys.* **23** (2005) 287.

[215] R. Battesti et al., *Axion searches in the past, at present, and in the near future*, in *Axions: Theory, Cosmology, and Experimental Searches*, (Berlin, Heidelberg), pp. 199–237, Springer Berlin Heidelberg (2008), DOI.

[216] XMASS collaboration, *Search for solar Kaluza–Klein axions by annual modulation with the XMASS-I detector*, *PTEP* **2017** (2017) 103C01 [1707.08995].

[217] NEWS-G collaboration, *Solar Kaluza-Klein axion search with NEWS-G*, *Phys. Rev. D* **105** (2022) 012002 [2109.03562].

[218] M. Bastero-Gil, C. Beaufort and D. Santos, *Solar axions in large extra dimensions*, *JCAP* **10** (2021) 048 [2107.13337].

[219] I.G. Irastorza, *An introduction to axions and their detection*, *SciPost Phys. Lect. Notes* **45** (2022) 1 [2109.07376].

[220] J.M. Pendlebury et al., *Revised experimental upper limit on the electric dipole moment of the neutron*, *Phys. Rev. D* **92** (2015) 092003 [1509.04411].

[221] R.D. Peccei, *QCD, strong CP and axions*, *J. Korean Phys. Soc.* **29** (1996) S199 [hep-ph/9606475].

[222] E. Masso et al., *On axion thermalization in the early universe*, *Phys. Rev. D* **66** (2002) 023004 [hep-ph/0203221].

[223] G.G. Raffelt, *Axions: Motivation, limits and searches*, *J. Phys. A* **40** (2007) 6607 [hep-ph/0611118].

[224] P. Sikivie, *Axion Cosmology*, *Lect. Notes Phys.* **741** (2008) 19 [astro-ph/0610440].

[225] G.G. Raffelt, *Particle physics from stars*, *Ann. Rev. Nucl. Part. Sci.* **49** (1999) 163 [hep-ph/9903472].

[226] L.D. Duffy and K. van Bibber, *Axions as Dark Matter Particles*, *New J. Phys.* **11** (2009) 105008 [0904.3346].

[227] G. Raffelt, *Stellar evolution limits on axion properties*, *Nucl. Phys. B Proc. Suppl.* **72** (1999) 43 [hep-ph/9805400].

[228] A. Ringwald, *Axions and Axion-Like Particles*, in *49th Rencontres de Moriond on Electroweak Interactions and Unified Theories*, pp. 223–230, 2014 [1407.0546].

[229] E. Massó and R. Toldrà, *Photon spectrum produced by the late decay of a cosmic neutrino background*, *Phys. Rev. D* **60** (1999) .

[230] J.H. Hubbell, *Photon cross-sections, attenuation coefficients, and energy absorption coefficients from 10-KeV to 100-GeV* (1969).

[231] T. Dalton et al., *Probing the physical properties of the intergalactic medium using gamma-ray bursts*, *Mon. Not. Roy. Astron. Soc.* **502** (2021) 5981.

[232] A. Cooray, *Extragalactic Background Light: Measurements and Applications*, 1602.03512.

[233] G. Nordström, *On the possibility of unifying the electromagnetic and the gravitational fields*, *Phys. Zeit.* **15** (1914) 504.

[234] F. Ravndal, *Scalar gravitation and extra dimensions*, *Comment. Phys. Math. Soc. Sci. Fenn.* **166** (2004) 151 [gr-qc/0405030].

[235] N. Arkani-Hamed et al., *Large extra dimensions: A new arena for particle physics*, *Phys. Today* **55** (2002) 35.

[236] M. Tanabashi and others (Particle Data Group), *Extra dimensions*, *Phys.Rev.D* **98** (2018) 030001 [https://pdg.lbl.gov/2018/listings/rpp2018-list-extra-dimensions.pdf].

[237] D.J. Kapner et al., *Tests of the gravitational inverse-square law below the dark-energy length scale*, *Phys. Rev. Lett.* **98** (2007) 021101 [hep-ph/0611184].

[238] CMS collaboration, *Search for new physics in final states with an energetic jet or a hadronically decaying W or Z boson and transverse momentum imbalance at $\sqrt{s} = 13$ TeV*, *Phys. Rev. D* **97** (2018) 092005 [1712.02345].

[239] S. Hannestad and G.G. Raffelt, *Supernova and neutron star limits on large extra dimensions reexamined*, *Phys. Rev. D* **67** (2003) 125008 [hep-ph/0304029].

[240] S. Chang et al., *Axion model in extra dimensions with TeV scale gravity*, *Phys. Rev. D* **61** (2000) 084005 [hep-ph/9908515].

[241] N. Arkani-Hamed et al., *Stabilization of submillimeter dimensions: The New guise of the hierarchy problem*, *Phys. Rev. D* **63** (2001) 064020 [hep-th/9809124].

[242] I. Antoniadis et al., *New dimensions at a millimeter to a Fermi and superstrings at a TeV*, *Phys. Lett. B* **436** (1998) 257 [hep-ph/9804398].

[243] E. Witten, *Strong coupling expansion of Calabi-Yau compactification*, *Nucl. Phys. B* **471** (1996) 135 [hep-th/9602070].

[244] J.D. Lykken, *Weak scale superstrings*, *Phys. Rev. D* **54** (1996) 3693 [hep-th/9603133].

[245] K.R. Dienes et al., *Extra space-time dimensions and unification*, *Phys. Lett. B* **436** (1998) 55 [hep-ph/9803466].

[246] D. Dumitru and S. Nandi, *Gauge coupling unification with large extra dimensions*, *Phys. Rev. D* **62** (2000) 046006 [hep-ph/9906514].

[247] G. Dvali and S. Tye, *Brane inflation*, *Phys. Lett. B* **450** (1999) 72 [hep-ph/9812483].

[248] N. Arkani-Hamed et al., *Rapid asymmetric inflation and early cosmology in theories with submillimeter dimensions*, *Nucl. Phys. B* **567** (2000) 189 [hep-ph/9903224].

[249] G. Dvali and G. Gabadadze, *Nonconservation of global charges in the brane universe and baryogenesis*, *Phys. Lett. B* **460** (1999) 47 [hep-ph/9904221].

[250] N. Arkani-Hamed and M. Schmaltz, *Hierarchies without symmetries from extra dimensions*, *Phys. Rev. D* **61** (2000) 033005 [hep-ph/9903417].

[251] K.R. Dienes et al., *Neutrino oscillations without neutrino masses or heavy mass scales: A Higher dimensional seesaw mechanism*, *Nucl. Phys. B* **557** (1999) 25 [hep-ph/9811428].

[252] N. Arkani-Hamed et al., *Neutrino masses from large extra dimensions*, *Phys. Rev. D* **65** (2001) 024032 [hep-ph/9811448].

[253] K.R. Dienes et al., *Invisible axions and large radius compactifications*, *Phys. Rev.* **D62** (2000) 105023 [hep-ph/9912455].

[254] L. Di Lella et al., *Search for solar Kaluza-Klein axions in theories of low scale quantum gravity*, *Phys. Rev.* **D62** (2000) 125011 [hep-ph/0006327].

[255] J.E. Kim and G. Carosi, *Axions and the Strong CP Problem*, *Rev. Mod. Phys.* **82** (2010) 557 [0807.3125].

[256] G.G. Raffelt, *Astrophysical axion bounds diminished by screening effects*, *Phys. Rev. D* **33** (1986) 897.

[257] S. Turck-Chieze et al., *Solar neutrino emission deduced from a seismic model*, *Astrophys. J. Lett.* **555** (2001) L69.

[258] G.G. Raffelt, *Plasmon Decay Into Low Mass Bosons in Stars*, *Phys. Rev. D* **37** (1988) 1356.

[259] N.V. Mikheev et al., *On the resonant production of axions in a magnetar magnetosphere*, *JETP Letters* **90** (2009) 668.

[260] A. Caputo et al., *Revisiting longitudinal plasmon-axion conversion in external magnetic fields*, *Phys. Rev. D* **101** (2020) 123004 [2005.00078].

[261] E. Guarini et al., *Production of axionlike particles from photon conversions in large-scale solar magnetic fields*, *Phys. Rev. D* **102** (2020) 123024 [2010.06601].

[262] K. Van Tilburg, *Stellar basins of gravitationally bound particles*, *Phys. Rev. D* **104** (2021) 023019 [2006.12431].

[263] W. DeRocco et al., *First indirect detection constraints on axions in the Solar basin*, 2205.05700.

[264] P. Catapano, *Georges Charpak: hardwired for science*, *CERN Courier* **49** (2009) [https://cds.cern.ch/record/1734347].

[265] V. Lepeltier, *Review on TPC's*, *J. Phys. Conf. Ser.* **65** (2007) 012001.

[266] T. Francke and V. Peskov, *Micropattern Gaseous Detectors*, in *Innovative Detectors for Supercolliders*, pp. 158–179, Aug., 2004, DOI [physics/0404035].

[267] D. Santos et al., *MIMAC: A micro-tpc matrix for dark matter directional detection*, *J. Phys. Conf. Ser.* **460** (2013) 012007 [1304.2255].

[268] Y. Giomataris et al., *Micromegas: a high-granularity position-sensitive gaseous detector for high particle-flux environments*, *Nucl. Instrum. Meth. A* **376** (1996) 29.

[269] C. Couturier et al., *Directional detection of Dark Matter with the MIcro-tpc MAtrix of Chambers*, in *51st Rencontres de Moriond on Cosmology*, pp. 165–170, 7, 2016 [1607.08765].

[270] J. Billard et al., *Three-dimensional track reconstruction for directional Dark Matter detection*, *JCAP* **04** (2012) 006 [1202.3372].

[271] I. Giomataris et al., *Micromegas in a bulk*, *Nucl. Instrum. Meth. A* **560** (2006) 405 [physics/0501003].

[272] F.J. Iguaz et al., *Micromegas detector developments for Dark Matter directional detection with MIMAC*, *JINST* **6** (2011) P07002 [1105.2056].

[273] O. Bourrion et al., *Dedicated front-end and readout electronics developments for real time 3D directional detection of dark matter with MIMAC*, *EAS Publ. Ser.* **53** (2012) 129 [1109.2002].

[274] J.P. Richer et al., *Development and validation of a 64 channel front end ASIC for 3D directional detection for MIMAC*, *JINST* **6** (2011) C11016 [1110.4579].

[275] S.F. Biagi, *Monte Carlo simulation of electron drift and diffusion in counting gases under the influence of electric and magnetic fields*, *Nucl. Instrum. Meth. A* **421** (1999) 234.

[276] D. Combecher, *Measurement of w values of low-energy electrons in several gases*, *Radiat. Res.* **84** (1980) 189.

[277] I. Krajcar Bronic et al., *The mean energy required to form an ion pair for low-energy photons and electrons in polyatomic gases*, *Radiat. Res.* **115** (1988) 213.

[278] M. Tanabashi et al., *(Particle Data Group)*, *Phys. Rev. D* **98** (2018) 030001.

[279] P. Sigmund, *Particle Penetration and Radiation Effects: General Aspects and Stopping of Swift Point Charges* (01, 2006), 10.1007/3-540-31718-X.

[280] I. Krajcar Bronić, *W values and fano factors for electrons in rare gases and rare gas mixtures*, *Ionizing Radiation (Hoshasen)* **24** (1998) 101.

[281] A. Pansky et al., *Fano factor and the mean energy per ion pair in counting gases, at low x-ray energies*, *J. Appl. Phys.* **82** (1997) 871.

[282] D. Durnford et al., *Novel approach to assess the impact of the Fano factor on the sensitivity of low-mass dark matter experiments*, *Phys. Rev. D* **98** (2018) 103013 [1808.06967].

[283] L. Rolandi et al., *Particle Detection with Drift Chambers* (01, 2008), 10.1007/978-3-540-76684-1.

[284] M. Inokuti, *Ionization yields in gases under electron irradiation*, *Radiat. Res.* **64** (1975) 6.

[285] E. Waibel and B. Grosswendt, *Spatial energy dissipation profiles, w values, backscatter coefficients, and ranges for low-energy electrons in methane*, *Nucl. Instrum. Meth.* **211** (1983) 487.

[286] B. Smith and J. Booz, *Experimental results on w-values and transmission of low energy electrons in gases*, *6th Symposium on microdosimetry* (1978) 759.

[287] E. Waibel and G.J. Willems, *W values for low-energy protons in methane-based tissue equivalent gas and its constituents*, *Phys. Med. Biol.* **37** (1992) 249.

[288] B. Grosswendt et al., *W Values of Protons Slowed Down in Molecular Hydrogen*, *Radiat. Prot. Dosim.* **70** (1997) 37.

[289] I. Krajcar Bronic, *A Study of Argon-Isobutane Mixtures in a Proportional Counter: Gas Amplification, W Value, and Energy Resolution*, *Radiat. Prot. Dosim.* **61** (1995) 263.

[290] I. Krajcar-Bronić and D. Srdoč, *A comparison of calculated and measured w values in tissue-equivalent gas mixtures*, *Radiat. Res.* **137** (1994) 18.

[291] I. Krajcar Bronić et al., *The w values for photons and electrons in mixtures of argon and alkanes*, *Radiat. res.* **125** (1991) 1.

[292] L.G. Christophorou et al., *Electron interactions with CF4*, *J. Phys. Chem. Ref. Data* **25** (1996) 1341.

[293] I. Torres et al., *Electron-impact dissociative ionization of fluoromethanes CHF3 and CF4*, *J. Phys. B* **35** (2002) 2423.

[294] M. Saca and R.A. Lee, *A determination of w and g(h2) values for methyl fluoride and fluoroform*, *Can. J. Chem.* **48** (1970) 1812.

[295] C. Jiao et al., *Electron impact ionization and ion reactions in n-butane*, *J. Phys. D* **40** (2007) 409.

[296] P. Sorensen, *Atomic limits in the search for galactic dark matter*, *Phys. Rev. D* **91** (2015) 083509.

[297] J.F. Ziegler et al., *SRIM – The stopping and range of ions in matter (2010)*, *Nucl. Instrum. Meth. B* **268** (2010) 1818.

[298] J. Lindhard et al., *Integral equations governing radiation effects*, *Mat. Fys. Medd. Dan. Vid. Selsk* **33** (1963) 1 [https://www.osti.gov/biblio/4701226].

[299] F. Bezrukov et al., *Interplay between scintillation and ionization in liquid xenon dark matter searches*, *Astropart. Phys.* **35** (2011) 119–127.

[300] D. Santos et al., *Ionization quenching factor measurement of helium 4*, 0810.1137.

[301] EDELWEISS collaboration, *Measurement of the response of heat-and-ionization germanium detectors to nuclear recoils*, *Nucl. Instrum. Meth. A* **577** (2007) 558 [astro-ph/0607502].

[302] B. Al Atoum et al., *Electron Transport in Gaseous Detectors with a Python-based Monte Carlo Simulation Code*, *Comput. Phys. Commun.* **254** (2020) 107357 [1910.06983].

[303] L. Christophorou and R. Blaunstein, *Electron attachment in gases and liquids*, *Chem. Phys. Lett.* **12** (1971) 173.

[304] F. Sauli, *Gaseous radiation detectors: Fundamentals and applications*, Cambridge University Press (2014), DOI.

[305] W.S. Anderson et al., *Electron attachment, effective ionization coefficient, and electron drift velocity for CF4 gas mixtures*, *Nucl. Instrum. Meth. A* **323** (1992) 273.

[306] T. Zerguerras et al., *Single-electron response and energy resolution of a Micromegas detector*, *Nucl. Instrum. Meth. A* **608** (2009) 397 [0901.2882].

[307] S. Ramo, *Currents induced by electron motion*, *Proc. Ire.* **27** (1939) 584.

[308] W. Shockley, *Currents to conductors induced by a moving point charge*, *J. Appl. Phys.* **9** (1938) 635.

[309] R. Veenhof, *GARFIELD, recent developments*, *Nucl. Instrum. Meth. A* **419** (1998) 726.

[310] T. Heubrandtner et al., *Static electric fields in an infinite plane condenser with one or three homogeneous layers*, *Nucl. Instrum. Meth. A* **489** (2002) 439.

[311] L.-A. Hamel and M. Julien, *Generalized demonstration of ramo's theorem with space charge and polarization effects*, *Nucl. Instrum. Meth. A* **597** (2008) 207.

[312] P. De Visschere, *The validity of ramo's theorem*, *Solid-state Elec.* **33** (1990) 455.

[313] M. Dris and T. Alexopoulos, *Signal Formation in Various Detectors*, 1406.3217.

[314] D. Maire, *Development of a TPC for energy and fluence references in low energies neutronic fields (from 8 keV to 5 MeV)*, Ph.D. thesis, 2015.

[315] Y.M. Gavrilyuk et al., *High-resolution ion pulse ionization chamber with air filling for the ^{222}Rn decays detection*, *Nucl. Instrum. Meth. A* **801** (2015) 27 [1508.04295].

[316] W. Jolly et al., *Core-electron binding energies for gaseous atoms and molecules*, *At. Data Nucl. Data Tables* **31** (1984) 433.

[317] R.B. Firestone et al., *8th edition of the Table of Isotopes: 1998 Update*, in *APS Division of Nuclear Physics Meeting Abstracts*, APS Meeting Abstracts, p. BD.11, Oct., 1997 [https://ui.adsabs.harvard.edu/abs/1997APS..DNP..BD11F].

[318] NEWS-G collaboration, *Measurements of the ionization efficiency of protons in methane*, 2201.09566.

[319] E. Ferrer-Ribas et al., *Micromegas detector developments for MIMAC*, in *EAS Pub. Ser.*, vol. 53, pp. 165–171, 2012, DOI.

[320] R. Halir and J. Flusser, *Numerically stable direct least squares fitting of ellipses*, 1998.

[321] N. Sauzet et al., *Fast neutron spectroscopy from 1 MeV up to 15 MeV with Mimac-FastN, a mobile and directional fast neutron spectrometer*, *Nucl. Instrum. Meth. A* **965** (2020) 163799 [1906.03878].

[322] A. Hocker et al., *TMVA - Toolkit for Multivariate Data Analysis*, physics/0703039.

[323] V. Chazal et al., *Neutron background measurements in the underground laboratory of Modane*, *Astropart. Phys.* **9** (1998) 163.

[324] R. Hodák et al., *Characterization and long-term performance of the radon trapping facility operating at the modane underground laboratory*, *J. Phys. G* **46** (2019) .

[325] J. Burnens et al., *A spark-resistant bulk-micromegas chamber for high-rate applications*, 1011.5370.

[326] J. Galán et al., *Characterization and simulation of resistive-MPGDs with resistive strip and layer topologies*, *Nucl. Instrum. Meth. A* **732** (2013) 229 [1304.2057].

[327] W. Riegler, *Electric fields, weighting fields, signals and charge diffusion in detectors including resistive materials*, *JINST* **11** (2016) P11002 [1602.07949].

[328] J. Galán, *Signal propagation and spark mitigation in resistive strip read-outs*, *JINST* **7** (2012) C04009.

[329] C. Couturier et al., *Cathode signal in a TPC directional detector: implementation and validation measuring the drift velocity*, *JINST* **12** (2017) P11020 [1711.07301].

[330] J.F. Muraz et al., *A table-top ion and electron beam facility for ionization quenching measurement and gas detector calibration*, *Nucl. Instrum. Meth. A* **832** (2016) 214.

[331] R. Kersevan and M. Ady, *Recent developments of Monte-Carlo codes Molflow+ and Synrad+*, in *10th International Particle Accelerator Conference*, 6, 2019, DOI.

[332] H. Demers et al., *Three-dimensional electron microscopy simulation with the casino monte carlo software*, *Scanning* **33** (2011) 135.

[333] J.-H. Cheng et al., *Determination of the total absorption peak in an electromagnetic calorimeter*, *Nucl. Instrum. Meth. A* **827** (2016) 165 [1603.04433].

[334] V. Gressier et al., *AMANDE: a new facility for monoenergetic neutron fields production between 2 keV and 20 MeV*, *Rad. Prot. Dos.* **110** (2004) 49.

[335] V. Gressier et al., *Characterization of a measurement reference standard and neutron fluence determination method in IRSN monoenergetic neutron fields*, *Metrologia* **51** (2014) 431.

[336] D. Maire et al., *Neutron Energy Reconstruction and Fluence Determination at 27 keV with the LNE-IRSN-MIMAC MicroTPC Recoil Detector*, *IEEE Trans. Nucl. Sci.* **63** (2016) 1934.

[337] M. Cosack et al., *Monoenergetic neutrons of energies from 05 kev to 40 kev via the reaction 45Sc(p,n)45Ti*, *Fifth symposium on neutron dosimetry* (1985) 597.

[338] D. Tanuro, *Trop tard pour être pessimistes !*, Editions Textuel, translated from French by our means (2020).

[339] F.V. Böhmer et al., *Simulation of Space-Charge Effects in an Ungated GEM-based TPC*, *Nucl. Instrum. Meth. A* **719** (2013) 101 [1209.0482].

[340] E. Hellbär, *Ion Movement and Space-Charge Distortions in the ALICE TPC*, 2015, https://cds.cern.ch/record/2746298.

[341] M. Mooney, *The MicroBooNE Experiment and the Impact of Space Charge Effects*, in *Meeting of the APS Division of Particles and Fields*, 11, 2015 [1511.01563].

[342] S. Rossegger et al., *Analytical solutions for space charge fields in tpc drift volumes*, *Nucl. Instrum. Meth. A* **632** (2011) 52.

[343] P. Bhattacharya et al., *Investigation of Ion Backflow in Bulk Micromegas Detectors*, *JINST* **10** (2015) P09017 [1605.02896].

[344] C.S. Deaconu, *A model of the directional sensitivity of low-pressure CF4 dark matter detectors*, Ph.D. thesis, 2015. https://dspace.mit.edu/handle/1721.1/99314.

[345] S.I. Sandler and E.A. Mason, *Kinetic-theory deviations from blanc's law of ion mobilities*, *Chem. Phys.* **48** (1968) 2873.

[346] E. Carbone et al., *Data needs for modeling low-temperature non-equilibrium plasmas: The lxcat project, history, perspectives and a tutorial*, *Atoms* **9** (2021) .

[347] https://lxcat.net/.

[348] https://www.gnu.org/software/gsl/doc/html/index.html.

[349] H. Skullerud, *The stochastic computer simulation of ion motion in a gas subjected to a constant electric field*, *J. Phys. D* **1** (2002) 1567.

[350] J.D. Jackson, *Classical electrodynamics; 2nd ed.*, Wiley, New York, NY (1975).

[351] R. Brun and F. Rademakers, *Root — an object oriented data analysis framework*, *Nucl. Instrum. Meth. A* **389** (1997) 81.

[352] M. Angelou, *I Know Why the Caged Bird Sings*, Random House (1969).

[353] G. Gerbier et al., *NEWS : a new spherical gas detector for very low mass WIMP detection*, 1401.7902.

[354] I. Giomataris et al., *A novel large-volume spherical detector with proportional amplification read-out*, *JINST* **3** (2008) 09007 [0807.2802].

[355] NEWS-G collaboration, *Quenching factor measurements of neon nuclei in neon gas*, *Phys. Rev. D* (2021) [2109.01055].

[356] O. Guillaudin et al., *Quenching factor measurement in low pressure gas detector for directional dark matter search*, *EAS Pub. Ser.* **53** (2012) 119–127.

[357] B. Tampon et al., *Ionization Quenching Factor measurement of 1 keV to 25 keV protons in Isobutane gas mixture*, vol. 153, p. 01014, 2017, DOI.

[358] A. Hitachi, *Bragg-like curve for dark matter searches: binary gases*, *Radiat. Phys. Chem.* **77** (2008) 1311 [0804.1191].

[359] D.M. Mei et al., *A Model of Nuclear Recoil Scintillation Efficiency in Noble Liquids*, *Astropart. Phys.* **30** (2008) 12 [0712.2470].

[360] F. Izraelevitch et al., *A Measurement of the Ionization Efficiency of Nuclear Recoils in Silicon*, *JINST* **12** (2017) P06014 [1702.00873].

[361] A.E. Chavarria et al., *Measurement of the ionization produced by sub-keV silicon nuclear recoils in a CCD dark matter detector*, *Phys. Rev. D* **94** (2016) 082007 [1608.00957].

[362] Y. Sarkis et al., *Study of the ionization efficiency for nuclear recoils in pure crystals*, *Phys. Rev. D* **101** (2020) 102001.

[363] L. Balogh et al., *The NEWS-G detector at SNOLAB*, 2205.15433.

[364] NEWS-G collaboration, *Precision laser-based measurements of the single electron response of spherical proportional counters for the NEWS-G light dark matter search experiment*, *Phys. Rev. D* **99** (2019) 102003 [1902.08960].

[365] NEWS-G collaboration, *Copper electroplating for background suppression in the NEWS-G experiment*, *Nucl. Instrum. Meth. A* **988** (2021) 164844 [2008.03153].

[366] I. Savvidis et al., *Low energy recoil detection with a spherical proportional counter*, *Nucl. Instrum. Meth. A* **877** (2018) 220 [1606.02146].

[367] Q. Arnaud et al., *Spherical proportional counter: A review of recent developments*, *Jour. of Phys.: Conf. Series* **1029** (2018) 012006.

[368] A. Giganon et al., *A multiball read-out for the spherical proportional counter*, *JINST* **12** (2017) P12031 [1707.09254].

[369] I. Giomataris et al., *A resistive ACHINOS multi-anode structure with DLC coating for spherical proportional counters*, *JINST* **15** (2020) 11 [2003.01068].

[370] NEWS-G collaboration, *First results from the NEWS-G direct dark matter search experiment at the LSM*, *Astropart. Phys.* **97** (2018) 54 [1706.04934].

[371] F. Duncan et al., *The construction and anticipated science of SNOLAB*, *Ann. Rev. Nucl. Part. Sci.* **60** (2010) 163.

[372] S. Cecchini and M. Spurio, *Atmospheric muons: experimental aspects*, 1208.1171.

[373] B. Henke et al., *X-ray interactions: Photoabsorption, scattering, transmission, and reflection at e = 50-30,000 ev, z = 1-92*, *At. Data Nucl. Data Tables* **54** (1993) 181.

[374] D. Srdoč and B. Clark, *Generation and spectroscopy of ultrasoft x-rays by non-dispersive methods*, *Nucl. Instrum. Meth.* **78** (1970) 305.

[375] I.K. Bronić and B. Grosswendt, *Ionization yield formation in argon-isobutane mixtures as measured by a proportional-counter method*, *Nucl. Instrum. Meth. B* **117** (1996) 5.

[376] EDELWEISS collaboration, *Measurement of the response of heat-and-ionization germanium detectors to nuclear recoils*, *Nucl. Instrum. Meth. A* **577** (2007) 558 [astro-ph/0607502].

[377] CDMS collaboration, *Nuclear-Recoil Energy Scale in CDMS II Silicon Dark-Matter Detectors*, *Nucl. Instrum. Meth. A* **905** (2018) 71 [1803.02903].

[378] J.I. Collar et al., *Response of CsI[Na] to Nuclear Recoils: Impact on Coherent Elastic Neutrino-Nucleus Scattering (CEνNS)*, *Phys. Rev. D* **100** (2019) 033003 [1907.04828].

[379] SCENE collaboration, *Measurement of Scintillation and Ionization Yield and Scintillation Pulse Shape from Nuclear Recoils in Liquid Argon*, *Phys. Rev. D* **91** (2015) 092007 [1406.4825].

[380] L. Thulliez et al., *Calibration of nuclear recoils at the 100 eV scale using neutron capture*, *JINST* **16** (2021) P07032 [2011.13803].

[381] A. Wapstra, *Energy calibration for 2–13 mev gamma rays*, *Nucl. Instrum. Meth. A* **292** (1990) 671.

[382] I. Katsioulas et al., *Ionisation quenching factors from W-values in pure gases for rare event searches*, *Astropart. Phys.* **141** (2022) 102707 [2105.01414].

[383] V. Rubin, *Seeing dark matter in the Andromeda galaxy*, *Physics Today* **59** (2006) .

[384] D. Maire et al., *First Measurement of a 127 keV Neutron Field with a μ-TPC Spectrometer*, *IEEE Trans. Nucl. Sci.* **61** (2014) 2090 [1310.6837].

[385] S. Burgos et al., *First measurement of the Head-Tail directional nuclear recoil signature at energies relevant to WIMP dark matter searches*, *Astropart. Phys.* **31** (2009) 261 [0809.1831].

[386] M.B. Chadwick et al., *ENDF/B-VII.0: Next Generation Evaluated Nuclear Data Library for Nuclear Science and Technology*, *Nucl. Data Sheets* **107** (2006) 2931.

[387] GEANT4 collaboration, *GEANT4–a simulation toolkit*, *Nucl. Instrum. Meth. A* **506** (2003) 250.

[388] F. Wilczek, *The Birth of Axions*, *Current Contents* **16** (1991) 8.

[389] B. Lakić et al., *Axions and large extra dimensions*, in *Axions: Theory, Cosmology, and Experimental Searches*, (Berlin, Heidelberg), pp. 73–82, Springer Berlin Heidelberg (2008), DOI.

[390] R. Horvat et al., *CERN Axion Solar Telescope as a probe of large extra dimensions*, *Phys. Rev. D* **69** (2004) 125011 [astro-ph/0312030].

[391] R. Horvat et al., *Recent searches for solar axions and large extra dimensions*, *Phys. Rev. D* **65** (2002) 087701 [hep-ph/0112224].

[392] I.G. Hannah et al., *First limits on the 3-200 keV X-ray spectrum of the quiet Sun using RHESSI*, *Astrophys. J.* **659** (2007) L77 [astro-ph/0702726].

[393] I. Hannah et al., *Constraining the Hard X-ray Properties of the Quiet Sun with New RHESSI Observations*, *Astrophys. J.* **724** (2010) 487 [1009.2918].

[394] J. Sylwester et al., *SphinX Measurements of the 2009 Solar Minimum X-Ray Emission*, *Astrophys. J.* **751** (2012) 111 [1203.6809].

[395] B. Sylwester et al., *Analysis of Quiescent Corona X-ray Spectra from SphinX During the 2009 Solar Minimum*, *Solar Phys.* **294** (2019) 176 [1912.03082].

[396] A. Boyarsky et al., *Strategy for searching for a dark matter sterile neutrino*, *Phys. Rev. Lett.* **97** (2006) .

[397] A. Boyarsky et al., *Constraints on the parameters of radiatively decaying dark matter from the dark matter halo of the Milky Way and Ursa Minor*, *Astron. Astrophys.* **471** (2007) 51 [astro-ph/0610961].

[398] A. Boyarsky et al., *Constraints on decaying dark matter from XMM-Newton observations of M31*, *Mon. Not. Roy. Astron. Soc.* **387** (2008) 1361–1373.

[399] A. Boyarsky et al., *Constraining DM properties with SPI*, *Mon. Not. Roy. Astron. Soc.* **387** (2008) 1345 [0710.4922].

[400] L. Glesener et al., *Accelerated electrons observed down to <7 keV in a NuSTAR solar microflare*, *Astrophys. J. Lett.* **891** (2020) L34 [2003.12864].

[401] H. Schlattl et al., *Helioseismological constraint on solar axion emission*, *Astropart. Phys.* **10** (1999) 353 [hep-ph/9807476].

[402] P. Gondolo and G.G. Raffelt, *Solar neutrino limit on axions and keV-mass bosons*, *Phys. Rev.* **D79** (2009) 107301 [0807.2926].

[403] N. Vinyoles et al., *New axion and hidden photon constraints from a solar data global fit*, *JCAP* **2015** (2015) 015 [1501.01639].

[404] K.R. Dienes et al., *Kaluza-klein towers in the early universe: Phase transitions, relic abundances, and applications to axion cosmology*, *Phys. Rev. D* **95** (2017) .

[405] J. Overduin and P. Wesson, *Dark matter and background light*, *Phys. Rept.* **402** (2004) 267–406.

[406] J. Lean, *The sun's variable radiation and its relevance for earth*, *Annu. Rev. Astron. Astrophys* **35** (1997) 33.

[407] J. Madej and A. Różańska, *X-ray irradiated model stellar atmospheres – III. Compton redistribution of thermal external irradiation*, *Mon. Not. Roy. Astron. Soc.* **347** (2004) 1266.

[408] B.J. Wargelin et al., *Chandra observations of the 'dark' moon and geocoronal solar - wind charge transfer*, *Astrophys. J.* **607** (2004) 596 [astro-ph/0402247].

[409] E. Armengaud et al., *Conceptual Design of the International Axion Observatory (IAXO)*, *JINST* **9** (2014) T05002 [1401.3233].

[410] S.K. et al., *The Spectrometer/Telescope for Imaging X-rays (STIX)*, *Astron. Astrophys.* **642** (2020) A15.

[411] M. Berger et al., *XCOM: Photon Cross Section Database (version 1.5)*, *National Institute of Standards and Technology, Gaithersburg, MD* (2010) .

[412] J. Redondo, *Solar axion flux from the axion-electron coupling*, *JCAP* **12** (2013) 008 [1310.0823].

Abstract

While converging observations motivate the existence of a dark matter accounting for 84% of the mass of the universe, the nature of such a particle remains unknown and extensive searches are carried out, in particular concerning the WIMP and the axion. Directional detection correlates the direction of WIMP-induced nuclear recoils with the motion of the solar system in the galactic dark matter halo, thus providing a unique signature for WIMP identification even beyond the neutrino floor. The gaseous directional detector MIMAC measures the energy of a particle and reconstructs its track in 3D. This thesis investigates directional detection in the keV-range, for probing WIMPs with masses down to GeV, only accessible when operating the MIMAC detector at high gain ($> 10^4$). We demonstrate that in these conditions, the interplay between the ionic and the electronic signals distorts the track reconstruction while it improves the detector sensitivity. The development of `SimuMimac`, a new simulation tool reproducing the MIMAC measurements, leads us to a procedure for extracting the electronic current from any measurements, allowing for head-tail recognition and providing new directional tools. We evaluate the directional performance of the MIMAC detector by the reconstruction of mono-energetic neutron spectra at 27 keV and 8 keV, achieving a 15° angular resolution and thus demonstrating for the first time that a detector can successfully access directionality in the keV-range. In this low-energy region, a nuclear recoil only releases part of its energy as ionization, and the kinetic energy must be inferred from the Ionization Quenching Factor (IQF). We measure the IQF of protons in methane in the keV-range and we conclude that this crucial quantity should no longer be determined by simulations. When operating at high gain, the MIMAC detector could also search for axions propagating in large extra dimensions. In this framework, axions with masses in the keV-range would be trapped into the solar gravitational field, for which we derive a number density of 10^7 cm^{-3} on Earth. By refining the model and updating the constraints, we reduce by orders of magnitude the $a \to \gamma\gamma$ event rate for the higher-dimensional axion in a MIMAC-like detector. The axion remains a promising probe for extra dimensions while it offers explanations for multiple puzzling solar observations.

Résumé

Alors que de multiples observations indiquent que la matière noire représenterait 84% de la masse de l'univers, la nature de cette particule demeure inconnue et les recherches expérimentales s'intensifient, notamment concernant le WIMP et l'axion. La détection directionnelle constitue une signature unique pour l'identification de WIMP par la corrélation entre la direction des reculs nucléaires induits par des WIMP et le mouvement du système solaire dans le halo galactique. Le détecteur gazeux directionnel MIMAC mesure l'énergie d'une particule et reconstruit sa trace en 3D. Cette thèse étudie la détection directionnelle dans la gamme du keV qui n'est accessible qu'en travaillant à haut gain ($> 10^4$). Nous démontrons que dans ces conditions, le signal ionique vient perturber la reconstruction de la trace tout en améliorant la sensibilité du détecteur. L'implémentation de `SimuMimac`, un nouvel outil de simulation en accord avec les données, nous a conduit à élaborer une procédure pour extraire le courant électronique dans nos mesures, permettant de ce fait la reconnaissance du sens de la trace et le développement de nouveaux outils directionnels. Les performances directionnelles de MIMAC sont évaluées par la reconstruction de spectres neutroniques mono-énergétiques à 27 keV et 8 keV. Nous obtenons une résolution angulaire de 15° ce qui démontre pour la première fois qu'un détecteur peut accéder à la directionnalité dans la gamme du keV. À ces basses énergies, seule une partie de l'énergie d'un recul nucléaire est déposée sous forme d'ionisation et l'énergie cinétique doit donc être déterminée à l'aide du facteur de quenching en ionisation. Nous avons mesuré ce facteur pour des protons dans du méthane et nous en concluons que cette quantité essentielle doit systématiquement être mesurée et non plus simulée. En travaillant à haut gain, MIMAC pourrait aussi détecter des axions se propageant dans des dimensions supplémentaires. Une partie de ces axions pourrait être attrapée dans le champ gravitationnel solaire et nous calculons une densité de 10^7 cm^{-3} au niveau de la Terre. En affinant le modèle et les contraintes correspondantes, nous réduisons de plusieurs ordres de grandeur le taux d'événement $a \to \gamma\gamma$ dans un détecteur tel que MIMAC. En plus d'expliquer plusieurs observations solaires, l'axion constitue une particule prometteuse pour tester l'existence de dimensions supplémentaires.